Hot cracking elimination strategies in aluminium alloys fabricated by PBF-LB/M

Giuseppe Del Guercio

Thesis

Submitted to University of Nottingham

for the degree of

Doctor of Philosophy

Faculty of Engineering

December 2022

To all my 83040 people.
Life is taking us apart,
but our hearts have never been closer.

Acknowledgments

In my early twenties, while I was spending countless hours at Polito fighting the laws of thermodynamics and getting poisoned by the 25 cents coffee, I fantasised about writing this section of my PhD thesis. I was so naive... in my mind, this would have been the last moment of my student life, the end of notions to be learnt and books to be read. As I am now actually writing these lines, I completely understand how wrong those thoughts were and I am fully aware of how the end of a PhD should not just answer your last research questions but inspire new ones. I would not have gained this awareness without the many people who supported me throughout this long journey.

First and foremost, I would like to express my immense gratitude to my supervisors Dr Marco Simonelli, Dr Nesma Aboulkhair, Prof Chris Tuck, Prof Adam Clare, and Prof Graham McCartney.

Marco, these few lines cannot describe how thankful I am to have found you at the beginning of this PhD. You taught me a lot of the lessons that I learned in these three years. You showed me how to approach a research question, develop plausible scientific pathways and reach the goals of my project. You always inspired something in me, either during the countless hours of our meetings or just over lunch and coffee breaks. Thanks for your patience, honesty, support and most importantly your friendship. Thank you.

Nesma, I want to express my gratitude to you for your endless guidance and help despite the time difference between the UK and the UAE. I am grateful not only for your advice, but for reminding me that a PhD is not just a series of questions to be answered, but lessons to be learnt. Thanks for your trust. I will do my best.

I want to thank Chris for his knowledgeable supervision and continuous support throughout these three years. Chris, from you I learned how to think beyond the boundaries of my research project and exploit its merits. You taught me precious lessons that will be key in my career, thanks a million.

Adam, thanks for inspiring me to enlarge the aims and scopes of this project. You taught me how to explain double the concepts in half of the time in a simple and engaging way. Thanks for your continuous presence, for all the valuable out-of-the-box questions that you placed in my brain, for all the laughs… and for Friday morning pastries. Thank you.

Graham, it is hard to fully describe how privileged and thankful I am for your presence in this supervision team. Your guidance always pushed me one step ahead and I feel that the numerous discussions we had in the last years were just priceless, your knowledge simply inspired me in pushing my limits forward. You've been my compass, thank you for your time and trust, I learned a lot from you.

I would like to thank all the technicians that I met at UoN, your support represents a core aspect of all research projects. A special thanks goes to Mark E. for creating a welcoming lab environment and Mark H. for helping me understand the working principles of the AM400…and how to fix it when it doesn't want to print! I want to express my sincere gratitude to Seb, for running the CFD simulations, for the countless times spent writing on a whiteboard together and for all the pints shared. Without your help, I would have never been able to write a Chapter of this thesis. Thank you. An additional thanks goes to Negar, Arielle, Shreeja, Diego, Alasdair, Huseyin, Zou and everyone else at CfAM who made my PhD such an enjoyable experience.

Abstract

Laser Powder Bed Fusion (PBF-LB/M) has shown to be an industrially relevant manufacturing process for the production of parts characterised by unique designs and made of several engineering materials. However, high-strength aluminium (Al) alloys, one of the most attractive material classes due to their great strength-to-weight ratio, suffer from extensive hot cracking which is yet to be fully understood and overcome. The aim of the present thesis is thus to determine multiple pathways to avoid the formation of hot cracks in high-strength Al alloys processed by PBF-LB/M.

The cracking behaviour of AA2024, a well-known material characterised by great mechanical and corrosion properties, was investigated as a function of various PBF-LB/M processing parameters and chemical composition. The presence of cracks was found to be largely affected by the laser scan speed, with slower regimes characterised by lower cracking intensities. Moreover, two different cracking morphologies were observed in the microstructures, suggesting that multiple cracking phenomena occurred during PBF-LB/M fabrication. It was suggested that hot cracks initiated during a single melting event with subsequent solid-state propagation resulting in the extensive presence of such features in the as-build condition. It was found that chemical composition directly affected hot crack formation, with an addition of 3 wt% of Ni to AA2024 being beneficial in limiting the formation of hot cracks and following cold propagation.

The mechanism leading to the formation of hot cracks were investigated coupling experimental observations and modelling results obtained via a multi-physics simulation of a AA2024 track surface melted using various laser regimes. This allowed the reconstruction of the spatio-temporal opportunity to form hot cracks, given by the

development of detrimental intergranular pressure drops. The results showed that volumes of material solidified during the inter-pulse temporal domain are associated with higher hot cracking driving forces. Moreover, pressure drops beyond the critical threshold for hot crack formation were found in the same regimes where such features were experimentally observed. A new material agnostic descriptor of hot cracking, referred to as 'global hot crack propensity', was then proposed to not only address the role of chemical composition on hot crack formation, but also that of processing parameters. Based on this identified crack-free regime, the build rate of AA2024 was improved by 150% without the formation of defects or loss of mechanical performance.

The previous investigations conducted on the effects of both chemical composition and manufacturing regimes on hot crack formation led to the identification of an experimental/modelling methodology aiming at the design of a bespoke crack-free alloy characterised by exceptional build rates and mechanical properties. The CALPHAD (CALculation of PHAse Diagrams) approach and micro-segregation models coupled with targeted powder-free experiments to empirically validate the simulation results proved to be an effective pathway to reduce designing times and costs. With the help of a new single metric to predict the intrinsic hot crack propensity of a given material, the custom ACN001 composition was identified, gas atomised and experimentally produced via PBF-LB/M. The results showed the absence of cracks in the as-build microstructure produced in scan speed regimes paired with extreme hot crack driving forces. Moreover, the ACN001 was found to be characterised by exceptional strength due to the presence of a fine solidification structures' network.

This thesis has developed an understanding of the various phenomena affecting hot crack formation in high-strength Al-alloys manufactured by PBF-LB/M. Moreover, the

developed knowledge on the hot cracking phenomenon could be applied to other rapid solidification processes, such as, Direct Energy Deposition (DED). The results illustrated in the present research work not only represent significant scientific achievements towards the understanding of the hot cracking phenomenon but provide practical pathways to increase the applications of high-strength Al-alloys in relevant industrial sectors.

Publications

G. Del Guercio, D.G. McCartney, N.T. Aboulkhair, C. Tuck, M. Simonelli, "Laser calorimetry as porosity minimisation method in PBF-LB/M", The laser user, Issue 102, Autumn 2021, ISSN 1755-5140

G. Del Guercio, D.G. McCartney, N.T. Aboulkhair, S. Robertson, R. Maclachlan, C. Tuck, M. Simonelli, "Cracking behaviour of high-strength AA2024 aluminium alloy produced by Laser Powder Bed Fusion", Additive Manufacturing, Volume 54, 2022, 102776, ISSN 2214-8604, https://doi.org/10.1016/j.addma.2022.102776

G. Del Guercio, M. Simonelli, "Increasing the build rate of high-strength aluminium alloy produced by laser powder bed fusion", Optics & Laser Technology, Volume 161, 2023, 109133, ISSN 0030-3992, https://doi.org/10.1016/j.optlastec.2023.109133

G. Del Guercio, S. Faron, D.G. McCartney, S. Robertson, N.T. Aboulkhair, C. Tuck, A.T. Clare, M. Simonelli, "Understanding the stochastic nature of hot cracking in additive manufacturing", - under review in npj Computational Materials

Conferences

MS&T20, virtual event, November 2-6, 2020. "High strength Al-alloys by PBF-LB/M: preliminary material characterization and implication for alloy development", <u>G. Del Guercio</u>, D.G. McCartney, N.T. Aboulkhair, C. Tuck, M. Simonelli.

TMS21, virtual event, March 15-18, 2021. "Characterization of cracks formed in AA2024 and implications for alloy design", <u>G. Del Guercio</u>, D.G. McCartney, N.T. Aboulkhair, C. Tuck, M. Simonelli.

TMS22, in person event, February 27 – March 3, 2022. "Towards new high-strength Al-alloys specifically designed for PBF-LB/M", <u>G. Del Guercio</u>, D.G. McCartney, N.T. Aboulkhair, C. Tuck, M. Simonelli.

TMS22, , in person event, February 27 – March 3, 2022. "Modelling informed strategy for the additive manufacturing of high-strength of Al-alloys", <u>G. Del Guercio</u>, W.J. Reynolds, S. Faron, A.T. Clare, M. Simonelli.

AAMS22, in person event, September 12-14, 2022. "Design and characterization of new high-strength Al-alloy composition for PBF-LB/M", <u>G. Del Guercio</u>, D.G. McCartney, N.T. Aboulkhair, C. Tuck, M. Simonelli.

TMS23, in person event, March 19-23, 2023. "A Powder-free Methodology to Develop New High-strength Al-alloys with Unique Microstructures and Mechanical properties", <u>G. Del Guercio</u>, D.G. McCartney, C. Tuck, M. Simonelli.

TMS23, in person event, March 19-23, 2023. "CFD Informed Strategy for the 3D Printing of Crack-free High-strength Al-alloys", <u>G. Del Guercio</u>, D.G. McCartney, S. Faron, A.T. Clare, M. Simonelli.

Table of contents

List of figures

List of tables

Abbreviations

PBF-LB/M	Laser Powder Bed Fusion
AM	Additive Manufacturing
3D	Three-dimensional
CAD	Computer Aided Design
EBM	Electron Beam Melting
DED	Direct Energy Deposition
SLM	Selective Laser Melting
BD	Building direction
CW	Continuous wave
PW	Pulsed wave
MMAM	Multi-material additive manufacturing
VED	Volumetric energy density
LOF	Lack-of-fusion
CSC	Crack susceptibility coefficient
RDG	Rappaz-Drezet-Gremaud
HCS	Hot-crack-susceptibility
UTS	Ultimate tensile strength

FCC-Al	Face-centred-cubic aluminium phase
CET	Columnar to equiaxed transition
GR	Grain refiner
OR	Orientation relationship
CP	Close-pack
GB	Grain boundary
PLC	Portevin-Le Chaterlier
RBV	Reduced build bolume
PD	Point distance
ET	Exposure time
DT	Delay time
PDV	Point distance variation
HIP	Hot isostatic pressing
OM	Optical microscopy
CCL	Cumulative crack length
SEM	Scanning electron Microscopy
SE	Secondary electron
SEI	Secondary electron imaging
EBSD	Electron backscattered diffraction

BSE	Back scattered electron
BSEI	Back scattered electron imaging
EDX, EDAX, EDS	Energy dispersive X-ray spectroscopy
TEM	Transmission electron microscopy
FIB	Focused ion beam
BF	Bright-field
HAADF	High-angle annular dark-field
FEG	Field emission gun
STEM	Scanning transmission electron microscope
XRD	X-ray diffraction
ICP-OES	Inductively coupled plasma optical emission spectroscopy
RAM	Resonant acoustic mixing
APS	Average particle size
LSD	Laser size diffraction
PSD	Particle size distribution
LMC	Laser micro calorimetry
CALPHAD	Calculation of phase diagrams
CFD	Computational fluid dynamics
UDF	User defined functions

VOF	Volume-of-Fluid
DPM	Discrete phase method
IPF	Inverse pole figure
PF	Pole figure
DC	Direct chill
HAGB	High angle grain boundary
TD	Transverse direction
CTE	Coefficient of thermal expansion
HCRZ	High cooling rate zone
LCRZ	Low cooling rate zone
HAZ	Heat affected zone
S/L	Solid/liquid
YS	Yield Strength
UTS	Ultimate Tensile Strength
EF	Elongation at Failure

Nomenclature

P	Laser power
v	Laser scan speed
h_d	Hatch distance
θ	Rotation angle increment in the meander scan strategy
Δz	Layer thickness
T	Temperature
T_{plat}	Platform temperature
L_F	Non-dimensional lack of fusion number
T_{peak}	Maximum temperature reached in the melt pool
T_{liq}	Liquidus temperature
T_{sol}	Solidus temperature
w	Melt pool width
d	Melt pool depth
A	Powder absorptivity
k	Thermal conductivity
ρ	Density
c_p	Specific heat

ΔH	Specific enthalpy
h_s	Enthalpy of melting
T_m	Melting temperature
σ	Laser spot radius
F	Force acting on the solid-liquid interface
γ	Solid-liquid interfacial tension
S	Cross sectional area
t_{film}	Liquid film thickness
f_s	Volume/molar fraction of solid
f_l	Volume/molar fraction of liquid
t_v	Time over which the alloy is vulnerable to cracking
t_R	Time available for stress relaxation
Δp_{max}	Pressure drop at the root of the interdendritic channel
λ	Dendrite arm spacing
G	Thermal gradient
β	Liquid-to-solid shrinkage factor
μ	Viscosity of the liquid
v_T	Solidification rate
$\dot{\varepsilon}$	Strain rate

$\hat{z}$	Interdendritic direction parallel to the dendrite growth direction
$v_{\hat{z}}$	Velocity associate with the liquid backfilling the interdendritic channel
d_{spot}	Laser spot diameter
ΔT_{UC}	Constitutional undercooling
P_{UC}	Undercooling factor
m_L	Slope of the liquidus line
k_e	Equilibrium partitioning coefficient
C_0	Nominal mass fraction
Q_{GRF}	Growth restriction factor
r	Development of constitutional undercooling
d_{eff}	Effective interatomic spacing
Δdir	Close-packed directions' match
th_{dir}	CP direction threshold
d_{hkl}	Interplanar spacing
Δpla	Close-packed planes' match
th_{pla}	CP plane threshold
ϕ	Angle between two matching crystallographic planes

ε_s	Surface mismatch crystallographic parameter
$\varepsilon_{\%}$	Lattice misfit parameter
a, b, c	Lattice parameters
C	Circularity
d_{max}	Major axis length
d_{min}	Minor axis length
φ_{angle}	Orientation angle
$d_{max,f}$	Maximum Feret diameter
$d_{min,f}$	Minimum Feret diameter
t	Time
φ	Volume fraction of metal or gas
Φ	Sum of the volume fraction of metal and gas
$\vec{u}$	Flow velocity
$\bar{\xi}$	General mixture property
ΔT	Solidification range
p	Pressure
$\vec{S}_m$	Momentum source term
$\vec{S}_d$	Darcy momentum sink source term

$\vec{S}_{st}$	Surface tension force source term
$\vec{S}_M$	Marangoni shear force source term
$\vec{S}_{rp}$	Recoil pressure term source term
A_{mush}	Permeability coefficient
C_ϵ	Small constant in the Carman-Kozeny equation
$\vec{n}$	Unit normal vector at the metal/gas interface
κ	Curvature of the metal/gas interface
p_0	Ambient pressure
L_{vap}	Latent heat of vaporisation
M	Molar mass
T_b	Boiling temperature
R	Universal gas constant
H	Enthalpy
S_e	Energy source term
L_{melt}	Latent heat of fusion
S_{rad}	Heat losses due to radiation
S_{vap}	Heat losses due to vaporisation
S_{laser}	Heat input provided by the laser source

σ_s	Stefan-Boltzmann constant
ϵ	Metal emissivity
Δx	Cell size
Q_{init}	Specific surface energy flux
Ab	Fraction of Q_{init} absorbed by the cell
$\hat{n}$	Complex refractive index
$\vec{R}$	New sub-ray direction
$\vec{I}$	Incident sub-ray direction
f_i	Frequency associated to a specific pressure drop value $\Delta p_{max,i}$
Δp_{glob}	Global hot crack propensity index
C_L	Composition of the liquid
D_i	Interface diffusivity
α	Coefficient of thermal expansion
$\dot{T}$	Cooling rate
σ_c	Critical stress needed to propagate the crack
K_{Ic}	Fracture toughness
L	Crack length
B	Dimensionless geometrical factor

A_{vuln}	Vulnerable region's area
$\dot{V}$	Build rate
γ	Surface energy
h	Liquid width
γ_{sl}	Interfacial energy associated with the solid/liquid interface
γ_{gb}	Grain boundary energy
δ	Interdendritic thickness
$C_{wt,i}$	Weight percentage of the i-solute
$\Delta\sigma_{ss}$	Increment of strength due to solid solution
G_{Al}	Aluminium's shear modulus
G_i	Shear modulus of the i-solute
$C_{at,i}$	Atomic concentration of the i-solute
$\Delta\sigma_{HP}$	Increment of strength due to grain size
k_y	Material constant in the Hall-Petch relationship
D	Grain size
I	Feeding integral
G_{rr}	Energy release rate per unit crack length
Π	Total potential energy

s   Unit crack growth area

Chapter 1

1 Introduction

Aluminium (Al) alloys represent key materials for a number of relevant industrial sectors, including the automotive and aerospace industries [1]. In order to limit the global emissions, Al alloys are expected to cover a pivotal role in the transport sectors due to their lightweight properties [2]. Weight reduction can be achieved also using Additive Manufacturing (AM), widely addressed also as "3D printing", a manufacturing approach defined as "a process of joining materials to make objects from 3D model data, usually layer upon layer, as opposed to subtractive manufacturing methodologies" [3]. In the last decade, AM processes, including Laser Powder Bed Fusion (PBF-LB/M), have started to gain the attention of the transport sector due to the possibility to produce complex lightweight parts in a number of high-value materials with limited fabrication waste [4,5]. In this context, high-strength aluminium (Al) alloys are of particular interest for the automotive and aerospace industries owing to their low density, great strength and corrosion resistance. However, these alloys are characterised by limited processability arising from the formation of detrimental hot cracks during the solidification process.

1

This phenomenon is accentuated during PBF-LB/M owing to the higher cooling rates with respect to traditional manufacturing techniques, such as, direct chill casting. Despite being largely known from the casting and welding literature, hot cracks are far from being comprehensively understood and successfully mitigated. This work focuses on the study of the origins of hot cracks and on the identification of multiple pathways to avoid the formation of such defects in high-strength Al alloys processed by PBF-LB/M.

1.1 Laser Powder Bed Fusion

Laser Powder Bed Fusion, also known as Selective Laser Melting (SLM), is a AM technique able to fabricate parts from powders adopting a laser beam. The process consists of a powder bed selectively melted by the energy source which is conveniently oriented by a series of mirrors. Between one layer and the next one, the platform lowers its position along the vertical axis (also known as building direction – BD) enabling the possibility to spread a new layer of powder carrying on the production of the parts. The PBF-LB/M process can be subdivided into three distinct phases: (i) formation of a scan track, (ii) formation of a layer due to scan track overlap in a direction perpendicular to the BD and (iii) formation of the 3D workpiece due to the layers overlap in the BD [6]. The correct overlap of these features is governed by the combination of multiple process parameters. The laser power P and the scan speed v directly control the energy deposited onto the powder bed and affect the continuity of the track [7]. Depending on the nature of the laser, the energy sources are subdivided into continuous-wave (CW) and pulsed-wave (PW) lasers. In the prior class, the energy is continuously delivered to the irradiated material whereas in the latter the laser spatio-temporal law is not linear. Each scan track is indeed subdivided into multiple single irradiations (pulses) equally spaced and characterised by a certain pulse distance, duration, and frequency. The hatch distance h_d represents another relevant process parameters chosen to guarantee the correct overlap of the scan tracks along the horizontal plane [8]. The pattern adopted to join these tracks is known as scan strategy (e.g., unidirectional, meander, chessboard, island) and is characterised by an angle θ which, for the meander scan strategy, represents the angle between the direction of the scan tracks in a certain layer and that of the next one [9]. Similar to h_d, the layer thickness Δz represents the thickness of a single layer of powder and affects the

correct overlap of subsequent layers [10]. Other relevant parameters affecting the melting dynamics during production are the platform temperature T_{plat} and the oxygen content in the build chamber. These parameters can be accurately changed to either minimise defects and/or control the microstructure. Therefore, they are often both experimentally and/or computationally optimised to highlight processing windows able to produce near-full dense parts with tailored microstructural features.

In the last decade, PBF-LB/M has gained the attention of several industrial fields due to the recent technical progresses achieved in the state-of-the-art systems. Specifically, major applications are found in the automotive and aerospace sectors [11,12] where the main drivers promoting the use of PBF-LB/M as manufacturing technique are represented by the possibility to produce complex lightweight structures characterised by an exceptional degree of design freedom [11]. Such substantial weight reductions are often paired with the use of topologically optimised designs [13] and/or the adoption of lattice structures [14–16]. Parts manufactured adopting such strategies find a wide range of applications not only for weight-reduction purposes but also in other relevant engineering applications, such as, energy absorption, biomedical implants, and thermal management [17].

1.2 Materials used in PBF-LB/M

The range of alloys available for use in PBF-LB/M has grown consistently in the last years as the understanding of the energy beam-material interaction progressed. However, the most used materials include Fe and Ti alloys. Steels (mainly tool and stainless steels) have been largely investigated due to their ease of processing and competitive feedstock prices [18,19]. Ti-based alloys (mostly Ti-6Al-4V) have also gained large attention from both the research and industrial communities owing to their advantageous combination of strength, relatively low density, and biocompatibility [20]. These two classes of materials have been largely investigated due to their limited formation of metallurgical defects during printing which results in readily PBF-LB/M fabrication [20]. Ni-based superalloys represent a relevant material class owing to their great mechanical properties at high temperatures and applications in aero-engines [21]. However, the correct production of some of these materials is hampered by the formation of detrimental cracks during PBF-LB/M which undermine their structural integrity and mechanical performances [22]. In the context of lightweight structural material, aluminium alloys represent one of the most promising class of materials thanks to their great strength-to-weight ratio achieved especially in the aged conditions [23]. Within Al-based materials, casting alloys (e.g., AlSi10Mg, AlSi12, AlSi7Mg) are paired with ease of manufacturing and limited presence of metallurgical defects in optimised processing windows. However, these compositions are characterised by mild mechanical performances and poor strength at relatively high temperatures [24]. Therefore, the scientific community has invested relevant resources in the investigation of high-strength Al-alloys characterised by superior strength both at high and/or room temperature. Nevertheless, similarly to Ni-based alloys, these materials are paired with poor PBF-LB/M processability due to the formation of hot

cracks that limit their structural integrity, resulting in limited industrial applications [6]. Despite this phenomenon has been extensively investigated in both casting, welding and PBF-LB/M literatures, the mechanism leading to hot crack formation in high-strength Al-alloys are not comprehensively understood. This results from the intricate nature of hot cracking, which involves contributions from material-related and processing-related phenomena, including alloy chemistry, microstructural features and dynamic thermal conditions developed during solidification.

1.3 Aim and objectives

The aim of the present research is to comprehensively understand all the relevant phenomena leading to pores and hot crack formation in high-strength Al-alloys, avoiding their initiation adopting appropriate PBF-LB/M regimes and modifying their chemical composition. This gained knowledge is expected to inform a strategy to design bespoke Al alloys with optimised processability and mechanical performances.

In order to achieve the aims of the present work, the following objectives were highlighted:

- Literature Review. A full review of the literature was carried out throughout the entire extension of the research project to underline relevant strategies and methodologies adopted to discuss and quantify the presence of pores and cracks in high-strength Al-alloys processed by PBF-LB/M. It was highlighted that standard wrought heat-treatable Al-alloys suffer from extensive hot cracking which seemed to be minimised in compositions from the 2xxx series. Grain inoculation was found to be the most widely adopted strategy to avoid hot crack formation and therefore, since largely investigated in literature, was not considered for further investigations. Lastly, a lack of practical methodologies to computationally assess hot cracking and design crack-resistant bespoke compositions was highlighted.
- Investigation of the cracking mechanisms in 2xxx series high-strength aluminium alloys. In order to achieve this objective, the AA2024 alloy was selected for the investigation of the effects of various strategies to minimise the presence of hot cracks during PBF-LB/M fabrication. Specifically, the hot cracking presence was

investigated with respect to various processing regimes and chemical composition modifications.

- Identification of crack-free PBF-LB/M regimes for a given alloy. To reach this objective, the solidification dynamics of AA2024 were simulated using a multi-physics simulation able to predict the hot crack driving force as a function of various laser regimes. These computations, paired with twin experiments, led to identification of a hot cracking parameter able to comprehensively capture the effects of not only alloy chemistry, but also microstructure and processing conditions on hot crack formation.

- Design and development of a new custom Al grade with optimal processability and strength. In order to achieve this objective, a powder-free methodology to highlight suitable bespoke Al compositions for PBF-LB/M was proposed. This was based on the use of the CALPHAD approach and a new indicator to predict the intrinsic hot crack propensity of alloys during solidification. The adopted strategy led to the identification of an Al grade characterised by extraordinary processability and mechanical performances.

Chapter 2

2 Literature Review

This chapter focuses on the review of the relevant literature needed to understand the Aluminium alloys, their defects, properties and microstructural features in the context of PBF-LB/M. Figure 2.1 depicts a schematic of the topics examined in the present chapter. First, aluminium and its alloys will be introduced with particular emphasis on their classification, temper designation and on the currently commercially available Al alloys for the PBF-LB/M process. Subsequently, the discussion will shift on the typical defects found in the as-built condition, namely porosity and hot cracks. These last features will be comprehensively discussed as they represent the major cause limiting the processability of such alloys by means of PBF-LB/M. The effects of grain morphology, processing conditions and alloy's composition on hot crack formation and intensity will be investigated to understand the limits of the currently available hot crack criteria and alloy design trends available in the literature.

Figure 2.1: table of contents discussed in the literature review conducted at the beginning of this PhD project.

2.1 Aluminium and its alloys

Aluminium alloys represent the second most used structural metal material after Fe-based alloys with a global production continuing to grow at a rate of around 6% per annum [25]. The industrial demand for these particular alloys comes from their great properties, including high corrosion resistance, low density and outstanding combination of mechanical and physical properties [26]. Al-alloys represent indeed great engineering materials for applications in the automotive, aerospace and power electronics fields [27,28]. Traditionally, following the ASTM standard classification, Al-alloys are subdivided into cast and wrought alloys [29]. Structural applications in the automotive and aerospace sectors mostly use high-strength Al-alloys, which are produced by either rolling, extrusion or forging and are available in rolled plates, sheets, foils and rods [30]. Moreover, these materials are often heat treated after production to improve their mechanical performances. It is therefore of interest to focus on this alloy class and their commonly adopted heat treatments.

2.1.1 <u>Wrought Al alloys classification and temper designations</u>

Based on their alloying elements, thermophysical properties and applications, wrought aluminium alloys are subdivided into series (or classes) with the designation $yxxx$. The number y indicates the specific series, while the x digits are referred to each single alloy. It is possible to distinguish:

- 1xxx series: alloys from this class are considered commercially pure aluminium alloys and contain only traces of solutes. Consequently, these materials are

characterized by exceptional thermal and electrical conductivity at the expenses of mechanical properties.

- 2xxx series: this class contains alloys mainly refined with Cu and additions of Mg, Fe, Si and Mn, which lead to their poor weldability. Their great combination of high strength and corrosion resistance ensure a vast number of applications in the aerospace sector.

- 3xxx series: alloys from this class are characterized by Mn, Cu, Mg, Si and Fe as main solutes. They possess moderate strength and workability.

- 4xxx series: similar to the previous class, these alloys are characterized by moderate strength and by Si, Cu, and Mg as main solutes.

- 5xxx series: these alloys are based on the Al-Mg binary system, refined with Mn, Si, Fe and Zn. This class is characterized by good weldability and corrosion resistance.

- 6xxx series: this class contains highly formable and weldable alloys displaying moderate to high strength. Their major alloying elements are Mg and Si while other traces of Zn, Fe and Mn can be found within the compositional ranges. They are used for structural purposes in architectural and automotive fields.

- 7xxx series: alloys from this class are characterized by the highest strength and fatigue resistance. Their main adoption lies indeed in the aerospace and military industries. Zn and Mg are their main alloying elements, followed by Si, Fe, Cu, Zr and in some cases Ag.

- 8xxx series: alloys from this class represent custom compositions with properties and alloying arrangement that do not fall in any of the previous series.

An additional sub-classification of these series can be conducted considering their heat-treatability. Aluminium alloys are considered heat-treatable when they can undergo aging cycles with the specific aim to increase their strength via precipitation hardening. Among the previously discussed classes, alloys from the 2xxx, 6xxx and 7xxx series are heat-treatable and therefore they are often referred to as high-strength Al-alloys. Based on the temporal and thermal conditions of the heat treatment, several temper designations have been introduced to distinguish the type of thermal cycle conducted on the alloy [26]:

- F, as fabricated: this condition represents alloys that, after the production by either cold working, hot working, or casting, did not receive any specific control over their cooling thermal conditions.

- O, annealed: this temper designation applies to alloys that, after fabrication, have been annealed with the aim of improve their ductility or thermal stability.

- H, strain-hardened: this condition represents a specific case of the F temper for wrought products only and indicates alloys strengthened by strain hardening without any supplementary heat treatment to improve their ductility and reduce their strength.

- W, solution heat-treated: this temper designation applies to alloys whose strength spontaneously changes at room temperature in the course of months/years after a solution heat treatment.

- T, stably tempered: this condition applies to alloys whose strength is stable after a temper heat treatment.

The T temper designation is one of the most common in heat-treatable aluminium alloys, as it corresponds to the aged condition. Specifically, depending on the temporal and

thermal conditions adopted during the heat treatment, it is possible to distinguish a few relevant designations:

- T3: this temper designation applies to alloys that undergo a solution heat treatment and a subsequent natural ageing, in which their mechanical properties and microstructure are stabilised at room temperature.
- T6: this condition applies to alloys that, after a solution heat treatment, are artificially aged by a thermal cycle conducted at relatively low temperatures for a specific time that leads to optimal precipitation and therefore secondary phase strengthening.

2.1.2 Relevant commercially available Al alloys for PBF-LB/M

Despite some high-strength aluminium alloys are considered weldable, filler metals are used during processing to locally change their composition avoiding the formation of detrimental defects, such as, hot cracks (Section 2.2.2). For this reason, most of the commercially available aluminium alloys for PBF-LB/M were originally designed for casting. Cast alloys have short solidification ranges ensured by their near-eutectic composition and therefore were the first to be investigated for PBF-LB/M suitability. Their microstructure in the as-built condition is generally composed of columnar grains epitaxially growing and aligned with the building direction. Within the grains, an array of cells or dendrites surrounded by eutectic secondary phases can be found [31]. The extensive formation of this eutectic at the last stage of solidification is one of the factors promoting the inhibition of hot crack formation [32]. These alloys are AlSi7Mg, AlSi10Mg, AlSi12 and AlSi9Cu3. Despite the great interest of the industry in these materials, their

mechanical properties are limited and can be further decreased via heat treatments, such as, stress relief or ageing.

An alternative to these cast alloys was proposed by the Airbus Group with the patent of the Scalmalloy®, a material characterized by a yield strength of 508 MPa, an ultimate tensile strength of 514 MPa and an elongation at failure of 5% [33]. Additionally, the mechanical behaviour of this alloy is not affected by subsequent thermal cycles because of its most influential alloying element: scandium. Scalmalloy® can be indeed considered a modification of a 5xxx series alloy in which Sc has been added. Upon solidification, this element reacts with Al promoting the precipitation of Al_3Sc [34]. This phase is able to refine the grain structure promoting a fine equiaxed microstructure, limiting the hot crack susceptibility of the alloy. Zirconium is also present in the system because of its ability to act as substitute element for Sc [35], promoting the precipitation of Al_3Zr, also able to refine the grain morphology. The as-built microstructure of Scalmalloy® is characterized by bands of $Al_3(Sc,Zr)$ at the melt pool boundaries and therefore the grain refinement takes place only in these specific areas. Other areas are characterized by columnar grains, growing from these bands and pointing towards the middle of the melt pool as a consequence of the heat dissipation direction. This particular grain arrangement forms the so called "bimodal" microstructure. The mechanism behind its formation is depicted in Figure 2.2. During printing, the interaction between the laser and the material creates liquid flow (also known as Marangoni flow) from the periphery of the melt pool towards its core, which promotes the disruption of the oxidation membrane. Upon cooling, the primary $Al_3(Sc,Zr)$ precipitates and the oxidation debris are caught in the Marangoni flow, aggregating at the melt pool boundaries.
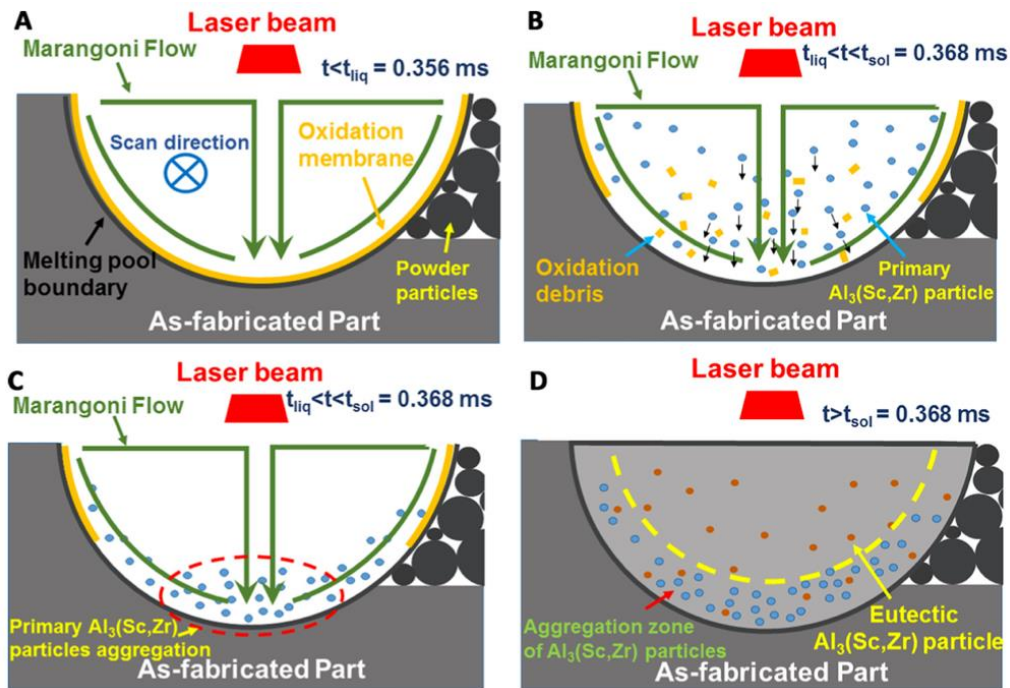
Figure 2.2: various stages of the aggregation zone's formation of the Scalmalloy® [35].

Another commercially available alloy using this criterion to avoid hot crack formation is A20X™, a product based on the A205 alloy with the addition of TiB_2 which, just like Al_3Sc and Al_3Zr, promotes grain refinement.

In conclusion, PBF-LB/M Al-alloys are mainly composed by cast and grain refined alloys. High-strength alloys, such as, materials from the 2xxx, 6xxx and 7xxx series, are not commercially available due to their poor processability by means of PBF-LB/M. Porosities and hot cracks arise during printing, limiting structural integrity and mechanical performances. Therefore, in order to enable the correct processability of wrought alloys or correctly design new materials, the formation of such defects needs to be understood and subsequently limited.

2.2 Major defects of Al alloys processed by PBF-LB/M

Aluminium alloys processed by PBF-LB/M are characterized by several defects arising from the laser-powder interaction. Depending on the process parameters and the amount of energy deposited onto the powder bed, it is possible to distinguish formation of porosity and/or cracks. It is therefore useful to define a parameter that sums the amount of energy adopted for fabrication. One of the most commonly used metrics to describe a PBF-LB/M regime is represented by the Volumetric Energy Density (VED), described by:

$$VED = \frac{P}{v \cdot h_d \cdot \Delta z}$$
<div style="text-align:right">Equation 2.1</div>

where P is the laser power, v represents the laser speed, h_d is the hatch distance and Δz represents the layer thickness. It is therefore of interest to first understand the dynamics leading to the formation of pores and cracks as a function of different PBF-LB/M regimes and their relative energetical differences. Here, a note of care regarding the hot cracking nomenclature is needed. In Section 2.2.2 of the present Paragraph, the mechanism of solidification cracking will be illustrated and discussed. This cracking phenomenon is not the only "hot cracking" mechanism as liquation cracking is indeed also another phenomenon occurring at high temperature. However, this cracking mechanism will not be discussed in the present Thesis as it does not affect high-strength Al-alloys processed by PBF-LB/M. In the AM community, solidification cracks are well-known to be addressed as "hot cracks" or "hot tears". Therefore, this nomenclature will be carried over the entire length of the Thesis.

2.2.1 Porosity: types, morphologies and associated formation mechanisms

Porosity represents one of the most common defects found in parts processed by PBF-LB/M. The presence of various types of pores is indeed found in all classes of materials and thus their minimization often represents the first objective of studies using PBF-LB/M as a manufacturing technique [6]. Among all material's classes, aluminium alloys represent one the most prone to form pores during processing. Buchbinder et al. [36] attributed this propensity to aluminium powders' low absorptivity (namely the portion of laser energy absorbed by the material) at the common PBF-LB/M lasers' wave length of 1070 nm. This phenomenon is found to be more accentuated in PBF-LB/M regimes characterized by lower hatch distances since a higher portion of solid metal – having lower absorptivity with respect to the powders [37,38] – is remelted. Additionally, materials processed by PBF-LB/M, including aluminium, steels and titanium alloys, are known to suffer from a drastic absorptivity variation caused by the change of melting mode [39]. As a result, these Al alloys are affected by an extensive propensity to form porosity during PBF-LB/M which often results in narrow processing window. Based on their formation mechanism, different types of porosity can be found in PBF-LB/M processed parts.

Gas pores are found even distributed within the melt pools and are characterized by a circular shape with a characteristic size up to tens of microns [40]. These pores represent a well-known defect from the welding literature [41]. During the melting process, the evaporation of hydrogen may result in the formation of gas bubbles in the molten metal. In this stage, two different phenomena influence the mobility of these bubbles [42]: (i) in the event that the melt pool is dominated by surface tension gradient forces, the molten metal tends to push downward the formed bubbles; (ii) in case the melt pool is

dominated by electromagnetic forces, the bubbles tend to float and consequently escape towards the building chamber. Considering, on the other hand, the PBF-LB/M process, the absence of an electrode and currents on the free surface avoids the formation of electromagnetic forces. This results only in the presence of buoyancy-related forces which tend to push the gas pores towards the free surface. However, as a result of the high cooling rate, solidification takes place before these bubbles are able to escape the melt pool, resulting in the formation of gas pores in the material. This type of porosity may be often already found in the powders as a result of the gas atomisation process and can be accentuated by the presence of moisture on the feedstock material [6]. Drying cycles prior to PBF-LB/M processing have proven to be effective in reducing gas porosity in the as-built microstructure [43].

Lack-of-fusion (LOF) pores are defects arisen from incorrect overlap of melt pools during processing [44]. They are characterized by irregular shapes with common size in the scale of hundreds of microns and are often paired with unmelted powder [40]. Aluminium alloys suffer from extensive LOFs due to their strong tendency to oxidise, particularly at high temperature [45]. This results in limited wettability of the molten metal which hampers correct melt pool overlapping [46]. The presence of this type of porosity needs to be avoided due to the strong detrimental effect on part integrity and mechanical properties [47]. Many approaches have been proposed to limit LOF's formation during PBF-LB/M. Mukherjee and DebRoy [48] modelled heat transfer and fluid flow to calculate the temperature and melt pool dimensions and proposed a non-dimensional number L_F that considers PBF-LB/M process parameters and material properties. They found that the presence of LOF is limited in regimes providing high values of T_{peak}/T_{liq}, where T_{peak} represents the maximum temperature reached in the melt pool and T_{liq} is the liquidus

temperature of the alloy. Despite this method has proven to be effective in predicting the presence of lack of fusion defects, it is paired with high computational efforts. Tang et al. [49] proposed a geometrical approach also based on the evaluation of melt pool dimensions. Nevertheless, their LOF criterion did not consider melt pool's temperature profile, resulting in an easier implementation and minor computational effort. Following Tang's approach, complete melt pools' overlap is guaranteed when [50]:

$$\left(\frac{h_d}{w}\right)^2 + \left(\frac{\Delta z}{d}\right)^2 \leq 1 \qquad \text{Equation 2.2}$$

where h_d is the hatch distance, Δz represents the layer thickness, w and d are the melt pool's width and depth, respectively. These last two dimensions can be estimated using the temperature distribution via the Rosenthal equation [51]:

$$T = T_0 + \frac{AP}{2\pi k\sqrt{x^2 + y^2 + z^2}} \exp\left[-\frac{v\left(x + \sqrt{x^2 + y^2 + z^2}\right)\rho c_p}{2k}\right] \qquad \text{Equation 2.3}$$

In Equation 2.3 it is possible to recognise the temperature far away from the melt pool T_0, the powder absorptivity A, the laser power P, the thermal conductivity k, the laser scan speed v, the density ρ, the specific heat c_p and the spatial coordinates x, y and z.

Keyhole pores ,similarly to LOFs, they are characterized by a common size in the scale of hundreds of microns, but their shape is generally less irregular and similar to a dome [40]. They represent defects formed in high-energy laser regimes, when the melting mode changes from "conduction" to "keyhole" [52]. In the prior, melt pools are controlled by the thermal conduction and consequently their aspect ratio is similar to 1. On the other hand, during keyhole melting mode, a larger melting depth is achieved due to the formation of a vapor cavity which is highly susceptible to instabilities [53]. Deeper

cavities are associated with the presence of volatile elements (e.g., Zn and Mg) which in turn increase the chances of porosity formation [54]. During the keyhole melting mode, the recoil pressure causes strong melt flows which in turn result in the formation of a strong vortex of liquid metal caused by the Marangoni effect [55], a phenomenon arisen from the presence of surface tension gradients. These instabilities may cause the collapse of the back wall on the front wall of the cavity, resulting in the formation of a bubble [56]. This pore may be entrapped by the solidification front resulting in the presence of a keyhole. Recently, many studies focused on the observation, prediction and mitigation of keyholes in PBF-LB/M regimes [57–61]. One of the most interesting works was conducted by King et al. [61] who not only studied this phenomenon but provided a useful methodology to indirectly predict the formation of keyholes during solidification via the assessment of the normalized enthalpy given by the following ratio:

$$\frac{\Delta H}{h_s} = \frac{AP}{\pi T_m \sqrt{k \rho c_p v \sigma^3}} \qquad \text{Equation 2.4}$$

where ΔH is the specific enthalpy, h_s represents the enthalpy of melting, T_m is the melting temperature and σ is the spot radius. They estimated the threshold for keyhole porosity in terms of normalized enthalpy by the expression:

$$\frac{\Delta H}{h_s} > 6 \qquad \text{Equation 2.5}$$

Although this criterion has proven to be effective for stainless steel SS316L, its application needs to be proven for Al alloys.

The reported methods to predict the presence of LOF and keyhole pores have been widely used to discuss the formation of such defects as a function of different processing regimes

using both continuous wave and modulated lasers. However, Al powder absorptivity suffers from extensive changes as a function of laser power and scan speed. This may result in incorrect predictions of the presence of the presence of pores as a function of PBF-LB/M regimes.

2.2.2 Solidification cracks: origins, characteristics and currently available criteria to predict the hot crack propensity of a given alloy

Solidification cracks, also known as "hot tears" or "hot cracks" [62], are defects limiting the part integrity and mechanical properties of PBF-LB/M components [63]. Solidification cracking is strictly linked to alloys, in which solidification takes place over a temperature range given by the difference between T_{liq} and T_{sol}, the liquidus and solidus temperatures, respectively [64]. In this specific temperature range, solidification cracks form due to the rupture of thin liquid films found in interdendritic areas of the mushy zone [65], namely the semi-solid region between the liquid metal and the completely solidified material. The force acting on the solid-liquid interface F is directly proportional to the interfacial tension between the two phases γ, the cross-sectional area S and inversely proportional to the liquid film thickness t_{film} [64]:

$$F \propto \frac{\gamma S}{t_{film}}$$

Equation 2.6

Hot tears form predominantly in the last stage of the solidification, when the volume fraction of solid f_S is above 0.8 due to the progressive reduction of the t_{film} which causes the development of high forces at the solid-liquid interface [62]. This force F is the result

of the shrinkage given by the liquid-to-solid transformation, and may cause the rupture of the liquid film and the consequent formation of a solidification crack [32].

The analysis of solidification cracks' morphology and origin in the context of AM has always been hampered by technical challenges due to the size of these features and timescale over which they form. Over the last recent years, a few studies have focused on the characterisation of such features using synchrotron X-ray imaging [66–68]. Of particular interest is the study conducted by Kouraytem et al. [66] who used this technique to investigate the formation and morphology of hot cracks in AA6061 as a function of different PBF-LB/M regimes. A first stationary irradiation analysis revealed the cracking morphology as a function of the energy input (Figure 2.3), which is characterised by a 3D net developed in the material during solidification. It was found that an increase of power and dwell time not only is associated, as expected, to a change of melting, but also to a change of crack morphology. At low energy levels, the cracks appeared to be characterised by a predominant vertical orientation (Figure 2.3(b)). However, as the energy input increased (Figure 2.3(c) to 2.3(e)), horizontal branches started to form, increasing the complexity of the cracks' net. However, the size of these features never exceeded the extent of the solidified material, namely the melt pool. Subsequently, the formation and morphology of solidification cracks was investigated adopting a scanning laser. These features were found to originate at the back of the melt pool and propagate with a solidification velocity of about 1 m/s, value comparable to the laser scan speed adopted for fabrication.
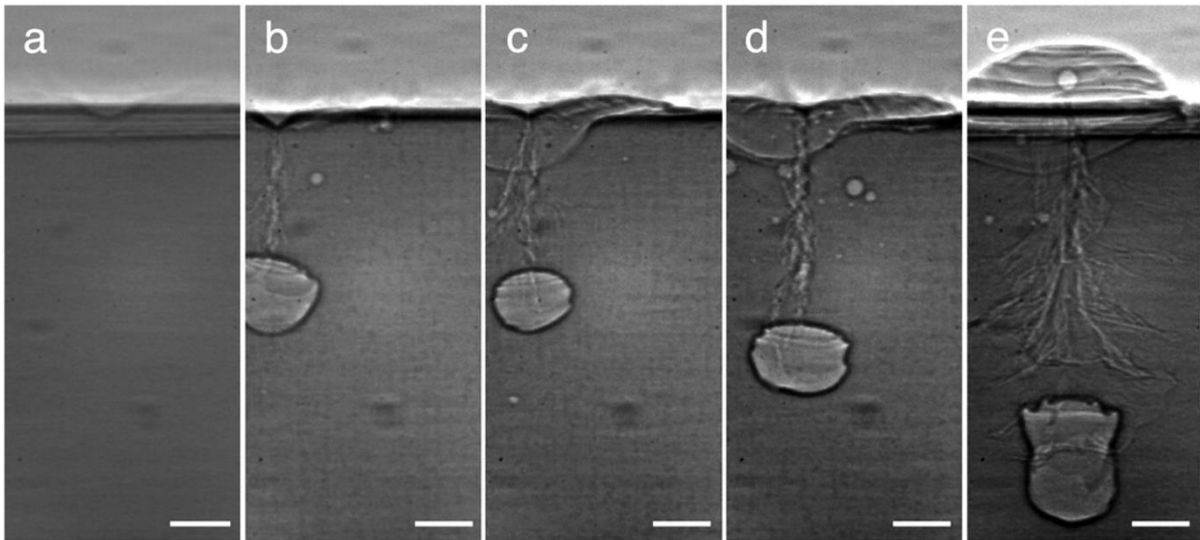
Figure 2.3: evolution of hot cracks morphology in stationary laser experiments as a function of different energy inputs, the scale bar is equivalent to 100 μm. (a) 311W, dwell time 3 ms, (b) 368 W, dwell time 1 ms, (c) 368 W, dwell time 1 ms, (d) 426 W, dwell time 1 ms, (e) 540 W, dwell time 1 ms [66].

The hot cracks observed via synchrotron X-ray imaging was investigated also using post process 2D electron microscopy (Figure 2.4(a)). In the plane perpendicular to the laser scan direction, the hot cracks' complex 3D net is cross sectioned and its trace results to be irregular and characterised by a predominant vertical orientation (Figure 2.4(b)). EBSD analysis revealed that this formation path is aligned with grain boundaries, meaning that hot cracks form in an intergranular fashion with different branches converging to the same point located at higher positions (Figure 2.4(c)).
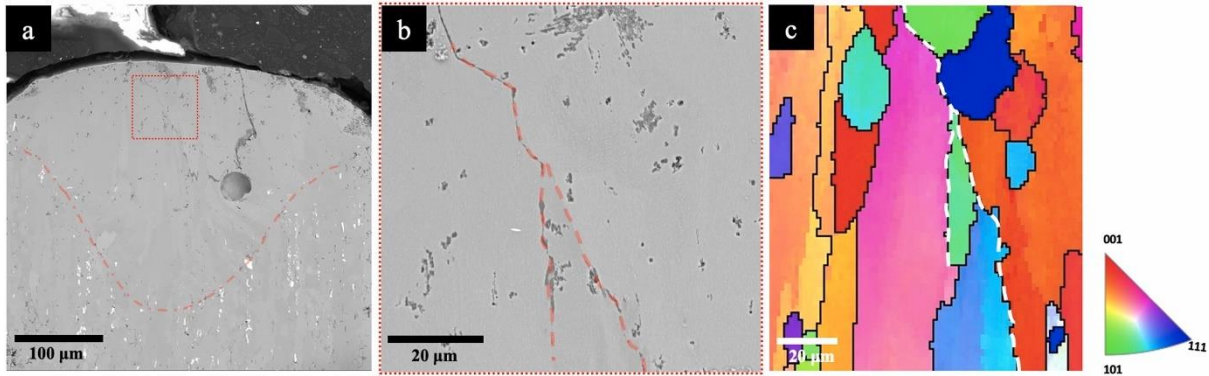
Figure 2.4: (a) 2D SEM cross section micrograph of the melt pool (outlined by a dash-dot line) in the plane perpendicular to the laser scan direction. (b) represents a higher magnification of the dotted region in (a). (c) EBSD orientation map of the crack region displayed in (b), the (001) direction is aligned with the vertical direction of each sub-figure [66].

Hot cracks have been widely reported and characterised in a similar way to that depicted in Figure 2.4 [69–71], However, these features are far from predictable in the context of PBF-LB/M. The prediction of hot crack formation is hampered by the high cooling and solidification rates of the PBF-LB/M process [6]. Moreover, hot cracking is difficult to be comprehensively described because of its complex dependencies from many mechanical and metallurgical contributions [72]. Mechanical phenomena are represented by strain and strain rate development due to the liquid-to-solid shrinkage and thermal contraction. On the other hand, metallurgical phenomena, which may occur concurrently, depends on the chemistry of the solidifying material, and include micro-segregation, diffusivity of the alloying elements, crystal structure, grain morphology and size. Specifically, micro-segregation plays a relevant role in rapid solidification processes, such as, PBF-LB/M. As solidification progresses, solutes are rejected from the solidifying dendrites, creating a rich liquid region which is characterised by a lower solidus temperature. This results in steep solidification gradients at the end of solidification which increase the hot crack susceptibility of a given composition [32].

All of these exhibit temporal and spatial dependencies, making hot crack formation dependent, in the context of PBF-LB/M, on the energy delivery associated to the laser [73]. Several criteria have been developed with an effort to link alloy constitution and/or solidification trajectories to hot cracking [74–79]. Due to the large number of factors affecting hot cracking, the first developed criteria and related hot cracking metrics are simple, mostly relying on the empirical observation that alloys having large solidification ranges are usually more hot cracking susceptible [80]. Clyne and Davies [74] studied the effects of chemical composition on the incidence of hot cracking in Al-Si and Mg-Al binary alloys. They highlighted four main mechanisms occurring over the solidification range that affect hot crack formation: (i) strain accommodation by solid movement, (ii) strain accommodation by liquid movement, (iii) interdendritic separation and (iv) interdendritic bridging. The authors' approach was based on the evaluation of the time over which the alloy is vulnerable to cracking t_V and the time available for stress relaxation t_R (Figure 2.5). Based on these evaluations, they proposed a cracking susceptibility coefficient CSC defined by:

$$CSC = \frac{t_V}{t_R} \qquad \qquad \text{Equation 2.7}$$

Figure 2.5: graphic representation of the vulnerable time and time available for stress relaxation [74].

Despite being one of the first attempts of predicting the cracking tendency of a material, the Clyne and Davies model possess intrinsic uncertainties related to boundaries of fraction of solid in which one should evaluate both t_V and t_R. Moreover, this criterion does not explicitly link the thermal conditions developed during solidification with the CSC index, effectively not considering the effects of cooling rates and thermal gradients on the material's hot crack susceptibility.

Rappaz, Drezet and Gremaud (RDG) [76] proposed the first model describing crack formation based on physical concepts, rather than experimental observations. They performed a mass balance at the interface between two growing dendrites. At this scale, the formation of a hot crack is affected by the solid deformation and shrinkage of the dendritic features, and by the liquid backfilling the interdendritic channel. Here, due to

27

these competing phenomena, a pressure drop is generated with maximum depressions at the dendrites' root. The hot crack propensity of the material is therefore assessed by the evaluation of the pressure drop at the root of the interdendritic channel Δp_{max}:

$$\Delta p_{max} = \frac{180}{\lambda^2 G}\left\{(1+\beta)\mu \int_{T_{sol}}^{T_{liq}} \frac{E(T)f_s^2}{(1-f_s)^3}\,dT + v_T\beta\mu \int_{T_{sol}}^{T_{liq}} \frac{f_s^2}{(1-f_s)^2}\,dT\right\} \qquad \text{Equation 2.8}$$

where λ represents the dendrite arm spacing, G is the thermal gradient, β represents the shrinkage factor, μ is the viscosity of the liquid, v_T represents the solidification rate and $E(T)$ is a term which can be described by:

$$E(T) = \frac{1}{G}\int_{T_{sol}}^{T_{liq}} f_s\dot{\varepsilon}\,dT \qquad \text{Equation 2.9}$$

which is a function of the strain rate $\dot{\varepsilon}$ induced by the cooling rate. Originally, developed for casting, the RDG criterion has been used to assess hot cracking in welding [81,82] and PBF-LB/M [83]. With respect to the CSC index [74], the pressure drop Δp_{max} represents an improved metric of the propensity of a given alloy to form hot cracks. Moreover, the thermal conditions developed within the mushy zone during solidification are directly linked to changes of Δp_{max}. This enables the possibility to assess the hot cracking tendency of a material processed via different manufacturing techniques, including PBF-LB/M. Considering Equation 2.8, here the empirical observation that alloys having a large freezing range finds a good match. The expansion of the solidification interval increases the boundaries over which the integrals in Equation 2.8 are computed, increasing the pressure drop at the root of the interdendritic channel and resulting in higher hot crack susceptibility.

However, the correct evaluation of Δp_{max} is hampered by the need of quantifying over the last solidification cycle of a volume of material very specific thermal conditions, such as, thermal gradient G and solidification rate v_T.

Recently, Kou [78] proposed a new hot cracking criterion based on the consideration of the liquid-solid dynamics occurring in the last stage of solidification, that is the final segment of the solidification path. Similar to the RDG criterion [76], the model considers the growth of columnar dendrites, which are subjected to tensile deformation perpendicular to their main axis. According to Kou's criterion, hot cracks form between solidifying dendrites when the following condition holds:

$$\left\{ \quad \dot{\varepsilon} \quad > \quad \sqrt{1-\beta}\frac{\sqrt{f_s}}{dT}\frac{dT}{dt} + \frac{d}{d\hat{z}}\left[\left(1 - \sqrt{1-\beta}\sqrt{f_s}\right)v_{\hat{z}}\right] \right\}_{\sqrt{f_s}\to 1} \qquad \text{Equation 2.10}$$

$$separation \quad > \quad growth \quad + \quad feeding$$

where $\hat{z}$ represents the interdendritic direction parallel to the dendrite growth direction and $v_{\hat{z}}$ is the velocity associated with the liquid backfilling the area in-between dendrites. Following Equation 2.10, Kou proposed an index to predict an alloy's hot-crack-susceptibility (HCS – Equation 2.11) based on the shape of the solidification path upon cooling [78,79] (also known as solidification trajectory), namely the relationship between temperature and fraction of solid within the solidification range.

$$HCS = \max\left|\frac{dT}{d\sqrt{f_s}}\right|_{\sqrt{f_s}\to 1} \qquad \text{Equation 2.11}$$

Compared to the maximum pressure drop of the RDG criterion [76], HCS represents an easy-to-evaluate parameter to quickly assess the propensity of an alloy to form hot cracks. It is therefore crucial to compute the solidification path of a given alloy, an operation which can be achieved combining the CALPHAD method with micro-

segregation models, such as, the Scheil-Gulliver equation which proved to be an adequate representation of the rapid solidification processes, such as, PBF-LB/M [84]. The *HCS* parameter can be evaluated by the computation of the maximum absolute value of the derivative of the temperature with respect to the square root of the fraction of solid at the last stage of solidification [79], with low *HCS* values considered beneficial against cracking. Casting alloys, having a composition close to the eutectic point, solidify with a squashed solidification path which results in low values of *HCS* and a consequent limited hot-crack-susceptibility. On the other hand, high-strength Al-alloys, being defined by lean compositions, show different solidification trajectories upon cooling. Figure 2.6 depicts the solidification path of several wrought alloys used for critical aerospace and automotive applications. As can be seen, the alloys from the 2xxx show lower *HCS* with respect to the 6xxx and 7xxx series. This clear difference arises from the different alloying elements linked to each specific series of wrought Al-alloys and suggests that alloys from the 2xxx series are less prone to form hot cracks upon rapid solidification. Additionally, since the solidification path is strictly dependent on the alloy's composition, it is of interest to study the effects of specific compositional changes and/or additions on the cracking tendency and resulting intensity.
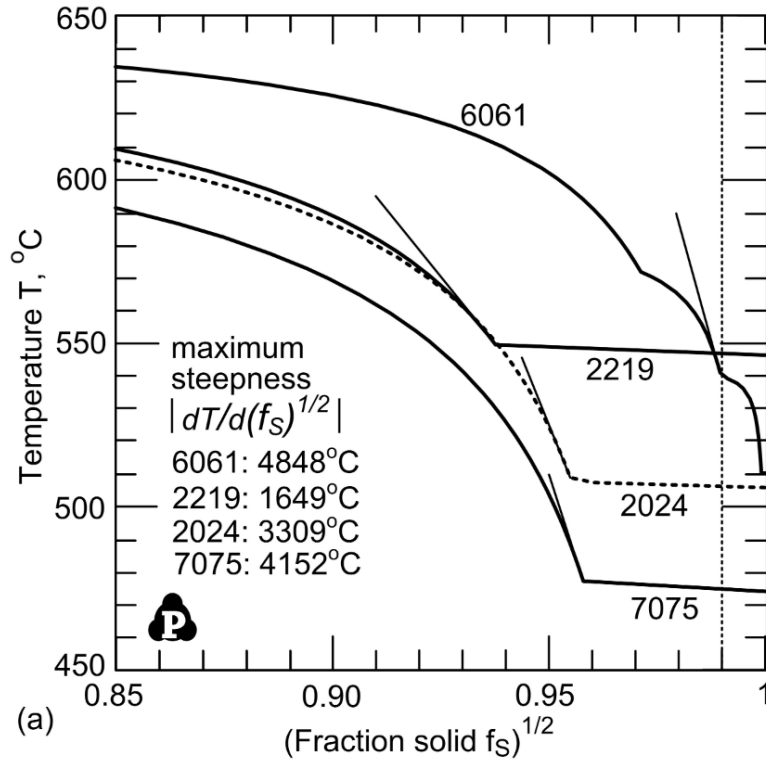
Figure 2.6: solidification path of several high-strength Al-alloys in plotted in a $T - \sqrt{f_s}$ graph [85]. In this specific chart, the HCS index, here called "maximum steepness", is represented by the maximum slope of the curves at the end of the solidification range.

Due to the vast number of variables affecting hot cracking, the recent developments in Artificial Intelligence (AI) and Machine Learning (ML) have enabled a new approach of investigating the formation of hot cracks in Al-alloys processed by PBF-LB/M [86–88]. Specifically, one of the pioneering works about this topic has been conducted by Mondal et al. [88]. Their approach consists in the evaluation of the effects of various variables linked to the hot cracking mechanism computed via mechanistic models and experimentally validated using ML algorithms. Specifically, the authors computed the stress developed during solidification, the solidification rate, the cooling rate, and thermal gradients and linked these process-related variables to the occurrence of hot cracking in the considered experimental twins. The results consisted in a laser power – scan speed process map where the occurrence of hot cracking was mapped for a specific

31

material. Although these findings represent a relevant step forward in the development process-structure-properties map related to the solidification cracking phenomenon, not all relevant phenomena affecting the formation of these defects were considered and this resulted in a lack of comprehensive understanding of the transition between the "processable" and "non-processable" regions. This proves the enormous challenge for the scientific and additive manufacturing communities that is represented by the solidification cracking phenomenon and confirms the need of further research on this topic.

2.3 Cracking behaviour, microstructure, and mechanical properties of high-strength Al-alloys processed by PBF-LB/M

This paragraph focuses on heat treatable high-strength Al-alloys from the standard 6xxx, 7xxx and 2xxx series. Their solidification during PBF-LB/M processing is discussed with the specific aim of understanding their cracking behaviour and the process-microstructure relationships leading to the presence of such detrimental defects. Additionally, the effects of post process heat-treatment are investigated to highlight the resulting microstructural changes leading to precipitation hardening in high-strength Al-alloys rapidly solidified by means of PBF-LB/M.

2.3.1 Processability, microstructure, and mechanical properties of 6xxx series alloys produced via PBF-LB/M

As mentioned in Section 2.1.1, 6xxx series aluminium alloys are characterized by great strength achieved in the heat-treated condition, which is the main driver for high standard applications in the architectural and automotive fields. Apart from minor traces of alloying elements, these alloys are based on the ternary Al-Si-Mg in proportions so that the magnesium silicide Mg_2Si can be precipitated during heat treatment. The most commonly used 6xxx series alloy is AA6061, whose composition is listed in Table 2.1:

Table 2.1: chemical composition (in wt%) of AA6061 following [45].

Si	Mg	Cu	Cr	Mn	Fe	Zn	Ti
0.4-0.8	0.8-1.2	0.15-0.4	0.04-0.35	< 0.15	< 0.7	< 0.25	< 0.15

The manufacturing of AA6061 using PBF-LB/M is hampered by several defects arising from the interaction between the laser beam and the powder bed. Louvis et al. [46] reported limited consolidation in a wide range of processing conditions due to the formation of oxide walls at the melt pool's boundary which led to considerably low values of relative density. These walls limit the wettability of the material increasing the processing window in which LOF defects can be found as a result of the incorrect melt pools' overlapping. Nevertheless, depending on the processing conditions, the oxide walls may be disrupted due to particularly vigorous Marangoni flow. The optimization of the process parameter is a key procedure to achieve near fully dense parts. A more structured approach to highlight pore-free processing windows was conducted by Fulcher and co-workers [89] who investigated a wide range of parameters starting from single scan tracks towards macroscopic components. This strategy led to the identification of processing regimes characterized by absence of macro-porosities. Nevertheless, the presence of macroscopic cracks aligned with the building direction, spanning multiple layers and reaching lengths of about 700-800 μm was found in the microstructure. This result was reported by several other works that investigated the consolidation of AA6061 under PBF-LB/M processing regimes [90–97]. These macroscopic cracks were found to develop exclusively along grain boundaries [94,96,97]. As long columnar grains aligned with the building direction (BD) are found in the as-built material as a result of the vertical heat flow and epitaxial growth, the peculiar cracks' alignment is the result of a specific grain arrangement. Moreover, it was found that in AA6061 cracks develop preferably aligned with grain boundaries characterized by a great degree of misorientation, namely high angle grain boundaries [96]. The presence of these macroscopic defects was found to be affected by multiple processing conditions. However, Mehta et al. [92] found that low scan speed regimes were able to mitigate their

extensive presence in the microstructure. One possible reason for this was proposed by Loh and co-workers [98] who conducted some preliminary modelling investigation of AA6061 under various laser regimes. The authors reported that low scan speed processing conditions are averagely paired with lower cooling rates, and therefore lower hot crack formation driving force following the RDG criterion [76]. However, they did not provide a detailed explanation of the critical thermal conditions leading to the formation of hot cracks during solidification, also neglecting the multiple melting events associated with the PBF-LB/M fabrication. Another plausible reason for the decreased cracking presence in low scan speed regimes could be the different grain morphology developed during printing. Sonawane et al. [96] reported that regimes characterized by lower cracking presence are generally paired with the development of lower solidification rate and thermal gradient, thermal conditions promoting the development of a mixed microstructure formed by equiaxed and columnar grains. For this reason, cracks can be more easily limited due to mass feeding phenomena and strains accommodation [99]. The effects of the cooling rate reduction were investigated also by Uddin et al. [93]. Nevertheless, instead of acting on the scan speed, the authors processed AA6061 with a platform temperature of 500°C. This condition is paired with an exceptional reduction of cooling rate which, apart from lowering the hot crack driving force, limits the development of thermal stresses.

As a result of the rapid solidification in PBF-LB/M, the microstructure of AA6061 is characterized by a fine dendritic net surrounded by secondary phases [93], such as, Mg_2Si and diamond Si [95]. The amount of these interdendritic compounds is generally limited due to the very lean composition of AA6061 (Table 2.1). The size of the dendrites is highly influenced by the cooling rate and therefore can be tuned acting on process parameters

such as laser power, scan speed and platform temperature. Figure 2.7 depicts microstructures generally observed in AA6061 samples produced by PBF-LB/M.
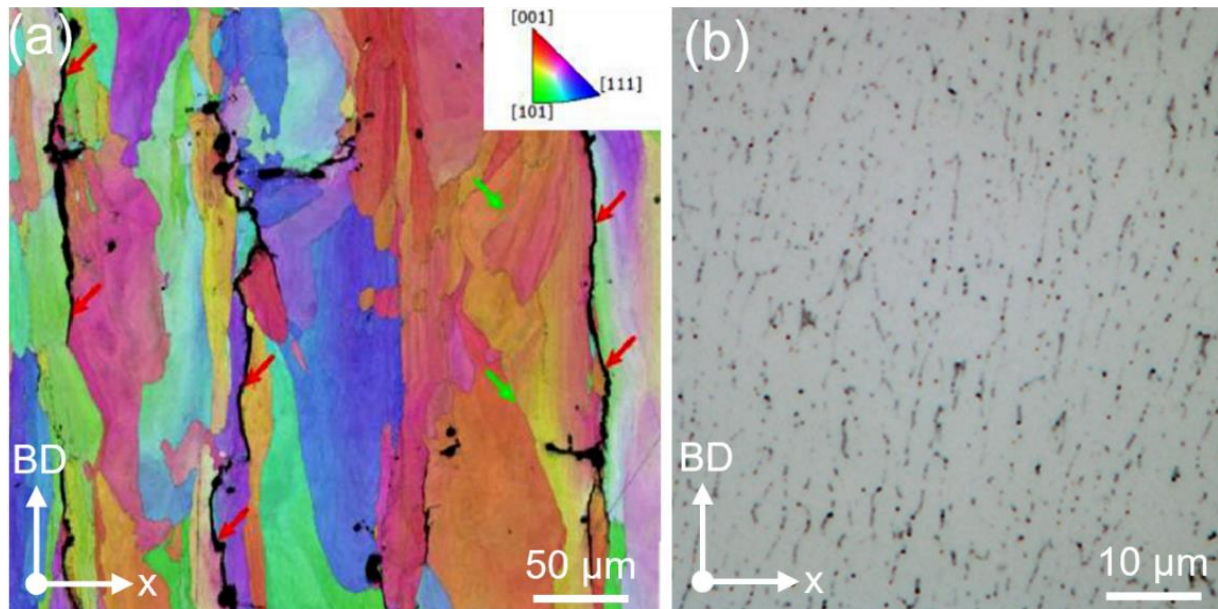
Figure 2.7: (a) IPF/EBSD map of the vertical plane of AA6061 [96]. Red arrows highlight high angle grain boundaries, where cracks are usually found, while green arrows identify low angle grain boundaries. (b) optical micrograph of the vertical plane of AA6061 in the as-built condition depicting the dendritic FCC-Al substructures of AA6061 (in grey) and the secondary compounds (in black) [95].

Due to the extensive cracking behaviour showed by AA6061 samples in the as-built condition, a limited number of studies have focused on the characterization of its mechanical behaviour and heat-treatability. Maamoun et al. [95] reported an increase in hardness in samples printed at high scan speed regimes. This was achieved due to the reduction of the dendritic structures caused by the increased cooling rate of these regimes. However, the increased hot crack propensity in this processing window limits the consolidation of the parts and possibility to conduct standard tensile tests. Despite achieving crack-free microstructures using a high temperature heated platform, Uddin et al. [93] reported limited strength due to the coarsening of the microstructure in the as-

built condition. In order to improve this condition, a T6 heat treatment was conducted, and the results showed an increase of UTS and yield strength at the expenses of a ductility reduction. A more comprehensive study was conducted by Liu et al. [100] who compared the effects of several heat treatments on the microstructure and mechanical behaviour of AA6061 processed by PBF-LB/M. The annealed condition led to a consistent reduction in strength paired with a significant increase in ductility. This microstructure showed the presence of FCC-Al, diamond Si, AlFeSi phases and coarse Mg_2Si compounds, which are thought to be the reason behind this change in mechanical behaviour. On the other hand, with respect to the as-built condition, the T6 condition was paired with minor reduction in strength along an exceptional increase in elongation at failure. This change in mechanical behaviour was due to the fine precipitation of secondary phases evenly distributed acting as obstacles for dislocation movement and therefore increasing its ductility. Despite the Y and UTS of PBF-LB/M components is close to the wrought products' one (Table 2.2), the elongation at failure *EF* of additively manufactured specimens is significantly lower. This proves the need to design custom heat treatments with the specific aim of optimizing the mechanical properties of rapidly solidified microstructures.

Table 2.2: yield strength (YS), ultimate tensile strength (UTS) and elongation at failure (EF) of AA6061 processed by PBF-LB/M and traditionally wrought.

Ref.	Condition	Y [MPa]	UTS [MPa]	EF [%]
[93][a]	F	-	145	14.8
	T6	280	310	3.50
[95]	F	232.3	290	-
[100]	F	-	315	2.01
	O	-	243	6.89
	T6	-	277	7.97
[26][b]	T6	276	310	12.00

(a) samples produced with a platform heated up to 500°C, (b) traditional wrought AA6061

2.3.2 Processability, microstructure, and mechanical properties of 7xxx series alloys produced via PBF-LB/M

Aluminium alloys from the 7xxx series, similar to the ones from the 6xxx class, are characterized by exceptional strength and fatigue properties achieved in the T6 condition. These alloys are mainly based on the Al-Zn-Mg system, with additions of Cu and traces of other solutes. Usually, the $MgZn_2$ is the main secondary compound and promotes strengthening after ageing due to precipitation hardening. Regarding the PBF-LB/M process, the research community has focused primarily on the investigation of the consolidation and cracking behaviour of AA7075, because of their well-known applications in the aerospace and military sectors. Table 2.3 lists the main compositions investigated in this section.

Table 2.3: chemical composition of the main 7xxx alloys investigated in this section.

Alloy	AA7075 [26]	AA7050 [26]	AlZnMg [101]
Zn	5.1-6.1	5.7-6.7	8.8-9.4
Mg	2.1-2.9	1.9-2.6	2.3-2.4
Cu	1.2-2	2-2.6	1.45-1.5
Cr	0.18-0.28	< 0.04	-
Mn	< 0.3	< 0.1	-
Si	< 0.4	< 0.12	-
Fe	< 0.5	< 0.15	-
Ti	< 0.05	< 0.06	-

Due to the presence of highly volatile elements, such as, Zn and Mg, 7xxx series usually show a loss of these solutes after PBF-LB/M fabrication [102]. This reduction was found to be minimised in regimes characterized by low volumetric energy [103]. Apart from elemental loss, the correct consolidation of 7xxx series alloys using PBF-LB/M is limited by the defects arising from the material-laser interaction. Qi and co-workers [104] investigated the melting modes of AA7050 as a function a multiple process parameters, such as, scan speed and focus position. They found that in regimes characterized by low scan speed (P = 200W), keyhole melting mode dominated when scan speeds lower than 115 mm/s were used. This condition was characterized by deep V-shaped melt pools with a depth-to-width ratio higher than 1. On the other hand, lower energies regimes ($v >$

900 mm/s) showed a pure conduction melting mode, characterized by very shallow melt pools with an aspect ratio of around 0.5. As a result, presence of keyhole pores was noted when pure keyhole melting mode dominated, while LOF porosities were found in conduction mode. Optimal consolidation without formation of macro-porosities was observed in the transition melting mode, a result achieved also by Kaufmann et al. [105] investigating AA7075. The defocusing distance was found to be a key parameter to alter the melting mode in regimes characterized by same energy density, enlarging the processing window of 7xxx series alloys by PBF-LB/M. These materials processed in transition melting mode showed optimal consolidation, but presence of macroscopic cracks spanning multiple layers and compromising part integrity in pore-free regimes [102,103,105–114]. These features were generally aligned with the building direction and found at grain boundaries. Therefore, the tortuosity of their path was highly altered by the grain morphology resulting from the solidification. Grain morphology was found to largely affect both the aspect of these features and their presence in the microstructure. PBF-LB/M regimes characterized by the predominance of the keyhole melting mode were found to limit epitaxial growth and therefore generate smaller columnar grains [111]. As a result, since they form at grain boundaries, cracks found in these regimes are characterized by a distinct twisting path. On the contrary, PBF-LB/M regimes predominantly characterized by the conduction melting mode, were associated to a strong development of epitaxial growth and presence of long columnar grains which resulted in a very regular vertical cracking path [112]. Low scan speeds were found to limit the presence of cracks in all the three alloys investigated in this section, promoting in some cases the presence of a crack-free microstructure [102,111,112,115]. These regimes are thought to be paired with a reduced cooling rate development and therefore minimization of the hot crack driving force. Other possible pathways for the reduction of

the hot crack propensity in 7xxx series alloys consists in methods to lower the cooling rate experienced by the material during processing. Kaufmann et al. [105] observed a reduction of cracking intensity when a heated plate was used for fabrication, a solution thought to reduce the cooling rate during solidification. In an analogous manner, laser defocusing was found to be useful to reduce the presence of cracks in AA7075 [109]. Tan et al. [112] reduced the cooling rate during processing acting on the thermal conductivity of the substrate. The authors added a ceramic layer within the platform, reducing the overall heat flow of the system and promoting the reduction of cooling rate.

The as-built microstructure of 7xxx series alloys is characterized by dendritic features of FCC-Al surrounded by a net of $MgZn_2$ and the eutectic η-$Mg(Zn,Cu,Al)_2$ [102]. Additionally, extensive silicon and copper segregation was observed at grain boundaries, along the hot crack tip [109]. This phenomenon leads to the introduction of low-temperature non-equilibrium eutectics which further enlarge the solidification range of the alloy, promoting the rupture of the solutes-enriched liquid and the consequent hot crack formation. Figure 2.8 depicts microstructures generally observed in 7xxx series alloys produced by PBF-LB/M.
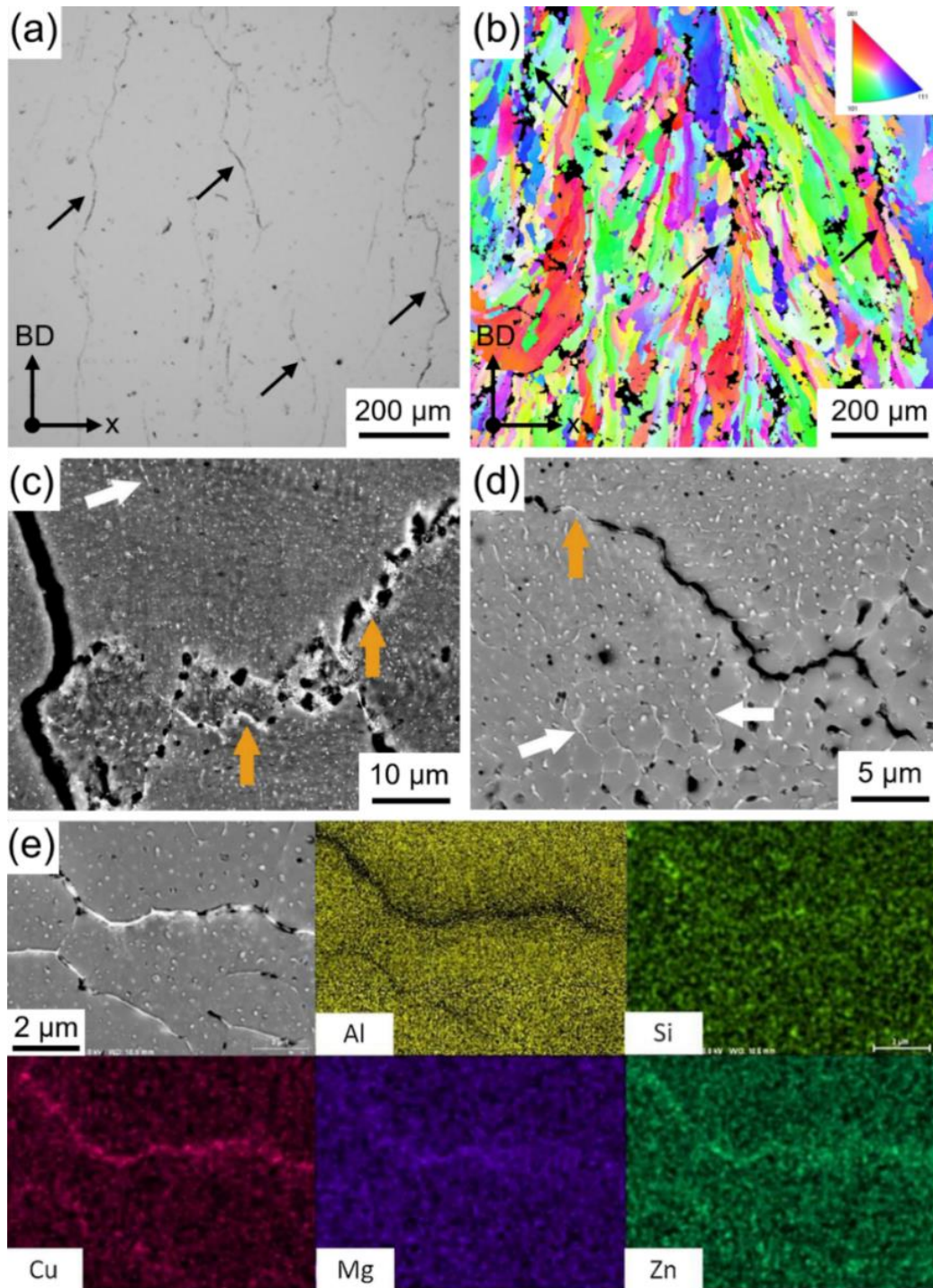
Figure 2.8: (a) optical micrograph [105] and (b) IPF/EBSD map [110] of the vertical plane of AA7075 with the cracks highlighted by black arrow. BSE images of the (c) vertical and (d) horizontal plane of AA7075 with arrows highlighting the eutectic η-phase particles found at grain (orange) and cells (white) boundaries [109]. (e) BSE and EDS maps of the horizontal plane of AA7075 showing the concentration of the alloying elements at the hot crack tip [109].

42

The hot crack susceptibility of Al-Zn-Mg alloys, as reported in Section 2.2, is significantly lower than 6xxx series alloys. Therefore, a considerably higher number of research works have investigated the mechanical properties of these materials in both the as-built and heat-treated conditions, as can be appreciated in Table 2.4 [108,110,115,116]. Part consolidation proved to be one of the main factors affecting the ductility of the material in the as-built condition, with samples failing prematurely due to presence of pores [108]. On the other hand, defect-free components were characterized by a more ductile behaviour and evidence of plastic fracture [115]. Heat treatments were reported to improve the mechanical properties of rapidly solidified 7xxx series alloys [116]. Solution heat treatment caused the greatest observed enhancement of ductility and strength reduction, with a maximum elongation at failure of 9.70% achieved due to the disruption of the as-built brittle compounds found at grain boundaries. Solutionising thermal cycles followed by quench and both natural and artificial ageing proved to be effective in increasing both yield and ultimate tensile strength. Nevertheless, a reduction in ductility was observed to the precipitation of strengthening compounds and consequent greater presence of brittle $FCC-Al/MgZn_2$ interfaces. The precipitation and clustering of these compounds at grain boundaries was found to be particularly detrimental for the ductility of the T6 condition [102]. Similar to 6xxx series, 7xxx series alloys are characterized by poor behaviour with respect to their traditionally wrought counterparts, specifically in the T6 condition, confirming that custom heat treatments have to be designed to maximize the mechanical behaviour of such materials processed by PBF-LB/M.

Table 2.4: yield strength (YS), ultimate tensile strength (UTS) and elongation at failure (EF) of AA7075 processed by PBF-LB/M and traditionally wrought.

Ref.	Condition	YS [MPa]	UTS [MPa]	EF [%]
[108]	F	-	203	0.50
	T6	-	206	0.56
[110]	T6	349	400	4.60
[116]	F	250	255	0.90
	O	171	261	9.70
	T3	297	387	4.20
	T6[a]	350	383	1.05
	T6[b]	407	447	1.90
[115]	F	214.3	306.7	5.50
[26][c]	O	103	228	17.0
	T6	503	572	11.0

(a) ageing time of 2 hours, (b) ageing time of 24 hours, (c) traditional wrought AA7075.

2.3.3 Processability, microstructure, and mechanical properties of 2xxx series alloys produced via PBF-LB/M

This series contains high-strength Al-alloys characterized by both high strength (especially in the aged conditions) and corrosion resistance. For this reason, they represent one of the most attractive engineering materials in the aerospace field. These alloys are based on the Al-Cu-Mg ternary system but, depending on the specific application and desired microstructural characteristics, they may contain Ni, Li, Mn and Ag. Usually, the main strengthening compounds are represented by Al_2Cu (also known as θ-phase), Al_3Mg_2 (β-phase) and Al_2CuMg (S-phase). Nevertheless, due to their chemical complexity, other compounds, such as, Mg_2Si, Al_xMn_y and Al(Fe,Mn)Si-phases, may form depending on processing conditions and heat treatment specifications. Despite still being susceptible to hot cracking, considering high-strength Al-alloys, the 2xxx series is

characterized by the less accentuated hot crack propensity, as described in Section 2.2.2. Therefore, the PBF-LB/M research community has focused on various compositions from this class, with particular attention to AA2024. Table 2.5 lists the compositions investigated in the present section.

Table 2.5: chemical composition of the main 2xxx series alloys investigated in this section.

Alloy	AA2022 [117]	AA2024 [26]	AA2195 [118]	AA2219 [26]	AA2618 [26]
Cu	4.5-5.5	3.8-4.9	3.7-4.3	5.8-6.8	1.9-2.7
Mg	0.1-0.45	1.2-1.8	0.25-0.8	< 0.02	1.3-1.8
Mn	0.15-0.5	0.3-0.9	-	0.2-0.4	-
Li	-	-	0.8-1.2	-	-
Ni	-	-	-	-	0.9-1.2
Fe	< 0.2	< 0.5	-	< 0.3	0.9-1.3
Si	< 0.15	< 0.5	-	< 0.2	0.1-0.25
Ti	< 0.15	< 0.15	-	0.02-0.1	0.04-0.1
Cr	< 0.05	< 0.1	-	-	-
Zn	0.05-0.3	< 0.25	-	< 0.1	< 0.1
Zr	-	-	0.08-0.16	0.1-0.25	-
Ag	-	-	0.25-0.6	-	-
V	-	-	-	0.05-0.15	-

Due to their great corrosion resistance and limited presence of Zn, the processing of 2xxx series alloys in the context of PBF-LB/M results easier with respect to the 6xxx and 7xxx

classes. Nevertheless, their correct consolidation is still hampered by the presence of porosities and cracks in the as-built condition. Considering industrially relevant regimes (e.g. scan speed of 0.50-1.50 m/s and power of 200-300 W), three macro-defects behaviour can be highlighted as a function of the processing parameters [119]. Lower energy regimes, achieved with the highest speed and lowest power values within the considered ones, displayed limited consolidation with the extensive presence of LOFs interconnected by short cracks. On the other hand, the higher energy regimes resulted in the presence of keyhole pores and cracking features. At intermediate energy levels, macro-porosities are usually avoided, but the correct consolidation is still limited by the presence of cracks and gas porosities. These three densification behaviours represent the direct consequence of the different melting modes caused by the laser-powder interaction. LOFs and cracks are obtained when incorrect consolidation is achieved via a conduction melting mode; similarly, strong keyhole melting conditions cause the formation of keyhole pores and cracks. As discussed for 7xxx series alloys, optimal consolidation is achieved in the transition melting mode, when intermediate energy levels are adopted for fabrication. Depending on the characteristics of the powder and chemical composition of the alloy, the optimal processing window may be narrow. Nie et al. [120] investigated changes of defocusing distance to alter the laser beam energy distribution and promote melting mode shifts. Enlarging the beam proved to be an effective pathway to decrease the deposited surface energy, promoting the change from keyhole to transition melting mode and enlarging the optimal processing window of AA2024 towards high power and low speeds regimes without the formation of keyhole porosities. Similar densification behaviours were observed also by studies for AA2022 [117], AA2219 [121] and A2618 [122] focusing on scan track consolidation.

Despite avoiding macro porosities, transition melting regimes are usually still characterized by the presence of long cracks aligned with the building direction with their path found at grain boundaries [117–120,123,124]. These specific features, in a similar way to the 6xxx and 7xxx series, arise from the grain arrangement of the as-built condition, characterised by columnar grains with their main axis aligned with the heat flow direction epitaxially growing one on top of the other [118,123–127]. These areas were often characterized by the presence of strong Cu and Mg segregation which may result in brittle interfaces and enhanced crack propensity [126]. The as-built microstructure of the 2xxx series is characterized by dendritic FCC-Al features surrounded by an intricate net of secondary phases [118,126], which for AA2024 was found to be formed by the θ-phase, S-phase, Mg_2Si and Al_xMn_y. These compounds are found at both cells and grain boundaries, precipitating one on top of the other in a shell-core structure as a result of the great liquid enrichment at the end of solidification promoted by the great chemical complexity of the composition. Figures 2.9 and 2.10 depict common microstructural features observed in AA2024, one of the most investigated 2xxx series alloys, when processed by PBF-LB/M.
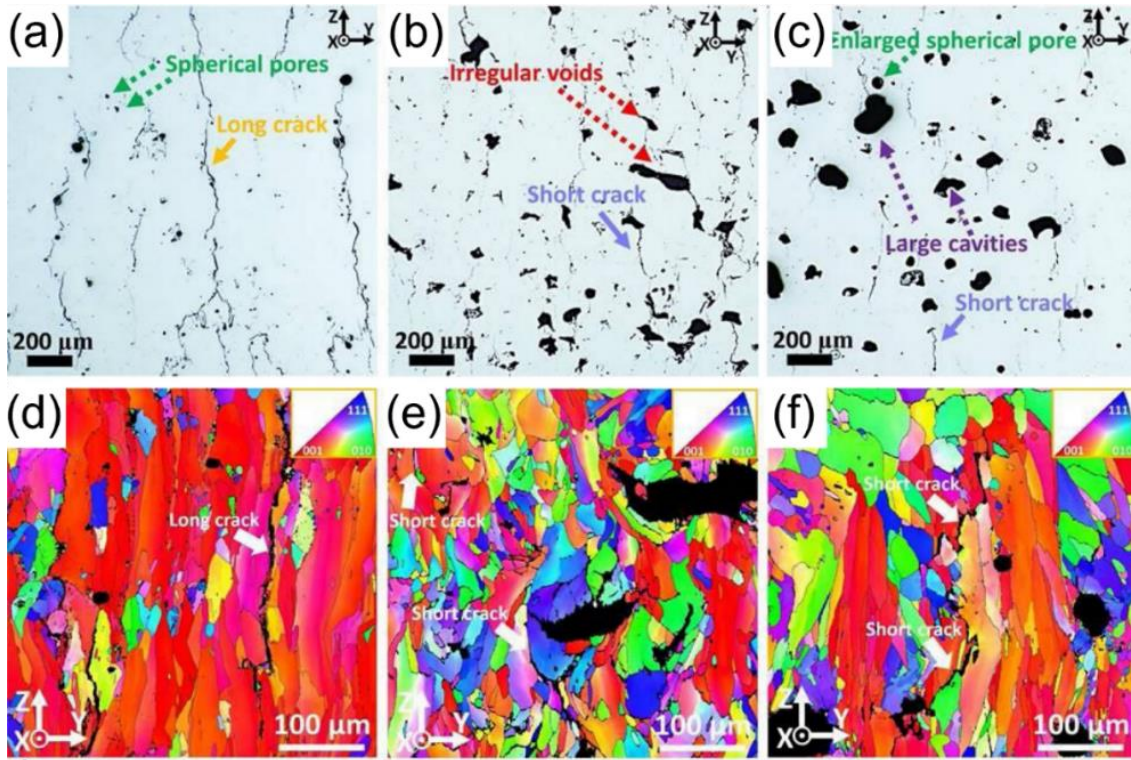
Figure 2.9: optical micrographs (a-c) and IPF/EBSD maps (d-f) of the vertical plane of AA2024 printed using the transition (a,d), the conduction (b,e) and keyhole (c,f) melting modes [119].
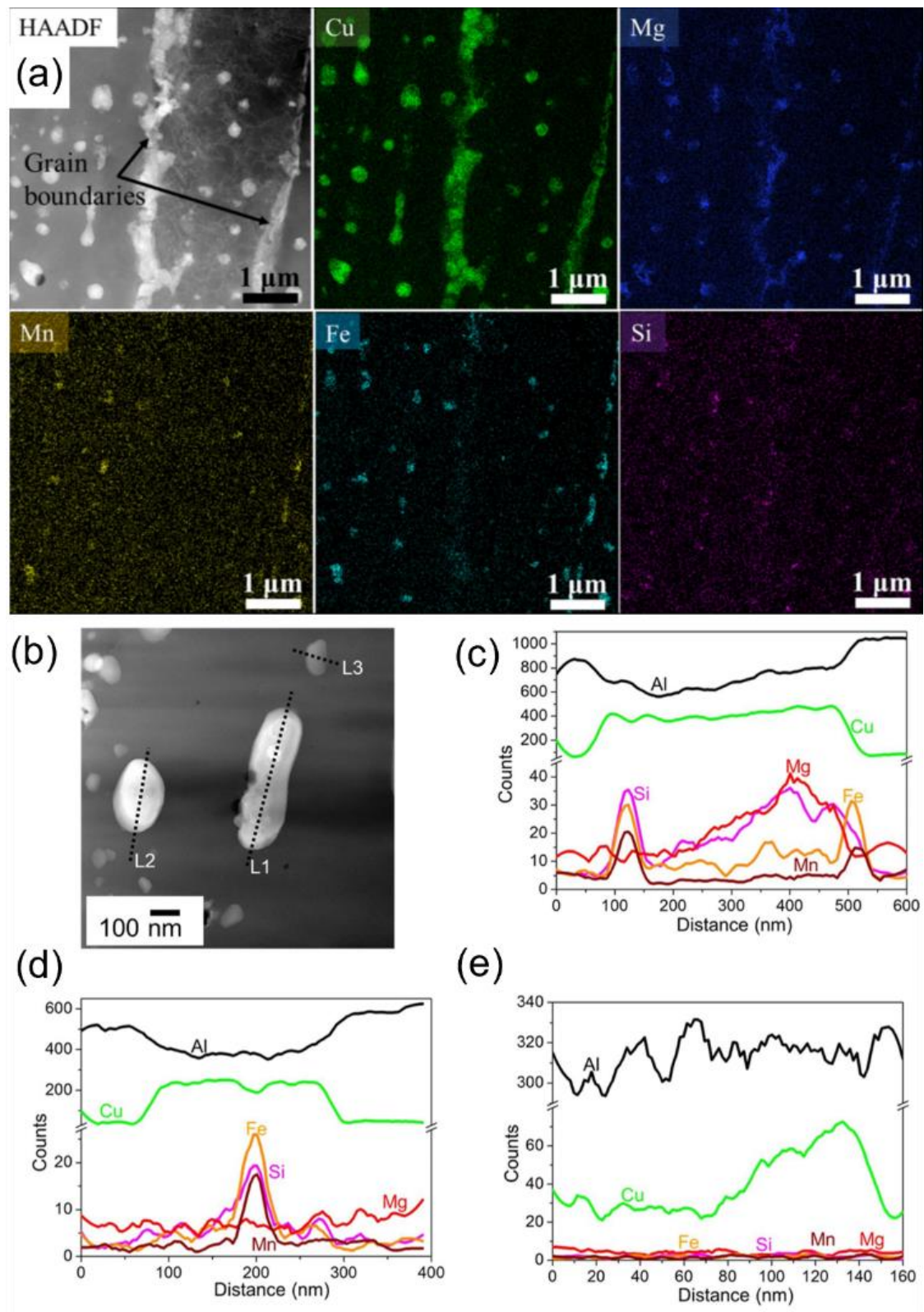
Figure 2.10: (a) HAADF-TEM micrograph showing the grain boundaries and concentration of alloying elements. A high segregation of Cu and Mg is observed at GBs, whereas Mn, Fe and Si are thought to form precipitates inside the interdendritic Cu-rich and Cu-Mg-rich compounds [126]. (b) HAADF-TEM micrograph showing a high magnification of the interdendritic secondary phases. EDX analysis is conducted along the (c) L1, (d) L2 and (e) L3 lines, the shell-core structure of these phases is clearly visible, with a more rich core of Fe, Mn and Si [128].

49

Low scan speed regimes were paired with a significant reduction in the crack intensity for all the 2xxx series alloys investigated in the present section [119,124–127], with similar results achieved also by laser defocusing [120]. This was attributed to the reduction of cooling rate and limited development of thermal stresses during printing with these highlighted regimes that eventually were able to manufacture crack-free microstructures [117,121–125,127,128]. The regimes able to produce defects-free AA2024 have been listed in Table 2.6.

Table 2.6: list of PBF-LB/M regimes able to print crack-free AA2024 microstructures (d_{spot}: spot diameter, P: laser power, v: scan speed, h_d: hatch distance, and Δz: layer thickness).

Ref.	Machine used	d_{spot} [μm]	P [W]	v [mm/s]	h_d [μm]	Δz [μm]
[127]	Custom-made	100	200	83-133	110	40
[128]	Concept Laser Mlab R	50	80	300	80	25
[123]	Custom-made	100	200	83-133	90	40
[125]	SLM 250HL	78	300	300	110	50
			200	200	110	50
			190	165	80	40
[124]	SLM 250HL	78	133	80	60	40
[126][a]	SLM 280	80	200-300	100	100	30
[129]	Custom-made	100	200	83	100	30

(a) platform heated at 150°C.

These regimes are characterized by very low scan speed and consequently not industrially competitive. However, the lower hot crack susceptibility of AA2024 makes

this alloy one of the most interesting high-strength Al alloys to investigate, owing to its ability to be printed with and without cracks. A lot of research work has been done in trying to investigate the mechanical properties of this alloy in both the as-built and heat-treated conditions [124,125,127–129]. As-built samples showed exceptional mechanical properties due to porosity and crack inhibition coupled with an extremely fine microstructure promoted by the PBF-LB/M's fast cooling. The more intricate secondary phases arrangement ensures better strength and ductility with respect to 6xxx and 7xxx series alloys, such as, AA6061 and AA7075, respectively. These properties were further increased operating a T3 heat treatment due to the partial dissolution of the secondary compounds and subsequent precipitation of nano-sized phases (mostly S-phase). Qi et al. [129] proved that the thermal and temporal dynamics of the temper treatment can affect the mechanical behaviour of AA2024. Specifically, an increase of Y, UTS and A was observed at higher solution temperatures (540°C), observed at a specific heat treatment time (1 h) and operating a quench in water. Despite largely increasing the yield strength, a T6 heat treatment was not able to further improve the elongation at failure and UTS of AA2024. Moreover, it was noted that, considering different artificial ageing temperatures, peak hardening appears at different times. With respect to traditionally wrought materials, AA2024-T3 produced by PBF-LB/M showed higher strength but lower elongation at break. Despite having this minor reduction in ductility, considering that the 3D printed material is characterized by a better oxidation resistance with respect to their wrought counterparts [128], AA2024 is characterized by the lower hot crack propensity coupled with best mechanical properties within the high-strength Al-alloys investigated in this chapter.

Table 2.7: yield strength (YS), ultimate tensile strength (UTS) and elongation at failure (EF) of AA2024 processed by PBF-LB/M and traditionally wrought.

Ref.	Condition	YS [MPa]	UTS [MPa]	EF [%]
[127]	F	276.2	402.4	6
[125]	F	233	366	6.2
	T6	368	455	6.2
[124]	F	227	387	18.1
	T3	295	478	18.3
[126]	F	199.6	243.8	2.93
[129]	F	253	389	6
	T3[a]	282	461	9.4
	T3[b]	292	475	10.3
	T3[c]	330	509	10.5
	T3[d]	338	535	13.8
	T3[e]	324	483	8.3
	T3[f]	321	499	11
	T3[g]	306	402	3.8
	T3[h]	205	313	5.9
	T6[d,i]	355	430	4.5
	T6[d,j]	400	460	3.5
	T6[d,k]	378	460	2.2
[26][l]	T3	345	483	17
	T6	393	476	10

(a) 480°C/1h then water quenched, (b) 500°C/1h then water quenched, (c) 520°C/1h then water quenched, (d) 540°C/1h then water quenched, (e) 540°C/0.5h then water quenched, (f) 540°C/1.5h then water quenched, (g) 540°C/2h then water quenched, (h) 540°C/1h then air cooled, (i) aged at 170°C/14h, (j) aged at 190°C/6h, (k) aged at 210°C/1h, (l) traditional wrought AA2024.

2.4 Effects of grain morphology on hot crack propensity of high-strength Al alloys

The detrimental hot cracking behaviour of high-strength Al-alloys processed by PBF-LB/M is the result of the combination of high hot crack driving forces and the formation of long columnar grains aligned with the BD. Gourlay and Dahle [99] experimentally investigated the differences in strain accommodation capabilities between a columnar and an equiaxed microstructure. Between these two configurations, they discovered that strains can be more easily accommodated in the latter due to the change of coherency temperature and suppression of large dilatant shear bands requiring additional liquid backfilling. Therefore, considering the same hot crack formation driving force, an equiaxed microstructure is preferred to absorb strains during solidification and reduce the hot crack propensity of the alloy.

2.4.1 The columnar to equiaxed transition

The control of grain morphology and size is a well-known topic in the casting and welding metallurgy of Al-alloys [130]. In the past decades, many models have been developed and proposed with the specific aim of predicting the grain morphology as a function of the thermal conditions experienced during solidification [131–133]. However, Hunt's model [133] is considered one of the most insightful. Following this model, a columnar dendritic solidification front is supposed to grow at a value of undercooling ΔT_c while the nucleation of equiaxed grains requires a value of undercooling named ΔT_n. In the event that $\Delta T_c > \Delta T_n$, equiaxed grains can grow ahead of the solidification front resulting in the columnar to equiaxed transition (CET). Hunt's approach [133] has been modified by Kurz

et al. [134] considering complex alloys rapidly solidified from the liquid. Based on these new assumptions, the authors proposed several processing maps mapping the occurrence of the CET as a function of the solidification rate v_T and the thermal gradient G. Despite these models provide key insights on the transition between a columnar and an equiaxed microstructure, several manufacturing conditions may not be able to ensure the thermal conditions needed for CET to occur. Therefore, in the past decades, a few alternative methods have been adopted to ease this transition. One of the most common is represented by grain inoculation, a technique which has been successfully adopted to promote the formation of refined microstructures via the CET ensured by an inoculant compound, also known as grain refiner (GR). The effectiveness of this technique is influenced by the potency of the GR (namely its affinity with the matrix), the number of nucleation sites and the presence of enough constitutional undercooling ΔT_c able to activate these sites ahead of the solidification front [135]. In the past decade, grain inoculation has been extensively adopted in PBF-LB/M to increase the processability of difficult-to-print alloys, such as, high-strength Al-alloys [31]. Based on their specific refining mechanism, it is possible to subdivide grain refining compounds in two macro-categories:

- Al based grain refiners (e.g., Al$_3$Sc): these are compounds that precipitate at the beginning of solidification, that is before the nucleation of the FCC-Al matrix begins. The GR's constituent elements can be added to the pre-alloyed powders or mixed with the base material that needs to be inoculated.

- Added GR (e.g., WC): these are compounds that, due to their high melting points, are unlikely to reach with the melt during solidification. They are usually ceramic

compounds, such as, borides and carbides, mostly added to the base material via mechanical mixing.

In the next section, a detailed description of the factors promoting the columnar-to-equiaxed transition and grain refining is presented.

2.4.2 Metrics adopted to predict the columnar to equiaxed transition

In order to promote the formation of an equiaxed microstructure, heat should be dissipated from the liquid/solid interface into the melt [136]. Nevertheless, in PBF-LB/M heat flows in the opposite direction, that is from the liquid/solid interface towards the solid and therefore substantial undercooling is required to promote heterogeneous nucleation. The degree of constitutional undercooling is affected by the segregation of the alloying elements [137], a phenomenon well present in rapid solidification processes, such as, PBF-LB/M. Considering a simple binary system, Greer et al. [138] proposed a simple index P_{UC} able to capture the development of constitutional undercooling as a function of the solute's mass fraction C_0:

$$P_{CU} = \frac{-m_L \cdot (1 - k_e) \cdot C_0}{k_e}$$

Equation 2.12

where m_L is the slope of the liquidus line in the equilibrium phase diagram and k_e represents the equilibrium partitioning coefficient. High P_{UC} are paired with great development of constitutional undercooling and therefore lower grain size. Nevertheless, this approach is limited because it is not able to capture the thermal factors promoting CET and heterogeneous nucleation. Other works [139,140] defined a growth restriction

factor Q_{GRF} considering the sum of all the alloying element's contribution to the formation of constitutional undercooling (with i representing each element):

$$Q_{GRF} = \sum_i \left[m_{L,i} \cdot (k_i - 1) \cdot C_{0,i} \right]$$ Equation 2.13

Considering rapid solidification processes, the early stage of solidification is extremely important to determine the resulting grain morphology. Substantial constitutional undercooling needs to be developed in the region of the mushy zone characterized by low fraction of solid ($f_s < 0.1$) in order to activate the present nucleation sites, avoiding strong thermal gradients that promotes columnar epitaxial growth [141]. Easton and StJohn [142] captured this phenomenon proposing the initial rate of development of a constitutionally undercooled zone r:

$$r = \left| \frac{d\Delta T_{UC}}{df_s} \right|_{f_s \to 0}$$ Equation 2.14

Alloys with a steeper temperature gradient at the early stage of solidification ($f_s \to 0$) exhibit higher values of r and are therefore expected to provide substantial constitutional undercooling in the liquid closer to the solidification front. The computation of the initial rate of development of ΔT_{UC} can be useful to design alloys that are able to provide the optimal thermal conditions at the beginning of the solidification, thus promoting the columnar-to-equiaxed transition.

Apart from constitutional undercooling, the potency of any grain refiner compound in a metal matrix is related to the free energy difference found at the interface where heterogeneous nucleation takes place [143]. In aluminium alloys, this condition is met in the event that the FCC-Al matrix and the grain refiner are coherent or partially coherent,

that is the case of the presence of a certain crystallographic orientation relationship (OR) between the two phases. Among the methods available to evaluate the strength of this OR and consequently the potency of a grain refiner, the edge-to-edge matching model [144] represents one which proved to be effective in highlighted suitable compounds for the Al-FCC matrix [110]. Following this theory, the interfacial energy between a matrix and a compound is minimised in the event a close-pack (CP) direction of each phase contains atoms arranged at similar distances [145]. Consequently, several parallel planes of both phases are set to create an interface containing the coupled CP directions, which will be stronger in the event these planes are CP, too. The result is an OR which can be evaluated following a few simple criteria.

- a matrix' direction $[uvw]_m$ couples a compound's direction $[uvw]_c$ when their effective interatomic spacing d_{eff} is similar. It is possible that the matching occurs between $d_{eff,m}$ and the double of $d_{eff,c}$, or vice versa. The CP directions' match between the FCC-Al matrix and a compound can be evaluated as:

$$\Delta dir = \frac{|d_{eff,m} - d_{eff,c}|}{d_{eff,m}} \leq th_{dir} \qquad \text{Equation 2.15}$$

This coupling is considered to be effective in case the parameter Δdir is lower than a threshold value th_{dir}, which is commonly equal to 0.1.

- once the matching directions have been identified, a similar process is conducted on the matrix' and compound's planes ($\{hkl\}_m$ and $\{hkl\}_c$, respectively). In this case, the crystallographic matching can be computed using the interplanar spacings d_{hkl} associated to the considered planes:

57

$$\Delta pla = \frac{|d_{hkl,m} - d_{hkl,c}|}{d_{hkl,m}} \leq th_{pla} \qquad\qquad \text{Equation 2.16}$$

Two different phenomena are needed to have an effective match between the two phases' planes. Firstly, similarly to the directions' match, the parameter Δpla needs to be lower than a certain threshold th_{pla}, which is still commonly equal to 0.1 following the edge-to-edge theory. Secondly, the matching CP directions need to be contained in the respectively matching CP planes (Equation 2.16):

$$[uvw]_m \in \{hkl\}_m \quad and \quad [uvw]_c \in \{hkl\}_c \qquad\qquad \text{Equation 2.17}$$

The resulting OR between a matrix and a compound is depicted in Figure 2.11.
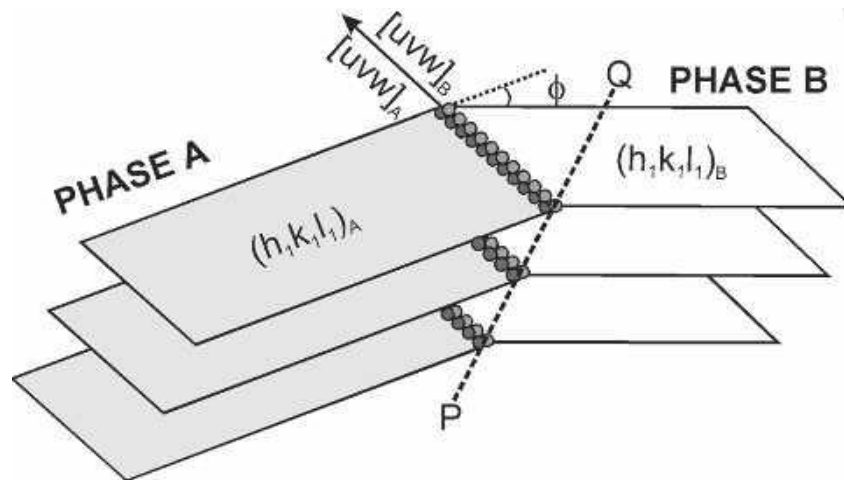
Figure 2.11: schematic view of the crystallographic match between a matrix (phase A) and a compound (phase B) [144]. The segment PQ is the track of the matching planar interface while ϕ is the angle between the two matching planes.

The potency of a grain refiner can be computed adopting the edge-to-edge theory and evaluating a surface mismatch parameter ε_s which considers not only the lattice misfits

and resulting effective interatomic spacing along the matching direction, but also the interplanar mismatch between the planes of the computed OR:

$$\varepsilon_s = \frac{|d_{hkl,m}d_{eff,m} - d_{hkl,c}d_{eff,c}|}{d_{hkl,m}d_{eff,m}}$$
Equation 2.18

This approach has been successfully adopted by Martin et al. [110] to rank several compounds and evaluate their potency in refining the microstructure of high-strength Al alloys processed by PBF-LB/M. An easier approach to evaluate the crystallographic matching between the matrix and inoculant compounds evaluates the misfits between two phases:

$$\varepsilon_\% = \frac{|a_m - a_c|}{a_m} \cdot 100$$
Equation 2.19

where a_m and a_c represent the matrix and compound lattice lengths. Despite being a less accurate method to compute crystallographic matching, Equation 2.19 has been largely used to compute the lattice misfits $\varepsilon_\%$ and evaluate the strength of potential grain refining compounds.

2.4.3 Alloys based on precipitation of Al based inoculant compounds

The promotion of in-situ precipitation of inoculant compounds represents one of the most widely used strategies to either design new alloys or improve the processability of wrought high-strength Al-alloys. As discussed in Section 2.1.2, this approach has been successfully adopted by the Airbus group for the design of Scalmalloy®. However, not only Sc and Zr are characterized by strong inoculation potential. Apart from these, other selected alloying elements, such as, titanium, erbium, and hafnium, form trialuminides

(Al$_3$X) that are characterized by extraordinary grain refining potency achieved due to their great crystallographic matching with the FCC-Al matrix [141] (Table 2.1).

Table 2.8: Crystallographic features of the most widely adopted inoculant compounds for in-situ precipitation [146].

GR	Structure	Lattice parameters $[\mathring{A}]$	Lattice misfit $\varepsilon_\%$ with FCC-Al [%]
Al$_3$Sc	FCC-L1$_2$	a = 4.103	1.32
Al$_3$Zr	FCC-L1$_2$	a = 4.080	0.75
	Tetragonal-D0$_{22}$	a = 4.014	-0.88
		c = 17.321	6.92
Al$_3$Ti	FCC-L1$_2$	a = 3.967	-2.04
	Tetragonal-D0$_{22}$	a = 3.848	-4.98
		c = 8.596	6.13
Al$_3$Er	FCC-L1$_2$	a = 4.215	4.08
Al$_3$Hf	FCC-L1$_2$	a = 4.048	-0.04
	Tetragonal-D0$_{22}$	a = 3.893	-3.87
		c = 8.925	10.20

Several approaches adopted the same strategy adopted for the design of the Scalmalloy®, that is the use of both Sc and Zr in the same alloy. The additions of these two elements and their effects on the microstructure and hot crack propensity were preliminary investigated in casting. Both simple binary compositions [147] and traditional wrought alloys [148] were found to solidify with grain refined microstructures. This highlights the great potential and stability of Sc and Zr inoculations in avoiding hot crack formation in a wide range of alloys and manufacturing techniques. Other studies focused on compositions not so distant from the one of Scalmalloy®, reporting very similar solidification behaviour and the presence of the bimodal microstructure in the as-built

condition [149–151]. Despite reporting these same findings, Yang and co-workers [152] found that the presence of cracks is highly influenced by the laser input. This confirms that PBF-LB/M regimes heavily affect the solidification dynamics and may promote hot crack formation also in grain refined microstructures. This result was confirmed by Bi et al. [153] who investigated Sc and Zr additions to AA7075. In addition, in case these inoculants are added to the base material via mechanical mixing, low energy PBF-LB/M regimes led to their uneven distribution and therefore discontinuities in the bimodal microstructural pattern which may cause hot crack formation. Apart from additions to base materials, the combined role of rare earth elements in refining the microstructure has been extensively investigated also as a main driver in different alloy design strategies [104,154]. In these studies, the effects of processing conditions were found to be crucial not only in promoting the bimodal microstructure formation, but also in increasing the strength capabilities of the custom compositions. Different PBF-LB/M regimes promote diverse melt pool overlap and, as a result, different fractions of equiaxed regions. Processing conditions paired with the correct development of the bimodal microstructures were found to be characterized by great mechanical properties before and after ageing.

Other approaches focused on the effects of single rare earth solutes. Specifically, several studies have focused on the use of Sc in their alloy design strategy in order to promote the precipitation of Al_3Sc and subsequent grain refinement. This mechanism is particularly promoted in rapid solidification processes, such as, PBF-LB/M, where Al_3Sc precipitates form a great number of nanoscale coherent dispersoids promoting a bimodal grain morphology [155]. Considering the Al-Mg binary system [156,157], this precipitation has proven to be stable in a wide range of processing conditions, ensuring

the possibility to produce crack-free parts at industrially-competitive PBF-LB/M regimes. The as-built mechanical properties of Sc-modified Al-alloys can be easily increased by a direct ageing characterized by fairly low times and high temperatures. Schmidtke et al. [156] reported indeed outstanding mechanical properties achieved after a direct heat treatment conducted on the as-built condition at 325°C for 4 hours. This is because Sc is characterized by poor diffusivity in the FCC-Al matrix and therefore is able to finely precipitate upon subsequent heat treatments, further improving the strength and ductility of the alloy [25]. Additionally, the authors reported similar mechanical properties for samples printed with different orientations, a result achieved due to the homogeneous grain morphology promoted by the precipitation of Al_3Sc. In order to maximize the mechanical properties, Jia and co-workers [158] designed an AlMnSc alloy with the specific aim of exploiting not only the strengthening provided by Sc addition, but also the great potential of Mn in increasing solid solution strengthening. Manganese has indeed high solid solubility in the FCC-Al matrix, which can be further increase as a result of the rapid solidification associated with PBF-LB/M [159].The designed composition showed exceptional printability paired with a yield strength of 556 MPa and an elongation at failure of 18%. Sc additions are not only beneficial to limit the formation of hot cracks, but they can also lead to increase in mechanical properties in alloys that are readily printable. Muhammad and co-workers [160] reported that the addition of 0.4 wt% of Sc to AlSi7Mg increased the strength and ductility of the base material towards high-strength Al-alloys. These properties were achieved due to the combination of the precipitation strengthening, ensured by the Al_3Sc dispersoids, and grain boundary strengthening, caused by the formation of a finely refined equiaxed microstructure. Although additions of Sc are paired with both great potential in suppress hot crack formation and increasing mechanical properties, this rare earth element is characterized

by high costs which, despite the minor additions, may triple or quadruple the price of the alloy [155].

After scandium, zirconium additions have been investigated due to their promotion of the in-situ precipitation of Al_3Zr, which takes place through a peritectic reaction [161]. Additionally, this compound is characterized by a great number of coupling orientation relationships with the FCC-Al matrix, ensured by the great crystallographic matching of both the $L1_2$ and $D0_{22}$ structures (Table 2.1). Hu et al. [162] demonstrated that Cu is able to stabilize the former crystal structure, which is paired with lower lattice misfits and therefore greater grain refining potential. Consequently, Zr is expected to be more effective when added to 2xxx series alloys which features copper as main solute [163]. Several studies have indeed focused on refining the microstructure of alloys from this series. Zhang et al. [164] and Nie et al. [165] added 2 wt% of Zr to AA2024 reporting the suppression of cracks in a wide processing window and the presence of a stable bimodal microstructure characterized by Al_3Zr in the middle of the equiaxed grains, copper segregation at grain boundaries (GB) and the occasional presence of ZrO. This compound may increase the number of nucleation sites, further promoting grain refining. In a subsequent study [166], the effects of various Zr wt% were investigated. It was found that higher Zr contents are able to eradicate the presence of cracks in PBF-LB/M regimes characterized by a higher scan speed. This is because of the progressive reduction of the grain size achieved when a higher number of dispersoids are precipitating during solidification which is also responsible for the increase of mechanical performances. The exceptional combination of strength and ductility of this alloying system was studied by Nie and co-workers [167] who investigated the role of Zr on the Portevin-Le Chatelier (PLC) effect. This phenomenon manifests as an unstable plastic flow during tensile

deformation of aluminium alloys which leads to the creation of a plastic plateau at the yield point resulting in high elongation at failure. This is the result of the intricate microstructure of AA2024+Zr, formed by fine equiaxed grains and the presence of Al_3Zr dispersoids in their core and secondary phases at their periphery (Figure 2.12(c)). All these features act as discontinuous obstacles for the dislocations resulting in plastic flow which becomes more obvious at higher Zr contents. Additions of zirconium have proven to be effective not only to AA2024, but also to several other wrought Al-alloys, such as, AA6061 [110] and AA7075 [110,168], and the binary Al-Mg system [169,170]. Specifically, Li et al. [168] found that PBF-LB/M regimes characterized by lower power show a higher degree of equiaxed regions with respect to the usual bimodal grain arrangement (Figure 2.12). This is because of the increased melt pools' overlap achieved in low energy regimes which results in the presence of only the equiaxed ribbon in the resulting microstructure. This effect was also observed by Griffiths et al. [170] who investigated the equiaxed degree of the Al-Mg-Zr system printed using different numbers of remelt of each layer.
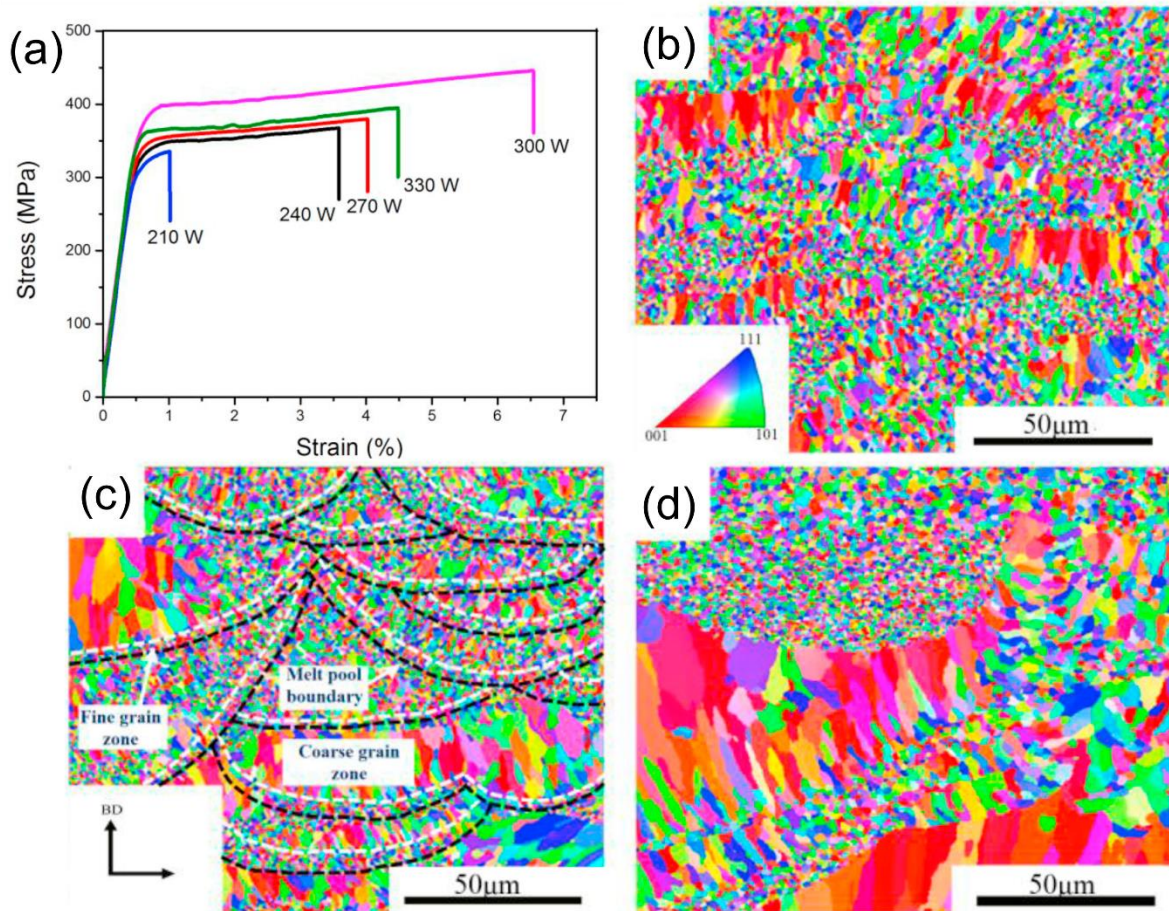
Figure 2.12: (a) stress-strain curves of samples printed at different laser power. (b), (c) and (d) depict the EBSD orientation maps of the specimens produced using 210 W, 300 W and 330 W, respectively [168].

Recently, titanium has been investigated as other potential inoculant to promote grain refining. In traditional casting of aluminium alloys, Ti is used to promote the columnar-to-equiaxed transition avoiding the formation of hot cracks and the use of rare earth elements, such as, Sc and Zr. For this reason, Zhang et al. [171] investigated the addition of 1.5 wt% to AA2024. Similar to Sc- and Zr-modified alloys, the material solidified with a cellular dendritic morphology arranged in a bimodal microstructure. The Al_3Ti compound was found in the middle of the equiaxed grains, while the ternary AlCuMg and Al_2Cu phases were found to precipitate at grain boundaries. The initial rate of development of constitutional undercooling r was computed combining the CALPHAD

65

approach and the ThermoCalc software. The results indicated that r grows when higher mass contents of Ti are added to AA2024 and therefore these compositions are well-expected to be most extensively refined. Tan et al. [172] conducted a similar investigation, refining AA2024 with Ti nanoparticles and reporting suppression of hot crack formation due to the bimodal microstructure. In addition to the cited phases, the presence of Al_3Mg_2 was reported. HRTEM analysis confirmed that the FCC-Al matrix grew with the [020] direction parallel to the [020] direction of Al_3Ti. This compound was found to precipitate with the metastable $L1_2$ crystal structure, which was promoted by rapid solidification of PBF-LB/M. Tensile tests conducted on the as-built samples showed great mechanical behaviour and the presence of the serrated flow resulting from the PLC effect. The heat treatability of the AA2024+Ti system was investigated conducting a standard T6. After ageing, the presence of Al_7CuFe was found in the microstructure, leading to a significant increase of yield and ultimate tensile strength without the presence of the serrated flow. Additions of Ti proved to be effective also on the AA7075 alloy [112]. Nevertheless, owing to the higher hot crack susceptibility of this alloy with respect to AA2024, the authors had to limit epitaxial growth adding ceramics in the building platform core, avoiding strong heat fluxes aligned with the building direction. A bimodal microstructure was found in the as-built condition, with $MgZn_2$ and Cu-rich phases at GBs. Similar to AA2024, the as-built samples showed the presence of the PLC effect which was avoided in the T6 condition. The precipitation of Al_3Ti was found to be effective not only in AA2024 and AA7075, but also in other alloys. Fan et al. [173] investigated the addition of the TiC compound to AlSi10Mg. This phase dissolved during melting, releasing Ti into the liquid which subsequently promoted the precipitation of Al_3Ti. Differently from the other systems, this grain refiner was characterized by the tetragonal-$D0_{22}$ crystal structure. Owing to the limited crystallographic matching of this structure with respect

to the L1$_2$ one, greater additions (4 wt%) were needed to promote the formation of the bimodal microstructure. Other elements, such as, erbium [174] and hafnium [175], have proven to behave similar to scandium, zirconium and titanium to either avoid hot crack formation in standard wrought alloys or to design custom compositions.

2.4.4   Alloys based on ceramic inoculant compounds

Apart from in-situ precipitation, the inoculation of Al-alloys in the context of PBF-LB/M has been conducted also adding ceramic compounds not reacting with the melt but also acting as dispersoids for heterogeneous nucleation. Ceramic compounds are characterized by lower crystallographic matching with the FCC-Al matrix, but they can be effective when added in significant amounts due to the introduction of a high number of potential nucleation sites [176]. This strategy is the same adopted in the A20X™ alloy, where TiB$_2$ are added to the base composition.

Similar studies have focused on the effects of titanium borides and di-borides on the grain morphology of Al-alloys. Fan et al. [177] conducted some preliminary investigations of the AlTiB system in the context of casting. The authors reported that the TiB$_2$ effectiveness increased in compositions in which Al$_3$Ti nucleated as an intermediate phase, that is prior to the FCC-Al matrix. This occurs because, between the tri-aluminide and the titanium diboride, the former has a better lattice misfit ensured by the L1$_2$ crystal structure. Similar findings were found by Huang et al. [178] who investigated the refinement behaviour of AA7075+TiB$_2$ processed by PBF-LB/M. The authors reported that the intermediate nucleation of Al$_3$Ti is driven by its lower Gibbs free energy. However, this property is highly affected by segregation and therefore the nucleation of

the trialuminides is influenced by the melt composition and solidification dynamics. The addition to the TiB_2 was found to be effective, as the as-built microstructure was characterized by the bimodal grain morphology. In the case of ex-situ additions, Patel et al. [179] proved that the main driver promoting grain refining, apart from the matrix-compound crystallographic matching, is the number of dispersoids introduced in the alloy. Therefore, especially in the context of rapidly solidified materials, the authors suggested that nanoparticles could be more effective than micro-sized powders as in equal mass additions are able to add a significantly higher number of nuclei. The addition of TiB_2 promotes hot crack inhibition also in AA2024 [180]. Nevertheless, as opposed to elements promoting in-situ grain refinement, significantly higher additions (5 wt%) had to be considered. The microstructure in the as-built condition showed the same phases often found when AA2024 is processed by PBF-LB/M, as the ceramic inoculant did not react with the melt. The presence of the PLC effect was found in as-built samples, proving that this particular plastic flow is mainly influenced by the arrangement of the microstructure and secondary phases, not by their nature. In addition, owing to their exceptional melting point and chemical stability, TiB_2 did not dissolve during ageing heat treatments, providing additional precipitation hardening to AA2024.

Similar to borides and di-borides, carbides additions to standard alloys have been investigated. Yi et al. [114] studied hot crack inhibition in AA7075 via WC-nanoparticles inoculation. Given the hexagonal crystal structure of WC, significant amounts (5.67 wt.%) were added to the base material. Nevertheless, crystallographic matching was found on the Al [111] and WC [0001] directions. Analogous to the case of AA2024, the microstructure of the resulted alloy was in essence the same of AA7075, with the bimodal grain morphology and presence of $MgZn_2$ at grain boundaries. Apart from WC, also TiC-

nanoparticles were found to be effective in avoiding hot crack inhibition when added to AA7075 [113]. The effectiveness of the compound was found only when a minimal amount (1 wt%) was added to the base material, highlighting the need to have enough particles to activate the columnar-to-equiaxed transition.

Lastly, several studies focused on the additions of hexaborides of La [181], Nd [182], Ce [183] and Ca [184,185] to Al-based alloys. This is because these compounds offer several available ORs for the FCC-Al matrix to heterogeneously nucleate. Alloys refined with hexaborides display all the characteristics of ex-situ grain refined alloys, such as, bimodal grain morphology in the as-built condition, great heat treatability due to secondary phase strengthening and exceptional ductility ensured by the PLC effect.

2.5 Effects of composition on hot crack propensity in high-strength Al alloys

Despite grain refining proved to be an effective method to avoid formation of hot cracks during PBF-LB/M fabrication, many other approaches have focused on the design of bespoke compositions tailored for the inhibition of such detrimental defects. A few main strategies can be highlighted:

- Several studies focused on the Al-Si binary system owing to its well-known castability with the specific aim to improve the ageing capabilities of casting alloys. Other studies added Mg focusing on the Al-Si-Mg ternary to investigate new composition laying in between PBF-LB/M casting alloys and wrought materials from the 6xxx series.

- On the other hand, several works investigated the Al-Cu binary with various additions of solutes to optimize hot crack propensity, heat-treatability, and mechanical properties. These studies based their design approach to this specific binary owing to the similarities with the 2xxx series and therefore enhanced hot crack inhibition properties.

- Lastly, some works focused on the design of bespoke high-strength Al-alloys with the specific aim of both reduce their hot crack propensity and increase their mechanical properties at high-temperature. These compositions are mainly based on the Al-Ce binary system.

2.5.1 Al-Si system

The equilibrium Al-Si phase diagram is presented in Figure 2.13. It is a relatively simple system, with the presence of a eutectic point at 577°C and 12.6 wt% Si and the maximum solubility of Si in FCC-Al phase of 1.6 wt%. Silicon is usually added to aluminium to increase the processability of the alloy during casting. This solute is indeed able to decrease both the melting temperature and the solidification range of the alloy due to the presence of the eutectic point. Moreover, Si improves the fluidity and reduce the thermal expansion resulting in an improvement in castability [186].
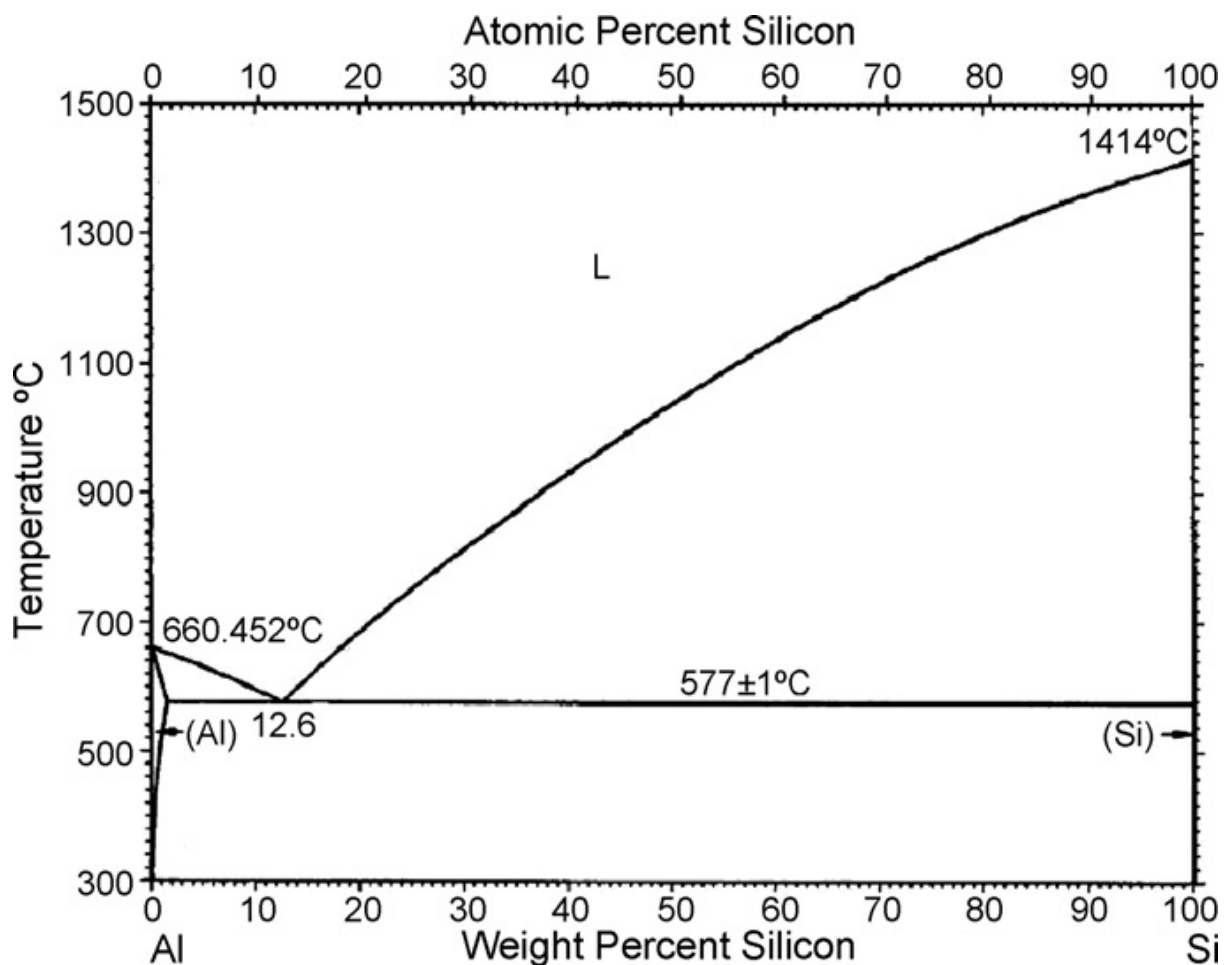
Figure 2.13: Al-Si binary phase diagram [187].

For these reasons, several studies focused on the investigation of various combinations from the Al-Si binary, including solid-solution [90,188], hypo-eutectic [188], near-eutectic [188] and hyper-eutectic [101,188] compositions. Lean alloys, with a Si content between 0.6 and 1 wt%, showed the presence of inter-granular cracks aligned with the building direction and reaching lengths of 500 μm or more [90,188]. These alloys were characterized by the presence of the FCC-Al and diamond Si phases in the as-built condition. Nevertheless, depending on the Si content, the morphology of the solidified substructures varied drastically. Solid-solution and hypo-eutectic compositions are typically characterised by a columnar dendritic morphology, while near-eutectic alloys solidified with a cellular microstructure similar to cast Al-Si-Mg alloys for PBF-LB/M. On the other hand, hyper-eutectic compositions showed the presence of primary petaloid structures due to the primary formation of diamond Si particles and subsequent growth of the FCC-Al matrix on top of them. The progressive addition of Si caused an increase of yield and ultimate tensile strength but a reduction in elongation at failure due to the formation of a progressively increased quantity of Si phases [188]. Moreover, for this specific reason, the coefficient of thermal expansion of the alloys is reported to decrease [101].

Owing to the merits of Si in improving the processability of aluminium alloys, several studies have focused on the addition of this solute to standard wrought compositions, such as, AA7075 [168,189–191]. Depending on the specific AA7075 composition and the PBF-LB/M processing conditions, additions of 3 to 5 wt% were reported to be able to avoid hot crack formation during printing. Montero-Sistiaga and co-workers [189] suggested that this was the result of the suppression of epitaxial growth and the

formation of a dual grain morphology formed by equiaxed grains at the melt pool boundaries and columnar grains in the core of the melt pool. This characteristic grain morphology, usually achieved by inoculation, is formed due to the increased constitutional undercooling resulting from the addition of Si [168]. Silicon was reported to not form detrimental intermetallics with other AA7075 solutes, precipitating at the end of solidification as diamond Si. The precipitation of this phase was reported to be beneficial in aiding the strain absorption during the last stage of solidification, limiting the hot crack propensity of the alloy. The heat-treatability of the AA7075+Si system was investigated by both conducting a direct ageing on the as-built condition, a T3 and a T6 heat treatment [189,191]. Maximum strength and minimum ductility reduction were achieved by means of a direct ageing conducted at 160°C for 6 hours because of the precipitation of Mg_2Si in addition to Mg_2Zn [191]. On the other end, with respect to AA7075, standard heat treatments caused a reduction of strength with respect to the as-built condition, which was the result of the easier over-ageing of the alloy caused by the Si addition [189].

In order to improve the mechanical properties and heat-treatability of Al-Si alloys, several studies focused on the investigation of the ternary Al-Si-Mg system [91,192,193]. A peak of hot crack susceptibility was found at a very low Si and Mg contents (approximately 0.2 wt% for both) as a result of the very steep solidification gradients developed at the last stage of solidification [192]. Geng et al. [193] investigated Al-Si8.1-Mg1.4, a composition similar to cast alloys but designed to improve the heat treatability of the ternary system. The alloy was reported to not form cracks in an industrially competitive process window, with the presence of a cellular microstructure in the as-built condition. The effects of direct ageing where comprehensively investigated, heat

treating the alloy at various temperatures and for several different durations. The dynamics of this thermal cycle proved to be crucial for the enhancement of the mechanical behaviour of the alloy, with optimal results achieved with a direct ageing conducted at 150°C for 8 hours. This optimal result was achieved because of the partial dissolution of the eutectic net and the promotion of the precipitation of finely dispersed Mg_2Si within the matrix.

2.5.2 Al-Cu system

The equilibrium Al-Cu phase diagram is presented in Figure 2.14. Despite this system is more complex (especially at the copper end), compositions close to the Al side are characterized by similar solidification features. It can be indeed noted the presence of a eutectic point at 548.2°C and approximately 33 wt% Cu, with a maximum solubility of copper in the FCC-Al phase of about 5.45 wt%. The presence of a near-stochiometric phase Al_2Cu, also called θ. The binary Al-Cu is the foundation of many alloys from the 2xxx series, the class of high-strength alloys characterized by lower hot crack propensity. Therefore, several works in literature based their alloy design strategy on this system.
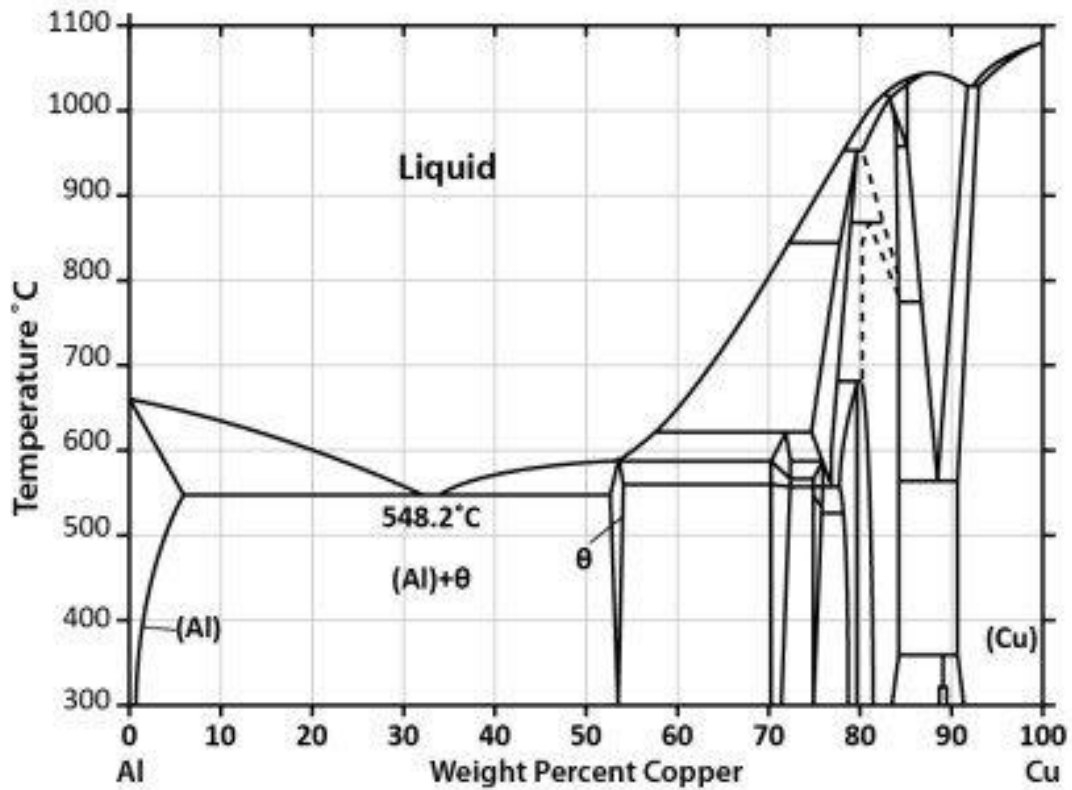
Figure 2.14: Al-Cu binary phase diagram [194].

The Al-Cu system has been investigated in a wide range of compositions, including solid-solution (4.5 wt% Cu), hypoeutectic (6 and 20 wt% Cu), near-eutectic (33 wt% Cu) and hyper-eutectic (40 wt% Cu) alloys, obtained mixing Al and Cu elemental powder [195]. Optimum consolidation and elemental mixing were reported by the authors, proving the merits of in-situ alloying to investigate custom compositions in the context of PBF-LB/M. The presence of cracks was found in the binary Al-Cu6 but not in the rest of the investigated compositions. Alloys with a composition equal or lower than 20 wt% Cu solidified with a predominant dendritic morphology characterized by the presence of an interdendritic net of secondary Al_2Cu phases. The eutectic alloy was formed by a very fine cellular structure formed by the eutectic FCC-Al/Al_2Cu morphology. Finally, Al-Cu40 was

75

characterized by primary θ phases surrounded by very fine eutectic structures. Despite the morphology was consistent within the samples, the size of the cells or dendrites was reported to increase at melt pool boundaries owing to the partial remelt of this region. The progressive addition of Cu caused an increase of strength paired with a reduction of elongation at failure owing to the greater presence of the brittle Al_2Cu phase.

Several other works were conducted on the Al-Cu5 binary, refined with the addition of Mn, Ti, V and Cd [196–199]. With respect to 2xxx series alloys, the absence of Mg causes a reduction of solidification range and *HCS* which results in a further reduction of hot crack propensity [85]. This composition proved to be able to produce crack-free microstructures at scan speeds of around 100-250 mm/s. However, hot cracks were found in the upper part of the melt pools of the last deposited layer. Within the sample, cracks were not found because of the melt pools' overlap between a layer and the next one (Figure 2.15). The as-built microstructure was characterized by small columnar grains promoted by the low scan speed regimes adopted for fabrication and limited presence of epitaxial growth, which helps in reducing the hot crack propensity of the alloy.
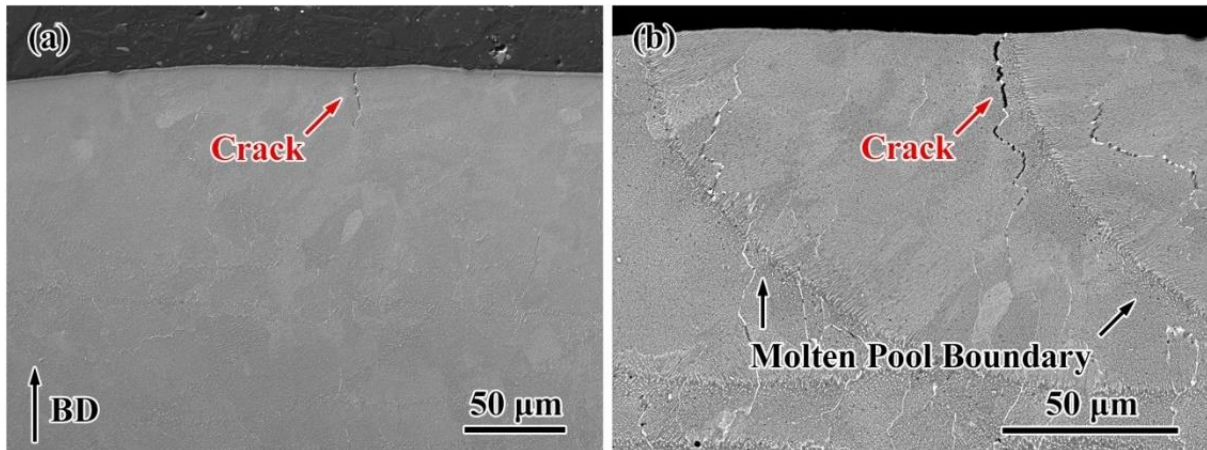
Figure 2.15: SEM/BSE images of the typical crack location within the molten pool. (b) is a magnification of (a) [199].

X-ray diffraction (XRD) measurements proved that the alloy was characterized by a dual phase microstructure formed by FCC-Al and Al_2Cu, which showed good strength and ductility in the as-built condition. The heat treatability of the system was investigated conducting several ageing cycling including a T3 and various T6 heat treatments conducted at different temperatures and times. These thermal cycles' features proved to play a fundamental role in the precipitation and morphology of the strengthening compounds. Specifically, optimum results were achieved with a T6 conducted at 153°C for 24 hours; the alloy was indeed characterized by a yield strength of 345.4 MPa, an ultimate tensile strength of 470.6 MPa and an elongation at failure of 11.76%. In this condition, precipitation hardening was found to cause the highest increase of mechanical strength due to the precipitation of nano-sized Al-Cu-Mn compounds homogeneously dispersed in the microstructure.

Other studies focused on the binary Al-Cu with the addition of selected solutes to improve processability and mechanical properties. Karg et al. [200] focused on the addition of nano-sized SiO_x powders to Al-Cu4-Mg1.5 with the specific aim of increasing the

flowability of the powder mixture. The resulting feedstock was characterized by a lower angle of repose, the nano-particles are indeed able to reduce the friction between the feedstock particles. In order to improve the mechanical properties at high temperature, Bahl et al. [24] studied the Al-Cu system with the addition of cerium (Al-Cu8-Ce5). Owing to its limited diffusivity in Al, Ce is able to form precipitates that are stable at high temperature and therefore preserve the mechanical properties of the alloy up to at least 250°C [201]. Moreover, the addition of Ce reduces the hot crack susceptibility increasing the solidus temperature of the alloy. The as-built microstructure was characterized by a eutectic structure with the presence of FCC-Al and the ternary Al_8Cu_3Ce intermetallic. The alloy was characterized by the presence of a dual grain morphology, promoted by the great development of constitutional undercooling promoted by the chemical complexity of the system. Therefore, the combination of less severe solidification characteristics (e.g., shorter solidification range and lower HCS) and presence of both equiaxed and columnar grains is reported to be ideal to avoid hot crack nucleation.

2.6 Summary

The processability of high-strength Al-alloys is hampered by the formation of detrimental defects such as, porosities and hot cracks. Specifically, macro-pores arising from either incorrect melt pools overlap (LOF) or excess of deposited energy (keyhole) largely affect the correct consolidation of the alloys, resulting in low relative density and a consequent reduction of mechanical properties. Nevertheless, pore-free processing windows can be identified by either extensive experimental trials or by the computation of the melting and solidification characteristics of the alloy.

In the as-built condition, the microstructure of high-strength Al-alloys is formed by dendritic features which are generally arranged in a columnar grain morphology. The presence of long intergranular cracks, spanning several layers and aligned with the building direction is often detected in the material. These features are thought to arise from the combination of high cooling rates in alloys showing high solidification range and steep cooling trajectories at the end of solidification. Several approaches have been proposed to mitigate the occurrence of these cracks, such as grain inoculation to promote grain refining and modification of alloy chemistry. Optimal results were achieved when these bespoke compositions were able to both avoid hot crack formation in as-built condition and maximize the strength after heat treatment.

Although the literature is populated with good works adopting these strategies to minimize the presence of cracks and maximize the strength of the resulted compositions, some gaps require more attention:

- despite the cracks detected in the as-built microstructure are often referred to as "hot cracks", their features are not the ones of defects arising from the liquid-to-

solid transformation. Specifically, the absence of segregation and oxidation coupled with their macroscopic morphology are key indicators that these features are perhaps arising from other phenomena. Therefore, in this thesis a widely used alloy (AA2024) has been selected to further investigate the cracking behaviour of high-strength compositions from the 2xxx series.

- some studies tried to link the reduction of cracking intensity noted in low scan speed regimes with the developed dynamic thermal condition influencing the hot crack driving force. Nevertheless, these attempts were somewhat limited as they only considered characteristic values of the cooling rates and thermal gradients, neglecting the multiple melting cycles taking place during PBF-LB/M and the relevance of only the last solidification event on hot crack formation. Additionally, these studies overlooked the somewhat stochastic nature of hot cracking which results from the development of strong driving forces along selected regions of the microstructure, namely grain boundaries. It is therefore of interest to model the solidification of the semi-solid and investigate the temporal and spatial distribution of hot crack driving force to comprehensively understand the dynamics leading to hot crack inhibition.

- a lot of works proposed new alloys characterized by reduced hot crack propensity and consequently crack-free microstructures. However, a number of limitations have been highlighted. Firstly, these bespoke compositions were often developed using either several pre-alloyed powders or mixing Al with nano-powders of elemental solutes. In addition, the resulted compositions were printed in low scan speed regimes, which are known to be paired with limited hot crack formation. Lastly, the choice of alloying elements was often conducted without the computation of design indices against hot cracking and without considering the

important role of the microstructure's morphology. It is therefore of interest to design a strongly hot-crack-resistant alloy, characterized by great strength and heat treatability using a powder-free methodology informed by computational tools, such as, the CALPHAD method.

This thesis aims to comprehensively characterize and understand high-strength Al-alloys' hot cracking dynamics in the context of metal additive manufacturing, proposing methods to avoid hot crack formation and design bespoke compositions tailored for the fast cooling of PBF-LB/M.

Chapter 3

3 Materials and methods

3.1 Laser Powder Bed Fusion (PBF-LB/M)

3.1.1 PBF-LB/M system adopted for the processing of the samples

All the samples investigated in the present work were produced using a Renishaw AM400 (Renishaw PLC, UK). The machine is equipped with a 400 W ytterbium fibre laser with a wavelength of 1070 nm and a spot size of 70 μm. The optical train is characterized by a maximum permitted scanning speed of 2 m/s and a positioning speed of 7 m/s which result in a maximum build rate of 20 cm³/hour. The build volume of the machine is characterized by an area of 248 × 248 mm² and a maximum vertical position of 285 mm. The AM400 has the possibility to heat the build platform up to 170°C. During all operations, the building chamber was maintained under an Ar atmosphere with an oxygen level below 400 ppm to minimise oxidation.

The AM400 can be used in two different configurations:

- full volume: in this configuration the machine is able to use its full volume capabilities.

- reduced build volume (RBV): in this configuration an ancillary is mounted on top of the build platform enabling the production of specimens using small quantities of powder ($0.25 \div 0.75$ dm³). The RBV is characterized by a 78×78 mm² and a maximum vertical position of 55 mm. In this configuration, the AM400 is not able to operate with the heated platform.

The Renishaw AM400 is a modulated wave laser system, this means that a single scan track is subdivided in multiple single static exposures. Consequently, with respect to continuous wave laser system, the scan speed is influenced by multiple parameters. Figure 3.1 depicts the spatio-temporal law associated to the optical train. A single scan track of generic length is subdivided in various segments (pulses) based on the point distance PD, namely the distance between adjacent irradiations. A single pulse is subdivided in two separate temporal segments: in the first the laser is on and irradiates the powder bed, in the second the laser is off and moves to the next firing position. The prior temporal segment represents the exposure time ET while the latter the delay time DT. Since a scan track is the sum of multiple pulses, the laser scan speed v can be computed from the speed linked to a single total irradiation cycle. This expression is presented in Equation 3.1:

$$v = \frac{PD}{ET + DT}$$

Equation 3.1
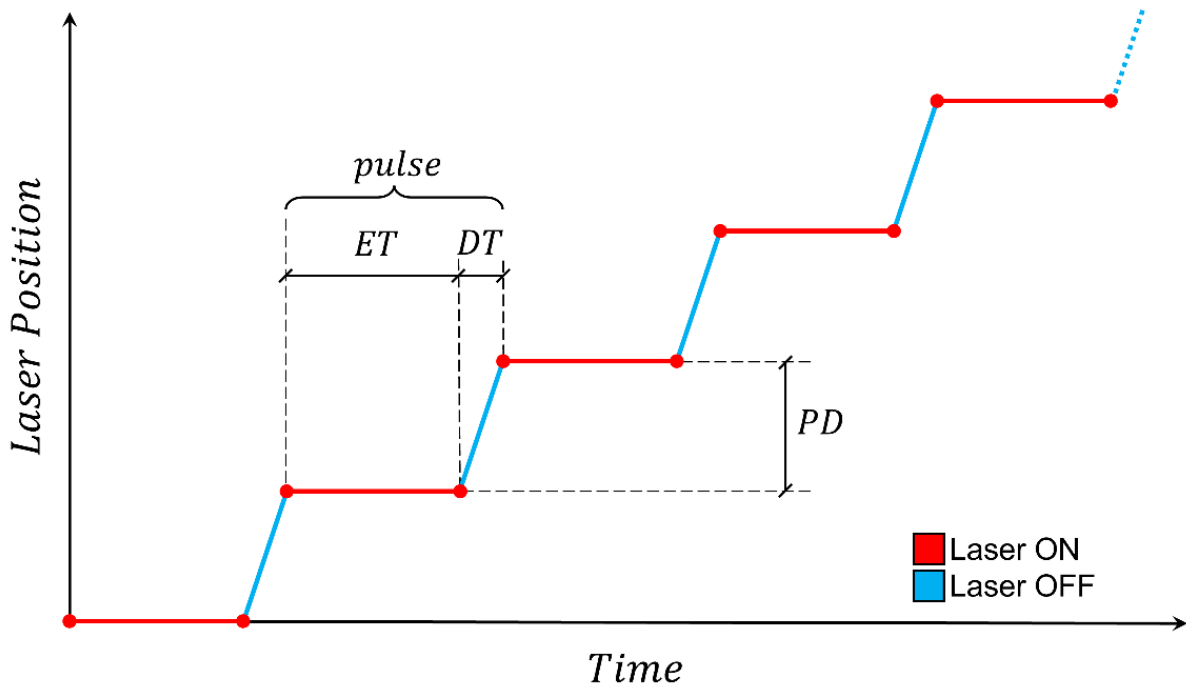
Figure 3.1: laser spatio-temporal evolution associated to the Renishaw AM400 system.

3.1.2 Production of AA2024 and AA2024+Ni3 samples towards the investigation of the effects of processing regimes and alloy chemistry on hot crack formation

AA2024 aluminium alloy was investigated in the first part of Chapter 4. In order to reduce thermal expansion and thermal gradients, the AA5053 aluminium build platform was kept at the highest permitted temperature of 170°C. Cubic samples with a 10 mm edge were produced with a powder layer thickness of 30 μm, using a meander scan strategy with a rotation angle of 67° and a 120 μm hatch distance. The point distance and delay time were kept constant at 60 μm and 20 μs, respectively, whereas the exposure time was changed to achieve difference in scan speed. In total, 35 unique combinations of power and exposure time were used to produce samples with various processing conditions. These are listed in Table 3.1.

Table 3.1: range of powers and exposure times used to fabricate the AA2024 samples in Chapter 4.

Parameters	Values
Power [W]	180, 200, 220, 240, 260, 280, 300
Exposure Time [μs]	40, 48, 60, 80, 120

In the second part of Chapter 4, a comparison between the consolidation and cracking behaviour of AA2024 and AA2024 blended with 3 wt% of Ni (AA2024+Ni3) was carried out. Within all the plausible aluminium's alloying elements, nickel was selected for strength and processability purposes. This element possesses one of the highest solid solutions strengthening factors among the Al solutes [202]. Additionally, it introduces a eutectic characterized by a temperature higher than copper, magnesium, and silicon, the three major solutes of AA2024 [202]. Therefore, the solidus temperature of the refined alloys is expected to grow, resulting in an advantageous decrease of the solidification range.

All the samples in this study were produced using the RBV due to the limited availability of the AA2024+Ni3 powder. Cubic samples with a 10 mm edge were produced with a powder layer thickness of 30 μm, a rotation angle of 67° and a 120 μm hatch distance. The point distance and delay time were 60 μm and 20 μs, respectively. Four different unique process parameters combinations were used to evaluate differences in densification within a wide range of processing conditions. These are listed in Table 3.2.

Table 3.2: range of power, exposure time and scan strategies used to fabricate both the AA2024 and AA2024+Ni3 samples in Chapter 4.

Parameters	Configuration			
	A	B	C	D
Power [W]	180	300	180	300
Exposure Time [µs]	120	40	120	40
Scan Strategy	Meander	Meander	Chessboard	Chessboard
Island Size [mm]	-	-	3	3

3.1.3 <u>Laser surface melting and production of AA2024 samples towards hot crack reduction and improved build rate</u>

In the first part of Chapter 5, the laser of the Renishaw AM400 system was adopted to conduct surface melting and investigate the hot cracking behaviour of AA2024 as a function of distinct melting regimes. A custom Point Distance Variation (PDV) scan track was created using a Python script able to individually specify the processing conditions of each pulse. The PDV track was characterized by four segments of five pulses each with process parameters listed in Table 3.3. These are addressed as PD15, PD30, PD45 and PD60 following their value of point distance *PD*.

Table 3.3: laser surface melting parameters adopted for the four segments of the Point Distance Variation (PDV) track.

Parameters	Values
Power [W]	200
Point Distance [μm]	15, 30, 45, 60
Exposure Time [μs]	120
Delay Time [μs]	20
Oxygen content in the building chamber [ppm]	400

The PDV track was performed on a AA2024-T351 disc characterised by a diameter of 10 mm and a thickness of 0.50 mm which was held at the laser focal plane.

In the second part of Chapter 5, in order to investigate the cracking behaviour in macroscopic parts, 10 mm cubic samples with same point distance, delay time, exposure time and power combinations discussed in the first part of this paragraph were produced. Following the AlSi10Mg datasheet from Renishaw, the layer thickness was set to 30 μm, the hatch distance to 120 μm, a meander scan strategy with a 67° rotation angle was adopted and the platform was heated to 170°C. In order to differentiate laser surface melting and PBF-LB/M regimes, these processing conditions are addressed as AM-PD15, AM-PD30, AM-PD45 and AM-PD60. The AM-PD15 and AM-PD60 regimes were adopted to produce cylinders characterized by a diameter of 8 mm and a length of 60 mm. These specimens were fabricated with their main axis perpendicular to the building direction and subsequently machined to obtain tensile specimens (dimensions are reported in Section 3.10).

In the third and last part of Chapter 5, a study focused on increasing the build rate of AA2024 was conducted. Cubic samples of 10 mm edge were produced using a Renishaw AM400 and a Reduced Build Volume set up. During processing, the build chamber was held under an Ar atmosphere to minimise oxidation with an oxygen content below 400 ppm. A meander scan strategy, where the direction of laser tracks was rotated by 67° at each layer, was adopted. As largely reported [10,13,14], hot crack formation results to be strongly affected by the scan speed with low values limiting the presence of such detrimental defects. In the present case, specimens were produced using a laser scan speed v of 0.107 m/s (point distance of 15 µm, exposure time of 120 µs and an inter-pulse delay of 20 µs) which proved to be effective to fabricate crack-free parts. The parameters that were investigated with the aim to increase build rate are summarised in Table 3.4.

Table 3.4: range of power, layer thickness and hatch distance used to investigate the effects of build rate.

Parameters	Values
Power P [W]	200, 220, 240, 260, 280, 300
Layer thickness Δz [µm]	30, 35, 40, 45, 50
Hatch distance h_d [µm]	120, 130, 140, 150, 160, 170, 180

3.1.4 Production of ACN001 samples via PBF-LB/M

The custom ACN001 composition was designed and fabricated in Chapter 6. This alloy was specifically developed to be hot crack resistant in high scan speed regimes. Therefore, 10 mm cubic samples were printed adopting a point distance of 60 µm, an

exposure time of 30 μs and the default delay time of 20 μs which resulted in a relatively high scan speed (1.20 m/s). The layer thickness was set to 30 μm, a meander scan strategy with a 67° rotation angle was adopted and the platform was kept at ambient temperature. In total, 12 unique combinations of power and hatch distance were investigated. These have been listed in Table 3.5.

Table 3.5: range of power and hatch distance adopted to study the consolidation of ACN001.

Parameters	Values
Power [W]	260, 280, 300, 320
Hatch distance [μm]	80, 100, 120

The sample produced with a power of 320 W and a hatch distance of 80 μm was found to be characterised with the higher relative density. Therefore, this parameters' set was used to produce cylinders characterized by a diameter of 8 mm and a length of 60 mm which were fabricated with their main axis perpendicular to the building direction and subsequently machined to obtain tensile specimens (dimensions are reported in Section 3.10).

3.2 Optical Microscopy (OM) and image segmentation analysis

In order to quantify the internal defects, all the samples produced in this work were cut parallel to the building direction and then mounted and polished according to standard practice with a final polish of colloidal silica. A Nikon Eclipse LV100 ND microscope was used to obtain optical micrographs which were afterwards analysed to quantify the presence of defects using an in-house developed Matlab routine. Using this approach, each micrograph was converted into grey scale and then binarized to highlight the defects from the solidified alloy. The material's relative density was computed by considering the ratio of the number of black pixels to the total number of pixels of each micrograph. The various defects were classified considering the geometrical features listed in Table 3.6.

Table 3.6: geometrical features of each defect type identified by the Matlab routine.

Property Name	Symbol	Description
Circularity	C	Roundness of the region, evaluated by $\frac{4 \cdot Area \cdot \pi}{Perimeter^2}$. For a perfect circle, the circularity value is 1.
Major Axis Length	d_{max}	Length of the major axis of the ellipse that has the same normalized second central moments as the region.
Minor Axis Length	d_{min}	Length of the minor axis of the ellipse that has the same normalized second central moment as the region.
Orientation	φ_{angle}	Angle between the horizontal axis and the major axis of the ellipse that has the same second-moment as the region.

		Maximum distance between any two boundary points on
Max Feret Diameter	$d_{max,f}$	the antipodal vertices of the convex hull that encloses the object.
Min Feret Diameter	$d_{min,f}$	Minimum distance between any two boundary points on the antipodal vertices of the convex hull that encloses the object.

In order to differentiate cracks and pores several geometrical constraints were applied to each feature. Defects satisfying the conditions expressed in Equation 3.2 were treated as cracks:

$$C \leq 0.9 \; ; \quad \frac{d_{max,f}}{d_{min,f}} \geq 2 \; ; \quad \left|\varphi_{angle}\right| \geq 45° \qquad \text{Equation 3.2}$$

All the other defects were treated as pores. Depending on pore size, it was then possible to differentiate macro-pores, derived from lack-of-fusion or keyholing, from gas pores. Specifically, porosity satisfying the condition expressed in Equation 3.3 was treated as gas porosity.

$$\frac{d_{max} + d_{min}}{2} \leq 0.02 \; mm \qquad \text{Equation 3.3}$$

The remaining pores were categorised as either lack-of-fusion and keyhole pores. Defects having a circularity of less than 0.7 were classified as lack-of-fusion, while the remaining were considered as keyhole pores. The thresholds present in Equation 3.2 and 3.3 were highlighted through an intensive iterative investigation.

To quantify crack density, a cumulative crack length (CCL) parameter was used with the scope of addressing the total length of the cracks found per unit area. CCL is defined as:

$$CCL = \frac{\sum_{i=1}^{N} d_{max,i}}{A}$$

Equation 3.4

where i is used to index the N cracks found in each micrograph and A is the total area of the micrograph. All the micrographs needed to conduct this type of analysis were collected at the same magnification and therefore their area resulted to be constant (7.11 mm²). An example of the application of the routine described in the present section is reported in Figure 3.2 which depicts the graphical output of the image segmentation analysis.

For each combination of laser power and speed experimentally analysed, four different micrographs were investigated to ensure a good level of repeatability in the measurements. Additionally, linear interpolation between experimental points was carried out to better identify the trends between specific process parameters and recorded defects. The Matlab code described in the present section is reported in Appendix A.
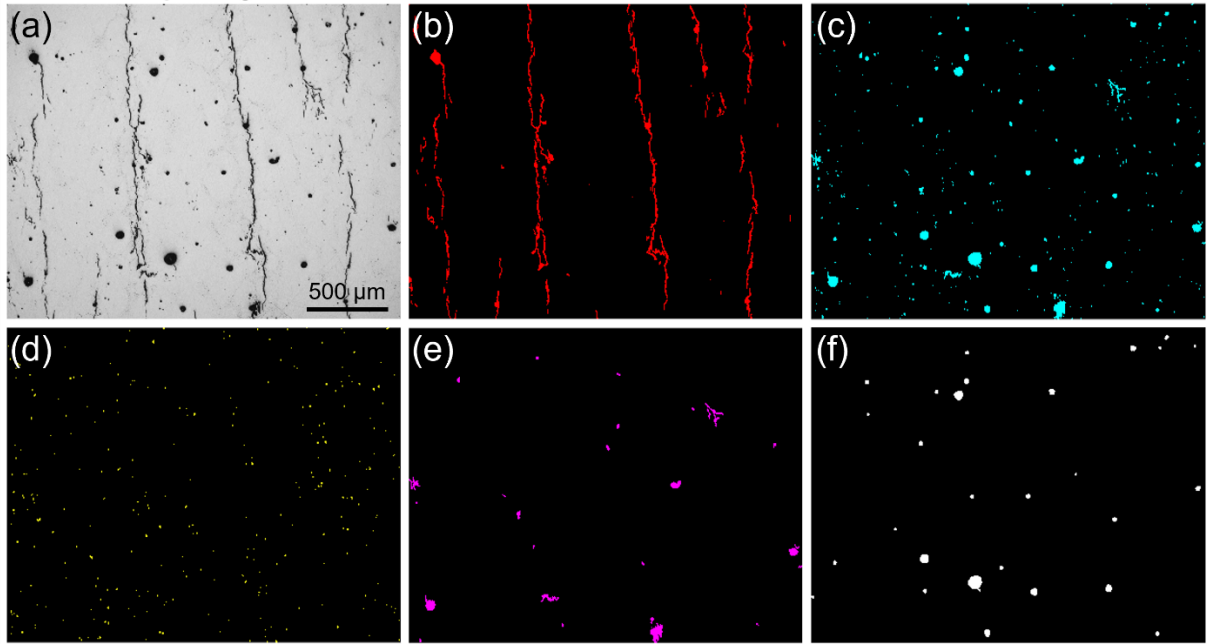
Figure 3.2: application of the image segmentation analysis to a micrograph. (a) represents the original image, (b) depicts the cracks and (c) all the pores found in the microstructure. These are then subdivided into (d) gas pores, (e) lack of fusion and (f) keyhole pores.

3.3 Scanning Electron Microscopy (SEM)

Scanning Electron Microscopy (SEM) consists in the analysis of a conductive sample using a focused electron beam. The interaction between the electrons and the specimen generates an interaction zone which represents the area where the electrons possess enough energy to penetrate and therefore interact with the sample. Depending on the energy associated with the focused electron beam, the interaction zone depth changes causing various effects (Figure 3.3) which can be generally subdivided in emitted and transmitted signals. This paragraph focuses on the study of the prior class of interactions, the latter will be analysed in Paragraph 3.4. The emissions analysed in this work consist of backscattered electrons (used for imaging and to obtain chemical and crystallographic information), secondary electrons (used for imaging and surface analysis) and x-ray radiations (used for chemical analysis).
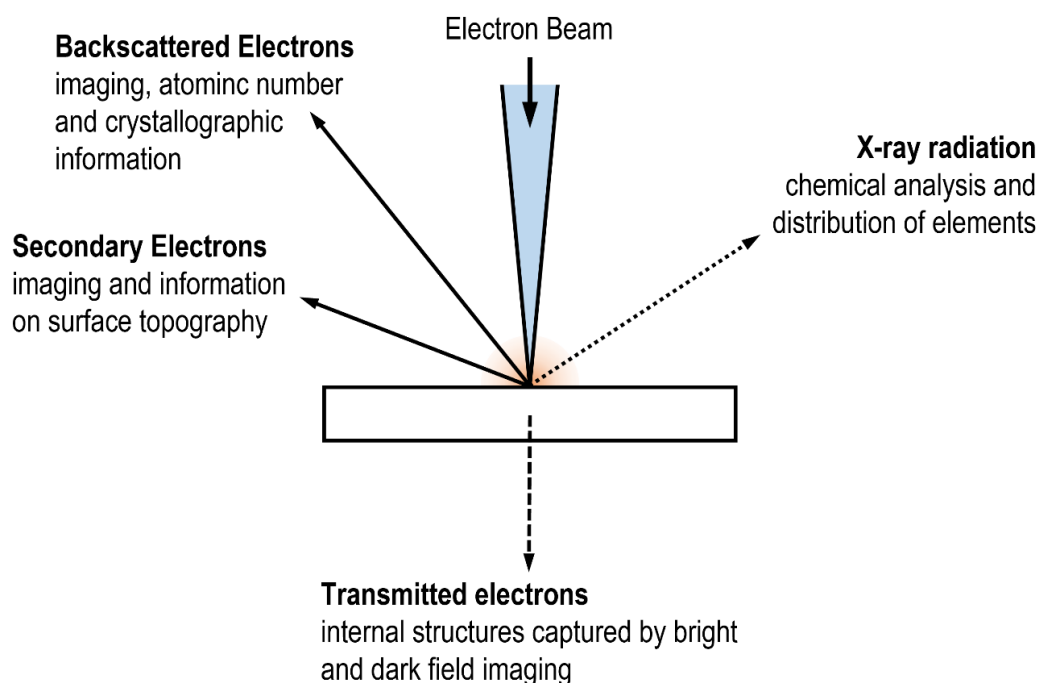
Figure 3.3: schematic representation of the interactions between the electron beam and the sample investigated in this work.

Secondary Electron Imaging (SEI) was used in this work to obtain topographic micrographs of the microstructure. Surface topography can be used as additional information about the arrangement of the phases in the material as these will be differently removed by the colloidal silica polishing step. With respect to optical microscopy, this method has the advantage of having a higher depth of field and a higher resolution achieved by the possibility to focus the electron beam to a smaller area. On the other hand, in order to have enough topographic information, the samples need to be over-polished resulting in a not perfectly flat surface not suited for other analysis, such as Electron Backscattered Diffraction (EBSD).

Backscattered electrons (BSE) are considered to be part of the electron beam which, after the interaction with the surface of the specimen, are deflected and turned back out of the interaction volume. Therefore, their energy state varies from the energy related to secondary electrons and the energy possessed before backscattering. Bishop [203] demonstrated that the amount of backscattering associated to the electrons increases with the increase of the atomic number of the atoms in the interaction volume. Therefore, the contrast detected capturing BSE represents differences in atomic number across the scanned area. For this reason, backscattered electron imaging (BSEI) result to be a solid technique to image the microstructure and detect the presence of secondary phases. This imaging technique works particularly well in the event the sample result to be an aluminium alloy because of the low atomic number of Al and the high atomic number of its most common alloying elements.

Raw Electron Backscattered Diffraction (EBSD) data were analysed in Matlab with the aid of the MTEX toolbox. Orientation mismatch of 8° was used as a threshold to segment

the grains. The colour legend of all the EBSD maps was set so that the {100} family of crystallographic directions of the Al-FCC matrix was aligned to the building direction. Ellipse fitting was used to approximate the grains and compute their size in planes parallel to the BD. The average minor and major axis were used to evaluate the average width and length of columnar grains. On the other hand, grain sin the plane perpendicular to the BD were approximated with circles to evaluate their average diameter. Additionally, the grain boundary misorientation was used to characterize the cracking interface, Pole Figures and Inverse Pole Figures were automatically generated using the toolbox.

Energy Dispersive X-ray Spectroscopy (EDX, also known as EDAX or EDS) adopts a semiconductor detector to classify the spectrum of the X-ray emission based on its characteristic signature. During the measurement, all the energy states are read, digitised, and stored in the memory of a computer. EDX analysis returns the number of counts associated to each energy step enabling the visualization of the collected spectrum. Comparing the detected peak position with the pure elements' nominal ones it is possible to assess not only the material's composition, but also the specific spatial distribution of the elements in the microstructure.

In the present work a few different scanning electron microscopes were adopted depending on the conducted investigation. The JEOL 7100F FEG-SEM, equipped with a NordlysMax3 EBSD detector, was used to conduct imaging (Section 3.6.2 and 4.1.7, Chapter 5 and 6) and collect crystallographic data (Chapter 5). For imaging, an accelerating voltage of 6kV was adopted, the current was set to 9 nA and the sample was moved to a working distance of 6 mm. On the other hand, EBSD data were collected tilting the sample at a 70° angle with respect to the horizontal and with an accelerating voltage

of 15 kV and a current set to 11 nA. The Thermofisher Scientific Helios G4 He$^+$ pFIB DualBeam™ FIB/SEM equipped with a Symmetry EBSD detector was used to collect large area images and crystallographic data of the AA2024 samples investigated in the first part of Chapter 4. In addition, this system was adopted to conduct a 3D EBSD/BSE reconstruction of the grain structures found in the vicinity of a hot crack. A 50 μm by 30 μm area was selected and analysed via lift out and subsequent sectioning: every 50 nm a BSE image was taken and every 150 nm an EBSD dataset was collected. These series of tiles were aligned and assembled in the Dream3D software allowing the 3D-reconstruction of the grains and crack tip in Paraview.

3.4 Transmission Electron Microscopy (TEM)

Transmission Electron Microscopy (TEM) focuses on the analysis of the transmitted signals caused by the interaction between the electron beam and the specimen (Figure 3.3). Bright-field (BF) TEM imaging represents one of the most common transmission electron microscopy imaging techniques in which an image is collected along the electron beam's axis [204]. High-angle annular dark-field (HAADF) imaging represents another TEM technique in which incoherently scattered high angle electrons form an annular dark field image. High atomic number elements cause scatter at greater angles due to the presence of more pronounced electrostatic interactions. Therefore, heavy elements appear brighter in the resulting images with respect to low atomic number metals. As a result, this technique is more sensitive to chemical inhomogeneity with respect to BF imaging, enabling the possibility to investigate the morphology of very small secondary phases' clusters.

TEM imaging was performed using a FEI Tecnai F20 field emission gun scanning transmission electron microscope (FEG-STEM) operated at an accelerating voltage of 200 kV. The TEM was equipped with Oxford Instruments energy dispersive X-ray spectroscopy with a 80 cm^2 sized windowless detector. BR and HAADF images, along with STEM/EDX maps for the elements of interest, were recorded to analyse the microstructure in the vicinity of a hot crack tip found in a AA2024 sample (Section 4.1.6).

3.5 X-ray diffraction (XRD)

X-ray diffraction (XRD) was used in this research to identify the solid phases present in the microstructure. XRD is based on the interference between X-rays and a crystalline sample [205]. The X-rays used for the analysis are generated by a cathode tube and consequently filtered to a specific wavelength, collimated, and directed towards the specimen. Once the X-rays interact with the atomic planes of the sample, they are diffracted at different angles producing a pattern which is unique for each phase's crystal structure. All the measurements in the present work were carried out with the use of a Bruker D8 Advance Da Vinci diffractometer (Siemens, Munich, Germany) equipped with a Lynxeye 1D detector. Data were acquired with a step size of 0.02° and a step time of 4 seconds scanning between $2\theta = 15°$ and $2\theta = 90°$. The detected diffraction peaks were then identified in the Bruker software Diffract.EVA with the aid of the ICDD database PDF+2.

3.6 Powder characterization and preparation

In this work, multiple materials were investigated. AA2024 aluminium powder was procured from TLS Technik GmbH & Co (Germany). The composition of the powder was measured using Inductively Coupled Plasma Optical Emission Spectroscopy (ICP-OES) and results are listed in Table 3.7. This powder was used to produce the samples investigated in Chapter 4 and 5 of the present work.

Table 3.7: chemical composition (in wt%) of the AA2024 alloy procured from TLS Technik GmbH & Co (Germany).

Si	Cu	Mg	Mn	Fe	Ti	Cr	Zn	Al
0.36	4.57	1.34	0.98	0.12	< 0.02	< 0.02	< 0.02	Bal.

A custom composition named ACN001 with the nominal composition shown in Table 3.8 was procured from ECKA Granules GmbH (Germany). The composition of the powder was measured using ICP-OES and results are also given in Table 3.8. This powder was used to produce samples investigated in Chapter 6 of this work.

Table 3.8: Nominal and measured chemical composition (in wt%) of the ACN001 custom alloy procured from ECKA Granules GmbH (Germany).

	Cu	Ni	Fe	Si	Al
Nominal composition	5.5 ÷ 6.5	5.5 ÷ 6.5	≤ 0.1	≤ 0.1	Bal.
Measured composition	5.6	6.2	0.1	0.02	Bal.

AA2024 was modified by the addition of Nickel powder using Resonant Acoustic Mixing (RAM) [206]. High purity (3N) Nickel powder with Average Particle Size (APS) of 2-3 μm was procured from Nanoshel UK Ltd. In order to obtain the desired AA2024+Ni3 composition, 30 grams of nickel were mixed with 970 grams of AA2024. A Resodyn™ resonant acoustic mixed LabRAM1 (USA) was used to blend the powders together; the feedstocks were mixed for a total time of 5 minutes with an acceleration of 30G.

The morphology of the powders was investigated via SEM/BSEI (Figure 3.4). AA2024 (Fig. 3.4(a)) was found to be characterized by spherical particles with the occasional presence of globular satellites (solid arrows). In addition to these features, AA2024+Ni3 (Fig. 3.4(b)) showed the presence of nickel flakes homogeneously distributed (dashed arrows). The custom alloy ACN001 (Fig. 3.4(c)) was characterized by near-spherical particles with the presence of fine and irregular satellites (solid arrows).
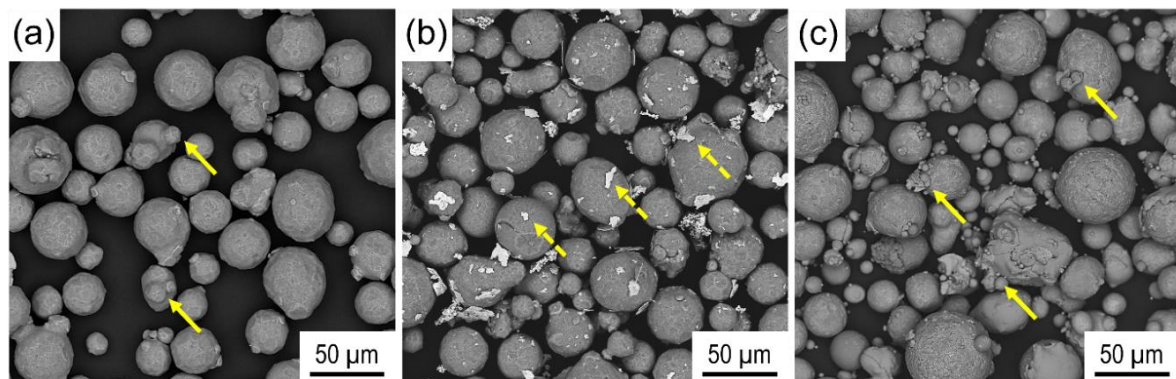
Figure 3.4: SEM/BSE micrographs showing the morphology of the (a) AA2024 powder, (b) AA2024+Ni3 powder and (c) ACN001 powder.

Laser Size Diffraction (LSD) was used to measure the particle size distribution (PSD) of the powders used in the present work. Figure 3.5 depicts the PSD of AA2024,

AA2024+Ni3 and ACN001. As requested to the powder suppliers, all the powders were found to have similar size distribution, with D10 close to 30 µm, D50 to 43 µm and D90 to 63 µm. AA2024+Ni3 (Fig. 3.5(a)) showed the presence of some micron-sized particles; these represent the loose nickel powders not stitched to AA2024. ACN001 (Fig. 3.5(c)) was also found to have a small volume fraction of micron-sized particles. These are believed to be the fine satellites detected in Paragraph 3.6.2 which were not fully attached to the bigger particles.
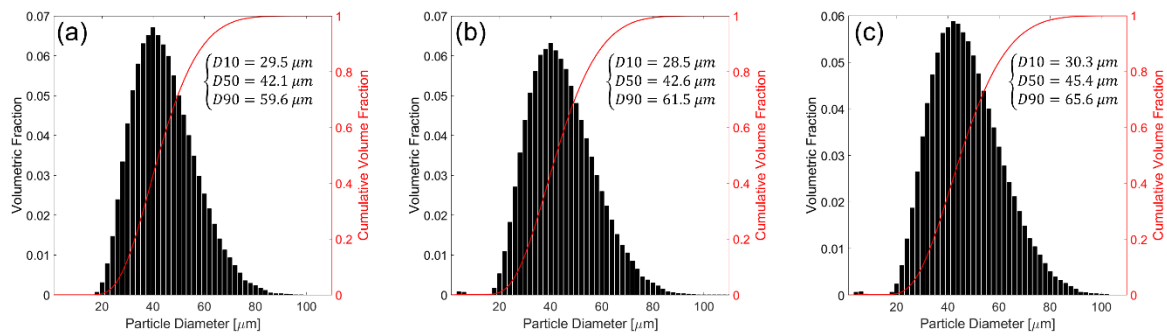
Figure 3.5: particle size distribution and cumulative particle size distribution of (a) AA2024, (b) AA2024+Ni3 and (c) ACN001

3.7 Laser Micro Calorimetry (LMC)

The absorptivity of the AA2024 powders was measured via Laser Micro Calorimetry (LMC) using a system developed at the University of Nottingham [39]. The LMC setup (Figure 3.6) consists of a 3D printed polymer holder which acts as fixture for both a pyrometer (Micro-Epsilon CT-CF22) and a disc. The holder is bolted to an adapted baseplate which is screwed onto the AM400 platform. A layer of powder is manually spread on top of the disc which is then placed on the holder. The test relies on temperature measurements from underneath the disc throughout the melting of a scan track. The absorptivity was measured by the integration of the recorded time-temperature trend, which enabled the evaluation of the fraction of nominal energy deposited onto the powder bed. This operation was performed using a script developed at the University of Nottingham (Appendix B).
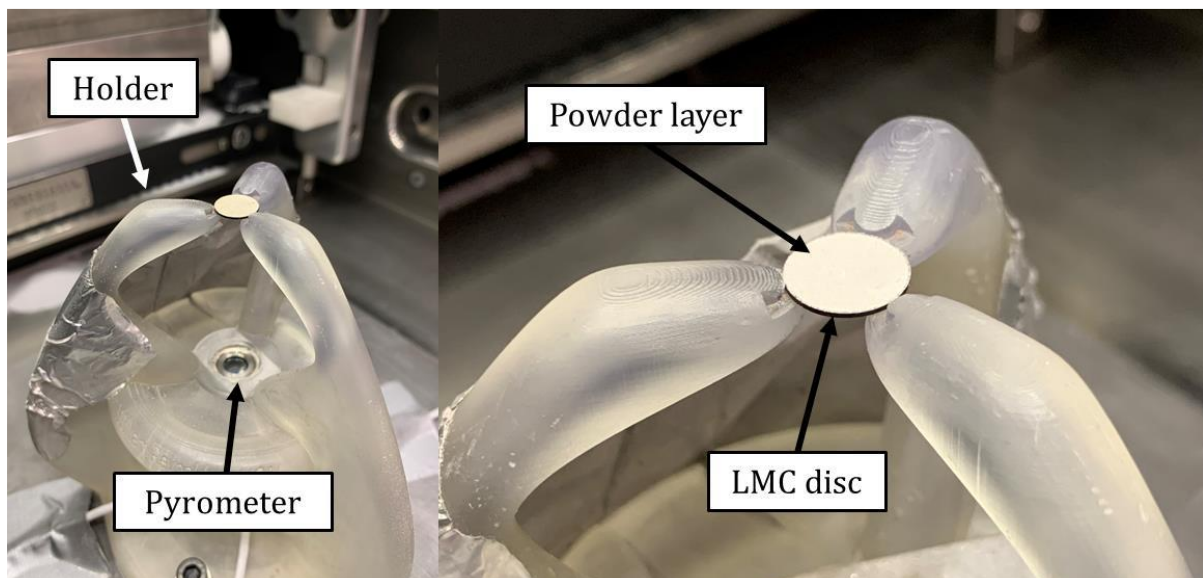
Figure 3.6: Laser Micro Calorimetry (LMC) setup used to measure the absorptivity of the AA2024 powder [39]

Several AA2024 discs characterized by a diameter of 10 mm, a thickness of 0.50 mm and a recess of 50 μm were machined and used as substrates. The underside of these discs was spray painted in a high temperature black paint to increase the emissivity of the disc and ensure optimal measurements. The Renishaw AM400 was used to perform 6 mm scan tracks with the parameters listed in Table 3.9.

Table 3.9: list of parameters investigated to measure absorptivity changes as a function of PBF-LB/M processing conditions.

Parameters	Values
Power [W]	50, 100, 150, 200, 250, 300, 350, 400
Scan speed [m/s]	0.5, 1, 1.5

3.8 Computational approaches

3.8.1 CALPHAD method

The CALPHAD (CALculation of PHAse Diagrams) approach, firstly introduced by Larry Kaufman, is used to evaluate kinetic, thermodynamic and various other properties of several material systems [207]. This computational method is used to model thermodynamic properties of each phase, simulating the behaviour of the resulting multi-phase component. The CALPHAD method is based on databases formed by experimental and simulated data including phase equilibria in system of two or more components. Moreover, relevant thermodynamic properties of singles phases are described using constituent models as a function of various parameters computed by the optimization of the models' fit to all the available information within the chosen database. After this fit, the phase diagram and phases' properties are re-evaluated resulting in the final iteration of the calculation.

The CALPHAD method is the foundation of many computational software packages. In this work ThermoCalc version 2019b [208] (and following releases) paired with the TCAL6 aluminium database [209] were adopted to predict the solidification path, phase nucleation sequence, volume fraction, phase composition and relevant phase diagrams. Specifically, the solidification path was computed using the Scheil-Gulliver micro-segregation model. The solidification simulations were performed in both classic Scheil-Gulliver conditions (assuming infinite fast diffusion in the liquid, no diffusion in the solid and presence of thermodynamic equilibrium at the interface) and Scheil-Gulliver conditions contemplating the presence of solute trapping. Differently from the prior, this last case contemplates changes of the partition coefficient k due to higher solutes retain

in the FCC-Al matrix. Based on the evaluated solidification paths and segregation profiles, relevant cracking indices were computed.

3.8.2 Multi-physics simulation

The thermo-fluid behaviour of AA2024 under distinct laser regimes was modelled using a Computational Fluid Dynamics (CFD) calculation implemented in ANSYS Fluent [210] with the help of a User Defined Functions (UDF) file, which allows more computational flexibility (Appendix C). Several thermal-fluid behaviours typical of laser processing are captured. The recoil pressure resulting vaporization acts on the metal/gas interface determining the shape of the melt pool. The Marangoni shear forces, which are related to the surface tension gradient, affect the flows within the melt pool and determine its heat distribution. The semi-solid is modelled with the Carman-Kozeny equation [211,212], considering the mushy zone as a porous medium. However, several assumptions were considered in the model's implementation: (i) the liquid metal flow is assumed to be laminar and Newtonian; (ii) the liquid metal solidifies following a lever rule [213] and not the solidification path computed using the Scheil-Gulliver micro-segregation model [84]; (iii) mass transfer due to phase transformation from liquid to vapour is not considered, hence all the resulting phenomena (elemental loss, plasma effects, laser-scattering due to nano-size particles in the plume [214]) are not modelled; (iv) the thermophysical properties of AA2024 are considered functions of temperature only and due to the lack of information in the literature some aluminium properties have been used.

Following these assumptions, a domain of $948 \times 300 \times 300$ µm³, discretized into an eulerian mesh with uniform cubic cells of 3 µm edge, was subdivided at $z = 150$ µm into a lower metal region and an upper argon one. A multi-phase flow approach has been considered, modelling a gas and a metal phase using the Volume-of-Fluid (VOF) method [210] and solving the conservation equations.

A volume fraction φ is introduced for each phase and is equal to 1 in a cell full of that phase and 0 if the same phase is not present in the cell. Specifically, φ_m represents the volume fraction of metal and φ_{gas} the volume fraction of gas. The sum $\Phi = \varphi_m + \varphi_{gas}$ is always equal to 1 and satisfies the volume fraction equation [210]:

$$\frac{\partial \Phi}{\partial t} + \vec{\nabla} \cdot (\Phi \vec{u}) = 0 \qquad \text{Equation 3.5}$$

where t represents the time and $\vec{u}$ is the flow velocity. Following this multi-phase approach, any mixture thermophysical property $\bar{\xi}$ is computed from ξ_m and ξ_{gas}, the properties of the metal and gas, respectively:

$$\bar{\xi} = \varphi_m \xi_m + \varphi_{gas} \xi_{gas} = \varphi_m \xi_m + (1 - \varphi_m) \xi_{gas} \qquad \text{Equation 3.6}$$

The solidification of the metal is modelled with the enthalpy-porosity technique, using a liquid fraction f_l and a solid fraction $f_s = 1 - f_l$ to solve the energy equation. For an alloy, the solid fraction is equal to 1 when the temperature T is below the solidus temperature T_{sol} and to 0 above the liquidus temperature T_{liq}. The evolution of the solid fraction within the solidification range $\Delta T = T_{liq} - T_{sol}$ is described using the lever-rule [213]:

$$f_s = 1 - \frac{T - T_{sol}}{T_{liq} - T_{sol}} \qquad \text{Equation 3.7}$$

In the enthalpy-porosity technique, the mushy zone is treated as a porous medium where the porosity of each cell is equal to its liquid fraction. Hence, the porosity is 0 in fully solidified materials and 1 beyond the liquidus temperature of the alloy.

The CFD model solves the conservation equations of mass, momentum, and energy. The conservation of mass is given by Equation 3.8:

$$\frac{\partial \bar{\rho}}{\partial t} + \vec{\nabla} \cdot (\bar{\rho}\vec{u}) = 0 \qquad \text{Equation 3.8}$$

where $\bar{\rho}$ is the density of the mixture. The conservation of momentum is given by:

$$\frac{\partial (\bar{\rho}\vec{u})}{\partial t} + \vec{\nabla} \cdot (\bar{\rho}\vec{u} \times \vec{u}) = -\nabla p + \vec{\nabla} \cdot (\mu\nabla\vec{u}) + \vec{S}_m \qquad \text{Equation 3.9}$$

In Equation 3.9, p is the pressure, μ is the liquid viscosity and $\vec{S}_m$ represents the momentum source term, which is given by the sum of the Darcy momentum sink $\vec{S}_d$, the surface tension force $\vec{S}_{st}$, the Marangoni shear force $\vec{S}_M$ and the recoil pressure term $\vec{S}_{rp}$. These are presented in Equations 3.10-3.13:

$$\vec{S}_d = -A_{mush}\frac{f_s^2}{(1-f_s)^3 + C_\epsilon}\vec{u} \qquad \text{Equation 3.10}$$

$$\vec{S}_{st} = \gamma\vec{n}\kappa|\nabla\varphi_m|\frac{2\bar{\rho}}{\rho_m + \rho_{gas}} \qquad \text{Equation 3.11}$$

$$\vec{S}_M = \frac{d\gamma}{dT}[\nabla T - (\vec{n}\cdot\nabla T)\vec{n}]|\nabla\varphi_m|\frac{2\bar{\rho}}{\rho_m + \rho_{gas}} \qquad \text{Equation 3.12}$$

$$\vec{S}_{rp} = 0.54p_0\exp\left[\frac{L_{vap}M(T-T_b)}{RTT_b}\right]\vec{n}\,|\nabla\varphi_m|\frac{2\bar{\rho}}{\rho_m + \rho_{gas}} \qquad \text{Equation 3.13}$$

In Equation 3.10, the permeability of the mushy zone is modelled using the Carman-Kozeny equation [211,212], where A_{mush} is the permeability coefficient and C_ϵ is a small constant to avoid division by 0. In Equation 3.11, γ is the surface tension, $\vec{n}$ is the unit normal vector at the metal/gas interface (computed by the normalized gradient of the metal volume fraction φ_m) and κ is the curvature of the interface, given by $-\vec{\nabla} \cdot \vec{n}$. In Equation 3.12, ρ_m and ρ_{gas} represent the metal and gas density, respectively. Finally, in Equation 3.13, p_0 is the ambient pressure, L_{vap} is the latent heat of vaporisation, M is the molar mass, T_b is the boiling temperature of the metal and R is the universal gas constant. The conservation of energy is given by:

$$\frac{\partial(\bar{\rho}H)}{\partial t} + \vec{\nabla} \cdot (\bar{\rho}\vec{u}H) = \vec{\nabla} \cdot (k_m \nabla T) + S_e \qquad \text{Equation 3.14}$$

In Equation 3.14, H represents the material's enthalpy, k_m is the metal's thermal conductivity and S_e represents the energy source term. The material's enthalpy can be described as [210]:

$$H = \int_0^T c_{p,m} dT + (1 - f_s)L_{melt} \qquad \text{Equation 3.15}$$

where $c_{p,m}$ and L_{melt} are the specific heat and the latent heat of fusion of the metal, respectively. The energy source term of Equation 3.14 is the sum of the heat losses due to radiation S_{rad} and vaporisation S_{vap}, and the heat input provided by the laser S_{laser}. Equations 3.16-3.17 describe the first two addends of the energy source term:

$$S_{rad} = -\sigma_s \epsilon (T^4 - T_0^4)|\nabla \varphi_m| \frac{2\bar{\rho}\bar{c}_p}{\rho_m c_{p,m} + \rho_{gas} c_{p,gas}} \qquad \text{Equation 3.16}$$

$$S_{vap} =$$

$$= -0.82 \frac{L_{vap}M}{\sqrt{2\pi MRT}} p_0 exp \left(\frac{L_{vap}M(T - T_b)}{RTT_b} \right) |\nabla\varphi_m| \frac{2\bar{\rho}\bar{c}_p}{\rho_m c_{p,m} + \rho_{gas} c_{p,gas}}$$

Equation 3.17

In Equation 3.16, σ_s represents the Stefan-Boltzmann constant, ϵ is the metal emissivity, while $c_{p,m}$ and $c_{p,gas}$ represent the specific heat of metal and gas, respectively.

The heat input provided by the laser S_{laser} is computed using the ray tracing method. This choice was conducted in order to take into account the metal-gas interface evolution during laser melting. Using the ray tracing method, the laser source is modelled thanks to a Euler-Lagrange approach, namely the Discrete Phase Method (DPM) of ANSYS Fluent. The laser is discretized in sub-rays based on the cell size of the mesh ($\Delta x = 3$ μm) and the laser centre position ($x_0; y_0$). Each sub-ray is characterized by a specific surface energy flux Q_{init} based on a Gaussian distribution:

$$Q_{init} = \frac{2P}{\pi\sigma^2} \exp\left[-2 \frac{(x - x_0)^2 + (y - y_0)^2}{\sigma^2} \right]$$

Equation 3.18

In Equation 3.18, P represents the laser power (200 W), σ is the beam radius (35 μm), while x and y represent the position of sub-ray. The laser y_0 coordinate is always 0; in order to mirror the PDV experiment (Section 3.1.3), the x_0 coordinate follow the same time-law, which is depicted in Figure 3.7.
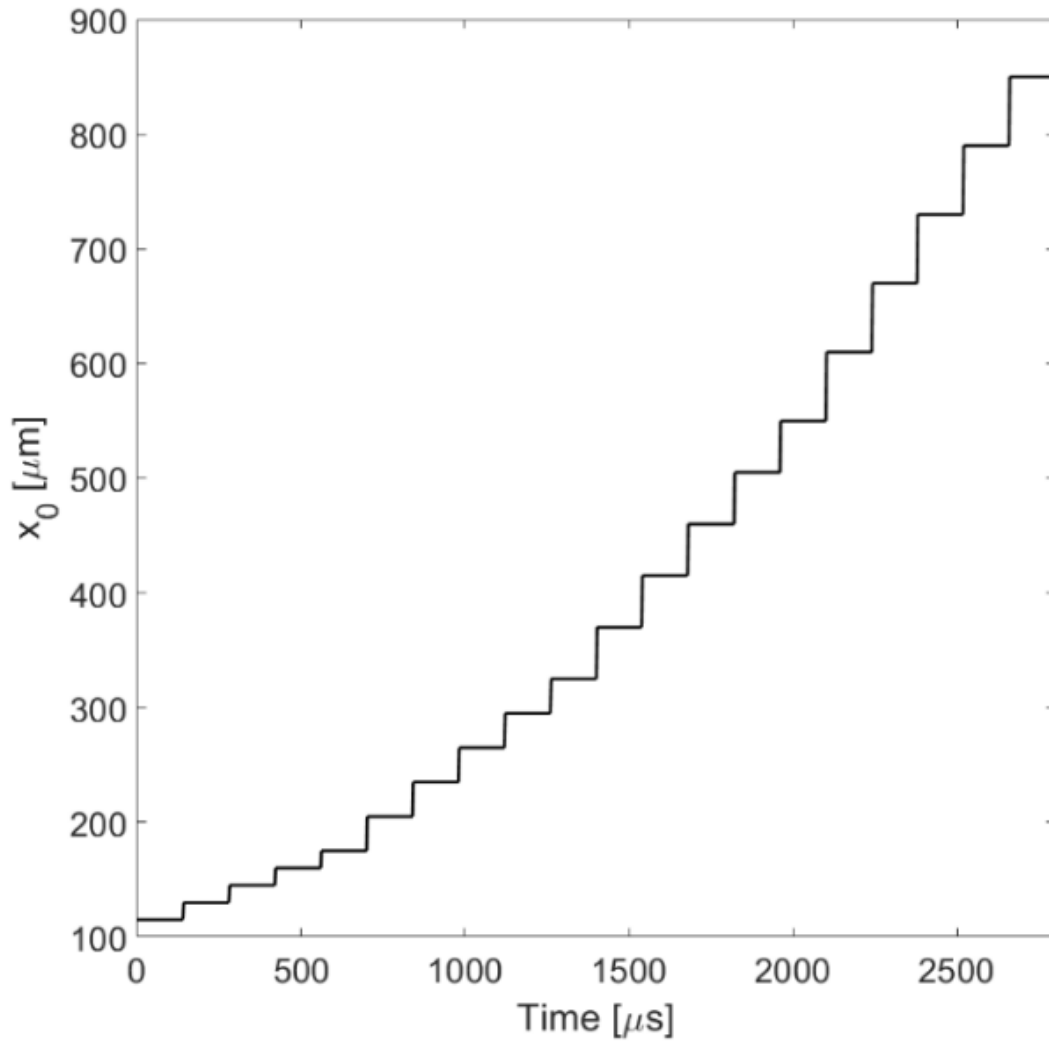
Figure 3.7: In order to replicate the PDV experiment, the laser has been modelled so that it follows the same time-law adopted for laser remelting. Each horizontal segment corresponds to a single pulse during which the laser is stationary at a specific x_0 value for a time of 140 μs, given by the sum of the exposure time ($ET =$ 120 μs) and the delay time ($DT = 20$ μs). The first five pulses are characterized by point distance PD of 15 μm, the second five by $PD = 30$ μm, the third five by $PD = 45$ μm and the last five by $PD = 60$ μm.

At each time step, the UDF checks if the particle encounters a cell containing metal. In this case, this cell will absorb a portion Ab of its surface energy flux in accordance with the Fresnel equations [215–217]. The components of Ab derived from the P polarized and S polarized components of the incident sub-ray are given by:

111

$$Ab_p = 1 - \left| \frac{\cos\theta - \sqrt{\hat{n}^2 - \sin^2\theta}}{\cos\theta + \sqrt{\hat{n}^2 - \sin^2\theta}} \right|^2 \qquad\qquad \text{Equation 3.19}$$

$$Ab_s = 1 - \left| \frac{\hat{n}^2\cos\theta - \sqrt{\hat{n}^2 - \sin^2\theta}}{\hat{n}^2\cos\theta + \sqrt{\hat{n}^2 - \sin^2\theta}} \right|^2 \qquad\qquad \text{Equation 3.20}$$

In Equations 3.19-3.20, θ is the angle of incidence of the sub-ray with respect to the surface normal and $\hat{n}$ represents the complex refractive index. The absorbed portion Ab is given by:

$$Ab = \frac{1}{2}Ab_p + \frac{1}{2}Ab_s \qquad\qquad \text{Equation 3.21}$$

After reflection, the new sub-ray direction $\vec{R}$ is updated based on the incident direction $\vec{I}$ and the normal direction of the metal/gas interface $\vec{n}$ and is given by:

$$\vec{R} = \vec{I} - 2(\vec{I} \cdot \vec{n})\,\vec{n} \qquad\qquad \text{Equation 3.22}$$

The sub-ray is tracked for a maximum of 4 reflections or up to the point that it goes out of the domain. Based on these calculations, the heat input provided by the laser S_{laser} can be determined by:

$$S_{laser} = \frac{\sum(Q_{init}Ab)}{\Delta x} \qquad\qquad \text{Equation 3.23}$$

The solidus, liquidus and boiling temperatures of AA2024 were computed using ThermoCalc 2021b and the TCAL6 database with the composition given in Table 3.7. The complex refractive index, used in Equations 3.19-3.20, is taken from Rakić [218], giving an absorptivity of 4.76 % with an angle of 0°, but is modified to artificially increase the absorptivity of the liquid metal. As a matter of fact, Krishnan and Nordine [219] showed

that the absorption of liquid aluminium at 1550 K does not change in respect with the wavelength. Furthermore, Trapp et al. [220] found that below a laser power of 220 W, the absorptivity of the AA1100 aluminium alloy was constant at 15.5 %. Hence, the refractive index was modified to increase the absorptivity up to 15 %. Table II lists the constants and thermophysical properties used in the multi-physics simulation.

Table 3.10: Thermophysical properties used in the multi-physics simulation.

Property	Unit	Symbol	Value
Solidus temperature	K	T_{sol}	781.5
Liquidus temperature	K	T_{liq}	910.2
Boiling temperature	K	T_b	2743
Latent heat of fusion [221]	J/kg	L_{melt}	399000
Latent heat of vaporization [26]	J/kg	L_{vap}	$10.78 \cdot 10^6$
Liquid viscosity [222]	$kg/(m \cdot s)$	μ	0.0013
Surface tension [223]	kg/s^2	γ	1.16
Surface tension coefficient [223]	$kg/(K \cdot s^2)$	$d\gamma/dT$	$-2.44 \cdot 10^{-4}$
Complex refractive index [218–220]	n/a	$\bar{n}$	$2.8 + 7.8i$
Specific heat of the gas [210]	$J/(kg\ K)$	$c_{p,gas}$	520.64
Density of the gas [210]	kg/m^3	ρ_{gas}	1.623
Universal gas constant [224]	$J/(mol\ K)$	R	8.314
Molar mass of the metal [136]	g/mol	M	27
Stefan-Boltzmann constant [224]	$W/(m^2\ K^4)$	σ_s	$5.67 \cdot 10^{-8}$

Emissivity [225]	n/a	ϵ	0.3
Permeability coefficient [210]	n/a	A_{mush}	10^6
Small constant [210]	n/a	C_ϵ	10^{-3}
Ambient pressure [224]	Pa	P_0	$101 \cdot 10^3$
Density of the solid metal [226]	kg/m^3	$\rho_{m,s}$	$2648 + 0.322T - 4.99 \cdot 10^{-4}T^2$
Density of the liquid metal [226]	kg/m^3	$\rho_{m,l}$	$2670 - 0.299T$
Thermal conductivity of the solid metal [226]	$W/(m\,K)$	$k_{m,s}$	$248 - 0.067T$
Thermal conductivity of the liquid metal[226]	$W/(m\,K)$	$k_{m,l}$	$33.9 + 7.892 \cdot 10^{-2}T - 2.099 \cdot 10^{-5}T^2$
Thermal diffusivity of the solid metal [226]	$10^{-5}m^2/s$	$a_{m,s}$	$7.023 - 9.31 \cdot 10^{-4}T$
Thermal diffusivity of the liquid metal [226]	$10^{-5}m^2/s$	$a_{m,l}$	$0.965 + 0.31 \cdot 10^{-2}T - 6.306 \cdot 10^{-7}T^2$

In order to not weaken the high fidelity of the multi-physics simulation, relevant thermophysical properties, such as, metal's density ρ_m, specific heat $c_{p,m}$ and thermal conductivity k_m, were considered to be a function of the temperature T and fraction of solid f_s in order to include the phase change. Considering χ_m as one the properties modelled with this approach, its evolution in thermal domain is given by:

$$\chi_m = f_s\chi_s + f_l\chi_l = f_s\chi_s + (1 - f_s)\chi_l \qquad \text{Equation 3.24}$$

where χ_s and χ_l are functions of temperature and represent one of the cited thermophysical properties of the solid and liquid, respectively. Leitner et al. [226] studied the evolution of relevant thermophysical properties of solid and liquid aluminium, proposing simple polynomial trends as a function of temperature. These trends were

used to compute ρ_m, k_m and a_m (thermal diffusivity) following the approach presented in Equation 3.24. The specific heat $c_{p,m}$ was computed from a_m by $c_{p,m} = \frac{k_m}{\rho_m a_m}$.

3.8.3   RDG criterion and data analysis

In Chapter 5 of this work, the RDG criterion [76] was used to compute the hot crack propensity of AA2024 under several PBF-LB/M regimes. Following this approach, the pressure drop at the root of the dendrite Δp_{max} is considered as a hot crack nucleation driving force and can be computed using Equation 3.25:

$$\Delta p_{max} = \frac{180}{\lambda^2} \frac{(1+\beta)\mu}{G} \int_{T_{sol}}^{T_{liq}} \frac{E(T)f_s^2}{(1-f_s)^3} \, dT + \\ + \frac{180}{\lambda^2} \frac{v_T \beta \mu}{G} \int_{T_{sol}}^{T_{liq}} \frac{f_s^2}{(1-f_s)^2} \, dT$$

Equation 3.25

where λ represents the dendrite arm spacing (0.86 μm, from experiments conducted in Chapter 4), β is the shrinkage factor (0.06 [76]), μ represents the viscosity of the liquid, G is the norm of the thermal gradient, f_s represents the fraction of solid, v_T is the solidification rate, T_{liq} and T_{sol} represent the liquidus and solidus temperatures, respectively. G is a direct output of the CFD model and is computed via the norm of the gradient of the temperature field $\overrightarrow{\nabla T}$. The term $E(T)$ is described by:

$$E(T) = \int_{T_{sol}}^{T_{liq}} f_s \dot{\varepsilon} \, dT$$

Equation 3.26

In Equation 3.26, $\dot{\varepsilon}$ represents the strain rate which can be evaluated from [227]:

$$\dot{\varepsilon} = \alpha \dot{T}$$

<div align="right">Equation 3.27</div>

where α is the coefficient of thermal expansion ($24.7 \cdot 10^{-6}$ 1/K [26], considered as a constant in this investigation) and $\dot{T}$ is the cooling rate. This has been considered evaluating the ratio between the difference of the temperature at the instant $t + 1$ and t divided by the time step (7 μs). Under the assumption of constant thermal gradient, cooling rate and strain rate, and considering that $\dot{T} = G \cdot v_T$, it is possible to extract strain rate out of the integral in Equation 3.26 and then derive the final expression for the pressure drop at the root of the dendrite:

$$\Delta p_{max} = \frac{180}{\lambda^2} \frac{(1+\beta)\mu\dot{\varepsilon}}{G^2} \int_{T_{sol}}^{T_{liq}} f_s \, dT \int_{T_{sol}}^{T_{liq}} \frac{f_s^2}{(1-f_s)^3} \, dT +$$

<div align="right">Equation 3.28</div>

$$+ \frac{180}{\lambda^2} \frac{\beta\mu\dot{T}}{G^2} \int_{T_{sol}}^{T_{liq}} \frac{f_s^2}{(1-f_s)^2} \, dT = \frac{180}{\lambda^2} \frac{\mu}{G^2} \left[(1+\beta)\dot{\varepsilon} I_A I_B + \beta\dot{T} I_C\right]$$

where I_A, I_B and I_C are given by:

$$I_A = \int_{T_{sol}}^{T_{liq}} f_s \, dT$$

<div align="right">Equation 3.29</div>

$$I_B = \int_{T_{sol}}^{T_{liq}} \frac{f_s^2}{(1-f_s)^3} \, dT$$

<div align="right">Equation 3.30</div>

$$I_C = \int_{T_{sol}}^{T_{liq}} \frac{f_s^2}{(1-f_s)^2} \, dT$$

<div align="right">Equation 3.31</div>

The integrals I_A, I_B and I_C can be computed knowing the relationship between the fraction of solid and the temperature that comes directly from the solidification path computed using ThermoCalc. It is now needed to evaluate characteristic values of G, $\dot{T}$ and $\dot{\varepsilon}$ referred to the last solidification cycle of each location of the simulated track. During PBF-LB/M a single point may undergo several melting events characterized by different thermophysical properties. The resulting microstructure and the event of a hot crack nucleation will be determined by the last solidification cycle which therefore needs to be identified.

For each point of the XZ plane of the domain, relevant thermophysical properties such as temperature, temperature gradient, cooling rate and metal fraction φ_m were exported every 7 μs to text files. The analysis of these data was performed in Matlab R2019b using an in-house developed routine. Time steps in the last solidification event have been identified for each point of the domain posing the following conditions: (a) metal fraction equal to 1, (b) temperature between the solidus and liquidus temperature of AA2024 and (c) subsequent temperature always smaller than current temperature. Based on these highlighted values, averages of G, $\dot{T}$ and $\dot{\varepsilon}$ were computed enabling the possibility of calculating the pressure drop Δp_{max} at the last solidification across the entire track's extension. In the time domain, Δp_{max} is assigned to the latest time step present in the highlighted last solidification cycle of each point. The computed values of the pressure drop were normalized between 0 and 1 considering the maximum value found in the entire dataset.

Based on the timestep, the pressure drop of the points melted during the PD15, PD30, PD45 and PD60 pulses were divided into sub-datasets. The distribution of the pressure drop was computed with a bin resolution of 0.01 evaluating the frequency f_i related to

each value of $\Delta p_{max,i}$. In order to attribute to every point distance a representative value of the pressure drop, a weighted average considering the frequency as weight was performed within each sub-dataset using Equation 3.32:

$$\Delta p_{glob} = \frac{\sum_i[f_i \Delta p_{max,i}]}{\sum_i f_i} \qquad \text{Equation 3.32}$$

3.9 Arc Melting and buttons surface melting

The composition studied in Chapter 6 were produced from elemental feedstocks. Aluminium and copper shots of 5N purity were procured from ESPI Metals (USA), while the nickel powder is the same one described in Section 3.6.1. These elements were separately weighed in specific proportions to produce various Al-Cu-Ni compositions in between AlCu6Ni3 and AlCu6Ni9 (wt%). A Compact Arc Melter MAM-1 (Edmund Bühler GmbH, Germany) was adopted to produce button specimens. During operations, the feedstocks are placed inside a copper crucible and an electric arc is generated at the tip of a tungsten electrode. The system works in a controlled atmosphere, achieved due to the presence of a vacuum chamber which is gassed down and filled with argon. Multiple vacuum/purge cycles were adopted to minimize the presence of oxygen in the chamber. During operation, the electric arc closes on the crucible melting the feedstock materials placed in between. In order to achieve homogeneous elemental distribution, the samples were melted multiple times. The resulting samples assumed a near round shape with a flat surface given by the contact plane with the crucible. The cooling rate associated with arc melting is ultimately proportional to the size of the samples produced. All the samples were produced from a total of 3 grams of feedstock materials to achieve comparable cooling rates and microstructures.

After arc melting, the samples were glued to a RBV platform with the flat side facing upwards. They were manually levelled so that these faces were in the 2 mm focal range of the Renishaw AM400. The samples were surface melted using a power of 200 W, a point distance of 60 μm, an exposure time of 60 μs, a delay time of 20 μs and a hatch distance of 120 μm. This enabled the possibility to have a 50 μm layer characterized by a microstructure solidified under PBF-LB/M conditions.

3.10 Mechanical testing

As mentioned in Sections 3.1.3 and 3.1.4, cylinders with a diameter of 8 mm and a length of 60 mm were manufactured by PBF-LB/M for both AA2024 and ACN001. Cylindrical dog-bones with the dimensions depicted in Figure 3.8 were subsequently machined according to the Test Methods for Tension Testing of Metallic Materials with designation ASTME8/E8M [228]. The resulting samples were tested on an Instron 5969 universal testing machine (Instron, MA, USA) and a video gauge was adopted to collect stress-strain curves. The cross-head speed was set to 0.2 mm/min and tests were performed at room temperature.
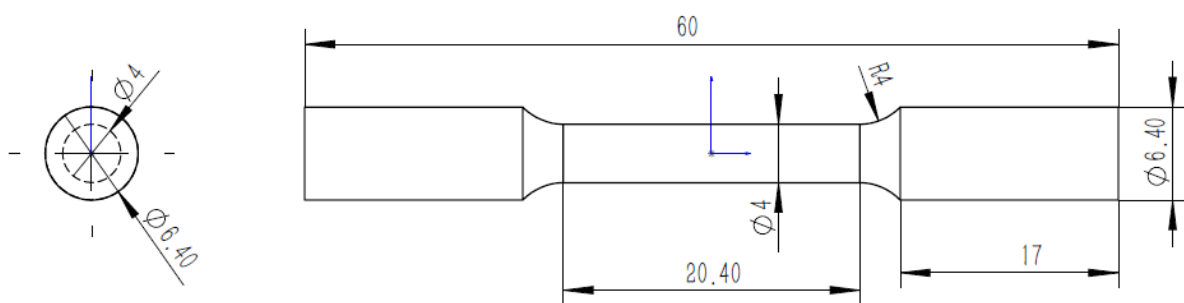
Figure 3.8: technical drawing of the geometry adopted to perform tensile tests in this work. All dimensions are given in millimetres.

Due to the limited amount of material available, the mechanical behaviour of custom compositions studied in Chapter 6 was assessed using micro-hardness measurements. A Wilson VH3100 (Buehler Ltd.) was used to indent the buttons according to the Test Method for Micro Indentation Hardness of Materials with designation ASTM E384-08 [229]. The hardness of the buttons was measured carefully placing the indents within the melt pools of the surface melted PBF-LB/M layer. For each sample a force of 50 g was employed to create 10 indentations which were performed using a 10 second dwell time.

Chapter 4

4 Densification and cracking behaviour of AA2024 under various PBF-LB/M processing regimes

The processing of high-strength Al-alloys by means of PBF-LB/M is hampered by the formation of detrimental cracks aligned with the building direction. These features have been often addressed as "hot cracks", despite their morphology and size is not typical of solidification cracks. Moreover, considering a certain alloy, their occurrence and severity seem to be largely affected by the processing parameters adopted for PBF-LB/M fabrication.

In this Chapter the densification and cracking behaviour of the aluminium alloy AA2024 manufactured by PBF-LB/M are studied. Firstly, the absorptivity of the powders is

measured as a function of laser power and scan speed using micro-calorimetry. The computed absorptivity trend will be coupled with various methodologies found in the literature able to predict the presence of lack-of-fusion and keyhole defects.

Based on these calculations, an optimized process window characterized by minimal porosity is identified and printed using the Renishaw AM400. Within this range of parameters maximising relative density, the cracking behaviour of AA2024 is thoroughly investigated. Two samples, both characterized by minimal porosity but significantly different cracking intensities, are highlighted and analysed. A detailed characterization of the microstructure of these specimens is conducted in order to study the presence of secondary phases, grain morphology and texture. Two different cracking morphologies are identified, suggesting the occurrence of not only hot tearing but also crack propagation in the solid. A non-propagated hot crack tip is comprehensively investigated via a combination of site-specific TEM/EBSD. The cracking behaviour of AA2024 is then discussed with the help of the solidification paths and experimental evidence.

The chemical composition of AA2024 is modified by the addition of nickel to reduce the hot crack propensity of the material and improve PBF-LB/M processability. The solidification path of AA2024 plus various nickel addition is computed using ThermoCalc and the CALPHAD method. Based on these trajectories, a dual-indices design map is proposed to isolate an alloy less susceptible to hot cracking (AA2024 + 3 wt% Ni). The optimized alloy is then printed, and its cracking behaviour is compared to AA2024 in order to prove the merits of the adopted design approach.

4.1 Results

4.1.1 AA2024 absorptivity trends as a function of laser power and scan speed

Figure 4.1(a) depicts the computed absorptivity A values as a function of the Linear Energy Density LED, computed via the ratio of the laser power P and scan speed v. It is possible to observe that generally the powders absorptivity increases in regimes characterised by progressively higher linear energy density. Figure 4.1(b) depicts the computed absorptivity A values as a function of power P for the three different investigated scan speeds listed in Table 3.7. Generally, an increase of A with the increase of P is detected. Additionally, comparing the three trends of Figure 4.1(b), higher values of absorptivity are measured in low scan speed regimes. A great range of values is measured in conditions paired with lower energy (e.g., low power, high scan speed), this is particularly evident in the 1.5 m/s curve. Here, at powers greater than 300 W, a plateau region characterized by relatively high absorptivity is detected. This can be also observed in the 1 m/s curve which additionally shows a plateau for power values lower than 200 W which is characterized by relatively low A values. These two near-constant segments can be clearly detected in the curve associated with a scan speed of 0.5 m/s. Thus, a progressive increase of absorptivity is detected between 200 and 300 W. This dual behaviour was also observed analysing cross sections of the tracks processed with the same power but different scan speed. Processing parameters associated with the low A plateau were indeed characterised by relatively shallow melt pools (Figure 4.1(c)) while on the other hand regimes characterised by high absorptivity showed very deep V-shaped melt pools (Figure 4.1(d)). This trend and similar values of absorptivity were also detected by Trapp et al. [220] investigating the AA1100 aluminium alloy. Additionally, similar results were also found by Clare et al. [39] who investigated the laser-powder

interaction of pure aluminium. Linear interpolation between these experimental points was adopted to compute a trend of absorptivity as a function of laser power and scan speed. This trend was used to evaluate the presence of macro-porosities in a wide range of processing conditions (Section 4.1.2).
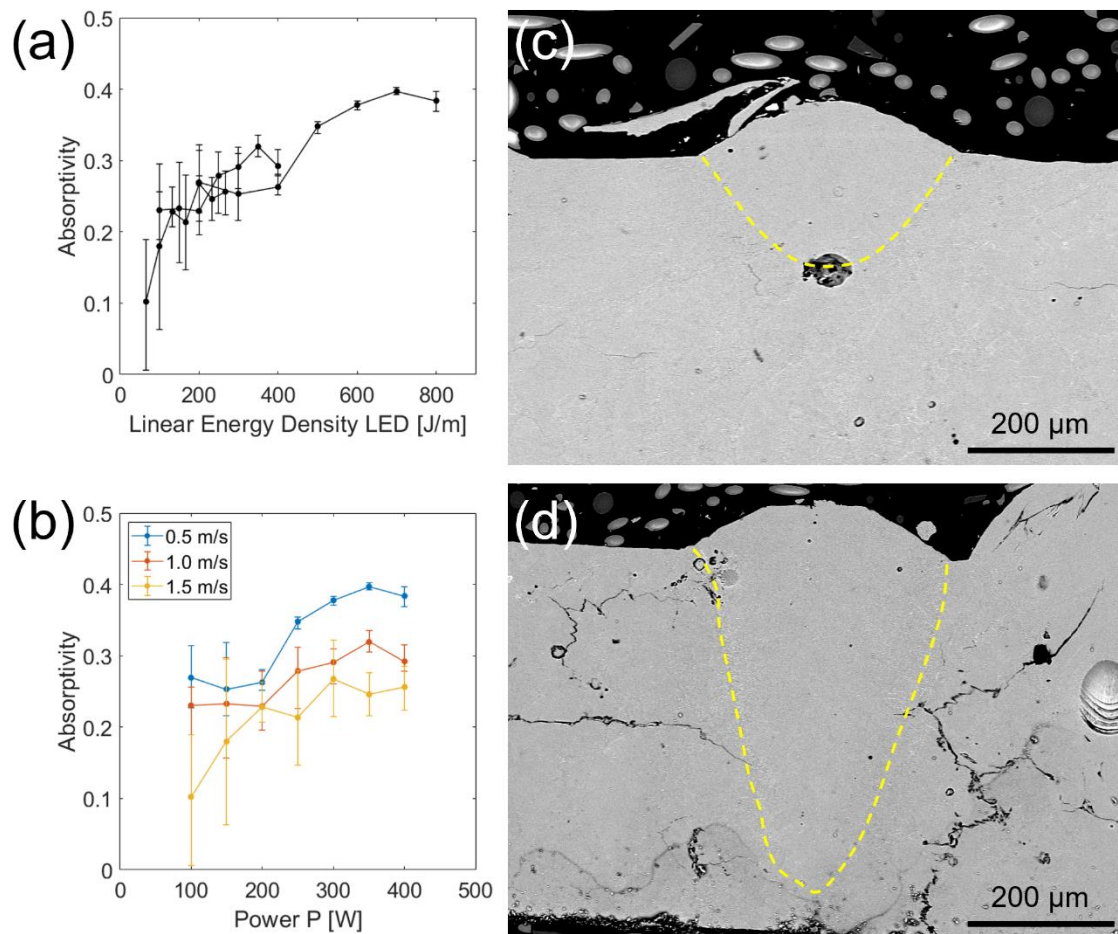
Figure 4.1: (a) absorptivity of AA2024 powders as a function of the Linear Energy Density *LED*. The tracks processed with a speed of 0.5 m/s are depicted in blue, those melted with a scan speed of 1.0 m/s in orange, and the tracks processed with a laser speed of 1.5 m/s are depicted in yellow. (b) absorptivity of AA2024 powders as a function of laser scan speed and power. The 0.5 m/s trend is depicted in blue, the 1.0 m/s values of absorptivity in orange and the 1.5 m/s trend in yellow. Cross section of the track processed using (c) 200 W and 0.5 m/s and (d) 400 W and 0.5 m/s.

4.1.2 Optimal PBF-LB/M process window for the manufacturing of AA2024 with minimized porosity

Porosity in PBF-LB/M arises from distinct mechanisms leading to the formation of gas, lack of fusion and keyhole pores. These last two types of porosity represent the most critical ones because of their significant size (greater than 50 μm) and consequent detrimental effect on mechanical properties [6]. A few criteria have been proposed in the literature to predict their presence as a function of laser power and scan speed [49,230,231]. These methodologies have been implemented in a Matlab routine (Appendix D) and used to screen P-v combinations that are more likely to result in the formation of either lack of fusion or keyhole porosities. In order to refine the calculations, absorptivity changes in the range of power and speed investigated were considered following the measurements illustrated in Section 4.1.1. The geometrical approach developed by Tang et al. [49] was used to screen P-v combinations expected present LOFs, while the normalized enthalpy method described by King et al. [231] was adopted to discern processing regimes leading to keyholes. The presence of only gas pores was assigned to P-v combinations where macro-porosities were not predicted.

Figure 4.2 depicts the output of this calculation where the tested processing regimes have been marked with black dots. It is possible to recognize three distinct areas. At relatively low power and high scan speed the presence of LOFs is predicted (grey region). On the other side of the map, at relatively high power and low scan speeds keyholes are expected to form (red region). In between these regions no macro-porosity is expected to form and therefore only gas pores are expected to be found (green region). Following these calculations, a refined zone (black box) was highlighted because of its minimal predicted porosity development and was experimentally investigated. Additionally, the presence of

a few $P - v$ combinations leading to macro-porosities can be experimentally verified to validate the adopted methodology and selected thresholds.
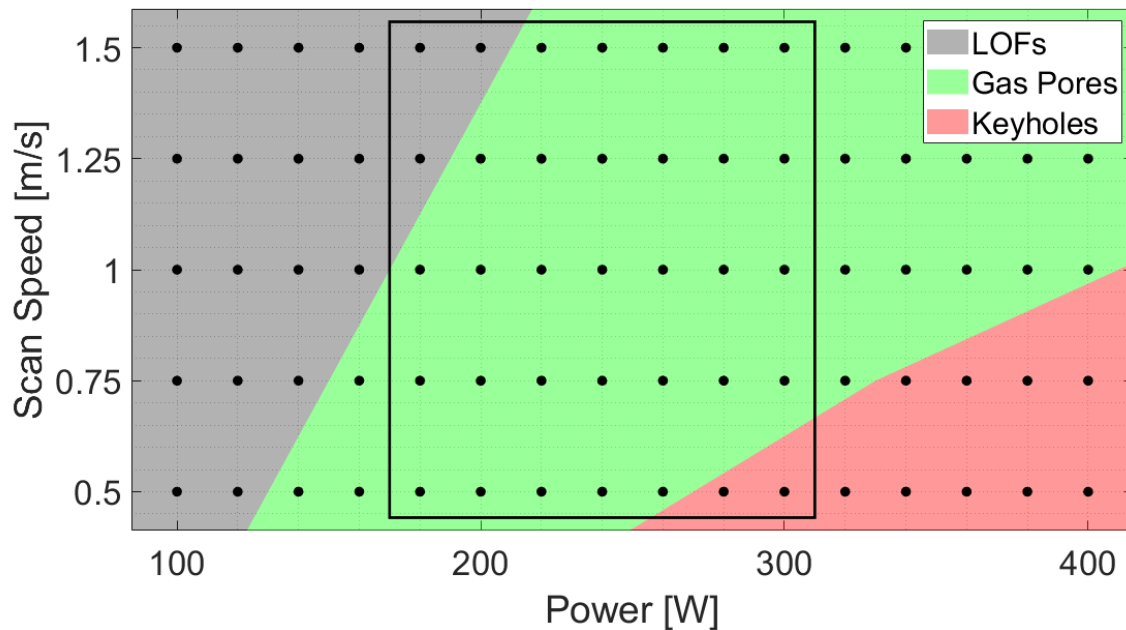
Figure 4.2: graphical output of the prediction of the presence of LOFs (grey region), keyholes (red region) and gas pores (green region). Each black dot represents one of the P-v combinations computationally investigated. The refined process window is enclosed by the back box.

4.1.3 Densification behaviour of produced samples

Figure 4.3(a) shows representative micrographs, in a plane parallel to BD, corresponding to the specimens obtained with the refined processing window highlighted in Section 4.1.2. Varying the combinations of P and v had a significant effect on porosity as well as a distinguishable effect on the formation of cracks. These features are known to form a complex 3D network, difficult to visualize and investigate using simple 2D imaging techniques. Nevertheless, since this study focuses on comparing crack intensities found at different processing conditions, the use of OM and SEM micrographs provides enough

information to conduct this comparison. Figures 4.3(b) to 4.3(d) present higher magnification images of these characteristic features. Nevertheless, for each combination of process parameters employed, the cracks were nearly straight and always parallel to the BD, as widely reported in the literature [105,110,172]. This arises from the occurrence of these cracking features at grain boundaries which are known to be aligned with the BD following the strong vertical orientation of the heat extraction in PBF-LB/M. Additionally, the presence of small pores, thought to be gas pores, was detected in each processing condition analysed. A representative example for the samples produced using low P and high v (180 W and 1.50 m/s) is presented in Figure 4.3(b). This specific condition is seen to be characterized by the presence of large irregular pores, typically associated with processing conditions where lack-of-fusion porosity dominates [119]. Additionally, it was observed that lack-of-fusion porosity was often interconnected by cracks. On the other hand, the outcome of using high P and low v (300 W and 0.50 m/s) can be seen in Figure 4.3(c); analogous microstructures were observed in specimens manufactured at similar conditions of high P and low v. This sample was characterized by the presence of large circular pores that are typically believed to arise as a result of keyhole formation in the melt pool [119]. In this processing regime, cracks were also seen as well as the keyhole type pores. Under the 260 W and 1.50 m/s processing conditions, lack-of-fusion and keyhole porosity were both minimised, as demonstrated in Figure 4.3(d). Similar microstructures were observed in samples produced with other P-v combinations in which only small micro-pores were detected. However, under these conditions, cracks were still apparent. Therefore, these results indicate that there is a trade-off between minimising porosity and cracking presence. Additionally, cracks were well-aligned with the BD and occurred as semi-continuous chains. These features will be fully characterised in Section 4.1.6.
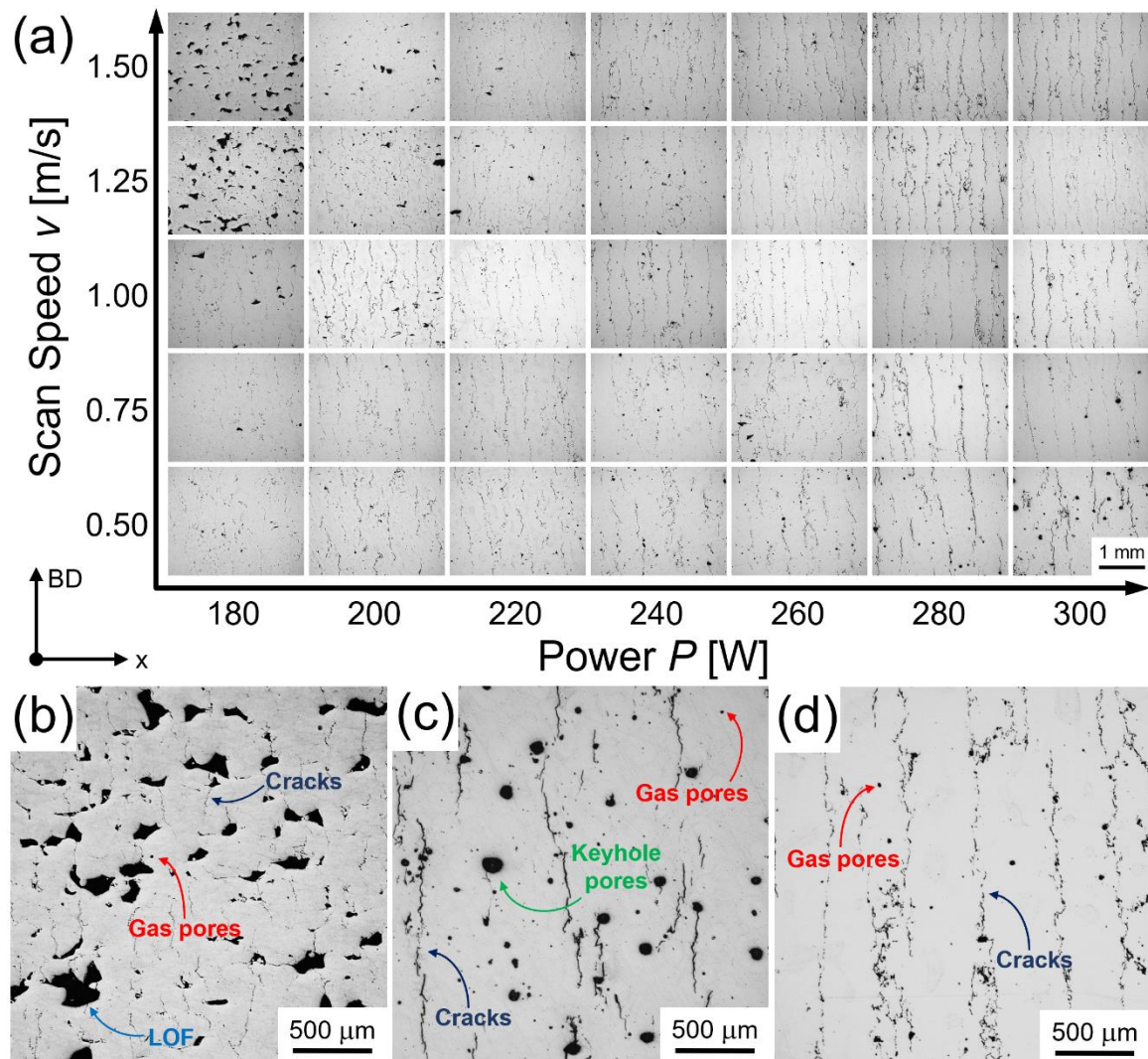
Figure 4.3: (a) optical micrographs parallel to the BD of all the $P - v$ combinations experimentally investigated in the present study; (b) shows a typical microstructure of sample manufactured at 180 W and 1.50 m/s showing the presence of LOF, gas pores and cracks; (c) 300 W and 0.50 m/s depicting keyhole pores, gas pores and cracks; (d) 260 W and 1.25 m/s showing the presence of only gas pores and cracks.

Defects were classified and quantified using the image analysis methodology described in Paragraph 3.2. The results of this analysis are shown in Figure 4.4 which depicts the contour plots of porosity, cumulative crack length (CCL) and relative density as a function of both P and v. According to Figure 4.4(a), porosity was minimised at two distinct processing regimes: (i) power of 260 W and scan speed of 1.50 m/s, and (ii) power of 180 W and scan speed of 0.50 m/s. In the remainder of the study, the samples produced

in the former and latter processing regimes will be denoted with H and L, respectively. For the sake of clarity, these processing conditions are marked in Figure 4.4 by a green and a magenta dot, respectively.

The contour plot of CCL in Figure 4.4(b) shows a maximum value at the highest scan speed combined with the highest power and a minimum at the highest scan speed paired with the lowest power. At low scan speeds, the CCL assumes intermediate values with minor variations in all the investigated power range. The sample produced in the H processing regime has higher CCL value (2.6$\pm$0.4 mm/mm^2) with respect to the one produced in the L processing regime (1.5$\pm$0.3 mm/mm^2). The relative density (Figure 4.4(c)) of the produced samples (which considers both porosity and cracking) was between 92.1% and 97.8% with samples L and H yielding some of the highest density values (97.3$\pm$0.5% for sample L and 96.7$\pm$0.2% for sample H). It is therefore noteworthy that despite either processing regimes H and L allowed similar amounts of porosity, distinctive values of the CCL are observed, suggesting a significant underlying effect of process parameters on microstructure and cracking development. This is discussed in detail in the subsequent sections with the aim to identify the critical features controlling the cracking behaviour of the alloy.
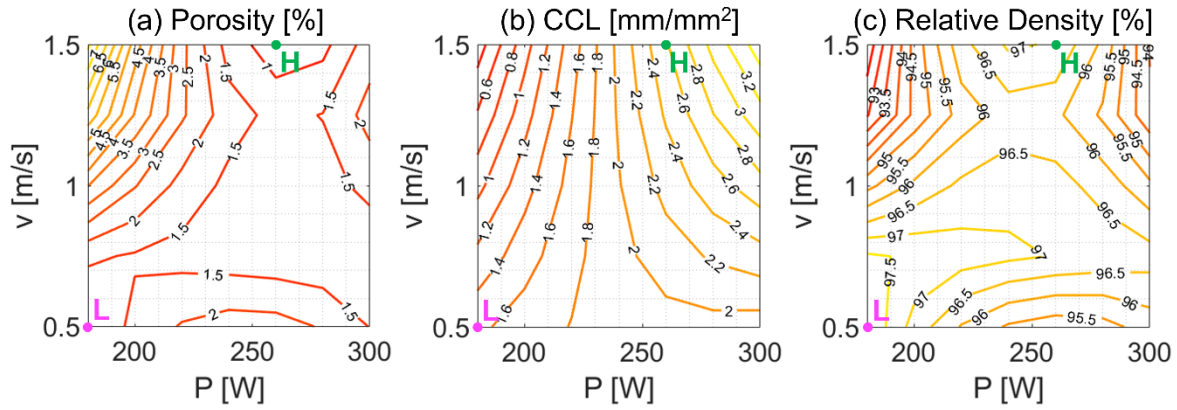
Figure 4.4: contour plots showing the trend of (a) porosity, (b) *CCL* and (c) relative density of samples produced in the investigated processing window as a function of power P [W] and scan speed v [m/s]. H (260 W, 1.50 m/s) and L (180 W, 0.50 m/s) processing conditions are highlighted in green and purple, respectively. Units on the colour lines are those of the respective graphs.

4.1.4 Phase identification and analysis

XRD analysis was carried out to identify the phases present in the PBF-LB/M samples prepared with conditions L and H, as well as the as-received powder (see Figure 4.5) as a benchmark. The peaks of the Al-FCC matrix are clearly visible in all specimens. In the powder spectrum, the relative intensity of all the Al-FCC peaks in the investigated 2θ range with respect to the {111} crystallographic plane agrees closely with the ICDD data for pure aluminium. Therefore, no preferred texture is found in the powder. On the other hand, the relative intensities of the {111} and {200} planes were inverted in both PBF-LB/M samples. This is commonly attributed to the presence of a preferred {100} crystallographic texture, likely due to the layer-by-layer solidification in PBF-LB/M, and a larger grain size. Several smaller peaks, associated with secondary phases were also present in the XRD diffractograms. Peaks corresponding to Al_2Cu (θ-phase) and Al_3Mg_2 (β-phase) were indexed in all three spectra. Additionally, the ternary compound Al_2CuMg (S-phase) was detected in the powder sample but not in the PBF-LB/M specimens.

Generally, the as-received powder showed peaks with lower intensities and larger widths than the as-built alloys. XRD peaks' broadening may happen due to several phenomena, such as, micro-strains caused by high dislocation density or other defects in the crystal structure, small coherent diffracting zone size, chemical lattice parameter's variation caused by inhomogeneous composition in the alloy. Pokharel et al. [232] studied stainless steel manufactured by PBF-LB/M and found that XRD peaks showed broadening because of the higher dislocation density, excluding chemical segregation as a contributing factor. On the other hand, the narrower peaks of the as-built samples suggest that these samples are characterized by a more ordered structure which could arise from the intrinsic thermal treatment associated with multiple passes of the laser beam during PBF-LB/M. Despite these valuable considerations, further studies conducted by either Rietveld analysis or Hall-Williamson method are required to comprehensively differentiate potential causes of peak broadening in AA2024 parts manufactured by PBF-LB/M. The presence of the observed phases is reported in the literature for AA2024 manufactured by PBF-LB/M [128,185]. The analysis shows conclusive evidence that both specimens H and L contained identical phases.
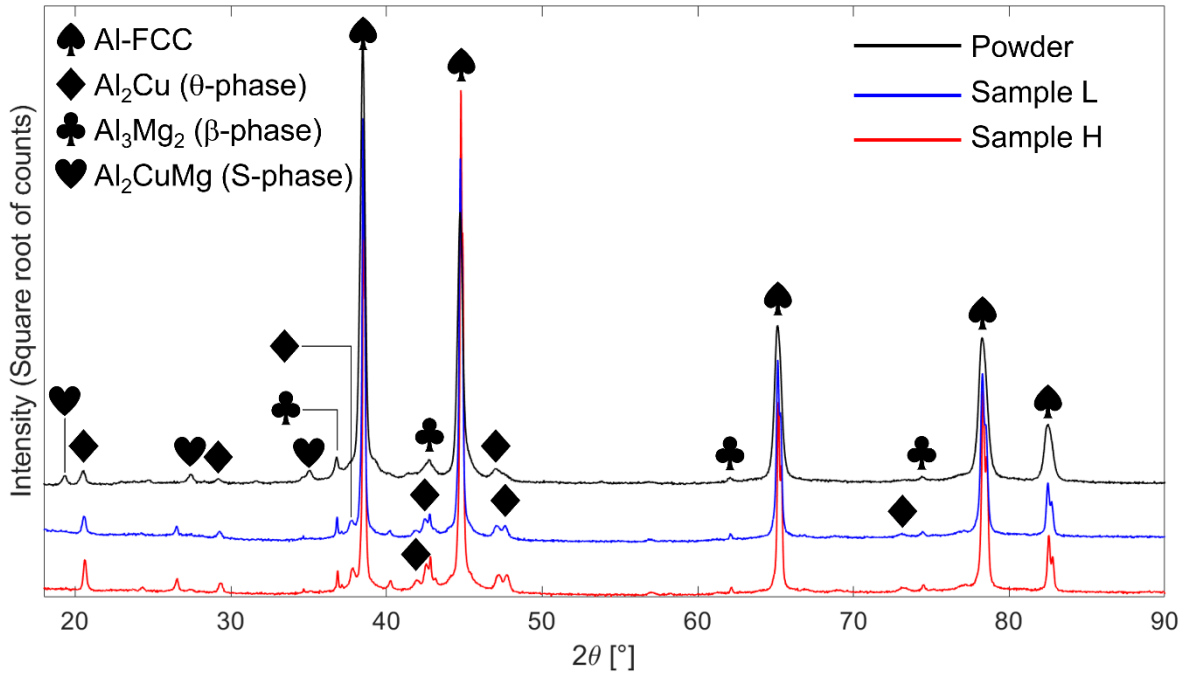
Figure 4.5: XRD spectra for the powder and samples produced by the L and H PBF-LB/M processing conditions. The Al-FCC peaks are indexed using spades, Al_2Cu is indexed with diamonds, Al_3Mg_2 peaks are indexed using clubs and finally the S-phase is indexed with hearts. This last compound was detected only in the powder sample.

4.1.5 Grain structure and crystallographic texture

Figure 4.6 shows SEM/BSE images of the microstructure on a plane parallel to the BD of samples L and H. The lower magnification images, Figures 4.6(a) and 4.6(b), show the melt pool (MP) boundaries, which are traced in yellow. The shape of the melt pool provides insight on the melting regime with which the samples have been manufactured. It was observed that for both processing conditions, the melt pools were relatively shallow. This confirms that specimens were melted, at least predominantly, in conduction mode, supporting the observed porosity trends (no keyhole porosity was detected in these processing conditions). Columnar grains elongated along the BD formed under both processing conditions (Figure 4.6). Figures 4.6(c) and 4.6(d) depict, at higher magnification, the microstructure in the vicinity of the melt pool boundaries. The

substructure in both specimens is characterized by a fine-scale cellular/dendritic solidification morphology, as typically reported for a variety of Al alloys [110,119,128,172,233] produced by PBF-LB/M.

Intercellular/dendritic regions comprise secondary phases, which appear in Figure 4.6 with a distinctive brighter contrast due to the higher mean atomic number. The apparent aspect ratio of the cells varied depending on the location within the melt pool (boundary, centreline). These sub-structures here appear coarser due to the formation of a low cooling rate zone caused by the decrease of the temperature gradient from the top part of the melt pool to the boundaries along the building direction [234]. The average cell width was measured at the melt pool boundaries considering 20 adjacent cells within a single grain growing with a (100) direction aligned with the direction of the heat. At the MP boundaries, a difference in cell width (λ) was observed between samples H and L. The former was characterized by an average cell width of 0.65$\pm$0.04 μm, which is slightly smaller than the L sample (0.82$\pm$0.12 μm). Analogous results and differences between the two specimens were generally observed in the microstructure.
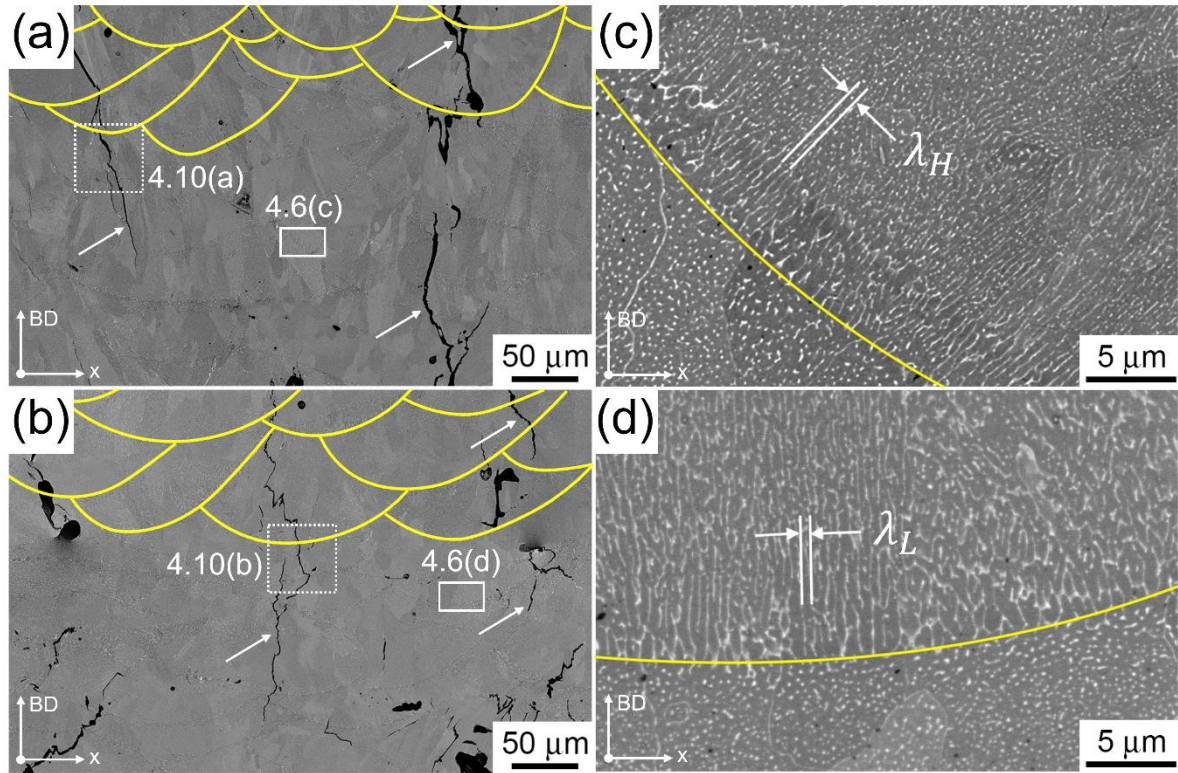
Figure 4.6: SEM/BSE images of the samples produced by the H (a-c) and L (b-d) processing conditions in the plane parallel to the BD. The melt pool boundaries are indicated by the yellow lines. Micrographs (c) and (d) are site specific details taken from the solid boxes of (a) and (b), respectively. (c) and (d) show the melt pool boundaries and its characteristic dendritic solidification mode. The dotted boxes in (a) and (b) depict the microstructure in the vicinity of the cracks which will be discussed in Fig. 4.10.

EBSD-derived data were used to analyse the crystallographic texture of samples H and L and identify differences in the grain structure and morphology. The EBSD maps in the planes parallel and perpendicular to the BD are presented in Figure 4.7. In the plane parallel to the BD of both specimens, grains are seen to be elongated along the BD with their main axes tending to align with the main (vertical) heat loss direction (Figures 4.7(a) and 4.7(b)). As the grains' lengths (which was in the order of 100 μm) exceed those of the melt pools, grains apparently grew epitaxially and span multiple layers, as widely reported in the PBF-LB/M literature [110,124,172]. On the plane perpendicular to the BD, grain appeared with a more evident equiaxed morphology (Figures 4.7(c) and

134

4.7(d)). It was noted that the cracks detected in the previous paragraphs are mostly found at grain boundaries but occasionally they cut through grains, as can be appreciated in Figure 4.7(c) and 4.7(d). This might depend on the thermal stresses value and direction developed during printing. Moreover, this may be influenced by the presence of lack-of-fusion defects which act as stress-concentration regions.

Grain size quantification on these planes showed that the grains in both L and H processing regimes were characterized by a grain diameter of 15.55±14.90 μm and 14.07±12.55 μm. Thus, it can be concluded that the morphology and size of the grains in sample L and H were similar.
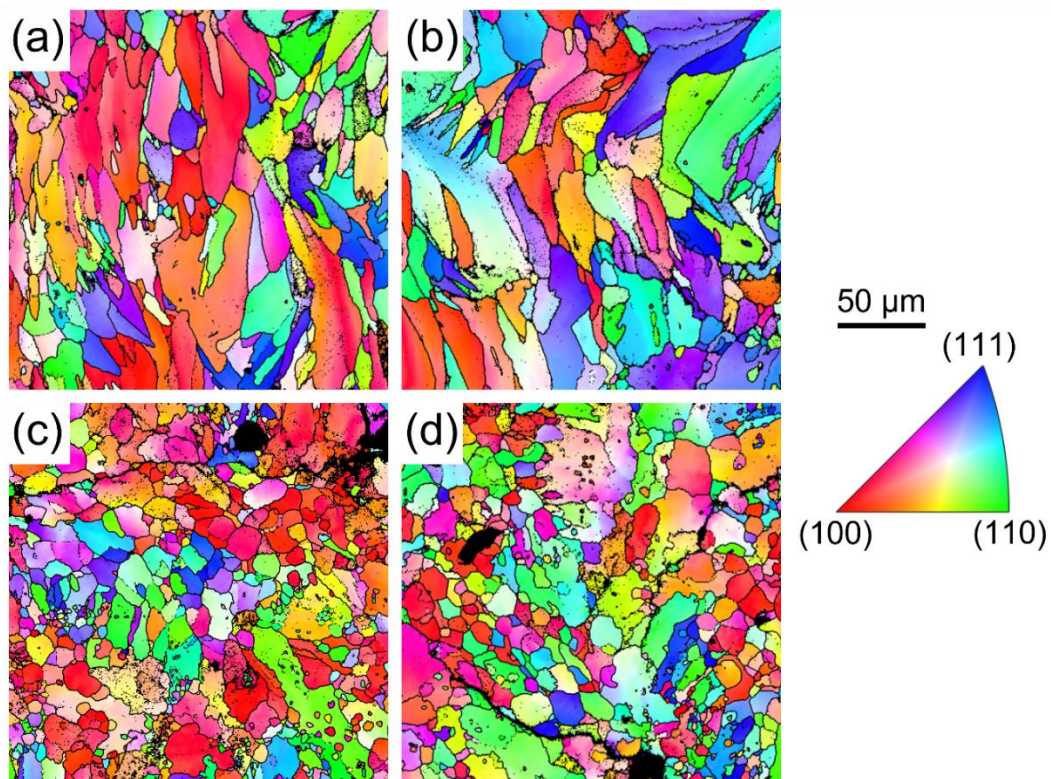
Figure 4.7: inverse pole figure (IPF) maps of samples H (a,c) and L (b,d) evaluated for both the planes parallel (a,b) and perpendicular (c,d) to the BD. The inset shows the scale bar and the IPF colour key in which the (100) orientation is aligned with the BD.

Figure 4.8 illustrates the pole figures of the two analysed samples from the vertical plane. Sample H showed a fibre texture, with a dominant texture component in which {100} is aligned to the BD and relatively weak axisymmetric intensities of the {111} planes around the BD (Figure 4.8(a)). On the other hand, a weak fibre texture was noted in the sample produced under processing condition L (Figure 4.8(b)).
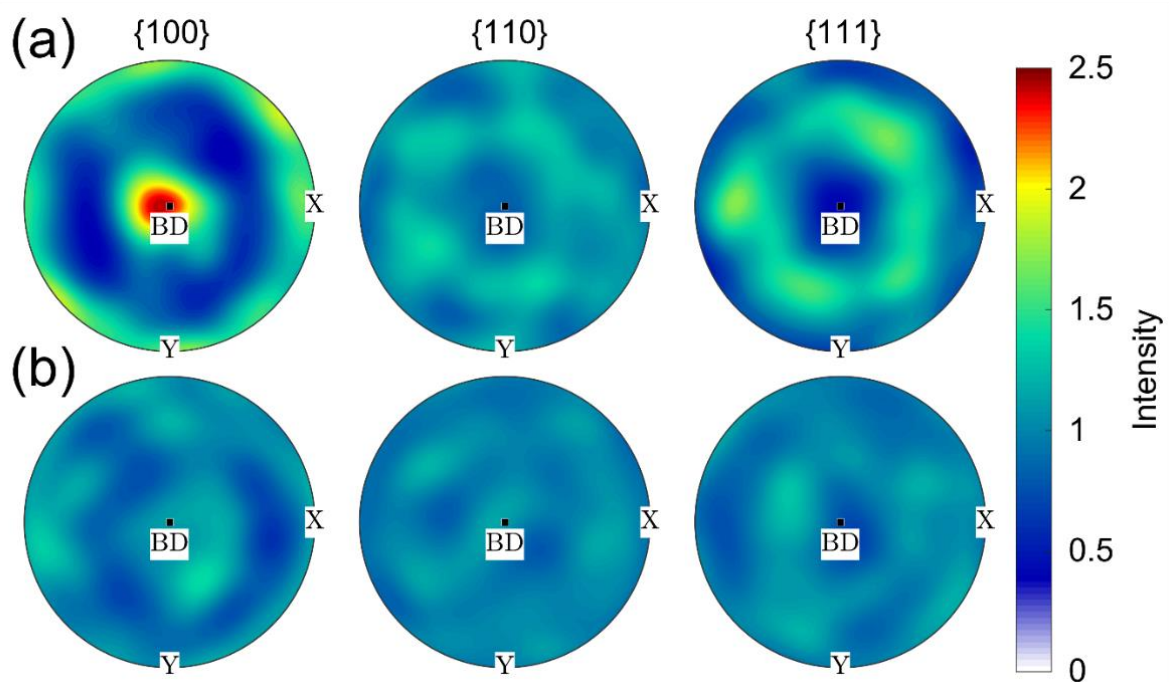
Figure 4.8: pole figures (PF) of (a) sample H and (b) sample L evaluated in the plane parallel to the BD. Sample H showed the presence of a fibre texture whereas a texture aligned to the BD was not detected in sample. L.

The distribution of the grain boundary misorientation angle for both H and L samples is plotted in Figure 4.9. The grain boundaries' misorientation was found between 15° and 62° for both sample H and L. The prior showed a slightly higher GB misorientation between 26° and 34° with respect to the latter. Although cracks were almost exclusively

found to be inter-granular, cracking was observed along a wide range of grain boundary misorientation angles.
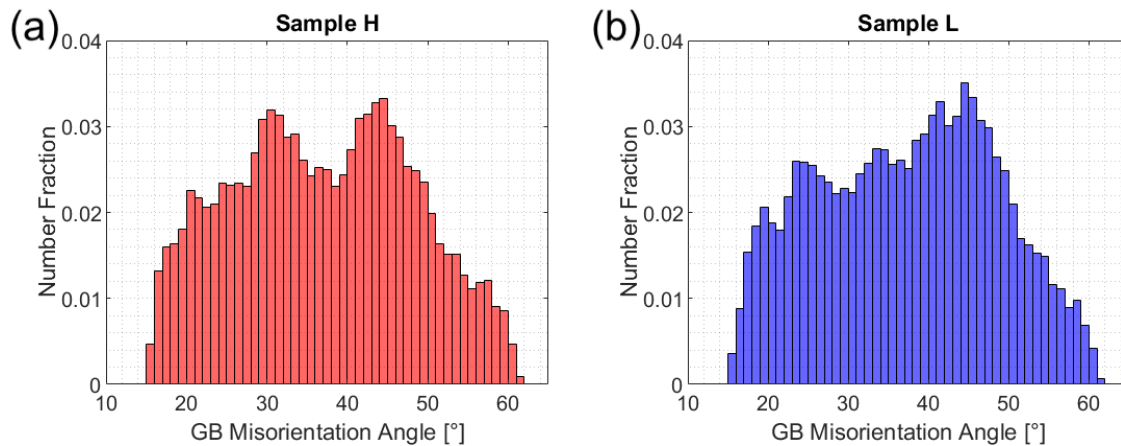
Figure 4.9: distribution of the grain boundary misorientation angles evaluated for the (a) sample H and (b) sample L in the plane parallel to the BD.

4.1.6 Crack morphologies and associated microstructural features

The high magnification SEM images in Figures 4.10(a-b) show that both H and L displayed cracks with similar but distinctive morphological features. Both samples contained shorter cracks (10÷20 μm) of complex morphology often accompanied by secondary phases (showing as bright contrast) at their tips and in between the exposed torn surfaces. Solid arrows indicate the typical morphology of the short cracks. The distinctive morphology and orientation of these short cracks indicates that these are most likely to be hot tears [32,42]. Long cracks spanning multiple layers are also present in the images and are indicated by dashed arrows. These long cracks, reaching lengths of 500÷600 μm or more, have instead a near-linear morphology. Moreover, as can be seen in Figure 4.10(c), their fracture surfaces are found to be flat, featureless, and dry. These long

continuous cracks must have propagated through a number of melt pools and so these are likely to be cracks that have propagated in the solid state (though they might have propagated originally from hot tears).
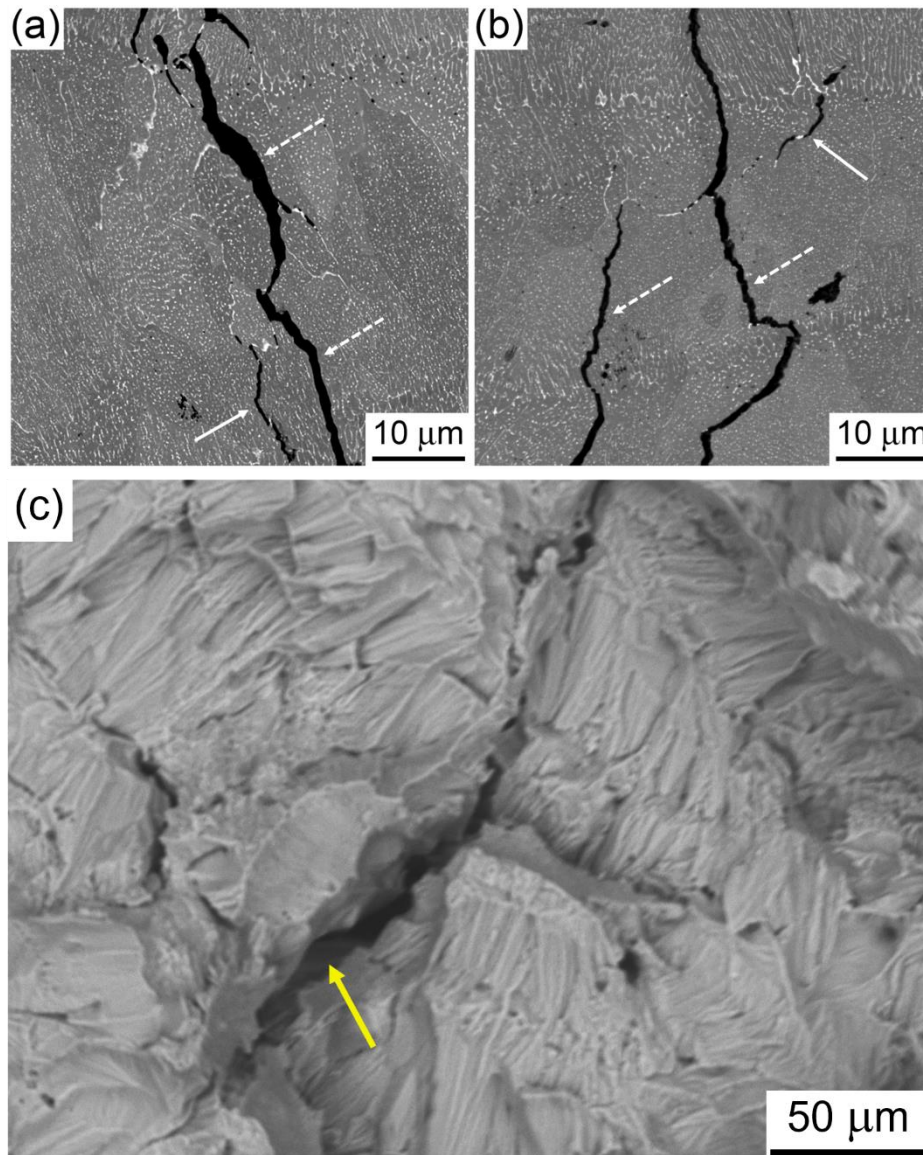
Figure 4.10: SEM/BSE micrographs of sample H (a) and L (b). Solid arrows indicate the typical morphology of the short cracks observed in the builds, while the dashed arrows indicate typical morphology of those cracks that span multiple layers. (c) SEM/BSE micrograph of the fracture surfaces (highlighted by the yellow arrow) of sample L.

EBSD analysis was conducted to gain further understanding of the morphology and crystallographic orientation of grains in the vicinity of the observed short cracks, thought

138

to be hot tears. Figure 4.11(a) illustrates the site of interest in a plane parallel to the BD. Incipient hot tears are denoted by the yellow arrows. These features are characterised by a pronounced presence of secondary phases in between crack surfaces. Additionally, the path of the analysed hot tears matches the grain boundaries, as can be seen in Figure 4.11(b). Although no particular orientation relationship between the grains surrounding the analysed cracks has been detected, their shape was elongated/columnar, and their main axes were aligned with the BD.
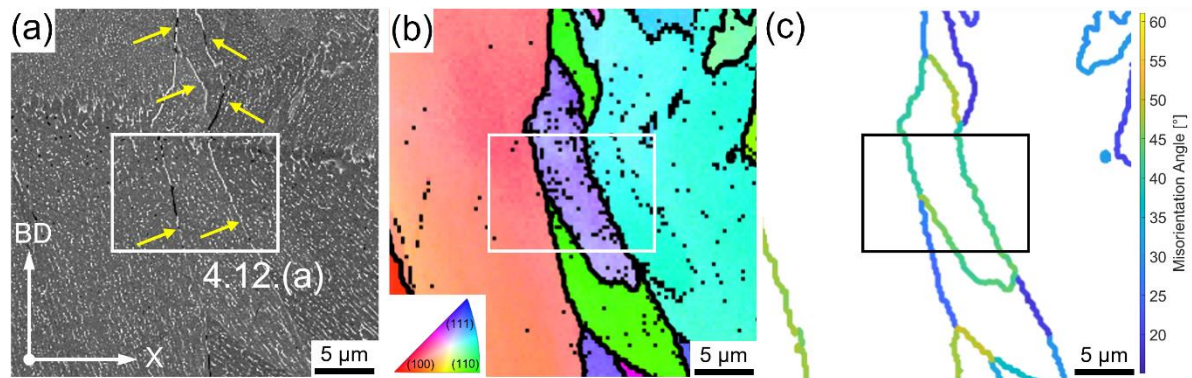
Figure 4.11: sample H. (a) BSE micrograph in a plane parallel to the BD showing the analysed short hot tears; (b) IPF map and (c) grain boundary misorientation angle map of the microstructure captured in (a). White boxes in (a,b) and black box in (c) represent the areas where a FIB lift-out thin foil for TEM was taken (Fig. 4.12(a)).

STEM imaging paired with EDS analysis was conducted to gain a further understanding of the nature of the secondary phases existing along the short cracks (thought to be hot cracks, which have not extensively propagated) present in the microstructure. Figure 4.12(a) illustrates the region of the microstructure that was prepared for TEM investigations, and this corresponds to the white box region shown in Figure 4.11(a). Figure 4.12(b) shows a HAADF-STEM micrograph of the microstructure surrounding a fine crack tip. This micrograph shows that the crack (highlighted by solid arrows) opens

along the solidification cell boundaries. Moreover, submicron-sized globular pores (highlighted by dashed arrows) were found within the grain in between dendrites. These features are thought to be gas pores that may have been originated either from gases trapped within the melt pool or from residual porosity in the powder [235]. Additionally, the analysis reveals the presence of sub-micron precipitates, ranging from 50 nm to 400 nm in width.

Figures 4.12(c-h) depict the EDS maps corresponding to Figure 4.12(b). It was observed that a portion of these precipitates are Cu-rich. These particles are believed to be the Al_2Cu phase detected by XRD. EDS maps also revealed the presence of Mg-rich precipitates, which in turn might correspond to the β-Al_3Mg_2 phase detected by XRD. Additionally, the investigation revealed the existence of other phases embedded in the Cu-rich matrix, such as, Si-rich, Si-Mg-rich and Fe-Mn-Si-rich phases in close-proximity to Al_2Cu and Al_3Mg_2. Although the cited compounds were found in all the areas of the studied microstructure, a difference in size and shape can be observed. Analysing these EDS maps, it is clear that the crack is characterized by an increased presence of Al_2Cu with respect to regions far away from the tip. Moreover, the Fe-Mn-rich phases appeared coarser with a better-defined globular shape. Despite not being detected by the XRD analysis, Fe-Mn-rich compounds are thought to be $Al_{15}(Fe,Mn)_4Si_2$ (also known as α-phase), as discussed in Section 4.2.3. No relevant difference in shape or size was detected for the Al_3Mg_2 phases, that appeared fairly equal at both the crack tip and in the bulk microstructure.
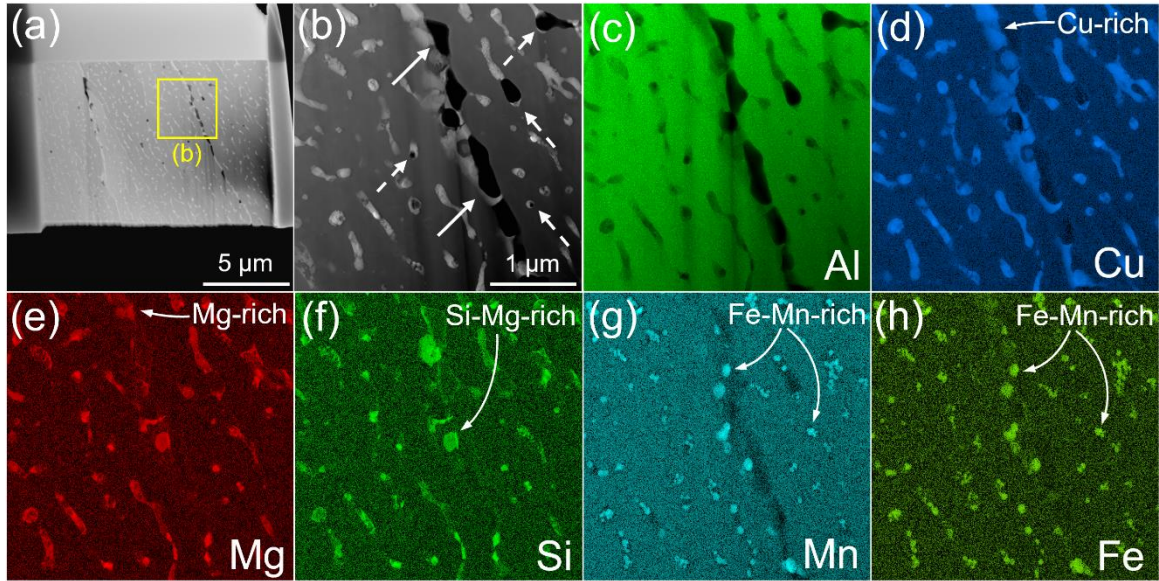
Figure 4.12: STEM imaging and EDS analysis of sample H. (a) HAADF-STEM of thin foil showing the microstructural overview in the vicinity of the crack investigated and the area where TEM-EDS was carried out (yellow box) (b) HAADF-STEM image presented with the (c-h) corresponding EDS maps of Al, Cu, Mg, Si, Mn and Fe.

4.1.7 AA2024 modification towards validation of alloy design indices

The presence of extensive cracking in the AA2024 suggests that, at least in the PBF-LB/M regimes investigated in the present chapter, the alloy is very prone to form hot cracks. As discussed in Chapter 2.5, other than grain inoculation, alloy chemistry is one the factors which can be tailored to limit the formation of hot cracks during solidification. Therefore, a modification of AA2024's chemical composition has been considered in the present section. This was conducted with a series of thermodynamic calculations driven by the CALPHAD method. A series of Scheil-Gulliver simulations was conducted to predict the hot crack susceptibility of AA2024 when refined with various Nickel amounts ranging from 0.5 to 6 wt% in steps of 0.5 wt%. This element has been selected because it presents a eutectic at higher temperature with respect to copper, the main solute of AA2024 [29,202]. As a result, it was hypothesized that this phenomenon could increase the

141

solidus temperature of the alloy, resulting in a reduction of the solidification range and an improvement of the hot crack resistance of the modified AA2024+Ni alloy.

Figure 4.13(a) depicts the resulting solidification trajectories of the considered compositions. It is possible to observe a progressive flattening of the curves with the increase of Ni content. This trend is clear at low fractions of solid and relatively high temperatures. Based on these solidification trajectories, the HCS index and the freezing range ΔT were computed and are depicted in Figure 4.13(b). A progressive reduction of ΔT up to a nickel addition of 2.5 wt% is noted; beyond this limit the freezing range increases. The hot crack susceptibility index HCS records a progressive decrease up to an addition of 5 wt% of Ni. In order to reduce the hot crack susceptibility of AA2024, these two indices have to be reduced. Therefore, the values of HCS and ΔT of AA2024 were selected as thresholds and a design zone was highlighted in green in Figure 4.13(b). Within the investigated compositions, additions of Nickel up to 5 wt% satisfied both design constraints and are thought to improve the hot crack resistance of AA2024. An addition of 3 wt% was selected for experimental investigation because represents a good compromise in trying to minimize both hot cracking parameters simultaneously.
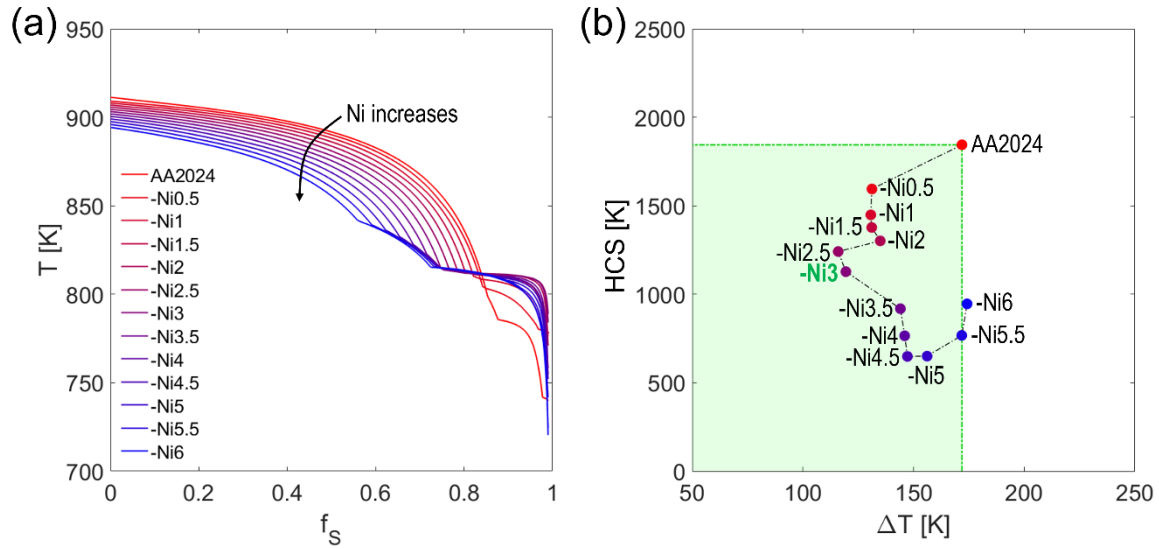
Figure 4.13: (a) solidification paths of AA2024 and AA2024 enriched with Nickel (AA2024 is red and progressively becomes blue as Ni is added up to a quantity of 6 wt %). (b) design map for the compositions investigated in this study where in green is depicted the available design zone.

AA2024+Ni3 was obtained mixing AA2024 and Nickel powders using Resonant Acoustic Mixing (Section 3.6.1). A wide range of processing regimes was adopted to produce this alloy and compare the cracking presence with AA2024 counterparts. Figure 4.14 depicts optical micrographs of the vertical plane of the AA2024 (a-d) and AA2024+Ni3 (e-h) samples. Long cracks aligned with the building direction are found in the microstructure of AA2024 in all the investigated PBF-LB/M regimes. On the other hand, apart from the sample produced with a meander scan strategy, 300 W and 1.5 m/s (Figure 4.14(f)), AA2024+Ni3 showed a significant reduction of cracking intensity. Moreover, the sample produced with a chessboard scan strategy, 180 W and 0.5 m/s (Figure 4.14(g)) showed a limited cracking presence. Figure 4.14(i-l) depicts the values of cumulative crack length of each PBF-LB/M regime investigated, comparing AA2024 (in red) and AA2024+Ni3 (in blue). Apart from the processing conditions depicted in the second row of Figure 4.14, a substantial reduction of cracking intensity was recorded when AA2024 was refined with a 3 wt% of Nickel. This trend is more accentuated in the samples produced with a

chessboard scan strategy. These two processing conditions showed the highest reduction of cracking features. Moreover, it was noted that the AA2024+Ni3 sample produced with 300 W and 1.5 m/s (Figure 4.14) was characterised by substantial presence of keyhole pores interconnected by the presence of cracks. These features may be propagated from the pores, defects known to be stress concentration areas [236].
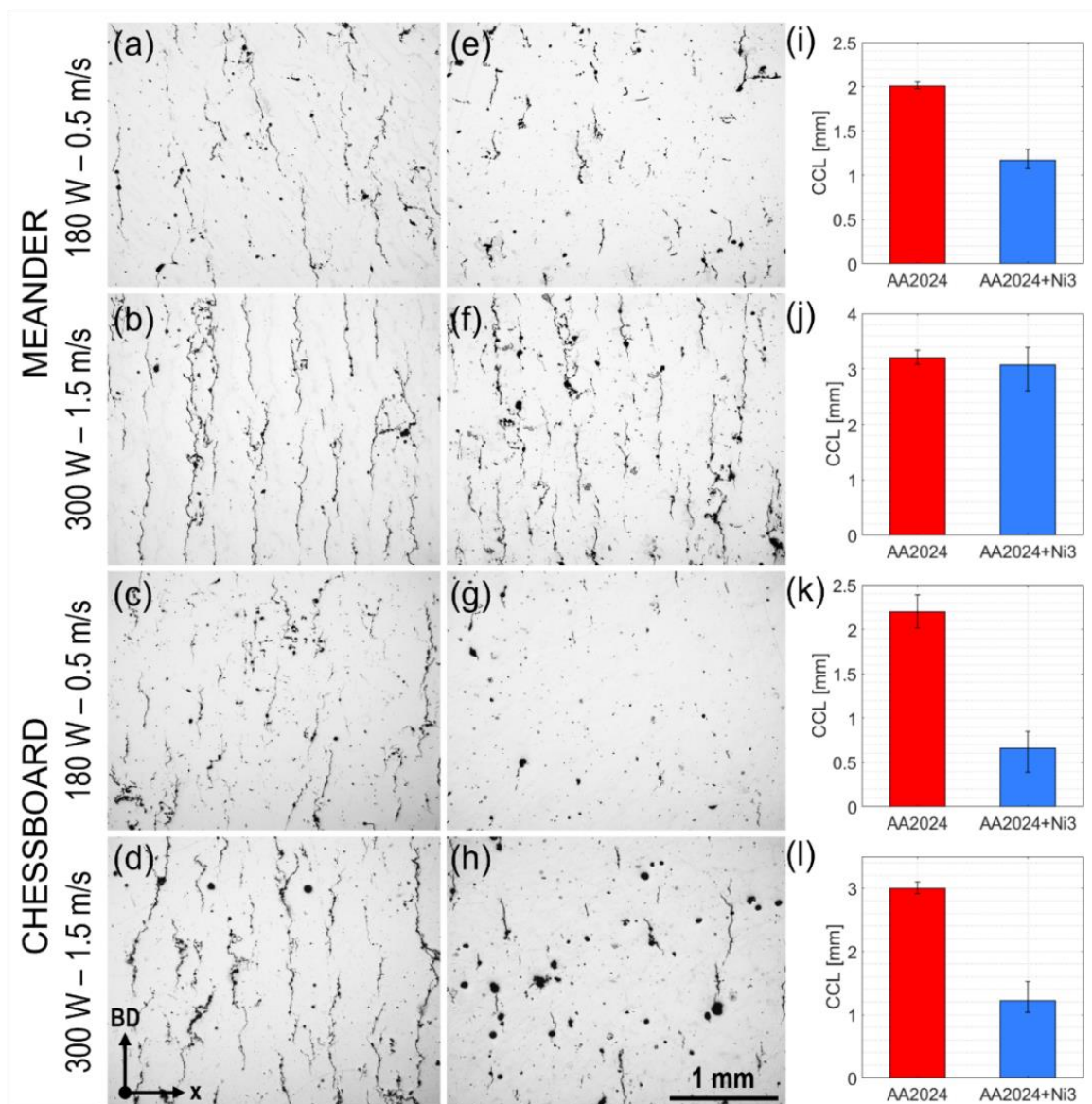
Figure 4.14: (a-h) optical micrographs parallel to the BD of the AA2024 (first column) and AA2024+Ni3 (second column) samples produced with the PBF-LB/M processing conditions listed on the left-hand side.

(i-l) bar charts depicting the values of cumulative crack length (CCL) measured for the processing conditions on the left for AA2024 (in red) and AA2024+Ni3 (in blue).

In order to compare cracking morphologies, the microstructure of the samples depicted in Figure 4.14(c,g) were selected for a further investigation. Figure 4.15 illustrates backscattered micrographs of AA2024 (a,c,e) and AA2024+Ni3 (b,d,f). The large field of view of (a-b) allows the visualization of all the crack morphologies found in the samples. Long cracks aligned with the building direction reaching a length of 100 μm or more can be easily identified (blue arrows) in both alloys. The morphology and size of these features confirms that, as discussed in Section 4.1.6, these represent cracks which have propagated in the solid-state from hot tears. Despite having similar morphologies, these cracks seem to be less pronounced in AA2024+Ni3. The length of the features in Figure 4.15(b) is indeed shorter than the ones found in the AA2024 counterpart. Additionally, large areas with limited amount of these long features can be highlighted. Figure 4.15(c-d) represent site specific insets of (a-b) depicting at a higher magnification the area in the vicinity of the propagated cracks. In both alloys, shorter cracks of complex morphology and paired with secondary phases (in bright contrast) were found. These features were found also in areas of the microstructure far from propagated cracks, as can be seen in Figure 4.15(e,f). As discussed in Section 4.1.6, their distinctive morphology and orientation indicate these features represent hot tears [32,42,64]. Despite solidification cracks were found in both samples, in AA2024+Ni3 these features were less present. The lower CCL found in AA2024+Ni3 (Figure 4.14(k)) confirms the beneficial effect of the nickel addition and the merits of the adopted design criteria. It should be noted that a higher reduction of HCS and ΔT is needed to eradicate the presence of hot cracks.
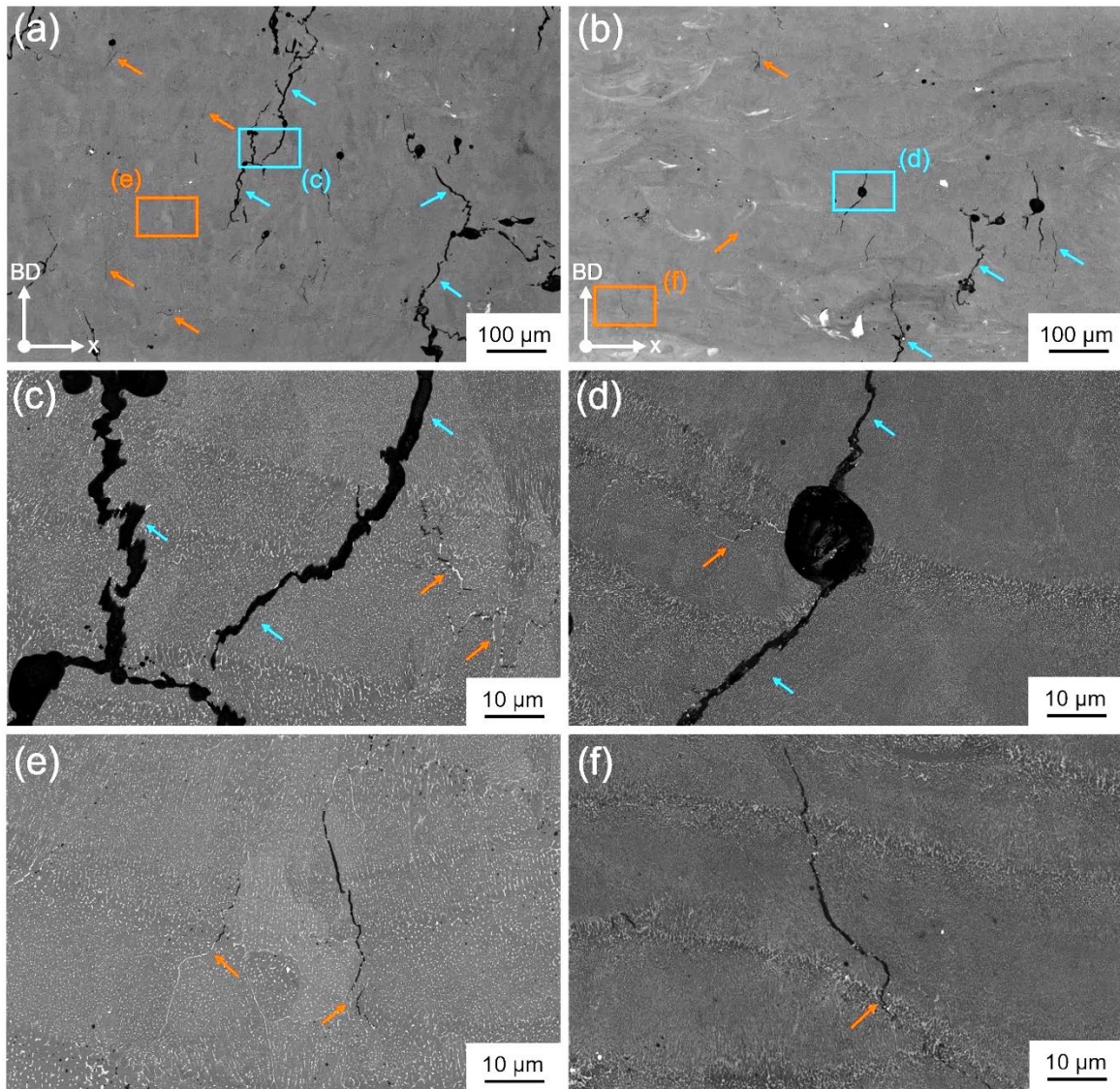
Figure 4.15: SEM/BSE micrographs of AA2024 (a,c,e) and AA2024+Ni3 (b,d,f). The blue arrows indicate cold cracks, while the orange arrows indicate non-propagated hot cracks. Micrographs (c,d) and (e,f) are site specific details taken from the solid boxes of (a) and (b), respectively. (c) and (d) depict the microstructure in the vicinity of a cold cracks in AA2024 and AA2024+Ni3, respectively. On the other hand, (e) and (f) depict the microstructure of AA2024 and AA2024+Ni3 near isolated hot cracks, respectively.

4.2 Discussion

4.2.1 Melting modes of AA2024 under different PBF-LB/M regimes

As discussed in Section 4.1.1, the absorptivity of AA2024 shows great variability as a function of laser power and scan speed (Figure 4.1). In the low power regime, A assumes relatively low average values characterized by a large scatter for each considered v. This happens due to incomplete melting of the powder bed and discontinuities in the track formation (specifically at lower scan speeds) causing inconsistent light scattering and poor energy absorption [220]. Laser powers exceeding 150 W were required to form continuous tracks and in turn more accurate A measurements. In the high-power regime, the A plateaus and is characterized by a less accentuated scatter. This trend is clear for a scan speed of 0.5 m/s. In between the low and high-power regime, a progressive rise of A values was noted which is more accentuated for lower scan speeds.

Absorptivity is directly associated with the interaction between the powder and the laser source that is the melting mode. Moreover, fluctuations of the layer thickness and powder inhomogeneities may influence the energy absorption and cause the scattering of the A values. Considering Al-based materials, this behaviour is strongly influenced by the laser P intensities. In the low-power regime, the cited interaction is dominated by the specular reflection between powder particles. In these conditions the conduction melting mode dominates. On the other hand, in high-power regimes, keyhole mode melting prevails. The high energy associated to the laser causes metal evaporation and the formation of deep V-shaped melt pools. This condition is associated with a higher interaction between the laser source and powder bed which results in the greater values of absorptivity of Figure 4.1. The detected rise of A in between the two considered power regimes is

147

associated to the gradual change of melting mode from conduction to keyhole. This behaviour is more accentuated for low scan speeds since these are characterized by a higher energy deposition.

The measured values of absorptivity and their drastic change within the combination of investigated process parameters highlight the need to consider A as a function of both power and speed. The use of a constant absorptivity value in the prediction of the consolidation behaviour of PBF-LB/M materials may cause discrepancies between predictions and experimental results. These differences may be particularly accentuated for Al-based materials which, as shown in Section 4.1.1, are characterized by a large range of A values as a function of PBF-LB/M processing regimes.

4.2.2   Consolidation of various PBF-LB/M processing regimes

This chapter investigated a P-v process window in which it was possible to optimize the relative density minimising the presence of macro-pores. The alloy showed a relatively wide processing window, the first requirement to produce good quality printed AA2024 parts. To further define the processing windows of AA2024 and reduce LOF defects, future studies may investigate the use of variable hatch distance. Lack-of-fusion often derives from incorrect overlapping of the melt pools and therefore a reduction of h may improve densification. However, it should be noted that h values below a certain threshold might lead to overheating and melt pool instabilities, particularly in regions of the build of variable cross section. Similarly, a further reduction in the nominal layer thickness might expand the processing window of AA2024, although this might require finer particle size distributions, which could affect spreading and in turn consolidation.

The rapid solidification and thermal cycling imparted by PBF-LB/M are responsible for the creation of complex microstructures shown in Figure 4.6 and 4.10. It is now well-established that the combination of thermal gradients and solidification speeds typical of PBF-LB/M promote columnar-dendritic solidification, where α-Al solidifies first, and solutes segregate at dendrite boundaries [6]. Dendrites are visibly coarser at the melt pool boundaries than in the melt pool core, due to the partial remelting caused by the laser beam during depositing successive layers and temperature differences in the solidifying melt pool [128]. Dendrites, developing from the melt pool boundaries are typically either aligned to the building direction or are slanted towards the melt pool centre (Figure 4.6(c-d)) following the thermal gradient. Occasionally, dendrites develop with an "out-of-plane" orientation, resulting in an apparent cell morphology on the vertical plane of the samples (Figure 4.6(c-d)). The average dendrite growth direction (and thus texture in Al-alloys [6]) is a function of the solidification front direction (typically perpendicular to the melt pool boundary) and thermal gradients, which in turn depend strongly on the melt pool morphology. Therefore, it is not surprising that the choice of the different combinations of laser power and speed were associated to various degrees of crystallographic textures, as observed in samples L and H. Macroscopically, the epitaxial growth of new grains over the previously deposited layer led to the development of a columnar morphology predominantly aligned with the building direction.

Considering the typical microstructures obtained after conventional manufacturing as direct chill (DC) casting of AA2024, it is possible to highlight significant differences. PBF-LB/M generates, as shown in this work, columnar grains generally aligned with the building direction of similar morphology and dimension within the sample. On the other

149

hand, the microstructure of DC casting products is characterized by fine equiaxed grains on the periphery of the ingot and coarse columnar grains pointing towards its centre [237,238].

4.2.3 Formation of cracks under PBF-LB/M processing regimes

The presence of hot cracks is a well-documented issue limiting the processability of high-strength Al-alloys during PBF-LB/M [110,119,124,185]. It is known that hot tearing is a cracking mechanism affecting materials that solidify over a large temperature range [64]. In the last stage of solidification, when the volume fraction of solid is above 0.85-0.95 [62], the liquid film of the mushy zone may part due to the high presence of thermal strains associated with the phase transition. It is thus critical to evaluate the solidification path of a given alloy. The shape of this trajectory is influenced by both the composition of the material in analysis and the manufacturing history and can be evaluated using the CALPHAD approach paired with appropriate micro-segregation models. This requires some considerations. The Scheil-Gulliver model (Equation 4.1, [84]), widely used to discuss the solidification path of additively manufactured alloys [110,124,128], assumes the presence of thermodynamic equilibrium at the solid-liquid interface, infinitely fast diffusion in the liquid and the absence of diffusion in the solid phase.

$$C_L(1-k)df_S = (1-f_S)dC_L$$ Equation 4.1

In Equation 4.1, C_L represents the composition of the liquid, f_S is the fraction of solid, k is the partition coefficient and corresponds to the one evaluated in equilibrium conditions k_e. Nevertheless, in rapid solidification processes, such as, PBF-LB/M, solutes may be "buried" in the solid phase due to the presence of high solidification rates [239]. This

phenomenon, known as solute trapping, results in alterations of the partition coefficient at the solid-liquid interface [240–242] which can be described by:

$$k = k_e + (1 - k_e)e^{-\frac{D_i}{v_T \lambda}}$$

Equation 4.2

where D_i is the interface diffusivity, λ represents the interatomic spacing and v_T is the solidification rate. This parameter is directly proportional to the laser scan speed following [243]:

$$v_T = v \cdot \cos \theta$$

Equation 4.3

where v represents the scan speed and θ the angle between the dendrites' growth and the laser directions. This angle has been considered equal to 45° in both cases with the specific aim of evaluating the solidification rate and the deviation of the partition coefficient from the equilibrium condition (Equation 4.2) in a region located in the rear of the melt pool which is more likely to not be remelted. Increments of v cause consistent variations of the partition coefficient which in turn alter the solidification trajectory of a given alloy.

Figure 4.16(a) depicts the solidification paths evaluated using the classic Scheil model and the solute trapping variant with 0.5 and 1.5 m/s. These two last conditions represent the processing conditions of L and H, respectively. It can be noted that with respect to the classic Scheil equation, the paths computed considering solute trapping are indeed shifted towards greater fractions of solid due to the different alloying elements content trapped in the Al-FCC matrix (Figures 4.16(b-d)). The solute trapping variant predicts a content of Cu, Mg and Si higher than the ones computed using the classic Scheil model. Moreover, an increment of solidification speed v causes a higher segregation in the Al-

FCC matrix given by the higher cooling rate [244]. The change of the solidification path depicted in Figure 4.16(a) is crucial to discuss and predict the hot cracking behaviour of a given alloy. The portion of the solidification path towards the end of solidification resembles the shape of a columnar dendritic grain near the grain boundary [78]. Therefore, solidification trajectories shifted towards higher fractions of solid are expected to have a narrower intergranular channel. This, as also proven by [83], increases the hot-crack-susceptibility of a given material as it will be harder for the liquid to percolate and backfill an opening crack. A note of care should therefore be considered when micro-segregation models that do not assume solute trapping are applied to PBF-LB/M as a change of the solidification path, as depicted in Figure 4.16(a), may impacts one's ability to predict the cracking behaviour of the alloy.
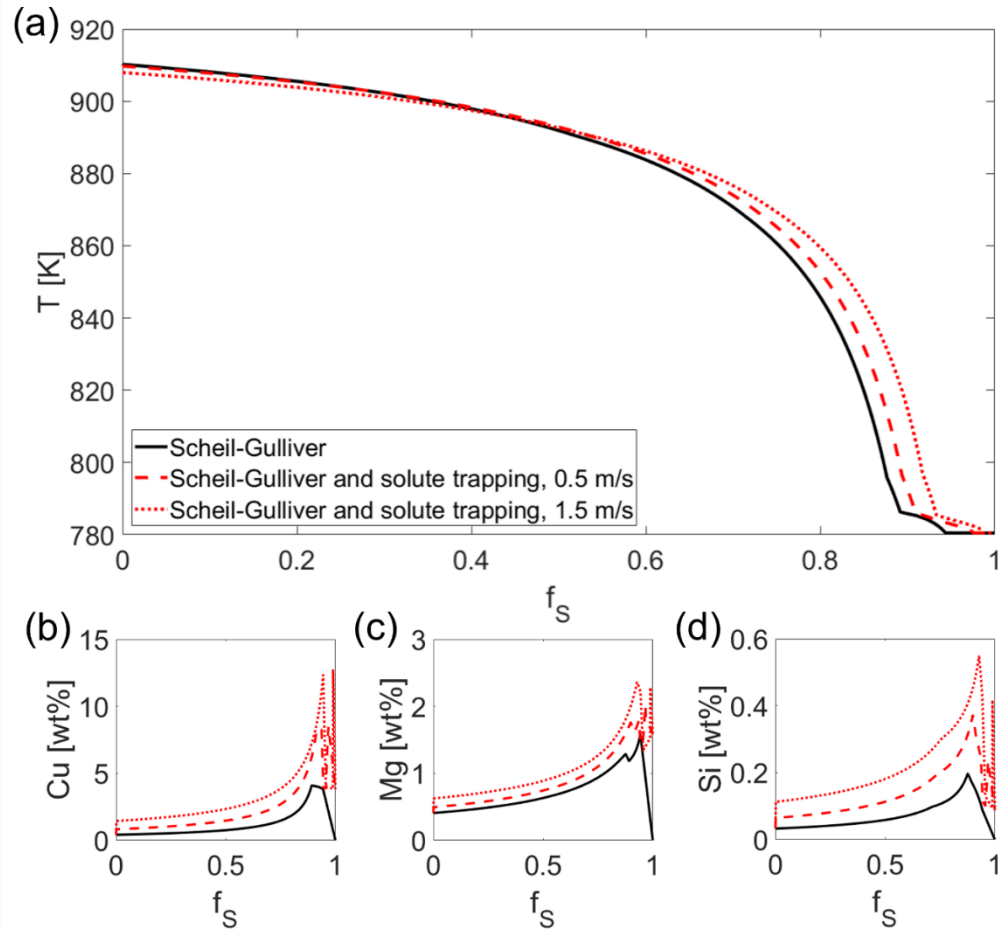
Figure 4.16: solidification paths of AA2024 evaluated using the Scheil-Gulliver equation and the solute trapping variant with 0.5 and 1.5 m/s (a); solute content of Cu (b), Mg (c) and Si (d) in the Al-FCC phase as a function of the fraction of solid evaluated using the classic Scheil model and the solute trapping variant.

In order to correctly discuss the cracking behaviour of AA2024 using the solidification path depicted in Figure 4.16(a), it is useful to compare the phases predicted by Thermo-Calc at the end of solidification with the compounds experimentally found in the microstructure. Table 4.1 lists the multi-phase regions predicted by Thermo-Calc for the AA2024 alloy under Scheil and solute trapping assumptions. These calculations predict that after the FCC-Al matrix, Al_6Mn is the first secondary phase that precipitates, followed by $Al_{15}(Fe,Mn)_4Si_2$ (α-phase), Mg_2Si, Al_2Cu (θ-phase) and then the S-phase (Al_2CuMg). Apart from the Al-FCC matrix, both the XRD and TEM analyses were able to detect the

153

presence of Al_2Cu and Al_3Mg_2. Additionally, the TEM-EDS maps revealed Si-Mg-rich and Fe-Mn-Si-rich zones in close proximity to the θ and β compounds. These phases are thought to be Mg_2Si and $Al_{15}(Fe,Mn)_4Si_2$. Although we could not detect the presence of the Al_2CuMg and the Al_6Mn phases (neither in the XRD nor TEM analysis), which might be kinetically suppressed by either the fast-cooling rates or intrinsic thermal treatment associated with PBF-LB/M, Scheil-Gulliver (with solute trapping) predictions find generally good correspondence to the observed microstructure.

Table 4.1: list of multi-phase regions predicted by Thermo-Calc for both the H and L processing regimes and the AA2024 alloy. The Scheil-Gulliver model applied with and without solute trapping assumptions led to the presence of the same multi-phase regions.

Multi-phase regions
Liquid + FCC
Liquid + FCC + Al_6Mn
Liquid + FCC + Al_6Mn + $Al_{15}(Fe,Mn)_4Si_2$
Liquid + FCC + $Al_{15}(Fe,Mn)_4Si_2$
Liquid + FCC + $Al_{15}(Fe,Mn)_4Si_2$ + Mg_2Si
Liquid + FCC + $Al_{15}(Fe,Mn)_4Si_2$ + Mg_2Si + Al_2Cu
Liquid + FCC + $Al_{15}(Fe,Mn)_4Si_2$ + Mg_2Si + Al_2Cu + Al_2CuMg

The solidification path of AA2024 is then considered using established cracking models and parameters in the literature. In the past decades, several theories have been

proposed to comprehensively discuss mechanisms that lead to hot cracking [74,76,78,79,245]. Clyne and Davies [74] proposed a hot-crack-susceptibility model based on the consideration of the time during which hot tearing takes place. They proposed an empirical cracking susceptibility coefficient defined as the ratio between the vulnerable time-period t_v and the time available for the stress relief process during solidification t_R. Despite being one of the first attempts of cracking tendency quantification, the Clyne and Davies approach possesses intrinsic uncertainties related to boundaries of the fraction of solid in which one should evaluate both t_v and t_R. A more recent approach was proposed by Rappaz, Drezet and Gremaud (RDG) [76]. The RDG model integrates both the fluid backfilling and the deformation in the mushy zone to describe the nucleation of a hot crack from a cavitation. Following this criterion, a void is formed when the liquid pressure drops below the cavitation pressure p_c. The computation of the pressure drop at the root of the interdendritic channel is hampered by the evaluation of the dynamic thermal conditions experienced during solidification. Therefore, it results difficult to discuss the hot crack driving force without a detailed computation of thermal gradients and cooling rates at a timescale relevant for hot crack formation.

Recently, Kou [78] proposed a new hot tearing criterion based on the consideration of the liquid-solid dynamics occurring in the last stage of solidification, that is the final segment of the solidification path. The model considers the growth of columnar dendrites, which are subjected to tensile deformation perpendicular to their main axis. According to Kou's criterion, hot cracks nucleate between solidifying dendrites when the condition in Equation 4.4 holds:

$$\left\{ \quad \dot{\varepsilon} \quad > \quad \sqrt{1-\beta}\frac{\sqrt{f_S}}{dT}\frac{dT}{dt} \quad + \quad \frac{d}{dz}\left[(1-\sqrt{1-\beta}\sqrt{f_S})v_z\right] \quad \right\}_{\sqrt{f_S}\to 1} \qquad \text{Equation 4.4}$$

(separation)   (growth)   (feeding)

where $\dot{\varepsilon}$ is the strain rate upon cooling, β is the solidification shrinkage, f_S is the fraction of solid in the mushy zone, T represents the temperature and v_z the velocity associated with the liquid backfilling the area in-between dendrites. Following Equation 4.4, Kou proposed an index to predict an alloy's hot-crack-susceptibility (HCS – Equation 4.5) based on the shape of the solidification path upon cooling (also known as solidification gradient) [78,79]. This parameter is evaluated by the computation of the maximum absolute value of the derivative of the temperature with respect to the square root of the fraction of solid at the last stage of solidification [79], with low HCS values considered beneficial against cracking.

$$HCS = \max\left|\frac{dT}{d\sqrt{f_S}}\right|_{\sqrt{f_S}\to 1} \qquad \text{Equation 4.5}$$

Figure 4.17 depicts the solidification paths of AA2024 evaluated under Scheil-Gulliver and solute trapping assumptions and the direct application of Equation 4.5. Considering that the curves depicted in Figure 4.16 are formed by several subsequent i-th points, the derivative of the temperature with respect to the square root of the fraction of solid has been computed considering the ratio between $T_{i+1} - T_i$ and $\sqrt{f_{s,i+1} - f_{s,i}}$. Therefore, HCS corresponds to the maximum absolute value of these incremental ratios. Table 4.2 lists the value of HCS calculated for AA2024 (sample H and L) and other common high-strength Al-alloys. It is observed that AA2024 has a HCS value of 2198 K and 2307 K in the L and H processing regimes, indicating, as expected, a significant sensitivity of

cracking to the manufacturing history, and the higher propensity of sample H to crack.

For a given solidification speed, comparatively to other high-strength Al alloys, such as,

AA6061 and AA7075, AA2024 has the lower hot-crack-susceptibility. Nevertheless, its

extensive cracking suggests that HCS values in the order of 2000 K are not enough to

avoid crack nucleation during PBF-LB/M.

Table 4.2: values of hot-crack-susceptibility (HCS) for AA2024 (this study, samples H and L) and characteristics high-strength Al-alloys found in the literature.

Alloy	HCS [K]
AA2024, sample H	2307
AA2024, sample L	2198
AA6061 [110]	10420
AA7075 [246]	2871
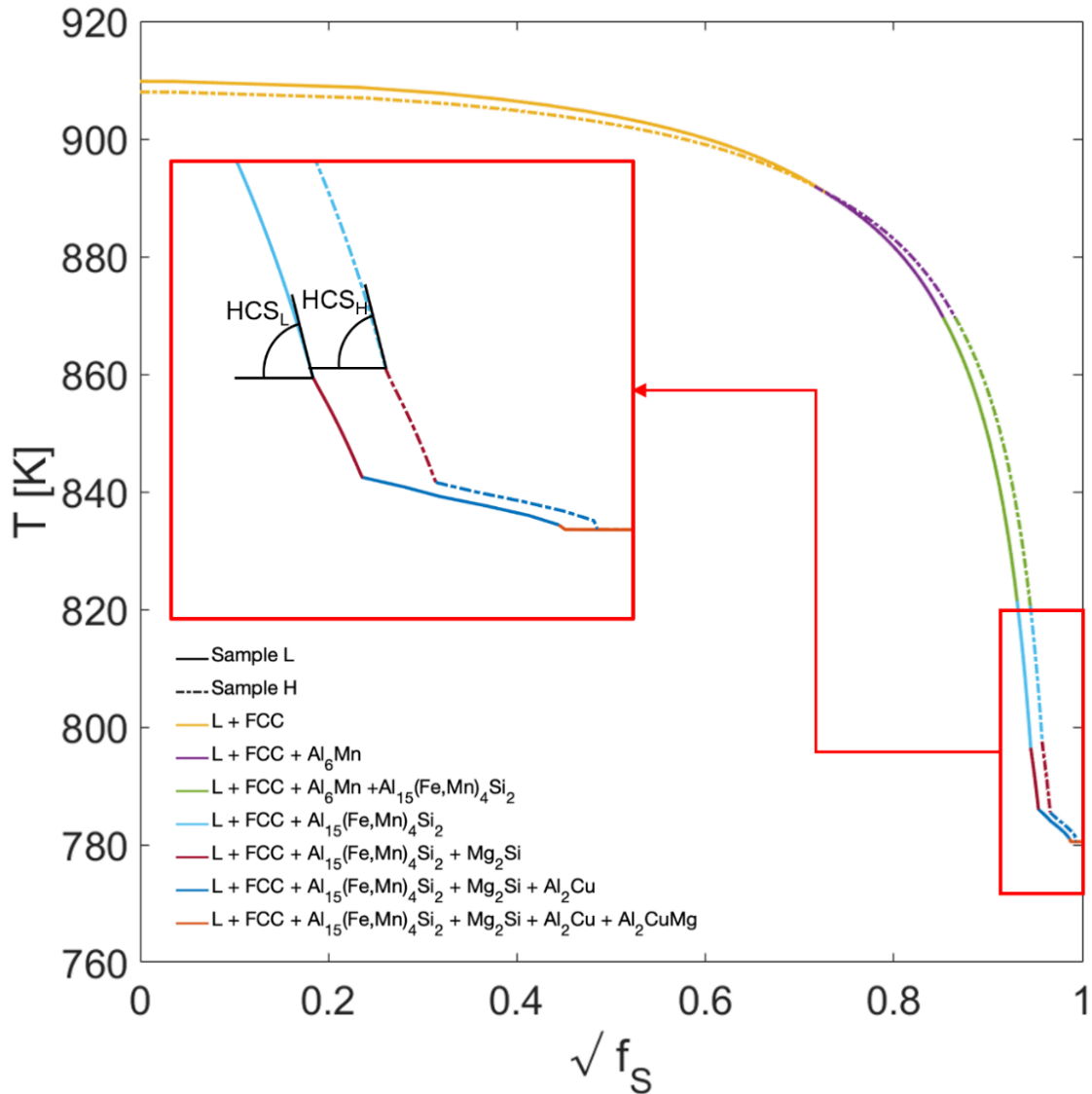
Figure 4.17: square root of mole fraction of solid forming in AA2024 using Scheil-Gulliver model of micro-segregation and solute trapping (Thermo-Calc 2020a, TCAL6 database). The plot displays the solidification path of both sample L and H, showing the sequence of the phases that form at the various stages of solidification. The inset depicts the critical region in which the *HCS* parameter is evaluated.

A note of care should be considered when Sc, Zr and/or Ti are added to the base alloy; the addition of these elements promotes the precipitation of compounds at the beginning of solidification characterized by a high crystallographic matching with the Al-FCC matrix, promoting the presence of an equiaxed microstructure achieved via heterogenous nucleation. In this case, the solidification path of the resulting alloy does not significantly

change towards the end [110] and as a result the *HCS* of the non-refined and the grain-refined alloy is not expected to change. Additionally, other microstructural features not contemplated in Kou's criterion and in *HCS* influence the nucleation of hot cracks. Chandra et al. [247] demonstrated that in Ni-based superalloys hot cracks are more prone to be found in correspondence of divergent grain boundaries. Sun et al. [83] showed that in high-entropy alloys, in opposition to what has been found in the present work, the hot cracks' surfaces are not characterized by solutes' segregation. This highlights the intricate and vast phenomena that affects hot tearing and the need to comprehensively study microstructure evolution when discussing the hot-crack-susceptibility of a specific alloy. Although the *HCS* parameter is not able to comprehensively capture the dependence of hot cracking on the microstructure, it offers a good perspective on the processability of a given alloy.

Noteworthy is also a consideration of how processing conditions and the thermo-mechanical behaviour of the alloy investigated can impact hot-cracking nucleation (separation term in Equation 4.4). The nucleation of hot cracks is largely influenced by the strain rate developed in the mushy zone, which, during PBF-LB/M, is located at the melt pool tail's periphery. In this area, strains perpendicular to the scanning direction develop as a consequence of the limited shrinkage and contraction of the material [248]. Drezet et al. [227] proposed the following expression to evaluate the strain rate at the rear of the melt pool created by a moving laser:

$$\dot{\varepsilon} = \alpha \dot{T}$$

Equation 4.6

where α represents the thermal expansion coefficient while $\dot{T}$ is the cooling rate. Clearly, the high cooling rates associated with rapid solidification processes such as, PBF-LB/M,

promote the development strain rates large enough to favour the formation of hot cracks. The cooling rate at the melt pool's tail can be estimated using the following [230]:

$$\dot{T} = 2\pi k \left(T_{sol} - T_{plat}\right)\left(T_{liq} - T_{plat}\right)\frac{v}{AP} \hspace{3cm} \text{Equation 4.7}$$

where k is the thermal conductivity, A is the absorptivity, P is the laser power, T_{plat} represents the platform temperature while T_{sol} and T_{liq} are the solidus and liquidus temperatures, respectively. For a given alloy, it can be evinced that cooling rates and strain rates are directly affected by the ratio between the scan speed and power. Sample H and L have been produced with v/P ratios of 5.77 and 2.78 mm/J, respectively. Consequently, the cooling rate at the melt pool's tail experienced by sample H was significantly higher than in the case of sample L. This difference agrees with the characteristic dendrite width measured in Section 4.1.5. The cell width λ value is indeed influenced by the cooling rate following the relationship reported by Matyja [249] for rapidly solidified Al-alloys, according to which the increase in $\dot{T}$ is paired by a decrease in dendrite width. This might also explain why sample H is characterized by higher cracking intensities than sample L. As a result, to minimise the nucleation of hot cracks, processing regimes characterised by low laser scan speeds and low v/P ratios are advised. Evidence that in these regimes cracks can be minimized or inhibited is ample [125,127,250]. Nevertheless, these processing conditions are paired with high energy densities, which may result in the formation of keyhole porosities, and are characterized by values of scan speed not commercially competitive using currently available laser beams. The need to change processing parameters to reduce the hot tears' nucleation tendency of a given material is a well-known practice also in traditional manufacturing

techniques. M'hambdi et al. [251] illustrated indeed that a reduction of the casting speed is able to reduce the presence of hot cracks in materials processed by DC casting.

4.2.4 Propagation of cracks during PBF-LB/M of AA2024

The extensive cracking behaviour in Figure 4.6 is thought to be the result of solid-state propagation (cold cracking) of hot tears. The CCL can therefore be used as an effective parameter to quantify the overall cracking propagation behaviour in the alloy. The first attempt to understand the mechanisms associated to the propagation of defects was proposed by Griffith [236] who studied crack growth in brittle materials. This theory was later extended by Orowan [252] to crystalline materials considering the presence of plastic deformation occurring at the tip of the crack. The growth of a crack is directly linked to the energy release rate G_{rr} per unit crack length [253]:

$$G_{rr} = -\frac{\partial \Pi}{\partial s} \qquad\qquad \text{Equation 4.8}$$

where Π is the total potential energy and s is the unit crack growth area. In critical conditions, the crack departs and propagates quickly resulting in the extensive cracking observed in Figure 4.6(a) and 4.6(b). Here the critical stress to activate this fast propagation is given by [253]:

$$\sigma_c = \frac{K_{Ic}}{B\sqrt{\pi L}} \qquad\qquad \text{Equation 4.9}$$

where σ_c is the critical stress needed to propagate the crack, K_{Ic} is the fracture toughness of the alloy, L represents the crack length and B is a dimensionless geometrical factor. Compared to steels or Ti-alloys, Al-alloys show relatively low values of K_{Ic} [254].

Additionally, the fracture toughness of a material is influenced by temperature and microstructural features [253]. The presence of long grain boundaries characterized by segregation may further lower the fracture toughness of AA2024, promoting crack propagation. Despite the extensive cracking found in the microstructure is thought to be the result of a solid-state propagation, hot tears nucleated in previous layers may propagate in the current one when they are intercepted by the fusion boundary. In this case, the characteristic length of the crack a increases, resulting in a reduction of the critical stress σ_c necessary to propagate the defect.

For a given alloy of fracture toughness K_{Ic} one ought to minimise the stress state imparted by the manufacturing process to reduce cold cracking. It is well-known that PBF-LB/M materials are inherently affected by high residual stresses, which develop as a consequence of the high thermal gradients across the melt pool boundary [255]. Nevertheless, stress distribution during PBF-LB/M is primarily affected by the melt pool's aspect ratio and, in turn, by the laser power and speed used to manufacture the parts [256]. For example, Mukherjee et al. [257] proved that residual stresses are reduced by adopting processing windows characterised by low v/P ratios. The different $CCLs$ measured in the samples H and L can be rationalised considering a likely different stress state in the materials. It is noteworthy that other process parameters may reduce the formation of stresses and the propagation of cracks. Scan strategies that minimise the scan vector length, such as the checkerboard island or "stripe" strategy, which anecdotally mitigate the presence of large cracks could be explained with similar reasoning [256]. Additionally, an increase in the platform temperature T_{plat} could lower the thermal gradients across the melt pool boundaries (particularly in low melting point alloys such as those of Al) [255,258].

Finally, one should consider the potential fracture toughness anisotropy associated with PBF-LB/M microstructures. As expected, we observed cracks developing along columnar grain boundaries, weak microstructural features owing to the presence of segregates and brittle precipitates. Recent research has elucidated the importance of controlling grain boundary segregation to maximise dendrite bridging and heal hot tears [259].

EBSD analysis in both planes parallel and perpendicular to the BD revealed that most grains were characterised by high angle grain boundaries (HAGBs) with misorientation angles greater than 15°. It is thought that HAGBs are more prone to hot cracks due to lower coalescence temperature (the temperature of bridging initiation between adjacent dendrites) and predominance of HAGB cracking is a well-documented issue in the Ni-based superalloys [260,261]. It is therefore plausible that cracks, once nucleated, might preferentially grow along these grain boundaries.

4.2.5 Limitations and merits of the used hot crack susceptibility indices

The analysis of the cracking behaviour of AA2024 in PBF-LB/M conditions has highlighted the presence of both hot tears and cold cracks. Cracking seems, therefore, an issue intrinsically related to the composition of AA2024 and the processing conditions imposed by PBF-LB/M fabrication. The only investigation describing the PBF-LB/M production of crack-free AA2024 samples (Gharbi et al. [128]) reports an incidental higher content of Si (0.78 wt% of Si, as opposed to 0.5 wt%, which is the maximum Si content for nominal AA2024). Silicon addition is a well-reported method to improve the processability of high-strength Al-alloys when processed by PBF-LB/M. Silicon can

reduce the alloy's liquidus temperature, introduce a new low melting point eutectic and improve the alloy's fluidity [168,246].

It is noteworthy however, that AA2024 and AA2024+Si possess similar values of HCS (and thus, at least nominally, similar propensity to nucleate hot cracks). Moreover, Li et al. [233] report the manufacture of crack-free AA7075+Si samples (associated to a HCS of 3960 K, thus significantly higher than the HCS of the AA2024 in our study). This suggests, as also proposed by Benoit et al. [262], that a single parameter, such as HCS, cannot alone capture the complexity of hot-crack susceptibility of high-strength Al-alloys during PBF-LB/M. It is proposed instead that *all* terms of Equation 4.4 should be assessed in detail. As discussed in Sections 4.2.3 other mechanisms affecting crack nucleation (such as, shape of dendrites, size and morphology of secondary phases at the crack tip, liquid feeding and strain rates associated to specific PBF-LB/M conditions) are not contemplated by the HCS parameter but appear to be significant factors affecting the alloy's crack susceptibility. Finally, mechanical properties of AA2024 are maximized by aging heat treatments with the specific aim of promoting the formation of finely dispersed Al_2CuMg and Al_2Cu [128,263]. Silicon in excess of the standard allowable is likely to cause precipitation of undesirable phases and thus have a poisoning effect (analogous to that reported by Li et al. [233], who describes the occurrence of Mg_2Si instead of a desirable Mg_2Zn in AA7075). This sheds light on one of the most challenging aspects of the alloy design in AM. The development of new high-strength Al-based materials for the PBF-LB/M process needs to be conducted bearing in mind not only processability constraints, such as hot-crack-susceptibility and residual stresses, but also design constraints, such as precipitates' nature and strength. The integration of these two

classes of conditions in the alloy development process will enable the formulation of new materials with tailored properties, specifically designed for the PBF-LB/M process.

The effect of nickel on the processability of AA2024 was investigated to prove the merits of dual-indices design map for hot cracking. As discussed in Section 3.1.2, nickel is able to decrease the solidification range of Al-alloys because of the introduction of an eutectic characterised by a higher temperature with respect to those of silicon and copper [202]. Additionally, as observed in Figure 4.13, the investigated additions of Ni are paired with a further beneficial reduction of the liquidus temperature. The combination of these two competing factors results in alloys with a decrease freezing interval which is beneficial for hot cracking. The observed reduction of cracks confirms the benefits of a multi-indices design map to discuss and design the material's intrinsic hot crack propensity. However, a further reduction of both HCS and ΔT needs to be achieved to produce crack-free alloys. Moreover, it is found that, despite the dual-indices map is beneficial in increasing the strength of our calculation, the hot-crack-susceptibility and the solidification range are not completely able to describe the shape of the solidification path. Additionally, the use of a dual-indices design map may result in difficulties in ranking the expected processability of alloys characterized by similar values of HCS and ΔT. Therefore, to increase the confidence in the calculations, a new single index able to capture all the factors affecting the intrinsic hot crack propensity of a given material needs to be computed.

4.3 Summary

This Chapter focused on the characterisation of the understanding of the effects of processing conditions and alloy chemistry on the densification and hot cracking behaviour of AA2024 processed by PBF-LB/M. Specifically, a series of experiments was carried out to study the effects of different processing regimes on the pores and crack formation. Moreover, a modification of the chemical composition of AA2024 was conducted to explore the merits of the state-of-the-art design indices available in the literature. It was observed that:

- The powder absorptivity is largely affected by both laser scan speed and power. However, the melting mode experienced during melting is more predominantly ruled by the latter. At powers lower than 200W, conduction mode dominates. On the other hand, at powers beyond 300W, the samples showed the presence of extensive keyhole porosities arising from the keyhole melting mode. At powers in between these two thresholds, a transitional regime was observed with the presence of minimal porosity.

- The densification of AA2024 under various power and scan speeds regimes showed that, despite porosity can be actively minimised, cracks are still found in the microstructure. However, their intensity is largely affected by both power and scan speed.

- Two samples (L and H) characterised by both minimal porosity but different cracking intensities were investigated via EBSD analysis. The results showed that, despite both samples were characterised by epitaxial columnar grain growth, the sample produced at higher power and scan speed (sample H – higher cracking intensity) showed the presence of a mild fibre texture. On the other hand, sample

L (produced at lower power and scan speed – lower cracking intensity) did not show any preferred orientation.

- Two different cracking morphologies were observed in samples characterised by minimal pore formation. Long cracks spanning multiple layers and aligned with the building direction were found to dominate the microstructure. These were classified as cold-propagated defects. The presence of shorter, irregular cracks was also observed. These were addressed as non-propagated hot cracks.

- Hot cracks were found predominantly at high-angle grain boundaries. Their formation path was characterised by coarser precipitation of secondary compounds (Cu- and Fe-Mn-rich phases) and the presence of micropores.

- A modification of AA2024 involving the addition of 3 wt% of Ni was carried out using a dual indices design map adopting the solidification range ΔT and the hot-crack-susceptibility index HCS to predict the hot cracking behaviour of bespoke compositions. With respect to the unmodified alloy, AA2024+Ni3 showed a sensible improvement in hot crack intensity throughout a wide range of processing regimes. However, hot cracks were still found in the microstructure.

Chapter 5

5 Modelling informed strategy for the PBF-LB/M of crack-free high-strength Al-alloys

Considering a certain alloy, it has been noted that the processing conditions adopted for PBF-LB/M fabrication have a great impact on the processability and hot crack formation. Specifically, low laser scan speed regimes have been widely reported to be characterised by crack-free microstructures paired with optimal mechanical performances. However, the reasons behind this abrupt change of processability are still not completely understood and the methods adopted in the literature fail to comprehensively link the process parameters adopted for PBF-LB/M fabrication and the formation of hot cracks.

In this Chapter the hot cracking behaviour of AA2024 is investigated as a function of four distinct process parameters sets using a combination of an experimental and modelling approach. Based on the result of Chapter 4, it is proposed that laser regimes characterised by lower scan speed are beneficial for hot crack suppression. A Point Distance Variation (PDV) melt track, characterised by four different scan speeds segments, is performed on

a bare AA2024-T351 substrate with the specific aim of highlighting laser regimes leading to hot crack formation. The thermal history and development of selected dynamic thermal condition is predicted by the implementation of a multi-physics simulation which computes a digital twin of the PDV experiment. Based on these data, the pressure drop at the root of the interdendritic channel in the mushy zone is computed for the first time at a resolution relevant to the solidification of the alloy during processing. Pressure drop peaks, which can lead to hot crack formation, are demonstrated to be associated to distinct temporal and spatial transient thermal conditions. A novel index to describe the stochastic nature of hot cracking by the investigation of the distribution and frequency of detrimental pressure drops is then proposed. This parameter rationalises for the first time anecdotal evidence that hot cracks become a severe issue when laser speed is increased. The found crack-free processing window is then investigated to improve its build rate with obvious implications for industrial settings.

5.1 Results

5.1.1 Experimental PDV track: hot cracking behaviour and model's validation

Figure 5.1(a) shows a longitudinal section along the centreline of the track with distinct processing conditions highlighted in different colours. The identification of the laser melted zone is straightforward thanks to the vastly different scale of the microstructures between the substrate (which is characterized by micron-sized secondary phases aligned with the z-axis direction of Figure 5.1(a)). On the other hand, the microstructure of the laser-irradiated track consists of a fine-scale cellular solidification substructure within large columnar grains which grow epitaxially from the substrate as expected. The solidification structure is typical of several Al alloy grades manufactured via PBF-LB/M [110,128,172,233,264]. The Al matrix phase (in grey) contains secondary intermetallic phases which appear brighter due to the higher mean atomic number. At the melt pool boundaries, the cells appear coarser due to the partial re-melting experienced in these areas. Consequently, melt pools can be easily identified and investigated. The four laser regimes are characterized by different lengths due to the progressive increase of the point distance in the laser scan direction. Hot cracks were found only in the PD45 and PD60 regimes (boxes in Figure 5.1(a)) and magnified in Figure 5.1(b-c). Within the PDV track, these features are limited to one melt pool, suggesting that their formation relates to single solidification events with no (or negligible) influence of the subsequent thermal pulses from the advancing laser. Both crack paths accurately follow grain boundaries characterized by a high value of misorientation angle (HAGBs), as can be observed in the EBSD analysis depicted in Figure 5.1(d-e).
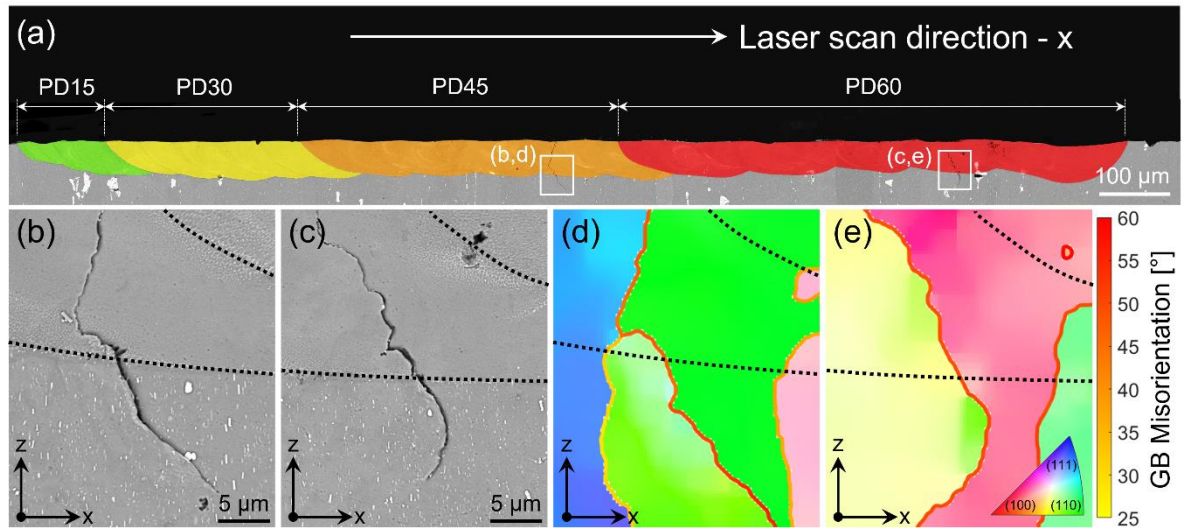
Figure 5.1: (a) SEM/BSE micrographs depicting the middle vertical plane of the PDV track. The four laser regimes have been isolated by the identification of the five melt pool boundaries associated with their pulses. These have been highlighted using distinct colours: green (point distance of 15 μm – PD15), yellow (PD30), orange (PD45) and red (PD60). These features have been magnified in (b) and (c) where melt pool boundaries are highlighted by black dotted lines. EBSD analysis was conducted in the vicinity of the hot cracks depicted in (b-c), the inverse pole figure (IPF) maps are plotted in (d) for PD45 and (e) for the PD60. The IPF colour key has been chosen so that the {100} orientation is aligned with the laser scan direction x.

In order to explain the dynamics leading to the cracking behaviour observed in the PDV experimental track (Figure 5.1), a high-fidelity multi-physics simulation was used to assess the thermo-fluid conditions experienced by the material under the four investigated regimes. Figure 5.2(a) presents a geometrical comparison of the PDV experiment (upper half) with the outcome of the simulation (lower half). The melted region is depicted in red, while the unmelted substrate in blue. In the first part of both tracks, melt pools were difficult to distinguish in this plane view due to the large overlap between two adjacent pulses. On the other hand, the melt pools of the PD45 and PD60 segments resulted easy to locate as their round shape was clearly visible due to the limited overlap, this can be clearly appreciated comparing the very last melt pool of the PD60 segment found at the larger x-coordinate in Figure 5.2(a). Both tracks were measured to validate the modelled PDV track. Figures 5.2(b) and 5.2(c) depict the values

171

of track's length and widths, respectively. Specifically, since the PDV track is formed by four different parameters sets, the track width was measured at the centre of each point distance *PD* segment. Great geometrical match was found for both the track length and widths and suggesting that the model captures with high-fidelity the thermal cycles experienced by the material during the track deposition. Consequently, the development of the dynamic thermal conditions in the XZ plane affecting hot crack formation was analysed using the methodology described in Section 3.8.3.
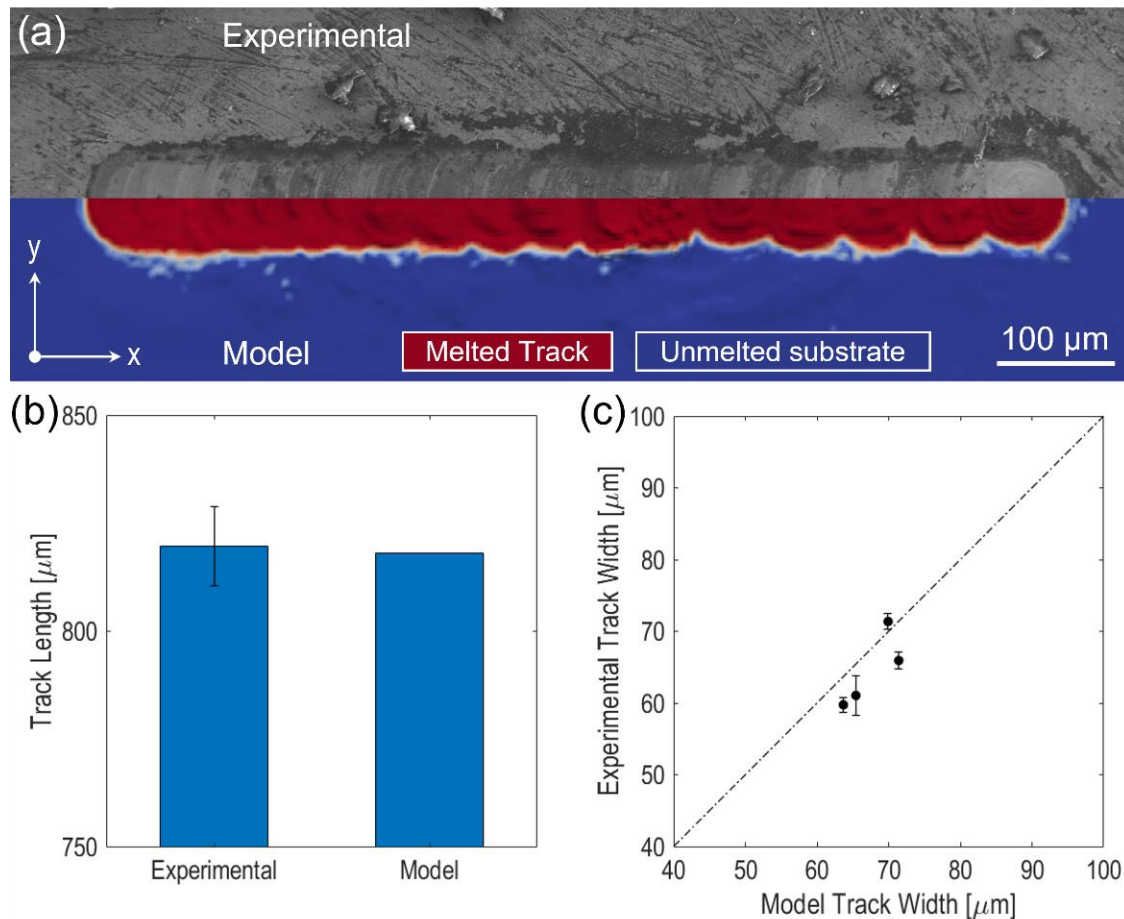
Figure 5.2: (a) plan view of the experimental PDV track (upper half – SEM/SE micrograph) and the output of the model (lower half). both tracks are presented with the same scale. (b) comparison of the experimentally and modelling determined track length. (c) the PDV track is characterized by four different laser regimes; therefore, the track width was measured at the centre of each point distance (*PD*) region for both the experimental and modelling case. Similar to the track length, excellent match was found between the computed PDV track and its experimental twin.

5.1.2 Temporal and spatial evolution of the local hot crack propensity

Hot cracking represents a problem regarding the liquid-to-solid transition experienced by the alloy. However, depending on the laser spatio-temporal law, a single volume of material may undergo several melting events. In order to correctly investigate hot crack formation, it is therefore crucial to consider the so-called vulnerable regions, namely volumes of material found in their last solidification event. The study of the appearance, size, and evolution of these areas as a function of time is presented in Figure 5.3(a). Within a single pulse, the presence of vulnerable regions is driven by the melt pool's fluctuations caused by the Marangoni flow and changes of recoil pressure given by the different incident angle of the rays during irradiation [265]. A steep increase of the vulnerable region's area A_{vuln} is detected between adjacent pulses for all the regimes investigated. This is the consequence of the movement of the laser focal axis from the prior location to the following one. In these time steps, A_{vuln} is found to generally be significantly smaller in PD15 and PD30 with respect to PD45 and PD60.

The development of a vulnerable region between the fourth and fifth pulse of each laser regime is magnified in Figure 5.3(b) to 5.3(e). The choice of this transition was because hot cracks were typically found in the fourth melt pool of the PD45 and PD60 regimes (Figure 5.1(b-c). All the investigated process parameters combinations showed maximum A_{vuln} in the first time step available after the end of the previous pulse. Nevertheless, the size of the vulnerable region reached for the first two investigated processing regimes was significantly lower than the second ones. In order to further investigate this behaviour, the time steps listed in Figure 5.3(b-e) of the middle vertical plane of the simulation are depicted in Figure 5.3(f-u) where the hot crack propensity,

defined as the local pressure drop at the interdendritic channel, has been qualitatively plotted on the vulnerable region. For each processing regime, the first of these chosen time steps (Figure 5.3(f,j,n,r)) is paired with minimal vulnerable region development. The second of these investigated timeframes (Figure 5.3(g,k,o,s)) is characterized by a vulnerable region with a similar morphology, which consists of the thin mushy zone region located at the back of the melt pool. Although the third time steps (Figure 5.3(h,l,p,t)) are characterized by a similar thickness of the vulnerable region (7 to 10 μm), some differences can be highlighted within the investigated processing conditions. The vulnerable region size increased with increasing point distances. In higher *PD* regimes, the laser focal axis is shifted a greater distance along the x-axis prior to the next pulse. As a result, during the delay time, a greater portion of the material will solidify at the back of the melt pool of the previous pulse and will not be subsequently remelted. Regardless of these morphological differences, the local hot crack propensity recorded in the vulnerable regions of the first three characteristic time steps can be considered similar. Therefore, it is reasonable to state that the chances to form cracks are similar in these timeframes. On the other hand, the fourth time steps analysed in Figure 5.3(i,m,q,u) show significant differences when the first and second two laser regimes are compared. The vulnerable region is found only in PD45 and PD60 and consists of a portion of the melt pool in Figure 5.3(p) and 5.3(t). Most importantly, the local hot crack propensity of these regions suffers a steep increase, recording the highest values within the investigated time steps of Figure 5.3(f-u). As a result, a higher chance to form hot cracks in the PD45 and PD60 regimes is well expected and in agreement with the experimental findings of Figure 5.1(a).
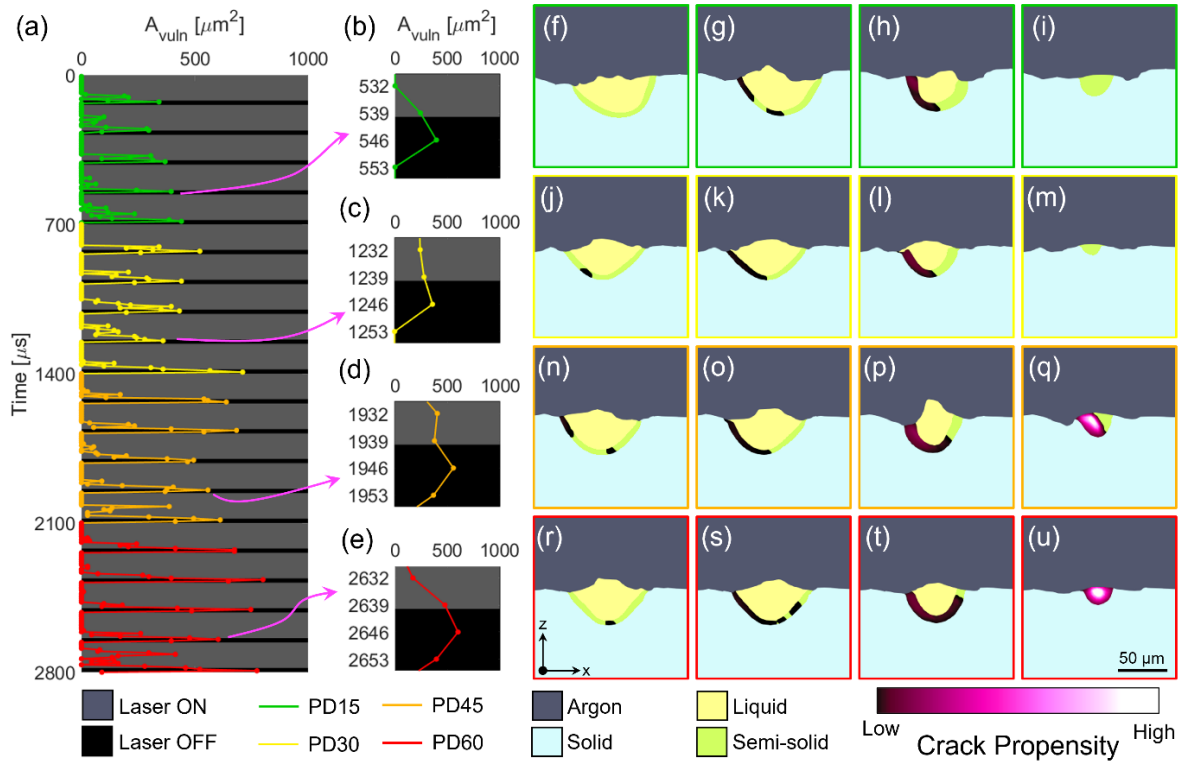
Figure 5.3: (a) area of the vulnerable region as a function of time. The grey areas indicate the time steps in which the laser irradiates the metal domain (laser ON), while the black stripes highlight the pauses in between two adjacent pulses (laser OFF). The four laser regimes investigated in the present work are highlighted in different colours: PD15 in green, PD30 in yellow, PD45 in orange and PD60 in red. (b-e) represent magnification of the time between the fourth and fifth pulse of PD15, PD30, PD45 and PD60, respectively. The vertical plane of the multi-physics simulation in the time steps highlighted in (b-e) is shown in (f-i) for the PD15 regime, in (j-m) for PD30, in (n-q) for PD45 and in (r-u) for PD60. Pastel colours have been used to highlight the solid (blue), the liquid (yellow) and the semi-solid (green). The regions of the mushy zone that become vulnerable are highlighted by the plot of the crack propensity.

The results of Figure 5.3 highlight the presence of a higher local hot crack propensity in the transition from one pulse to the next. It is now possible to collect all these values and plot them as a function of their x and z coordinates (Figure 5.4). Note that the core of each melt pool is characterized by a higher local hot crack propensity. It is therefore of interest to evaluate the trend of pressure drop as a function of the longitudinal axis of the track (Figure 5.4(b)). Peaks of Δp_{max} are found periodically in the laser direction with higher median and maximum values in the PD45 and PD60 regimes. In these segments, the positions of the Δp_{max} peaks correspond to the laser coordinate adopted to irradiate the

pulses. Additionally, the maximum recorded values of pressure drop were significantly above the critical pressure drop for hot crack initiation in aluminium which is given by Campbell as 176 MPa [266], in agreement with the observation of cracks in these segments (Figure 5.1(b-c)). It is important to note that in the PD30 regime the computation of the local Δp_{max} resulted in a value of 213.4 MPa found at a x coordinate of about 190 μm, but the presence of hot cracks was not detected in the PD30 segment of Figure 5.1(a).
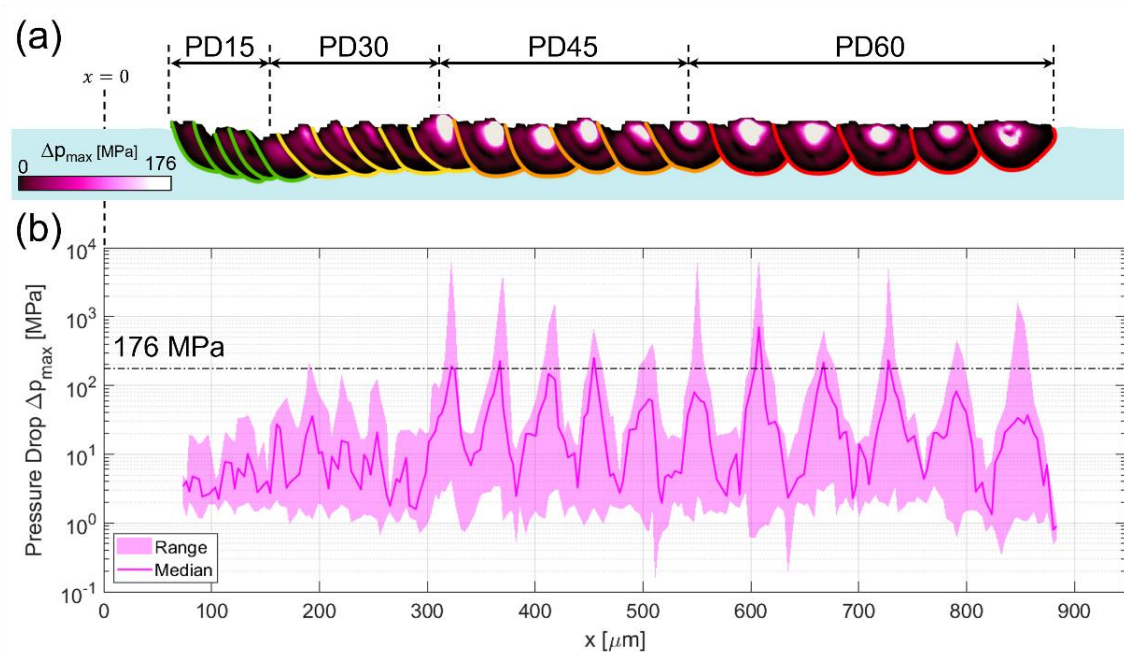
Figure 5.4: (a) spatial distribution of the local hot crack propensity of AA2024 within the PDV track. Melt pools corresponding to the four investigated processing regimes have been highlighted in green for PD15, yellow for PD30, orange for PD45 and red for PD60. Higher Δp_{max} values are detected in the core of the melt pools. (b) trend of Δp_{max} as a function of the longitudinal axis of the PDV track. The median has been chosen to highlight differences in distribution, while the range is given by the minimum and maximum pressure drop found at each x value.

5.1.3 <u>Microstructural and mechanical characterization of PBF-LB/M cubic samples</u>

Based on the combination of both experimental and modelling results presented in Sections 5.1.1 and 5.1.2, our approach was applied to PBF-LB/M parts. The hot cracking behaviour of AA2024 as a function of the four investigated processing regimes was explored by the production of cubic samples – details about the fabrication of these specimens are provided in Section 3.1.4.

Figures 5.5(a-d) depict BSE micrographs of a plane parallel to the building direction of samples AM-PD15, AM-PD30, AM-PD45 and AM-PD60, respectively. Apart from the AM-PD15 condition, the specimens showed the presence of macroscopic cracks aligned with the BD and spanning several layers (yellow arrows). As discussed in Section 4.2.4, these features represent cracks propagated in the solid state from hot cracks due to the combination of residual stresses and low fracture toughness K_{Ic}. To further support this argument, a closer look at the microstructure (Figures 5.5(e-h)) reveals the presence of hot cracks (purple arrows) only in PBF-LB/M regimes where the macroscopic features were found. The AM-PD15 sample was characterized by the presence of only residual gas porosity which led to optimal consolidation and a relative density of 99.84 ± 0.03 %.
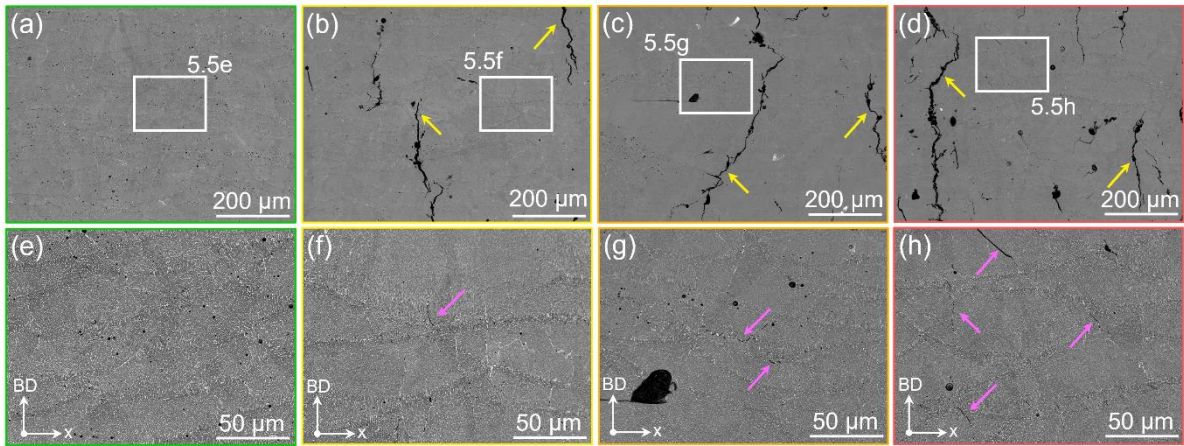
Figure 5.5: SEM/BSE micrographs of samples produced with the AM-PD15 (a,e), AM-PD30 (b,f), AM-PD45(c,g) and AM-PD60 (d,h) PBF-LB processing regimes. Long cracks spanning multiple layers (yellow arrows) were found only in the AM-PD30, AM-PD45 and AM-PD60 samples. These cracks represent features propagated in the solid state from hot cracks. The boxes in (a-d) are magnified in (e-h). Individual small cracks (marked with purple arrows) were found only in the samples produced with a point distance of 30, 45 and 60 μm. These might represent hot cracks which could be propagated in planes parallel to the cross-sections displayed in this figure.

In order to investigate the grain morphology development within the AM-PD regimes considered in the present section, EBSD analysis was conducted considering samples produced with the lower and higher scan speed. The EBSD maps a plane parallel to the building direction are presented in Figure 5.6(a) and 5.6(b) for the AM-PD15 and AM-PD60 samples, respectively. In both regimes, grains are seen to be elongated along the BD with their axis following the heat loss direction. The AM-PD15 seemed to grow with their main axis aligned towards the centre of the melt pool. On the other hand, the AM-PD60 conditions was paired with slightly longer grains which grew with their axis clearly aligned with the BD. Therefore, it seems that epitaxial growth is somewhat limited in the processing regime characterized by lower speed. Ellipse fitting was conducted for the grains of both conditions with the specific aim of investigating their aspect ratio (Figure 5.5(c)). AM-PD15 showed an aspect ratio of 1.8 ± 0.9, while AM-PD60 was characterized by an aspect ratio of 2.2 ± 0.9. Despite this minor difference, which results to be

statistically irrelevant, it can be concluded that both AM-PD15 and AM-PD60 are characterized, at least predominantly, by columnar grains. Therefore, it is thought that the observed difference in hot crack formation is not significantly influenced by grain size and morphology. The area of the microstructure in the vicinity of a hot crack tip found in the AM-PD60 sample was isolated and analysed with a combination of EBSD and BSE 3D reconstruction (Figure 5.5(d)). This hot crack was found to be oriented with its surfaces parallel to the BD and with a discontinuous path, as highlighted by the arrows. These discontinuities result, as illustrated in Section 4.1.6, from the presence of secondary phases between crack surfaces, a feature typical of AA2024 when processed by PBF-LB/M. Additionally, the 3D reconstruction of the grain structure indicates that hot cracks closely follow HAGBs, as also observed in Figure 5.1(d-e) for the laser track performed on the bare substrate. This clearly shows that the cracks found in the PDV experiment (Figure 5.1) and in the PBF-LB/M cubic samples (Figure 5.5(f-h)) originate from the same hot cracking mechanisms. Since the grain morphologies of the AM-PD samples produced may be considered similar, the change in cracking behaviour with processing regimes results to be caused by the different thermo-fluid behaviour caused by the distinct laser regimes.
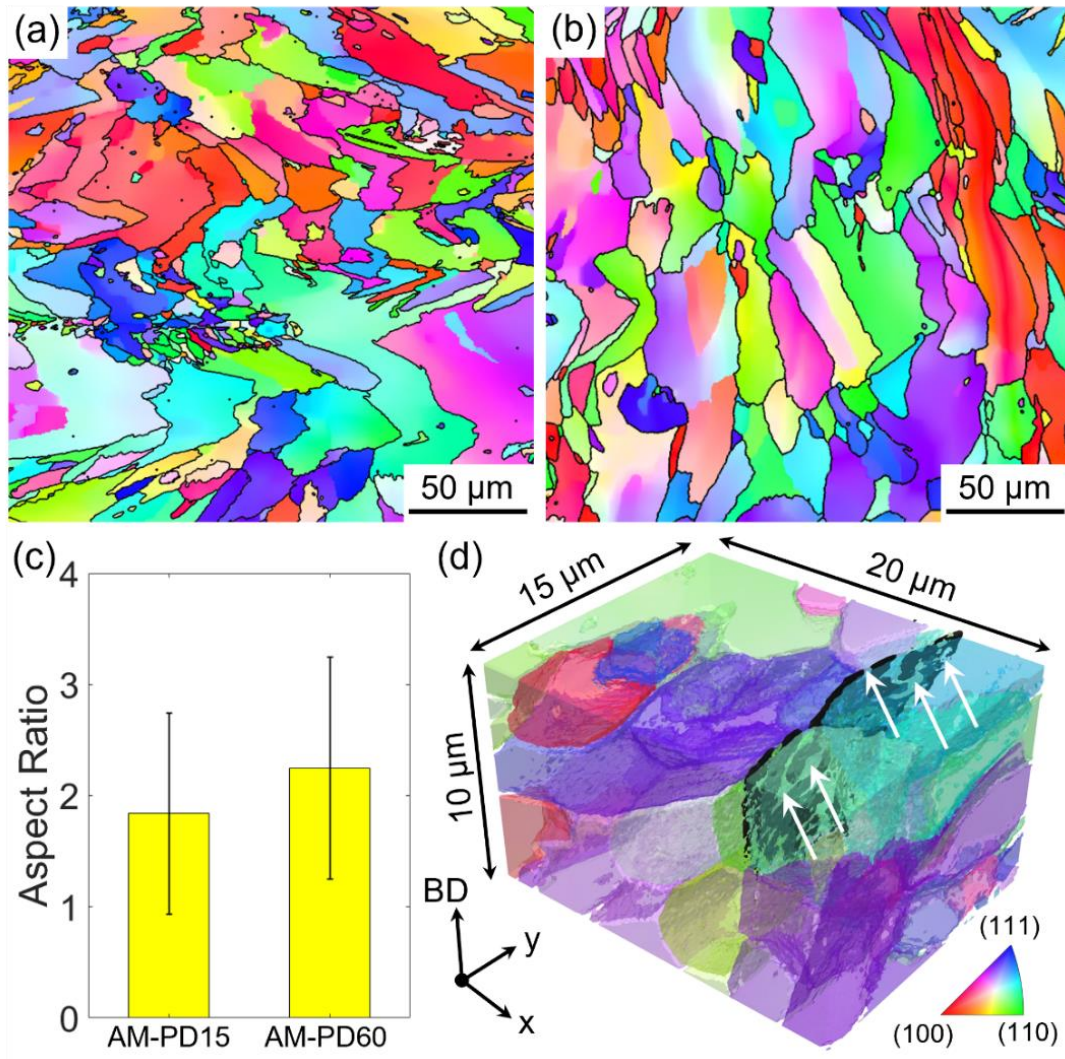
Figure 5.6: Inverse pole figure (IPF) maps of samples produced with the (a) AM-PD15 and (b) AM-PD60 processing conditions evaluated in a plane parallel to the building direction (BD) which is pointing upwards. The IPF colour key has been chosen so that the (100) direction is aligned with the BD. (c) bar chart depicting the aspect ratio of grains computed after ellipse fitting. (d) 3D EBSD/BSE grain reconstruction conducted at the tip of one of the non-propagated hot cracks found in the AM-PD60 sample. The hot crack tip is depicted in black while white arrows highlight the gaps found in its path.

The mechanical performances of samples produced with the AM-PD15 and AM-PD60 regimes were investigated printing a set of dog-bone samples which were subsequently tested in uniaxial tensile load conditions. The resulting engineering stress-strain curves of the AM-PD15 (in green) and AM-PD60 (in red) specimens are depicted in Figure 5.7. In total, five samples per processing conditions were tested. However, four of the AM-

PD60 specimens failed at minimal amount of applied load due to the extensive presence of cracks in the microstructure and therefore only one is presented in the graph. As expected, this was characterized by very poor mechanical performances which led in an extremely premature failure. Regarding the AM-PD15 specimens, curves of similar colour indicate replicate samples. These specimens were characterized by optimal tensile properties, showing a yield strength of 255.49 ± 3.35 MPa, an ultimate tensile strength of 375.85 ± 23.88 MPa and an elongation at failure of 6.33 ± 2.57 %. These properties are found to match those reported in previous investigations on AA2024 studying its tensile behaviour in the as-built PBF-LB/M condition [124–127].
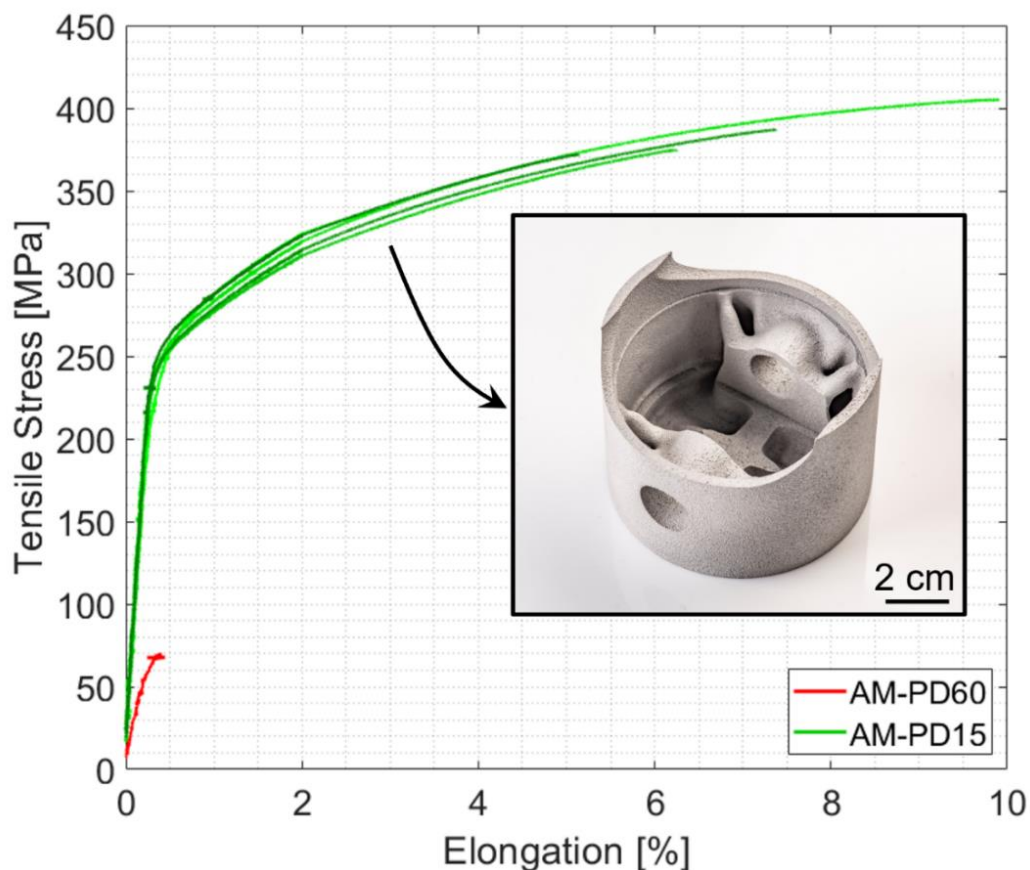
Figure 5.7: tensile curves of the samples built with the AM-PD15 (in green) and AM-PD60 (in red) processing conditions. In total, five samples per processing regime were tested. However, four of the AM-PD60 specimens failed at minimal amount of applied load due to the extensive presence of cracks in the

microstructure and therefore only one is presented in the graph. On the other hand, the AM-PD15 curves (similar colour indicate replicate samples) showed optimal strength and elongation at failure. This regime was used to fabricate a crack-free topologically optimized AA2024 piston (inset).

5.1.4 Increasing the PBF-LB/M build rate of AA2024

In order to minimise the formation of lack-of-fusion porosity, a modelling approach based on the Rosenthal solution [51] and prediction of melt pool geometries [49] (described in Section 2.2.1) has been used to predict the consolidation behaviour of AA2024 in a wide range of processing regimes (Section 3.1.3). The absorptivity has been implemented as a variable with respect to the laser power which, as shown in Section 4.1.1, highly influences the amount of energy absorbed by the powder during PBF-LB/M fabrication.

Figure 5.8(a) shows the relationship between the predicted melt pool size and the nominal values of layer thickness and hatch distance. It is widely known that to avoid the formation of lack-of-fusion it is necessary to satisfy the condition posed by Equation 2.2 [49]. Graphically, the various processing regimes are represented by distinct points in Figure 5.8(a), where points comprised within the area of the graph shaded in green are considered adequate regimes against the formation of lack-of-fusion defects. Figure 5.8(b-g) depicts optical micrographs of the typical microstructure of samples produced with 260W but different h_d and Δz. It can be observed that these specimens investigated have indeed minimal porosity (predominantly gas pores). Even more importantly, no cracks are visible. Similar results have been observed in all other processing regimes investigated in the present work. The graph in Figure 5.8(a) shows that the specimen depicted in Figure 5.8 (b) is extremely conservative and that the fusion zone created by newly deposited layers extend significantly in the prior layers as well as a large overlap between adjacent melt tracks exists. As all process parameters except layer thickness are

kept constant, it is assumed that the increase in layer thickness (from (b) to (c)) will cause a reduction in layer overlap along the build direction. Similarly, the increase in hatch distance (from (d) to (g)) will cause a reduction in transverse melt pool overlap. Nevertheless, as predicted and experimentally observed in Figure 5.8, these regimes result to be within an acceptable processing map paired with near-full dense defects-free parts.
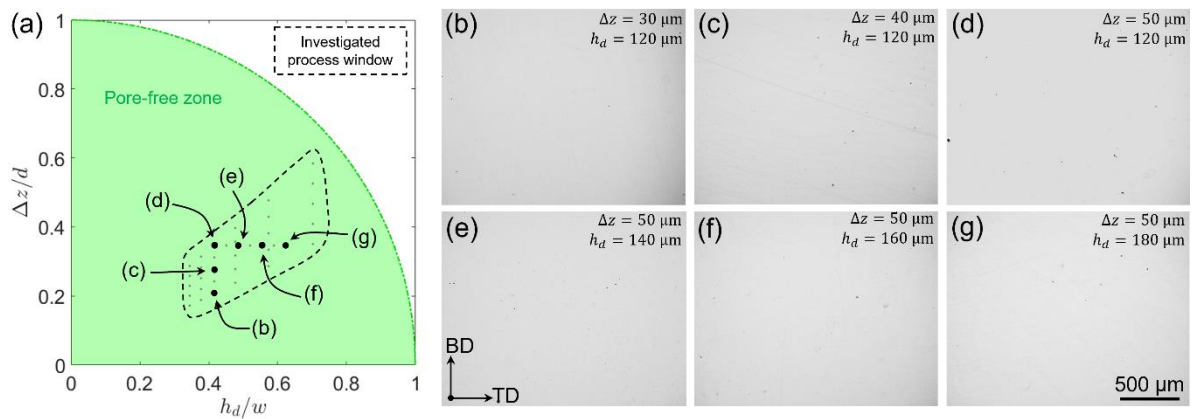
Figure 5.8: (a) Graphical prediction of processing regimes where lack-of-fusion defects are avoided. All the processing regimes investigated in the present work are expected to be characterised by optimal overlap in both the transverse (TD) and building direction (BD) resulting inn defects-free parts. (b-g) Optical micrographs of selected samples printed with a $P = 260W$ and a progressive increase of (b-d) layer thickness and (d-g) hatch distance.

The build rate $\dot{V}$ was calculated using the model proposed by Buchbinder et al. [36]:

$$\dot{V} = \Delta z \cdot h_d \cdot v \qquad\qquad\qquad \text{Equation 5.1}$$

Figure 5.9 is a contour plot that shows how build rate varies with respect to layer thickness and hatch spacing. It can be observed that, within the process parameters range here investigated, to achieve maximum build rate both the layer thickness and the hatch spacing need to be increased. It can also be noticed that the contour lines have a relatively

low gradient with respect to the h_d, that is build rate is predominantly influence by Δz. We therefore compare in detail three build regimes within the range of parameters investigated to establish a pathway to fabricate good quality AA2024 parts. These regimes are labelled in Figure 5.9 and correspond to Figure 5.8(b) (point A), 5.8(d) (point B) and 5.8(g) (point C). Point A, considered as reference specimen, represents the sample fabricated with a layer thickness of 30 μm which is the default Δz used to process "difficult-to-weld" materials [119,126]. This is then compared to point B, a material produced by increasing the layer thickness to 50 μm, leading to an increase in build rate of approx. 50%. Finally, we investigate an additional point in the processing map (point C), where the hatch spacing is increased from 120 to 180 μm to achieve a further 50% increment in build rate.
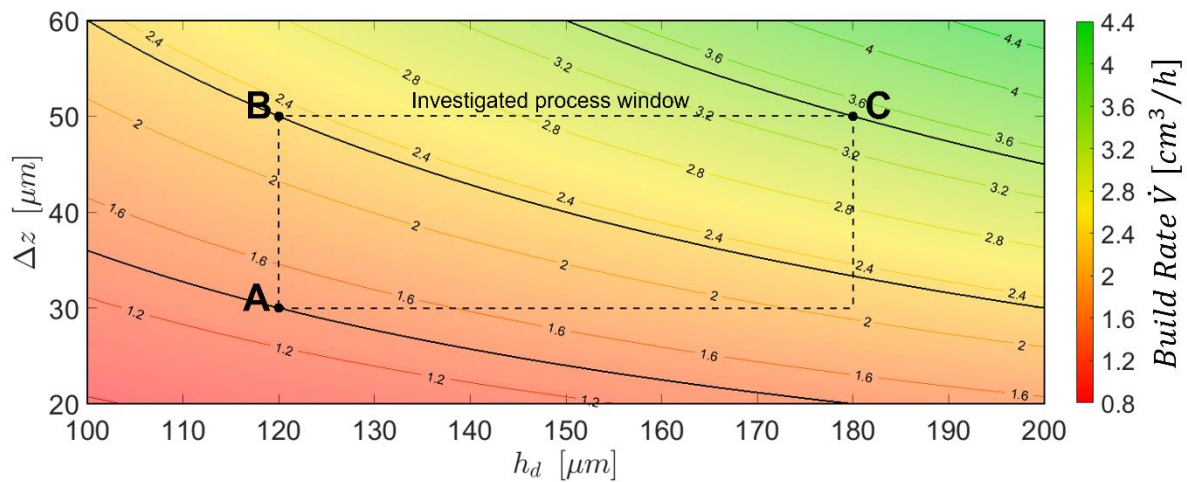
Figure 5.9: Contour plot of the build rate with respect to hatch distance and layer thickness. Within the processing window (dashed box), three regimes (A,B, and C) are considered to investigate the evolution of the microstructural features and hardness as a function of the build rate.

Figure 5.10(a-c) depicts a comparison of the experimental (left half) and predicted (right half) melt pool traces of samples A, B and C, respectively. As can be observed, the

computation of the melt pool traces with the adopted methodology finds great agreement with the experimental findings. The first striking difference in the microstructure of the specimens is a different prevalence of the fusion boundaries in the micrographs. Although these are projections of the melt pool traces in 2D planes, it is possible to observe that specimen A is characterised by a large number of melt pool boundaries, while these become progressively less obvious in specimen B and C. This is justified considering that at every laser pass, the laser creates a melt pool and a heat affected zone (delimited by fusion boundaries) where the solidification structure appears coarser, giving rise to the boundaries observed in the micrographs. The larger melt pool overlap in point A would cause an increase in the number of these features in the micrographs. The underlying Al-FCC grain structure also appears to be affected by the processing regime. It is observed that point A is characterised by grain predominantly elongated towards the build direction (Figure 5.10(a)). This appears less obvious in the point B and then C where stray grain morphologies also develop (Figure 5.10(c)).
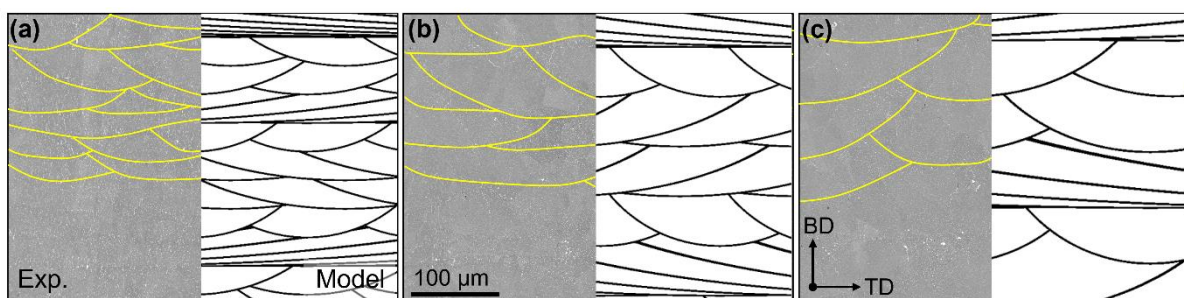
Figure 5.10: Melt pool overlap comparison between the experimental samples (BSE micrographs - left, fusion boundaries highlighted in yellow) and the predicted traces obtained by implementing the Rosenthal solution corrected by experimentally measured absorptivity values (right, in black). (a), (b) and (b) depicts specimens A, B and C, respectively.

Consistently to that reported Chapter 4, the phase constituents found in the specimens appear to be Al-FCC matrix (grey contrast in the micrographs) with Al_2Cu (θ-phase) and Al_3Mg_2 (β-phase) appearing at the grain and dendritic boundaries (bright contrast in the micrographs). Additionally, it is found that the typical solidification structure has similar size across the specimens investigated (Figure 5.11(a)). The values of hardness measured for the considered samples are reported in Figure 5.11(b). It can be observed that the hardness of the specimens is not significantly different. These values well agree with previous experimental findings reported in the literature for both PBF-LB/M processed specimens [123,267] and traditionally wrought products [26].
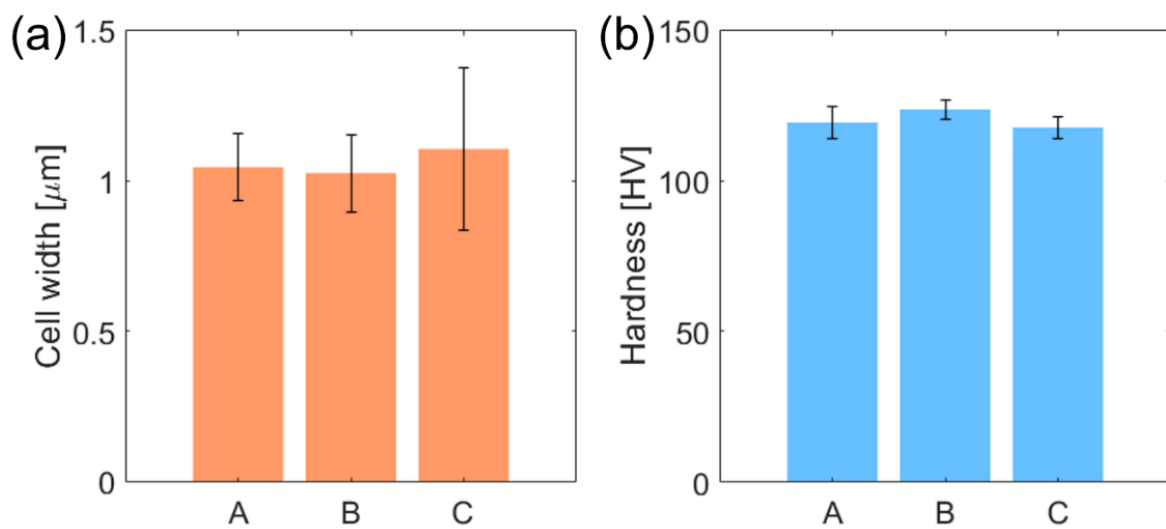
Figure 5.11: (a) cell width and (b) hardness values measured for specimens A, B and C.

5.2 Discussion

5.2.1 <u>Hot crack driving force in distinct laser regimes</u>

In this work hot cracking has been investigated combining experimental observations and modelling results. For the first time, hot cracking has been analysed by the direct computation of the intergranular depressions leading to hot crack formation. Moreover, this investigation has been conducted considering the thermal history developed in the vulnerable temporal range over which last solidification occurred. This analysis showed that distinct processing conditions are associated with different depressions. Following the RDG approach, these changes of local hot crack propensity should arise from distinct developments of critical dynamic thermal conditions, such as, cooling rate, thermal gradient, and strain rate. Considering the results displayed in Figure 5.3(f-u), for each laser regime the time step showing higher local hot crack propensity can be isolated and considered for further analysis. This is done with the specific aim of understanding the development of the relevant transient thermal conditions leading to the observed different cracking behaviour. The strain rate in the semi-solid can be approximated with:

$$\dot{\varepsilon} = \alpha \dot{T}$$

Equation 5.2

where α represents the coefficient of thermal expansion of the alloy [227]. Considering α as a constant, the strain rate is directly proportional to the cooling rate. Consequently, under the assumptions of this work, the local hot crack propensity is proportional to only the cooling rate and the thermal gradient via the expression:

$$\Delta p_{max} \propto \frac{\dot{T}}{G^2}$$

Equation 5.3

Figure 5.12 depicts the distribution of (a-d) cooling rate and (e-h) thermal gradient for the timeframes of each laser regime where the highest local hot crack propensity was found in Figure 5.3. A progressive increase of $\dot{T}$ was noted when a higher point distance is adopted for laser melting. Figure 5.12(i) depicts the median of the cooling rate found in Figure 5.12(a-d) with the error bars representing the minimum and maximum values recorded for each timeframe. The PD15 and PD30 regimes showed a significant variability of $\dot{T}$ characterized by relatively low median values. On the other hand, the vulnerable regions in PD45 and PD60 highlight a significant increase in cooling rate. Overall, due to the periodic heat source input, the measured values are significantly higher with respect to those typically associated with continuous-wave lasers [265]. The steep increase of cooling rate in PD45 and PD60 is the result of the different temperature evolution found in their most critical time steps. In these two regimes, the vulnerable region appears indeed in both time steps without exposure allowing the solidification of the inner part of the melt pool. This zone, apart from being in contact with the substrate acting as a heat sink [265], will transfer heat also from the metal-argon interface enabling the development of higher cooling rates in the vulnerable region. The evolution of the thermal gradient is shown in Figure 5.12(e-h). As opposed to the cooling rate, a progressive decrease of G is found moving from PD15 and PD60 (Figure 5.12(j)). The direction of the thermal gradient follows the heat transfer, pointing towards the middle of the solidifying area and corresponding to the direction of growth of the cells [268]. This correlates well with the morphology of the cracks found in the PD45 and PD60 regimes (Figure 5.1(b-c)). Given the progression of the cooling rate and thermal gradient, a corresponding increase of Δp_{max} and consequently local hot crack propensity is to be expected in laser regimes characterized by a point distance of 45 and 60 μm (Figure

5.12(k)). Overall, these results clearly demonstrate the profound influence of laser parameters on the melt pool dynamics, development of the vulnerable regions, and ultimately the local hot crack propensity of the material. Therefore, it is proposed that a correct control of the thermal gradients and cooling rates is crucial for the production of crack-free parts. Considering pulsed-wave systems as the one adopted in the present work, the laser speed can be altered considering not only different point distance values, but also various exposure and/or delay time. The approach proposed in this Chapter can be easily adapted to investigate the effects of these parameters on hot crack formation.

In addition to the discuss change of hot crack driving force via pressure depressions at the root of the interdendritic channel, a progressive increase of scan speed is known to be paired with a higher development of thermal stresses. Consequently, both the formation and propagation of hot cracks are phenomena that coupled together may result in an exponential worsening cracking behaviour limiting the production of defects-free microstructures.
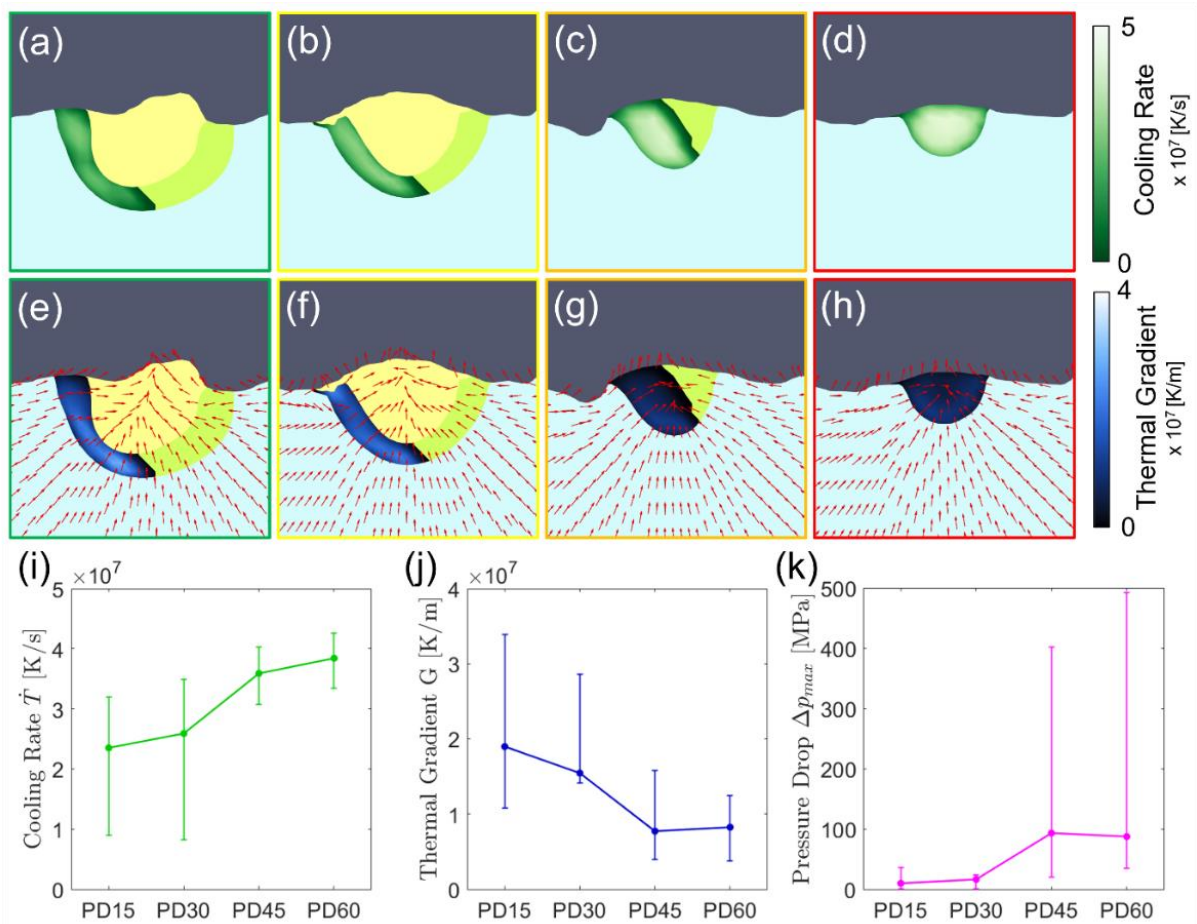
Figure 5.12: (a-d) distribution of cooling rate and (e-h) thermal gradient for the most critical time steps of Figure 5.3, namely 5.3(h) for PD15, 5.3(l) for PD30, 5.3(q) for PD45 and 5.3(u) for PD60. (a,e) refer to PD15, (b,f) to PD30, (c,g) to PD45 and (d,h) to PD60. The median, minimum and maximum values of (i) cooling rate, (j) thermal gradient and (k) pressure drop have been analysed to extract significant values associated to each one of the four investigated PBF-LB/M regimes.

5.2.2 Hot cracking stochastic nature and global hot crack propensity index

The hot cracking differences found within the *PD* laser regimes investigated in the presence work where ascribed to the development of distinct dynamic thermal signatures over the last solidification of a volume of material. However, in order to comprehensively discuss and quantify the hot crack propensity of an alloy not only considering its solidification path but also the processing conditions adopted for fabrication, a few microstructural characteristics need to be considered.

It is well established [42] that hot crack form upon solidification close to the root of the dendrites in the mushy zone, the region of the solidifying metal where liquid and solid coexist. However, rather than forming between two adjacent dendrites of the same grain, their paths typically develop along grain boundaries, especially those characterised by a great degree of misorientation as seen in the previous and present Chapters. Rappaz et al. [269] have elucidated the reason for this in terms of the surface energy differences between grain and dendrites boundaries. Considering two growing dendritic structures, the surface energy γ found at the interface can be described as a function of the liquid width h as:

$$\gamma(h) = 2\gamma_{sl} + \left(\gamma_{gb} - 2\gamma_{sl}\right) \exp\left(-\frac{h}{\delta}\right) \qquad \text{Equation 5.4}$$

where γ_{sl} is the interfacial energy associated with the solid/liquid interface, γ_{gb} represents the grain boundary energy and δ measures the interface thickness. Within a grain, γ_{gb} is equal to 0 as dendrites grow in a near-parallel fashion characterized by very low misorientation angle. Therefore, this condition is characterised by a lower energetical state which "attracts" the two dendrites, limiting hot crack formation. On the other hand, two dendritic features of distinct grains are paired with a greater surface energy which ultimately depends on the value of γ_{gb}. This grain boundary energy depends on the misorientation angle found between the two growing grains, HAGBs are thus characterized by great γ_{gb} values. In the event a very high misorientation between the grains is found, $\gamma_{gb} > 2\gamma_{sl}$ and the interface is considered to be "repulsive", favouring hot crack formation. Whilst the driving force for hot crack initiation is given by the combination of cooling rate $\dot{T}$ and thermal gradient G (as discussed Section 5.2.1), it appears that the formation of such features depends on the availability of HAGBs.

Therefore, the need to have both a favourable driving force and an available initiation site gives a stochastic character to hot crack formation.

In order to take this into account, and attribute to every processing regime a representative global hot crack propensity index, the presence of any pressure drop value $\Delta p_{max,i}$ needs to be considered along with its frequency f_i. Therefore, a global pressure drop Δp_{glob} is proposed to assess the hot crack propensity of a material under a specific laser processing regime, this is given by:

$$\Delta p_{glob} = \frac{\sum_i [f_i \Delta p_{max,i}]}{\sum_i f_i} \qquad\qquad \text{Equation 5.5}$$

Following Equation 5.5, pressure drops characterized by higher f_i will appear more frequently during fabrication and therefore are thought to be more representative of the hot crack propensity of a given material in specific processing regimes.

The evaluation of Δp_{glob} for the four laser regimes investigated in the present Chapter is depicted in Figure 5.13. A progressive increase of the global hot crack propensity in regimes characterised by a higher point distance can be observed. Moreover, similar high values of Δp_{glob} are found for the PD45 and PD60 regimes. Therefore, as experimentally observed in Figure 5.1(b-c), these processing conditions are expected to be paired with analogous hot cracking behaviour. On the other hand, the PD15 laser regime is characterised by a global hot crack propensity index which is less than half of the ones showing hot cracking presence. As a result, hot cracks are well expected to be limited during laser melting. The PD30 regime shows an intermediate value of Δp_{glob} and deserves some further considerations. It is noteworthy that while no cracks were found in the PD30 segment of the PDV track (Figure 5.1(a)), the printed samples that used AM-

PD30 displayed significant cracking. This regime appears to be a transition, with the local hot crack propensity analysis (Figure 5.4(b)) revealing the possibility to develop Δp_{max} values beyond the critical pressure drop for crack formation. Given the vastly high number of vulnerable regions that arise during the consolidation of a PBF-LB/M part, it is thought that statistically there is a higher change to develop critical values of Δp_{max} along HAGBs where hot cracks can be more easily initiate.
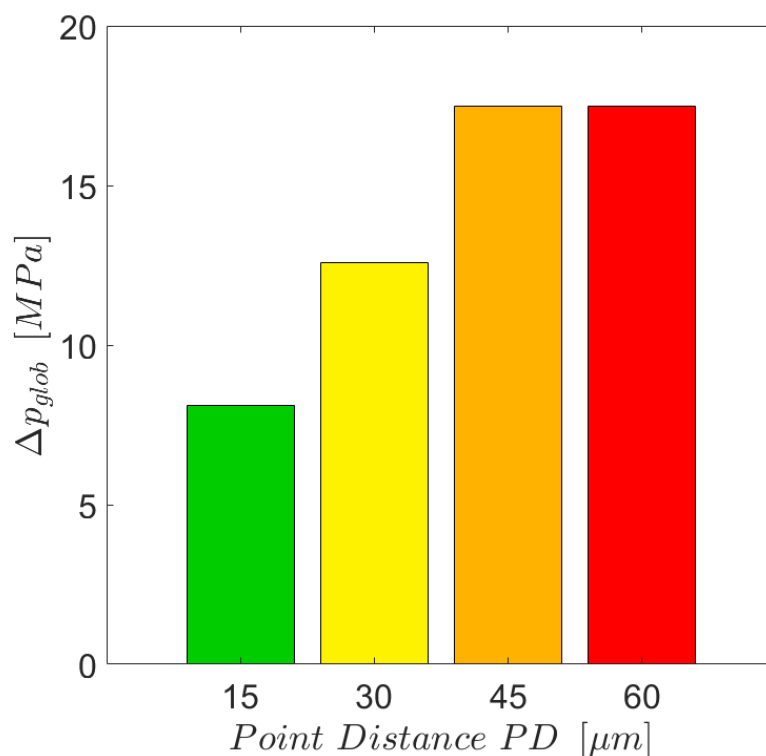
Figure 5.13: global hot crack propensity index Δp_{glob} of AA2024 under the four investigated processing regimes. This index is measured using a weighted average of the pressure drop values $\Delta p_{max,i}$ with respect to their frequency f_i. Thus, this parameter not only considers the driving force for hot crack formation, but also the spatio-temporal opportunity to form one.

Considering an equivalent speed for the pulsed laser, Δp_{glob} shows good agreement not only with our experimental results (Figure 5.1), but also with other studies that investigated the hot cracking behaviour of aluminium alloys [123,164,172,193,264]. The

global hot crack propensity index proposed in the present work thus represents a combination of both the driving force, and the spatio-temporal opportunity to form a hot crack during laser processing.

5.2.3 <u>A pathway to improve the build rate of crack-free high-strength Al-alloys produced by PBF-LB/M</u>

Section 5.1.4 shows a pathway for the production defect free high strength aluminium alloys. It is shown that thicker layers can increase throughput significantly, with no penalty to microstructure development or mechanical performance. This is valid when the melt pool can be described by the conduction mode melting and their stability does not vary with increased target penetration depth. This is the case when medium laser powders are used (in the range between 200 and 300W in the present investigation) and keyholing is largely avoided. This is reflected in the measured values of absorptivity (Figure 4.1) which show the plateau keyhole regime at powers greater than 300W (never exceeded in the present investigation).

It is noteworthy that no cracks are observed in any of the investigated samples. This is explained by the fact that the solidification dynamics which promote the formation hot crack are mainly influenced by the energy input (chiefly, the laser power and laser scan speed) and the platform temperature [88]. Since these process parameters are largely unchanged, the driving force for initiation of hot cracks is similar in all the investigated specimens and below the threshold for crack formation in AA2024. The findings clearly show that layer thickness and hatch spacing have minor influence in the formation of hot cracks, at least in the range of processing regimes investigated in this study.

It is expected that the use of thicker layers would invoke penalty in dimensional accuracy and surface finish due to coarser slicing and inevitable staircase effect [270]. This is subject of ongoing investigations. However, it is noted that most structural applications of AA2024 will require some post-processing machining steps and therefore at least a relative increase in surface finish this does not appear to be of crucial importance.

5.3 Summary

This Chapter focused on the identification and characterisation of processing window characterised by the absence of hot crack formation. In order to achieve this, a combined modelling and experimental approach was carried out to investigate hot cracking at a relevant spatial and temporal resolution. Specifically, a Point Distance Variation (PDV) scan track, characterised by four different laser regimes (PD15, PD30, PD45 and PD60), was experimentally and digitally performed to highlight regimes paired with lower hot crack driving force development. It was observed that:

- In the PDV experiment hot cracks were found only in the segments melted with the PD45 and PD60 laser regimes. Moreover, as observed in previous investigations (Chapter 4), their path accurately follows high-angle grain boundaries.

- The multi-physics simulation successfully predicted PDV track geometries such as track's length and widths in the different considered PD segments. Therefore, vulnerable regions (namely cells in their last solidification cycle) were isolated.

- In the temporal domain, vulnerable regions appeared in a larger extent in the time between two adjacent pulses. Moreover, the values of pressure drop (Δp_{max}) were found to be higher in the PD45 and PD60 regimes.

- In the spatial domain, peaks of Δp_{max} were found aligned with the laser x position of each pulse. Their values was significantly higher than the threshold for hot crack formation (176 MPa) and therefore hot cracking is well expected in segments melted with such laser regimes.

- The PD15 regime was characterised by minimal pressure drop development, whereas in the PD30 segment the pressure drop assumed values approaching that of hot crack formation in molten aluminium.

- Cubes samples were produced with same laser regimes investigated in the PDV experiment and hot cracks were found only in the samples produced with a point distance equal or higher than 30 μm.

- The microstructure of all the specimens was considered to be similar, with the development of columnar grains epitaxially growing aligned with the building direction.

- A hot crack found in the sample produced with the AM-PD60 PBF-LB/M regime was isolated and characterised via 3D-EBSD/BSE reconstruction. The hot crack initiation path was found to accurately follow the grain boundaries and as observed in Chapter 4 was characterized by micro-voids.

- The AM-PD15 PBF-LB/M regime was able to achieve optimal densification which resulted in great mechanical properties which matched those of previous investigations on AA2024.

- A strategy to increase the build rate of this low scan speed regime (AM-PD15) was proposed. This involved the use of a mixed experimental and modelling approach for the prediction of melt pools' overlap.

- It was found that an increase of hatch distance and layer thickness is able to improve the build rate of AA2024 of the 250% without introducing defects, such

as, pores and/or cracks. This was achieved without altering the microstructure and the hardness of the AA2024 which resulted to be comparable.

Chapter 6

6 Development of new custom Al-alloy ACN001 with optimized hot crack resistance and maximized strength

One of the main factors affecting the shape of the solidification path and therefore hot crack formation is represented by the alloy chemical composition. Although showing great strength and processability by hot working, standard alloys from the 2xxx, 6xxx and 7xxx series are not designed for the high cooling rates of the PBF-LB/M process, resulting in the severe observed hot cracking tendency when 3D printed. Therefore, it is reasonable to consider the design and development of bespoke compositions tailored for the thermal history of PBF-LB/M with the specific aim of preserving the great mechanical performances of standard heat-treatable materials but reducing the tendency to form hot crack upon printing.

In this Chapter a new custom Al-alloy tailored for the PBF-LB/M process is designed and characterized. Firstly, the base ternary composition is investigated using a tailored alloy design methodology which involves both computational and experimental approaches. The AlCu6 binary composition is chosen as starting point and several additions of nickel are considered. The solidification trajectory of bespoke compositions from the AlCu6-NiY pseudo binary system is computed using ThermoCalc and the CALPHAD method. Based on these curves, various indices are computed to predict the hot cracking behaviour of bespoke compositions. Additionally, performance indices capturing relevant strengthening mechanisms are computed with the specific aim of predicting the mechanical behaviour of the custom alloys. Based on these calculations, compositions that are thought to avoid hot crack formation and show considerable strength are experimentally investigated producing arc melted buttons which are subsequently laser surface melted to produce microstructures similar to the ones produced via PBF-LB/M. Based on this analysis, a base ternary composition is selected, and the role of impurities and allowable solutes' content is investigated. As a result, a custom alloy (ACN001) is identified, and gas atomized. The printability, microstructure and mechanical performances of the custom composition are then investigated to highlight the merits of the adopted design methodology.

6.1 Results

6.1.1 Computational alloy design methodology

The PBF-LB/M processability and mechanical behaviour of new custom Al compositions were evaluated directly from their composition using a series of indices based on established models. Specifically, the CALPHAD method was adopted to compute the solidification path of various alloys from the AlCu6-NiY pseudo binary system with Ni contents that varied from 0 to 9 wt% in increasements of 1 wt%. The solidification trajectories of these compositions were evaluated in ThermoCalc 2022b coupling the thermodynamic TCAL6 database with Scheil-Gulliver simulations. The AlCu6 binary system was selected because, despite showing poor processability by means of PBF-LB, it is able to develop upon cooling strong microstructures characterised by great heat-treatability [202]. Similarly to the analysis conducted on the AA2024+Ni system, nickel as selected for its capability of increasing the solidus temperature by the precipitation of Ni-rich phases at higher temperature with respect to the Al_2Cu phase [26,202].

The hot crack propensity is evaluated using multiple parameters, including the solidification range ΔT (computed by the difference between the liquidus and solidus temperatures of the Al-FCC matrix) and the hot crack susceptibility index HCS (Equation 2.11). However, due to the limits of these two parameters, a new hot cracking index is proposed. Following the RDG criterion [76] and considering constant values of semi-solid permeability, thermal gradient G, cooling rate $\dot{T}$ and strain rate $\dot{\varepsilon}$ over the solidification of a given alloy, the pressure drop at the root of the dendrite, considered as hot crack formation driving force, can be computed using the following expression:

$$\Delta p_{max} = \frac{180}{\lambda^2} \frac{\mu \dot{T}}{G^2} [(1 + \beta)\alpha I_A I_B + \beta I_C] = \frac{180}{\lambda^2} \frac{\mu \dot{T}}{G^2} I_{RDG} \qquad \text{Equation 6.1}$$

with

$$I_{RDG} = (1 + \beta)\alpha I_A I_B + \beta I_C \qquad \text{Equation 6.2}$$

Under these assumptions, the pressure drop Δp_{max} is directly proportional to the term I_{RDG}, which is a direct function of the solidification path (via the integrals I_A, I_B and I_C – Equations 3.29-3.31), the volumetric shrinkage β (assumed constant) and the coefficient of thermal expansion α. This parameter has been evaluated directly from the composition of the new alloys via the expression [45]:

$$\alpha = \left[1 + \sum_i \left(C_{wt,i} \cdot \delta_i^{CTE}\right)\right] \cdot \alpha_{Al} \qquad \text{Equation 6.3}$$

where $C_{wt,i}$ represent the weight percentage of each i-solute in the alloy and α_{Al} is the coefficient of thermal expansion (CTE) of pure aluminium ($23 \cdot 10^{-6} \ K^{-1}$ [45]). The term δ_i^{CTE} represent the specific change of CTE of each i-solute taken from [45]; alloying elements not reported here were assumed to have a δ_i^{CTE} value equal to 0. A reduction of I_{RDG} is paired with the decrease of Δp_{max} and therefore a reduced propensity of the alloy to form hot cracks. This newly proposed index, based on the RDG criterion with the further assumptions discussed in Chapter 5 of the present PhD thesis, can be computed in addition to the solidification range ΔT and the hot-crack-susceptibility HCS to increase the confidence and precision of the predictions.

The mechanical performances of the bespoke compositions are evaluated by the computation of strengthening indices. Solid solution strengthening represents one of the main strengthening mechanisms of the alloys manufactured by PBF-LB/M due to the

formation of a hyper-saturated FCC-Al matrix promoted by the fast cooling of the rapid solidification process. The increase of strength due to solid solution phenomena is given by [271]:

$$\Delta\sigma_{ss} = \sum_i \left(\frac{3.06}{700} G_{Al} \varepsilon_{ss,i}^{3/2} C_{at,i}^{1/2} \right) \qquad \text{Equation 6.4}$$

$$\varepsilon_{ss,i} = \left| \varepsilon'_{G,i} - 3\varepsilon_{b,i} \right| \qquad \text{Equation 6.5}$$

$$\varepsilon'_{G,i} = \frac{2\varepsilon_{G,i}}{2 + \left| \varepsilon_{G,i} \right|} \qquad \text{Equation 6.6}$$

$$\varepsilon_{G,i} = \frac{G_i - G_{Al}}{G_{Al}} \qquad \text{Equation 6.7}$$

$$\varepsilon_{b,i} = \frac{a_i - a_{Al}}{a_{Al}} \qquad \text{Equation 6.8}$$

In Equation 6.5 to 6.9, $\varepsilon_{ss,i}$ is the lattice strain induced by the i-th solute, G_{Al} and a_{Al} represent the shear modulus and lattice constant of the aluminium matrix, while $C_{at,i}$, G_i and a_i are the atomic concentration, shear modulus and lattice constant of each i-solute, respectively. In order to consider the detrimental effect of high-alloyed compositions on the density of the resulting alloys, the solid solution strengthening increment computed using Equation 6.5 has been subdivided by the density of the alloy ρ, computed using the expression:

$$\rho = \left[\sum_i \left(\frac{C_{wt,i}}{\rho_i} \right) \right]^{-1} \qquad \text{Equation 6.9}$$

where ρ_i represents the density of each i-solute. The ratio between $\Delta\sigma_{ss}$ and ρ represents the first parameter adopted to assess the mechanical behaviour of the investigated AlCu6NiY compositions.

Apart from solid solution strengthening, grain boundary strengthening represents one the major strengthening phenomena of PBF-LB/M materials. It is noteworthy that this mechanism obeys the Hall-Petch relationship [253]:

$$\Delta\sigma_{HP} = \frac{k_y}{\sqrt{D}}$$

Equation 6.10

where k_y is constant measuring the degree of pile-up behind an obstacle (i.e., a grain boundary) and D represents the size of the grains. Following Equation 6.11, fine grains are preferred to large ones because of the resulted increment of $\Delta\sigma_{HP}$. The refinement of grains has been extensively discussed in Section 2.4.1 of the present work, where it has been highlighted that alloys having a high growth restriction factor Q_{GRF} (Equation 2.13) are characterized by strong development of constitutional undercooling and therefore lower grain size. Therefore, Q_{GRF} can be used as a measure of the grain boundary strengthening increment of bespoke compositions.

In total, five different indices are therefore proposed. Three to predict the hot cracking behaviour of new alloys and two to assess their mechanical performances. These parameters can be computed for both the custom compositions investigated in the present Chapter and other alloys, such as, AA2024 and AA2024+Ni3, materials of known how cracking and mechanical behaviour which can be used as reference to set appropriate thresholds. Three design maps have been identified. The first two capture the hot cracking behaviour of the AlCu6NiY system and therefore AA2024+Ni3, the material investigated in the present work which showed better processability with respect to AA2024, was selected as reference material. The last design map sums the mechanical performances of the bespoke compositions and AA2024 has been selected as reference alloy because of its known mechanical performances.

The first design map (Figure 6.1(a)) depicts established hot cracking parameters, such as, the solidification range ΔT and the hot-crack-susceptibility HCS. Considering this design chart, low Ni compositions ($\leq$ 1 wt%) seems to be characterized by a hot crack propensity in between AA2024 and AA2024+Ni3. The other compositions satisfy the design criterion of this map, that is ΔT and HCS lower than the ones of AA2024+Ni3. Specifically, compositions with a Ni content greater than 3 wt% have stable and low values of ΔT and HCS and therefore it seems that these compositions are expected to be characterized by similar low hot crack propensity.

These observations are in fact confirmed by the second processability design map (Figure 6.1(b)) which depicts the values of the I_{RDG} derived from the RDG criterion as a function of the Ni content. However, the comparison results easier in this map as a single parameter is used to rank the various composition based on their intrinsic hot crack propensity. It is therefore concluded that AlCu6NiY alloys with a Ni content higher or equal to 2 wt% are expected to not form cracks during PBF-LB/M fabrication.

The third design map (Figure 6.1(c)) depicts the values of specific solid solution strengthening increment and Q_{GRF}. An increment of Ni is paired with an increase specific solid solution strengthening ($\Delta \sigma_{ss}/\rho$) and, as expected, an increment of growth restriction factor ensured by both the high content of Cu and Ni, two elements known to form great constitutional undercooling. Compositions characterized by a Ni content greater or equal to 6 wt% satisfy the design criteria of the present map.

In summary, these design maps inform that alloys with a Ni content greater or equal to 2 wt% are expected to not form cracks during PBF-LB/M fabrication. Additionally, compositions characterized by a Ni wt% greater of equal to 6 satisfy the design constrains and are expected to be characterized by better mechanical performances. In order to

prove these predictions, several arc-melted buttons were produced with different wt% of Ni to prove the efficiency of the present design strategy.
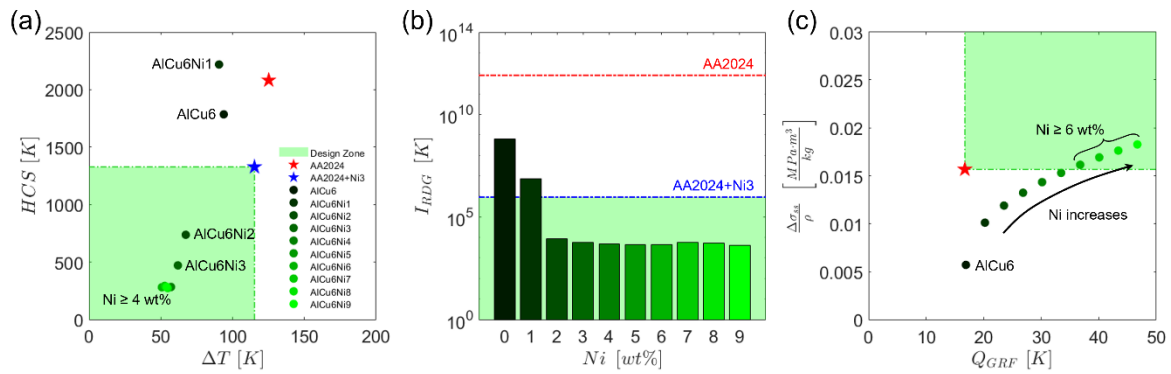
Figure 6.1: alloy design maps used for the evaluation of the hot cracking (a,b) and mechanical (c) behaviour of the bespoke compositions investigated in the present work.

Despite the proposed indices have been used in the discussed alloy design strategy, it is important to address their limits. The metrics adopted in the first two design maps have been computed based on the solidification trajectory evaluated adopting the CALPHAD approach paired with Scheil-Gulliver micro-segregation model and the TCAL6 thermodynamic database. Specifically, the solute trapping assumptions were neglected at this stage; this choice was conducted because the partitioning coefficient changes resulting from solutes being entrapped in the solidifying dendrites are ascribed only to the laser scan speed following Equation 4.2. Therefore, since this Chapter focuses specifically on the effects of alloy chemistry on hot cracking rather than those of the processing regime, the solute trapping assumptions were not considered. The solidification path experienced by a composition during solidification may diverge from the computed one due to several reasons, including back diffusion in the solid and variable dynamic conditions during cooling. Moreover, the indices adopted in the third

design maps were computed based on the nominal composition of the alloy. However, the solid solution strengthening is influenced only by the amounts of solutes trapped in solid solution in the as-built condition. Similarly, the growth restriction factor computed via Equation 2.13 represents an extension of the binary composition case to alloys containing more than one solute element.

6.1.2   The AlCu6NiY system: microstructural and mechanical characterization

In order to validate the alloy design methodology proposed in Section 6.1.1, the AlCu6NiY system was experimentally investigated producing several buttons with a fixed 6 wt% of Cu and various Ni contents between 3 and 9 wt% in steps of 1 wt%. These were subsequently surface melted to simulate temporal and spatial thermal fields similar to the ones experienced during PBF-LB/M fabrication.

Figure 6.2 shows representative micrographs of the buttons containing 3, 6 and 9 wt% of Ni in a plane parallel to the vertical direction z. No cracks were detected in both the arc melted and surface melted regions in all the samples investigated. Therefore, all the compositions experimentally investigated are found to match the predictions conducted in Section 6.1.1, satisfying the processability constrains. The lower magnification images (Figure 6.2(a,d,g)) show the melt pool boundaries, which are traced in yellow. These can be easily highlight due to the vastly different size of the substructures between the core of the buttons and their top surface which arises from the cooling rate difference between the arc melting and PBF-LB/M process. The melt pools appeared relatively shallow in all the buttons, indicating that they were surface melted predominantly in conduction mode.

Figures 6.2(b), 6.2(e) and 6.2(h) depict, at a higher magnification, the arc melted region of the -Ni3, -Ni6 and -Ni9 buttons, respectively. Despite formed using a different technique, these microstructures were still formed using a rapid solidification process and therefore provide insights on the secondary phases' precipitation sequence as a function of the Ni content. A quite complex microstructure composed by several different arrangements depending on the sample's composition is observed. The -Ni3 button (Figure 6.2(b)) is characterized by the presence of the FCC-Al matrix (which appears in grey) and two different morphologies of secondary phases (which appear with a brighter contrast due to increased mean atomic number). The prior secondary compounds' morphology is formed by lamellar structures which alternate with the FCC-Al matrix (solid arrow), while the latter assumes a more globular shape (dashed arrow). On the other hand, the -Ni6 (Figure 6.2(e)) and -Ni9 (Figure 6.2(h)) are characterized by different secondary phases' morphologies. The vast majority of the microstructure is formed by what appear to be primary two-phase dendrites of FCC-Al and secondary compound. These areas have been circled by yellow enclosures. At the periphery of these regions, globular secondary phases – highlighted by dashed arrows – appear. A closer look at these compounds reveals that their core has a different contrast than their outer skin. It is therefore proposed they are formed by two distinct phases which precipitate with this peculiar shell-and-core morphology.

Figures 6.2(c), 6.2(f) and 6.2(i) depict the region of the microstructure in the vicinity of the melt pool boundaries of the -Ni3, -Ni6 and -Ni9 buttons, respectively. At this magnification it is possible to appreciate the large substructures' size difference of the surface melted regions with respect to the arc melted cores. All the samples showed an extremely fine-scale cellular/dendritic solidification morphology which is typical of

various Al alloys produced by PBF-LB/M [110,119,128,172,233]. The aspect ratio of the cells varies drastically depending on the relative position with respect to the location within the melt pool (e.g., boundary or centreline). As also observed in AA2024, the cells appeared coarser in the proximity of the MP boundaries due to the partial remelting experienced in these areas. It appears that an increase of the Ni content promotes a reduction of the average cell width in the core of the melt pools, as can be qualitatively appreciated comparing Figure 6.2(c), 6.2(f) and 6.2(i). Intercellular/dendritic regions comprise secondary phases which are difficult to differentiate based on the BSE contrast due to their fine scale. Therefore, the surface melted region of the buttons containing 3, 6 and 9 wt% of Ni was further investigated via XRD analysis.
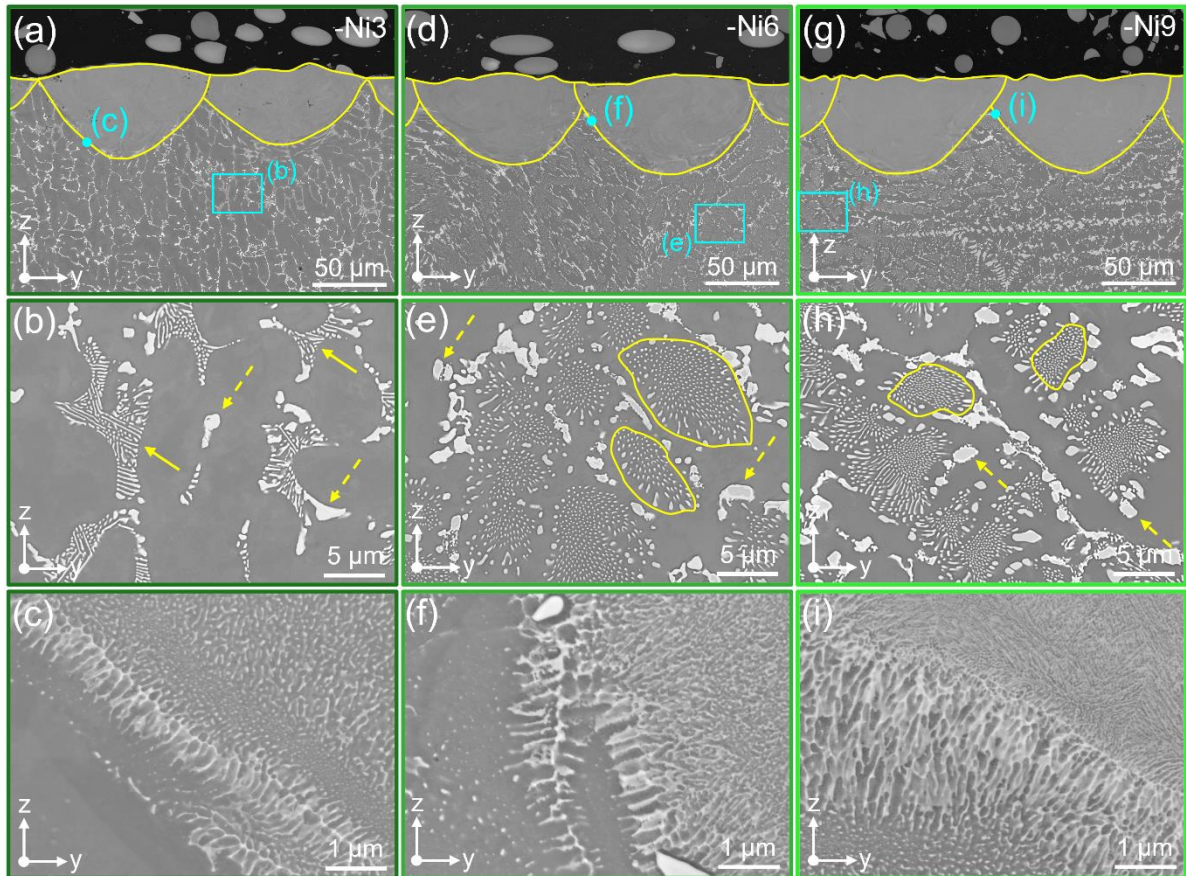
Figure 6.2: SEM/BSE micrographs in a plane parallel to the vertical direction z of (a-c) AlCu6Ni3, (d-f) AlCu6Ni6 and (g-i) AlCu6Ni9. The lower magnification micrographs (a,d,g) depict the region of the buttons which was surface melted with the melt pools indicated by yellow lines. Micrographs (b,e,h) are site specific insets of the microstructure found in the arc melted region while (c,f,i) depict the melt pool boundary of the -Ni3, -Ni6 and -Ni9 buttons, respectively.

Figure 6.3 depicts the XRD spectra of the surface melted region of the buttons containing 3, 6 and 9 wt% of Ni. All the samples showed the presence of a large number of peaks. Specifically, the peaks of the Al-FCC matrix are clearly distinguishable in all specimens. Additionally, several smaller peaks referred to the secondary compounds previously discussed are observed. The AlCu6Ni3 composition showed the presence of only the binary Al_3Ni_2 and the ternary Al_7Cu_4Ni phases. Similar phase identification was found also for the XRD spectra of the same samples collected in a cross-sectional plane parallel to the vertical z direction and consequently representative of the arc melted region. It is

therefore proposed that the dual morphology of secondary phases detected in Figure 6.2(b) arises from the precipitation of these two compounds. On the other hand, the -Ni6 and -Ni9 buttons showed far more complex patterns. Apart from the phases detected for the -Ni3 sample, the Al₃Ni was indexed in these greater Ni specimens. Thus, it is proposed that the three compounds' morphologies highlighted in Figures 6.2(e) and 6.2(h) are associated to these compounds.
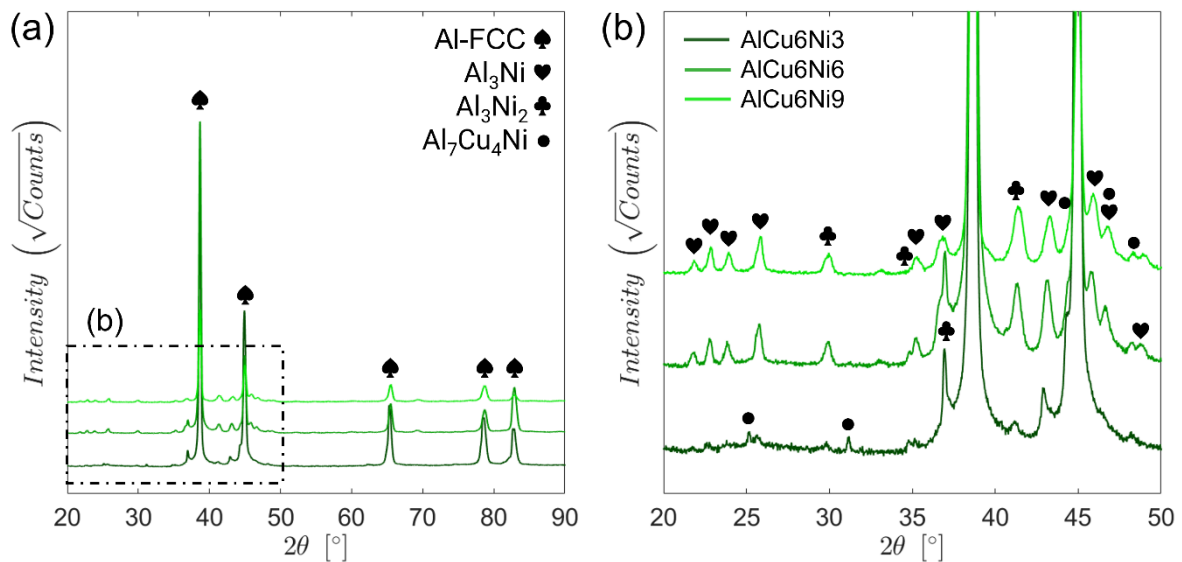
Figure 6.3: XRD spectra of the surface melted regions of the AlCu6Ni3, AlCu6Ni6 and AlCu6Ni9 buttons. The Al₃Ni₂ and Al₇Cu₄Ni phases were detected in all the investigated samples, but the Al₃Ni compounds was found only in the -Ni6 and -Ni9 specimens.

Once characterized the microstructural evolution of the AlCu6NiY system as a function of the Ni content, it is of interest to investigate its mechanical performances. Therefore, hardness measurements were conducted in these regions carefully positioning the indents in the core of the melt pools. The results of these measurements are presented in Figure 6.4. The HV values of all the buttons investigated in the present work are either equal or significantly higher than the reference alloy (AA2024) used as reference in the

previously discussed alloy design strategy. An increased Ni content in the AlCu6NiY system caused a progressive steady increase of hardness which assumed the highest values of 260.75 ± 12.81 HV for the -Ni9 button. It was observed that all the specimens were harder than AA2024 produced via PBF-LB/M. Additionally, compositions with a Ni content equal or higher than 5 wt% showed hardness values higher than the traditionally wrought AA2024 alloy in the T6 condition. As a consequence, all the samples predicted to have greater strength than AA2024 (namely compositions having a Ni content greater than 6 wt%, following Figure 6.1(c)) are experimentally found to show better hardness values and therefore satisfy both processability and mechanical performances constrains.

An increase of hardness is generally paired with a decrease of ductility and elongation at failure. In order to avoid this excessive fragility, the AlCu6Ni6 composition was chosen as base ternary for the development of the ACN001 composition.
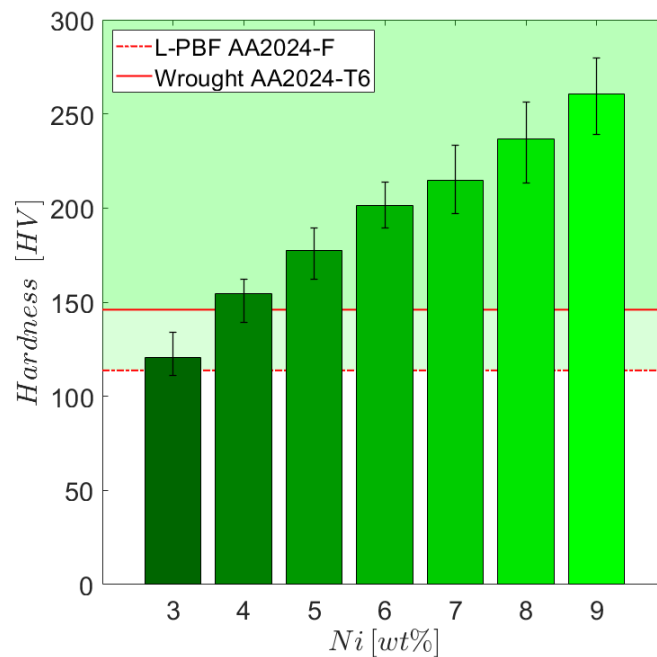
Figure 6.4: hardness values measured in the PBF-LB/M surface melted region of the ALCu6NiY buttons investigated in the present work. All the compositions are characterized by a higher toughness with respect

to AA2024 processed by PBF-LB/M (as-built condition, F). Compositions having a Ni content greater or equal than 4 wt% are additionally performing better than wrought AA2024 in the T6 temper designation.

6.1.3 Development of ACN001 custom composition

The combination of the computational alloy design methodology (Section 6.1.1) and the experimental work conducted on the AlCu6NiY pseudo binary system (Section 6.1.2) lead to identification of a base ternary – AlCu6Ni6 – which is expected to be characterized by a lower hot crack propensity and improved strength with respect to the considered reference alloys (AA2024+Ni3 and AA2024, respectively). However, in order to gas atomise the identified composition, further aspects need to be considered: (i) role of impurities (Fe and Si) and (ii) range of allowable solutes (Cu and Ni). The investigation of the design parameters' changes produced by the addition of impurities and variation of main solutes develops the designed AlCu6Ni6 base alloys identifying the definitive ACN001 composition.

Iron and silicon represent impurities always present in alloys made from commercially pure aluminium. The solid solubility of Fe in the FCC-Al matrix is extremely low at equilibrium (0.05 wt% [272]). Despite this threshold can be incremented in processes paired with high cooling rates [273], iron still forms detrimental intermetallics [274] which can alter the shape of the solidification path and lead to a potential deterioration of the hot crack resistance of the composition. These phenomena are also affected by the silicon content, as this element can introduce low temperature eutectic which enlarge the solidification range and may increase the intrinsic hot crack propensity of the alloy.

It is therefore of interest to study the effects of various concentrations of Fe and Si on the hot cracking and mechanical behaviour of the AlCu6Ni6 ternary system. Usually, these two impurities are given in the nominal composition with only the upper limit which is often the same for both elements (e.g., (Fe,Si) < 0.5 for AA2024 – Table 2.5). Therefore, various equal amounts of iron and silicon ranging from 0.05 wt% to 0.50 wt% in 0.05 wt% steps have been investigated to determine an ideal purity of the ACN001 alloy.

Figure 6.5 depicts the alloy development maps adopted to investigate the role of Fe and Si on the hot cracking and mechanical behaviour of the base AlCu6Ni6 composition. An increase of the content of both impurities produces a progressive increase of the hot cracking indices (HCS, ΔT and I_{RDG}) adopted in the present study (Figure 6.5(a,b)). Specifically, it seems that (Fe,Si) contents equal or higher than 0.35 wt% are expected to be characterized by a worse hot crack resistance than the reference alloy AA2024+Ni3. All the impurities compositions investigated are expected to improve the strength of the base AlCu6Ni6 (Figure 6.5(c)). Consequently, the maximum allowed amount of Fe and Si was chosen based on hot crack propensity reasons only. Although the immediate choice would be that of considering a level of impurities close to 0 wt%, these aluminium alloys are paired with production difficulties and extremely high costs. Therefore, following a discussion with ECKA Granules GmbH, a maximum amount of both Fe and Si equal to 0.10 wt% was selected.
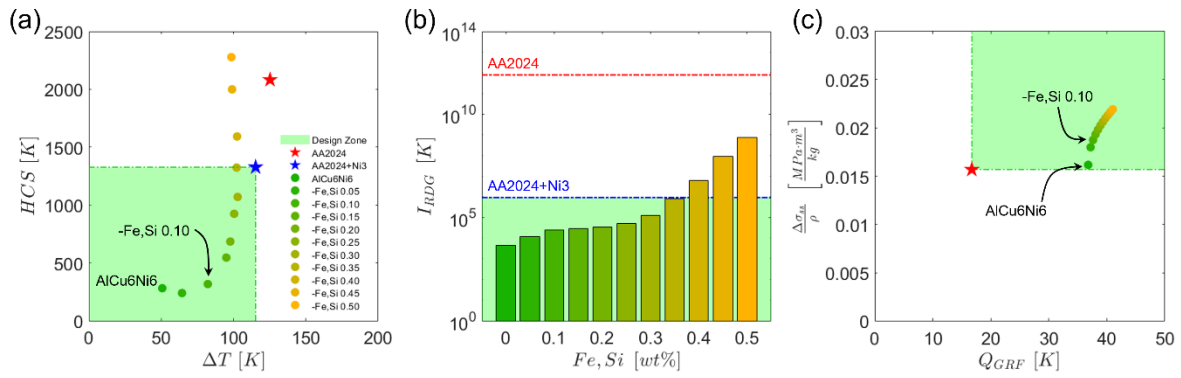
Figure 6.5: alloy development maps adopted for the investigation of the role of impurities on the hot cracking (a,b) and mechanical (c) behaviour of the AlCu6Ni6 ternary alloy identified through Section 6.1.1 and 6.1.2.

After discussing the role of impurities, the range of the allowable contents of the main Cu and Ni solutes needs to be investigated. Since (Fe,Si) amounts lower than 0.10 wt% are expected to improve the hot crack resistance of the alloy without altering much its strength (Figure 6.5), the content of Fe and Si was fixed to 0.10 wt%. Depending on the specific aluminium alloy, the range of each main solute may vary from a few decimal mass percentages up to 3 or 4 wt%. In the present work, in order to gas atomise a composition close to the designed base ternary, a range of 1 wt% was selected for both Cu and Ni. In total, 36 unique combinations of allowable Cu and Ni (ranging from 5.50 to 6.50 wt% in steps of 0.20 wt%) content were investigated.

Figure 6.6 depicts the outcome of this investigation. The hot cracking design indices were found to be near-constant in the whole considered solutes' ranges. The values of ΔT and HCS (Figure 6.6(a)) are indeed all located close to the nominal AlCu6Ni6(Fe,Si)0.1 composition and therefore, as also proved by the evaluation of the variability of I_{RDG} (Figure 6.6(b)), the hot crack resistance within the investigated ranges is expected to be similar. Additionally, since all the investigated compositions were found to fall in the

design zone of Figure 6.6(c), the selected ranges of Cu and Ni result to satisfy the design criteria adopted in the present study.

The investigation of the role of impurities and allowable main solutes conducted in the present Section permits to highlight the ACN001 composition (Table 3.5) which was gas atomised as discussed in Paragraph 3.6.
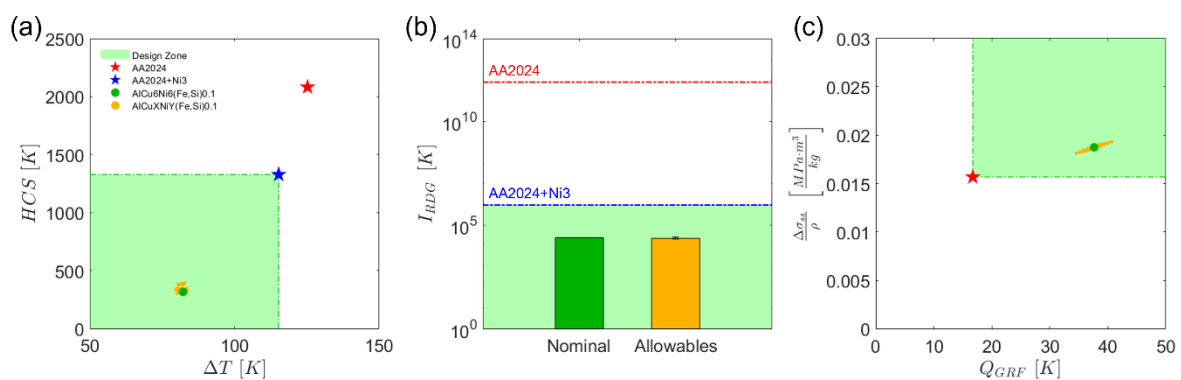
Figure 6.6: alloy development maps adopted for the investigation of the effects of the allowable Cu and Ni content on the hot cracking (a,b) and mechanical (c) behaviour of the AlCuXNiY(Fe,Si)0.1 system.

6.1.4 PBF-LB/M processing towards optimized relative density

In order to maximize the building rate of ACN001, PBF-LB/M regimes characterized by a relatively high scan speed (1.20 m/s) where investigated. This was achieved adopting a point distance of 60 μm, an exposure time of 30 μs and the default delay time of 20 μs. Under these conditions, the presence of lack of fusion porosity arising from not complete melt pools overlap is well expected unless the other available process parameters are correctly chosen. Therefore, multiple combinations of power and hatch distance were chosen with the specific aim of highlighting a processing regime leading to optimum relative density (Section 3.1.4).

Figure 6.7(a) depicts micrographs in a plane parallel to the building direction which corresponds to the specimens considered in the present analysis. No cracks or keyhole porosities were detected across the whole range of PBF-LB/M regimes investigated. However, varying the combination of P and h_d had a significant effect on porosity. The worse consolidation was found in the sample produced with the lower power (260 W) and higher hatch distance (120 μm), a greater magnification image of this specimen is presented in Figure 6.7(b). These low energy processing conditions led to the formation of large irregular pores which are typically formed in processing conditions dominated by lack-of-fusion porosity. In addition to LOF, the presence of relatively small gas pores characterized by a near-spherical shape and a diameter lower than 20 μm was detected. Processing regimes characterized by a progressively higher energy density, achieved by the reduction of h_d and the increase of P, were found to be beneficial in eradicating the presence of LOF. Specifically, within the investigated processing regimes, optimal consolidation was detected in the samples produced with the higher power (320 W) and lower hatch distance (80 μm). Figure 6.7(c) depicts a higher magnification of this regime, showing the presence of only gas pores. These results clearly indicate that the ACN001 composition designed in the present study results printable with optimal consolidation and absence of cracks.
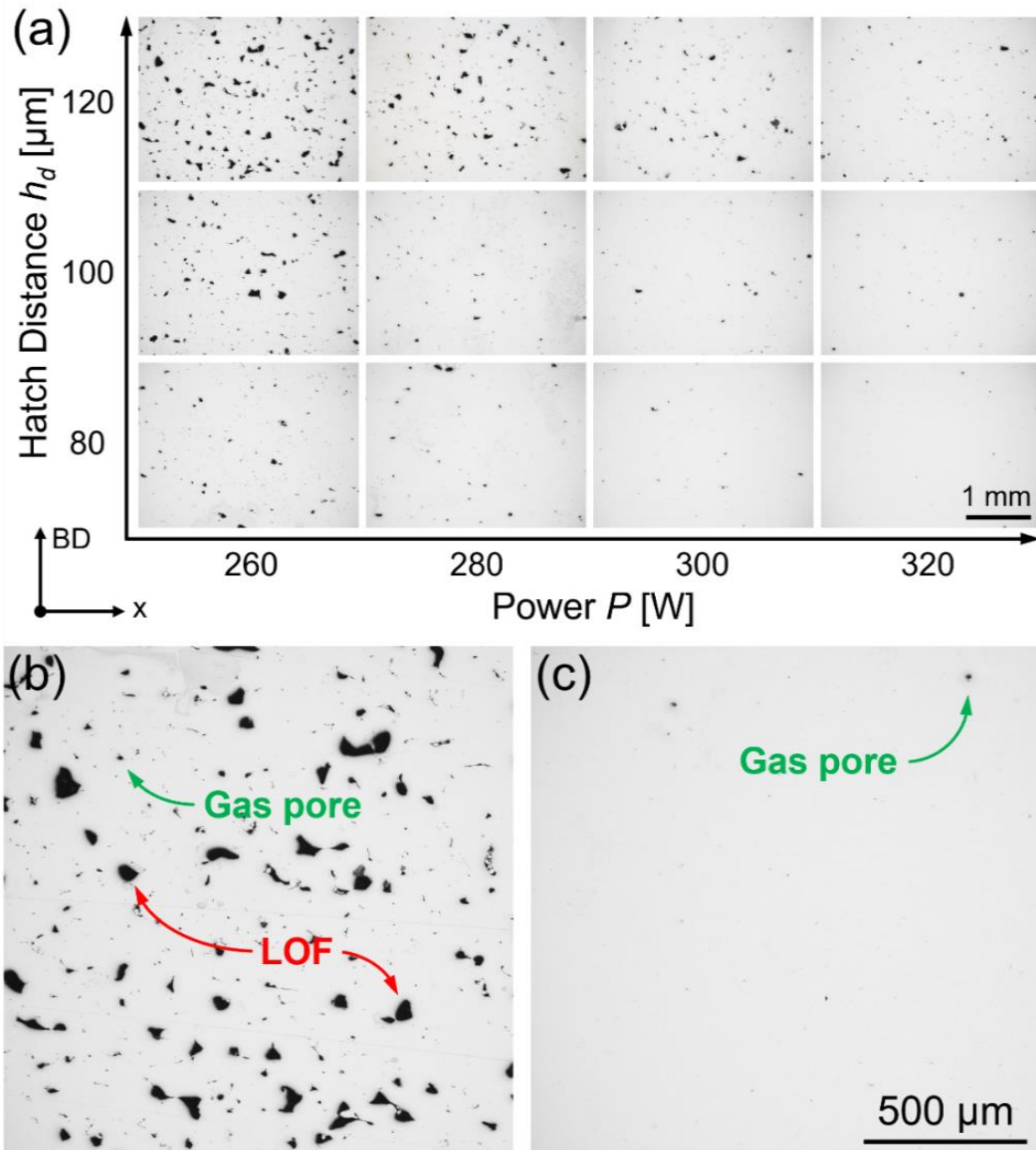
Figure 6.7: (a) Optical micrographs parallel to the BD of all the $P-h_d$ combinations experimentally investigated in the present analysis. (b) shows a typical microstructure of sample manufactured using a power of 260 W and a hatch distance of 120 μm depicting both LOF and gas pores. (c) 320 W and 80 μm showing the presence of only gas pores.

Adopting the image analysis methodology described in Paragraph 3.2, it was possible to classify and quantify defects evaluating the relative density of each specimen. Figure 6.8 depicts the results of this calculation. As expected, the sample produced with the lower energy density (260 W, 120 μm) was characterized by the larger amount of lack of fusion

pores (Figure 6.8(a)). Additionally, the trend of lack of fusion accurately follows the qualitative analysis previously conducted. Figure 6.8(b) depicts the quantified trend of gas porosity which was generally found to be sensibly lower than LOF due to the limited size of such defects. The sample produced with the higher energy density (320 W, 80 µm) was characterized by both lowest amount of both LOF and gas pores. Consequently, as depicted in Figure 6.8(c), showed the higher relative density (99.91%) calculated within the investigated processing window.
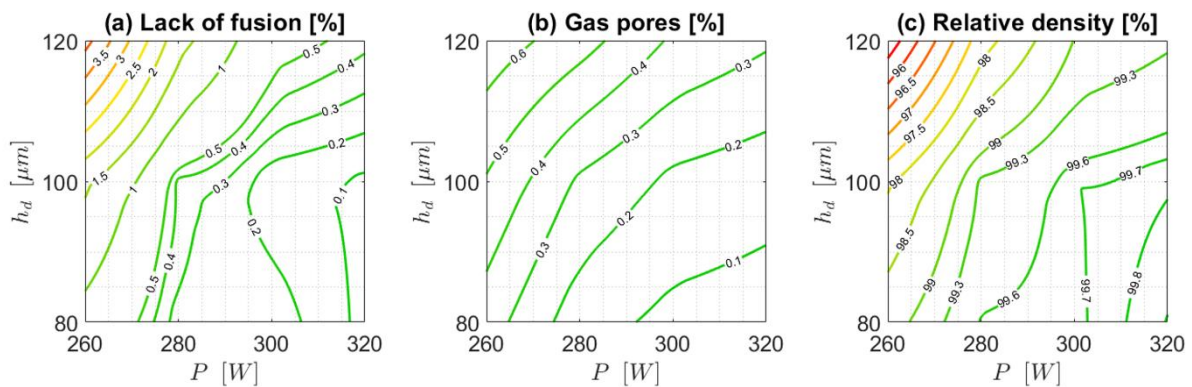
Figure 6.8: Contour plots showing the trend of (a) lack of fusion, (b) gas pores and (c) relative density of the specimen produced in the investigated processing window as a function of power P and hatch distance h_d.

This analysis proved that the ACN001 composition designed in the present work was characterized by an extremely high hot crack resistance which, in processing regimes suppressing macro-porosity formation, led to optimum consolidation and near fully dense samples. It is therefore of interest to characterize the microstructure and mechanical properties of ACN001 produced in the processing regime which ensured the highest relative density. This condition will be addressed as "as-built" in the following sections.

6.1.5 <u>Microstructural characterization</u>

XRD analysis was conducted with the aim of identifying the phases present in the as-built microstructure and in the as-received powder (Figure 6.9). Both samples showed the presence of a large number of peaks, as also detected in the buttons previously investigated. The peaks of the Al-FCC matrix are easily visible in both specimens with a relative intensity with respect to the {111} crystallographic plane which agrees with the ICDD data for pure aluminium. It is therefore proposed that both conditions are not characterized by texture development. Several smaller peaks referred to secondary compounds were also detected in the XRD spectra. In both samples the presence of Al_3Ni, Al_3Ni_2 and Al_7Cu_4Ni was indexed. However, a few peaks of the powder sample were not associated to any particular phase. As also detected in AA2024, the peaks indexed in the powder sample were characterized by lower intensities, but no significant XRD peaks' broadening was detected. It seems that the precipitation of this compound is somehow limited during PBF-LB/M fabrication. The presence of the detected phases well agrees with the preliminary investigations conducted on the arc melted buttons during the design of the ACN001 composition. It is now of interest to image the microstructure with the specific aim of understanding the arrangement of these phases and the solidification and grain morphology associated with the as-built condition.
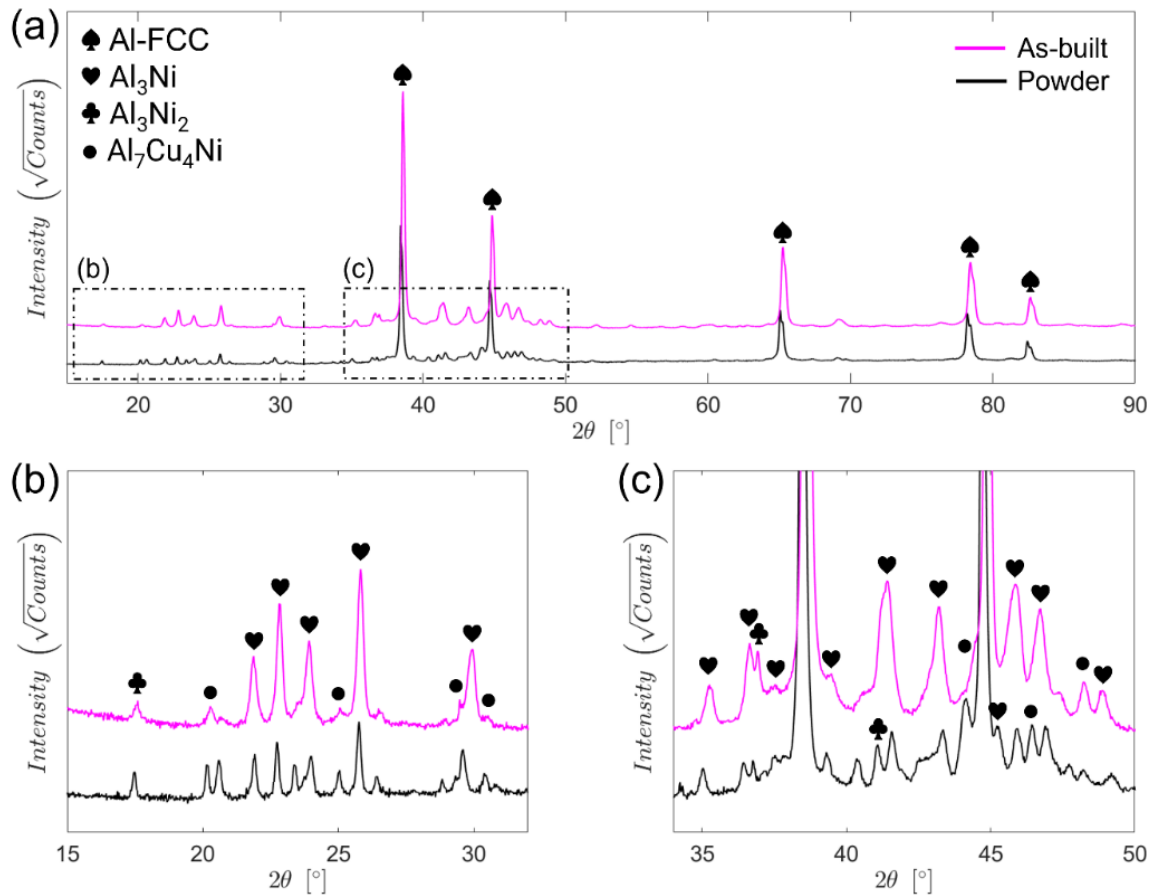
Figure 6.9: XRD spectra for the powder and as-built sample produced with the optimized PBF-LB/M regime identified in Section 6.1.4.

Figure 6.10 represents SEM/BSE micrographs of the microstructure on a plane parallel to the building direction of the as-built sample. Figure 6.10(a) shows the melt pool boundaries traced in yellow. These were found to be relatively shallow, confirming that the samples were melted in either the conduction or transition melting modes. This observation well agrees with the trends of porosity investigated in the previous section. This sample was indeed found to not be characterized by the presence of LOF or keyholes. The analysis of the BSE contrast provides preliminary insights onto the grain arrangement present in the microstructure, which seems to be characterized by a dual morphology. Small columnar grains growing from the MP boundaries towards the centre of the melt pool are found to dominate. On the other hand, it seems that an equiaxed grain

morphology dominates at the periphery of the melt pools. However, further investigations are needed to fully characterize the grain morphology of the as-built condition. Figure 6.10(b) represents a higher magnification of the microstructure in the vicinity of a MP boundary depicted in Figure 6.10(a). The substructure appeared to be characterized by an extremely fine-scale cellular/dendritic solidification morphology which, despite being typical of a variety of Al alloys produced by PBF-LB/M [110,119,128,172,233], seems to be paired with a significantly lower average cell width. Based on cell size and morphology, three different zones are identified in this region: a high cooling rate zone (HCRZ), a low cooling rate zone (LCRZ) and a heat affected zone (HAZ). During PBF-LB/M melting, the melt pool boundary (traced by the solid line in Figure 6.10(b)) is identified by the T_{sol} isotherm surface. In close proximity to this region, the previously melted material experienced an in-situ heat treatment during the laser ON time characterized by temperatures slightly lower than T_{sol}. This affected the size of the cellular dendritic features, identifying the HAZ zone. On the other side of the MP boundary, the material experienced temperature fields falling within the solidification range of the alloy. Therefore, with respect to inner areas of the melt pool, during solidification these areas will be cooled from a relatively lower T. As a result, lower cooling rates will develop in these regions with respect to the core of the melt pool, identifying the LCRZ and HCRZ zones [234], easily distinguishable due to the different average cell width (λ). This microstructural parameter was measured considering 10 adjacent cells in both the low cooling rate and high cooling rate zone. The former was characterized by an average cell width of 323 ± 95 nm, which is significantly higher than the λ measured in the HCRZ (132 ± 33 nm).
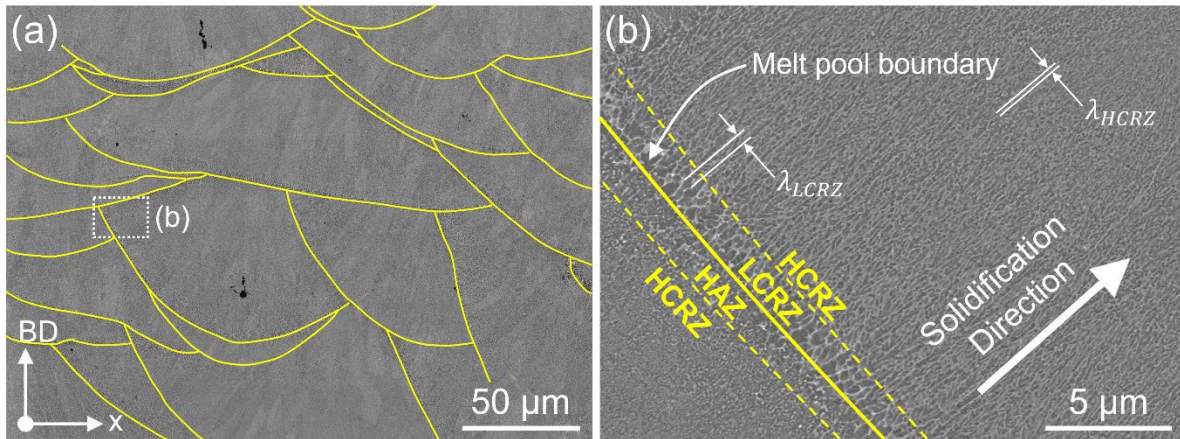
Figure 6.10: SEM/BSE images of the sample produced with the optimized PBF-LB/M regime in the plane parallel to the BD. (a) The melt pool boundaries are highlighted by yellow solid lines. (b) is a site-specific detail of (a) depicting the microstructure in the vicinity of the melt pool boundary.

6.1.6 Mechanical behaviour

The mechanical performances of ACN001 were investigated printing a set of dog-bone samples which were subsequently tested under uniaxial tensile load. The resulting engineering stress-strain curves are presented in Figure 6.13 in which each tested sample is depicted in a different shade of green. The samples were found to be characterized by consistent tensile curves and behaved in a relatively brittle fashion, with an elongation at failure EF of 2.77 $\pm$ 0.11 %. However, it seems that the plastic regime is characterised by the present of significant work-hardening. The observed limited ductility was paired with extremely high tensile strengths with respect to both standard wrought alloys. The yield YS and ultimate tensile strength UTS showed indeed exceptional values of 368.27 $\pm$ 21.48 MPa and 602.04 $\pm$ 7.36 MPa, respectively. These values well satisfy the design constrains considered in the design stage of the composition as the Y and UTS well exceed the ones of AA2024 manufactured by PBF-LB/M presented in Chapter 5. These results support the merits of the adopted alloy design methodology and prove that crack-free high-strength Al-alloy can be designed without the use of grain refiners.
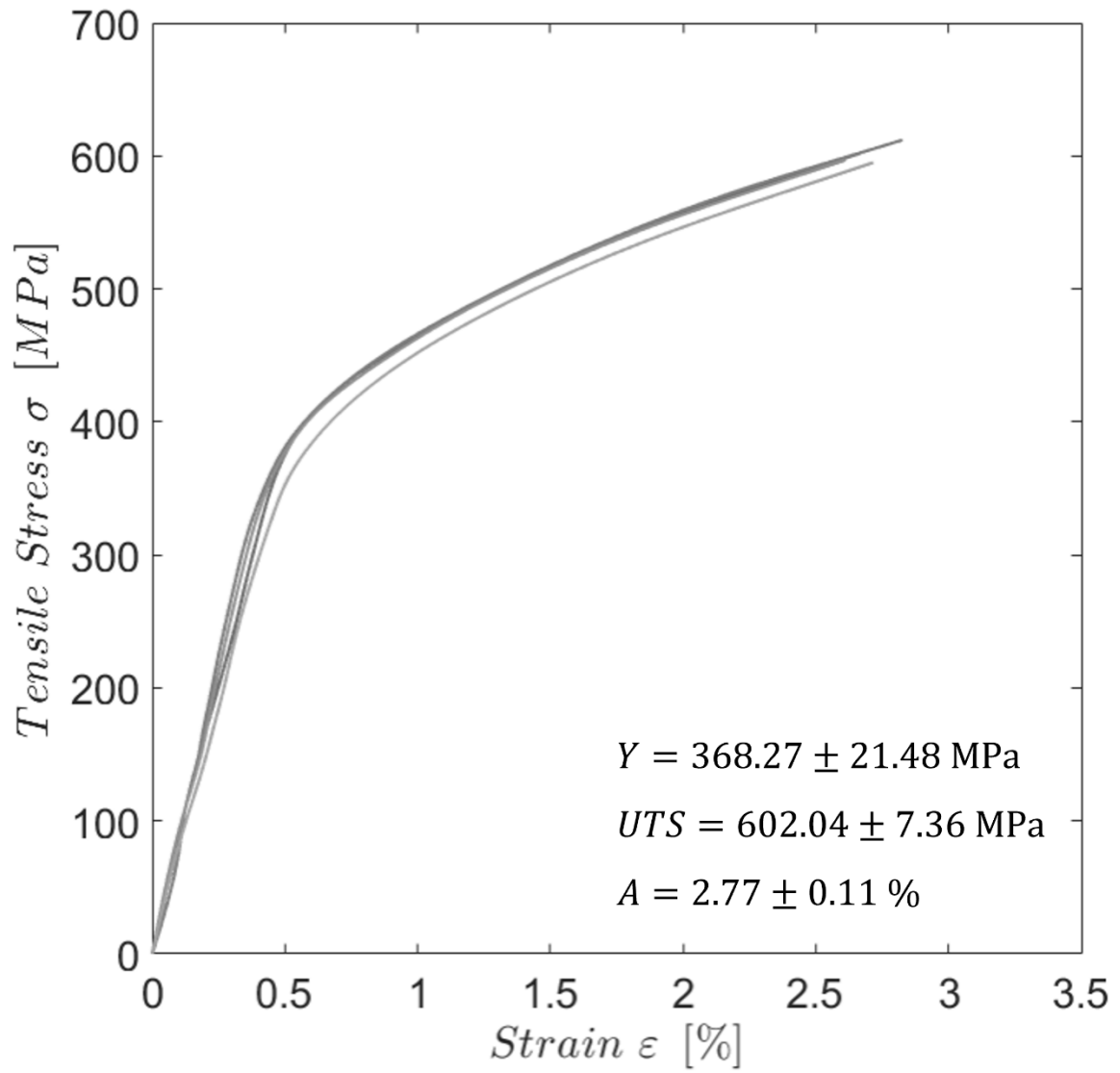
Figure 6.11: engineering tensile stress-strain curves showing the tensile behaviour of ACN001 in the as-built condition.

6.2 Discussion

6.2.1 <u>Solidification behaviour of bespoke alloys: a parallelism between computational and experimental results</u>

The hot cracking behaviour of the compositions considered in the present Chapter was predicted using a computational approach based on the CALPHAD method and subsequently investigated by the conduction of targeted experiments. The correct calculation of the design indices adopted to inform the identification of crack-resistant alloys highly depends on the accurate evaluation of their solidification path. Despite the shape of this trajectory is partially affected by the thermal history experienced by the material during solidification, the scope of this study was to assess the effects of the composition on the hot crack propensity within the AlCu6NiY pseudo binary system. Therefore, in contrast to what's been done for AA2024, solute trapping has not been considered and the CALPHAD simulations were conducted using the un-modified Scheil-Gulliver model [84].

Figure 6.14(a) depicts the solidification path of the buttons experimentally investigated in Section 6.1.2. Different line-types have been used to distinguish the various Ni content while different colours have been adopted to highlight the multi-phases regions computed for each composition during solidification. Regarding the -Ni3 composition, the calculation predicts that the first phase to precipitate is the Al-FCC matrix, followed by Al_3Ni_2 and lastly by Al_7Cu_4Ni. On the other hand, the -Ni6 and -Ni9 solidification paths show the additional precipitation of Al_3Ni. In addition to the Al-FCC matrix, the XRD analysis (Figure 6.3) was able to detect all the secondary phases predicted over the alloys' liquid-to-solid transition via the Scheil-Gulliver equation [84]. Therefore, the computed

solidification paths are considered to be representative of the precipitation and solidification history experienced by the various investigated compositions within the AlCu6NiY pseudo binary system.

Of particular interest is the precipitation sequence with respect to the Al-Cu-Ni phase diagram. Figure 6.14(b) depicts the liquidus projection of this ternary system computed in Thermo-Calc with the relevant multi-phase regions/lines highlighted using different colours. Each region corresponds to a liquidus surface, namely the surface over which the first primary phase solid particle nucleates. This surface is generally presented with isothermal lines to highlight the temperature evolution. However, this has been avoided since the temperature evolution of the computed compositions can be followed on the solidification path. Each line represents a univariant curve (also called cotectic or eutectic valleys) where the liquid and two different compounds are found at the same time. The pseudo binary AlCu6NiY system consists of the dash-dotted white line plotted in Figure 6.14(b). It is possible to observe that the -Ni3 and -Ni6 are hypo-cotectic compositions while -Ni9 is hyper-cotectic with respect to the $L+FCC+Al_3Ni$ eutectic valley. The composition of the liquid has been plotted in this chart to inform the evolution of its solutes' enrichment and consequent precipitation of secondary phases as a result of this micro-segregation (Figure 6.14(b)). The mass fraction of the precipitated compounds is plotted in Figure 6.14(c) to 6.14(e) as a function of the fraction of solid. At the start of the solidification, the liquid concentration of Cu and Ni is that of the nominal composition. As the cooling progresses, the -Ni3 composition does not meet the cotectic curve where liquid, Al-FCC and Al_3Ni coexist, directly intersecting the $L+FCC+Al_3Ni_2$ eutectic valley. This results in the absence of Al_3Ni and the late precipitation of Al_3Ni_2 and Al_7Cu_4Ni, as can be seen in Figure 6.14(d) and 6.14(e), respectively. It is therefore thought that the

lamellar and globular morphologies depicted in Figure 6.2(b) arise from the liquid's enrichment and solidification along the $L+FCC+Al_3Ni_2$ and $L+FCC+Al_7Cu_4Ni$ cotectics, respectively. Differently from the -Ni3 sample, the first eutectic valley encountered by the -Ni6 and -Ni9 compositions is the $L+FCC+Al_3Ni$ cotectic. The precipitation of the Al-FCC matrix and the nickel tri-aluminide takes places at a relatively early stage of the solidification (Figure 6.14(c)) as a result of the nominal compositions being close to the $L+FCC+Al_3Ni$ eutectic valley. In these conditions, the nucleation of two phase cotectic dendrites is expected [275], as depicted in Figure 6.2(e) and 6.2(h). As solidification progresses, the -Ni6 and -Ni9 compositions solidify along the $L+FCC+Al_3Ni_2$ and $L+FCC+Al_7Cu_4Ni$ cotectics. As a result, the remaining liquid will solidify in $FCC+Al_3Ni_2$ and subsequently in $FCC+Al_7Cu_4Ni$. It is thought that the shell-and-core structures observed in Figures 6.2(e) and 6.2(h) arise from the subsequent precipitation of these two compounds towards the end of the solidification.

This analysis demonstrates the potential of a coupled computational and experimental approach in investigating the solidification dynamics and microstructures arisen from rapidly solidified compositions. A note of care needs to be considered to discuss the solidification morphology of the laser melted regions of the AlCu6NiY compositions and the PBF-LB/M microstructure of ACN001. Although it was not possible to clearly distinguish the secondary phases' morphology, the fine scale of the microstructure requires analysis that go beyond the scope of the present characterization. Therefore, this investigation represents one of the main points of focus discussed in Chapter 8.
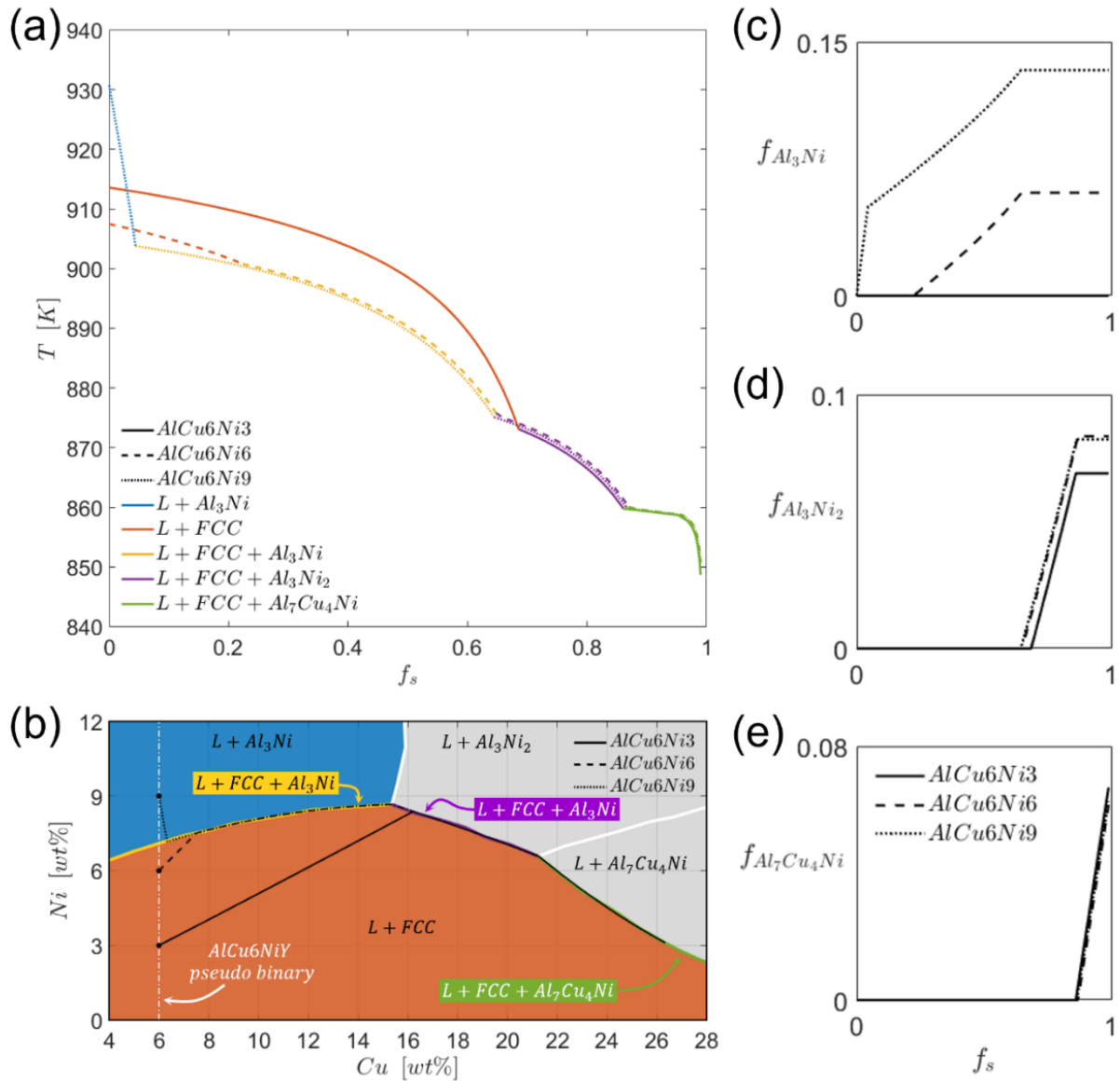
Figure 6.12: Computational investigation of the AlCu6NiY pseudo binary system. (a) solidification paths of AlCu6Ni3, AlCu6Ni6 and AlCu6Ni9 buttons. (b) liquidus projection of the Al-Cu-Ni ternary phase diagram. Weight fraction evolution of (c) Al3Ni, (d) Al3Ni2 and (e) Al7Cu4Ni with respect to the molar fraction of solid f_s. In all these panels solid lines represent -Ni3, dashed lines -Ni6 and dotted lines -Ni9.

The study of the precipitation behaviour of arc melted buttons represented a key step to understand the solidification dynamics of the base ternary chosen for the constitution of the ACN001. Nevertheless, due to the slightly different amounts of the main solutes and the additional presence of Fe and Si impurities, the solidification trajectory of ACN001 needs to be carefully investigated. Figure 6.15 depicts the solidification path of the

designed alloy computed in Thermo-Calc following the composition listed in Table 3.6. The solidification sequence of ACN001 results to be similar to the one of the AlCu6Ni6 button as their nominal composition is the same. However, the iron impurity alters the computed precipitation sequence. After the Al-FCC matrix, Al_3Ni is the first secondary phase that precipitates, followed by Al_9FeNi, Al_3Ni_2, $Al_{13}Fe_4$, Al_7Cu_2Fe and then Al_7Cu_4Ni. The mass fraction of these compounds is plotted in Figure 6.15(b) as a function of the solid molar fraction. It is possible to observe that the compounds containing iron are characterized by mass fractions which are nearly two orders of magnitudes lower than the ones of the Al-Ni and/or Al-Cu-Ni phases. Apart from the Al-FCC phase, the XRD analysis conducted on both the powder and as-built samples detected the presence of only the compounds that are computed in larger amount (Al_3Ni, Al_3Ni_2 and Al_7Cu_4Ni). The Fe-phases are therefore either suppressed by the fast cooling experienced during both gas atomization and PBF-LB/M fabrication or their presence is too limited to be detected by means of XRD measurements.

Although it is not possible to clarify the presence of the Fe-rich compounds, the solidification path computed via the Scheil-Gulliver model finds great match with the detected secondary phases. Therefore, it is thought that solidification trajectory depicted in Figure 6.13(a) represents a good approximation of the fraction of solid evolution during PBF-LB/M fabrication.
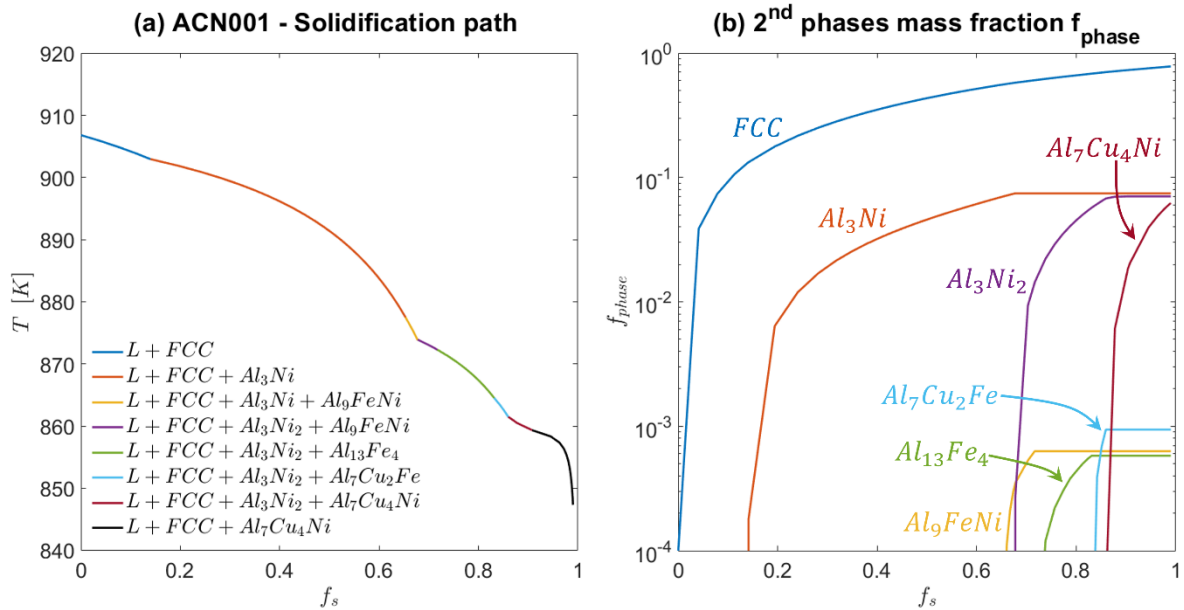
Figure 6.13: computational investigation of the ACN001 composition. (a) solidification path of the ACN001 alloy computed using Scheil-Gulliver assumptions. (b) mass fraction of the precipitating secondary phases as a function of the molar solid fraction. The compounds containing Fe do not alter drastically the shape of the solidification path and are present in limited amount at the end of solidification ($f_s = 1$).

6.2.2   A composition-driven approach to predict the intrinsic hot crack propensity of alloys during solidification

In the past decades, many parameters have been adopted to rationalise an alloy's intrinsic hot crack propensity, namely its relative fundamental inclination to promote hot crack formation during equal solidification thermal conditions. These indices include weldability parameters, the solidification range ΔT and the hot-crack-susceptibility HCS proposed by Kou [78,79]. These metrics have shown to be effective in ranking the intrinsic hot crack propensity of materials characterized by extremely different compositions and solidification paths (e.g., 6xxx series alloys are more prone to form hot cracks with respect to 2xxx series materials). However, the literature provides examples of alloys that, despite being characterized by similar ΔT and HCS values, show significant differences in hot cracking tendency [233,262]. These discrepancies arise from a few

relevant material-dependent phenomena which are not captured in the evaluation of these parameters.

During the liquid-to-solid transition, the volumetric shrinkage β represents one of the main factors increasing the hot crack formation driving force. Moreover, the coefficient of thermal expansion α directly affects the development of strain rate during solidification. These two phenomena, being exclusively material dependent, influence the intrinsic hot crack propensity of the alloy. In this work, a material dependent metric based on the RDG criterion [76] (I_{RDG}) has been proposed as an improved index to drive the prediction of the hot cracking behaviour as a function of the alloy's chemical composition. The effects of the changes of volumetric shrinkage and the coefficient of thermal expansion on the intrinsic hot crack propensity are straightforward to identify following Equation 6.2. Materials characterized by both lower β and α are indeed paired with limited development of pressure drops due to solid-to-liquid shrinkage and the solid's deformation, respectively [76]. Despite being considered as a constant in the present work, the inclusion of β represents an important step towards and hot cracking index able to compare not only Al-based alloys, but any material suffering from such detrimental defects (e.g., HEAs and Ni-based materials). On the other hand, the coefficient of thermal expansion α is actively affected by the composition of the alloy. Among the main engineering elements, Al is characterized by one of the highest thermal expansion coefficients [26] which consequently results in great strain rate developments. Despite the additions of nickel and copper to aluminium investigated in the present Chapter promote the reduction of α, the specific decrease promoted by Ni results to be 4.5 times greater than that of Cu. Between these two solutes, nickel is characterised by an enhanced

limitation of α which results in lower values of I_{RDG} and therefore a limited hot crack propensity.

Another relevant material phenomenon not captured by both the HCS and ΔT parameters is represented by intergranular liquid feeding. Alloys characterized by optimized volumetric flow are indeed able to backfill the intergranular space healing an opening hot crack. Despite this phenomenon has been largely discussed over the past decades, the hot cracking indices available in the literature do not address this issue. In order to isolate the role of liquid feeding, the $T - \sqrt{f_s}$ curves of two "artificial" alloys (named A and B) characterized by equal HCS and ΔT have been considered (Figure 6.16(a)). These two materials are characterised by equal solidification range and their solidification paths are so that they have the same HCS. Therefore, considering only these two metrics to predict their hot cracking behaviour, the two alloys are expected to be characterized by the same intrinsic hot crack propensity.

As suggested by Kou [78], $T - \sqrt{f_s}$ curves represent a good approximation of the solid/liquid (S/L) interface especially in proximity of the grain boundaries, regions where hot cracks are more likely to form. The S/L interfaces have been depicted in Figure 6.16(b) and 6.16(c) for Alloy A and B, respectively. Alloy A is characterized by an extremely narrow and long intergranular channel arising from the higher $\sqrt{f_s}$ coordinate in which the solidification path assumes its maximum derivative. On the other end, Alloy B presents a wider intergranular area as a result of the HCS being computed at a lower $\sqrt{f_s}$ value. Additionally, with respect to alloy A, the channel of Alloy B is shorter in the vicinity of the GB owing to the lower temperatures found at $\sqrt{f_s}$ values greater than 0.5. These distinct behaviours are directly associated with two different feeding dynamics.

Following the Hagen-Poiseuille law, the liquid flow through a channel is highly influenced by its shape [276]. An increased liquid volumetric flow is indeed achieved in channels characterized by shorter lengths and greater widths. Therefore, with respect to Alloy A, Alloy B is characterized by greater feeding which limits the formation of hot cracks. Liquid feeding, not included in both HCS and ΔT, needs therefore to be included in the formulation of an improved metric in order to comprehensively predict an alloy's intrinsic hot crack propensity,
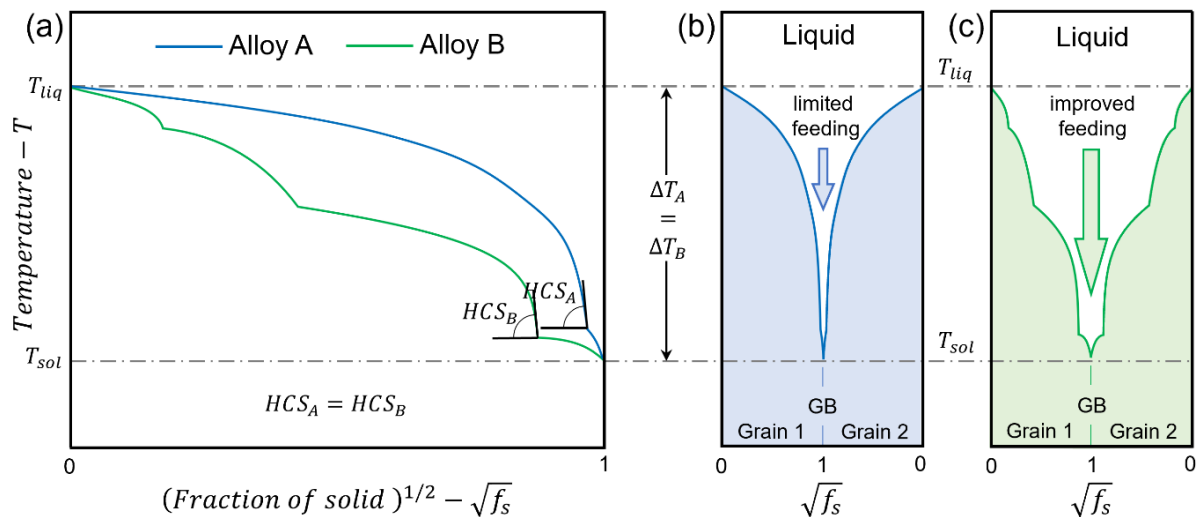
Figure 6.14: (a) $T - \sqrt{f_s}$ curves for two alloys characterized by the same solidification range ΔT and hot-crack-susceptibility HCS. Solid/liquid interfaces of (b) Alloy A and (c) Alloy B. The prior alloy is characterized by limited feeding achieved due to the presence of a long and narrow intergranular channel. On the contrary, the latter shows wider and shorter intergranular regions and therefore what is thought an improved liquid feeding.

Since solidification trajectories characterized by short solidification ranges and wide intergranular liquid channels are proposed to minimise the intrinsic hot cracking tendency of a given alloy, the shape of the solid-liquid interface (given by the $T - \sqrt{f_s}$ curve) results to be a relevant feature that needs to be considered to incorporate liquid

feeding. This can be addressed considering the area subtended by the S/L interface with respect to the temperature. This quantity can be computed considering the integral of the square root of the fraction of solid with respect to the temperature, evaluated between the solidus and liquidus temperature. This metric (Equation 6.11) will be addressed for simplicity as as *feeding integral I*:

$$I = \int_{T_{sol}}^{T_{liq}} \sqrt{f_s}\, dT = feeding\ integral \qquad \text{Equation 6.11}$$

A minimisation of I is paired with smaller channel lengths and/or greater intergranular widths which both result in improved volumetric flow. Moreover, changes of solidification range and HCS directly affect the shape of the solidification path, resulting in different values of the *feeding integral*.

Figure 6.15(a) depicts the solidification path of the ACN001 alloy and AA2024+Ni3, the reference material adopted in the design stage of the present work. The two $T - \sqrt{f_s}$ curves are characterized by distinct features. Firstly, as discussed in the Section 6.1.1, the solidification range of ACN001 results to be lower than the one of AA2024+Ni3. Analysing the S/L interfaces depicted in Figure 6.15(b) and 6.15(c), it is possible to observe that this results in a decreased intergranular channel. Moreover, due to the lower steepness of the ACN001 curves, liquid feeding results to be eased by the larger space between the two growing grains which results in a reduction of the alloy's intrinsic hot crack susceptibility. The feeding integrals of AA2024+Ni3 and ACN001 are graphically highlighted in Figure 6.17(b) and 6.17(c), respectively. It is possible to qualitatively appreciate that their value is extremely different. The custom ACN001 alloy is characterised by $I_{ACN001} = 46.24\ K$, while $I_{AA2024+Ni3} = 101.84\ K$. This significant

difference quantifies the limited feeding experienced by AA2024+Ni3 during solidification which led to the formation of hot cracks.

In Section 6.1.1, the I_{RDG} parameter has been adopted to guide the design of the ACN001 composition. This index is calculated from the equation of the maximum intergranular pressure drop which results to be a function of the three integrals $I_A \cdot I_B$ and I_C. Despite these terms are computed using expressions different than that of the feeding integral, their integrating functions result to be related to $\sqrt{f_s}$, the term inside the feeding integral. As a result, any change of I will be followed by an analogous change of both $I_A \cdot I_B$ and I_C. Therefore, these changes will be representative of the different feeding dynamics experienced by the compositions considered in the present work.
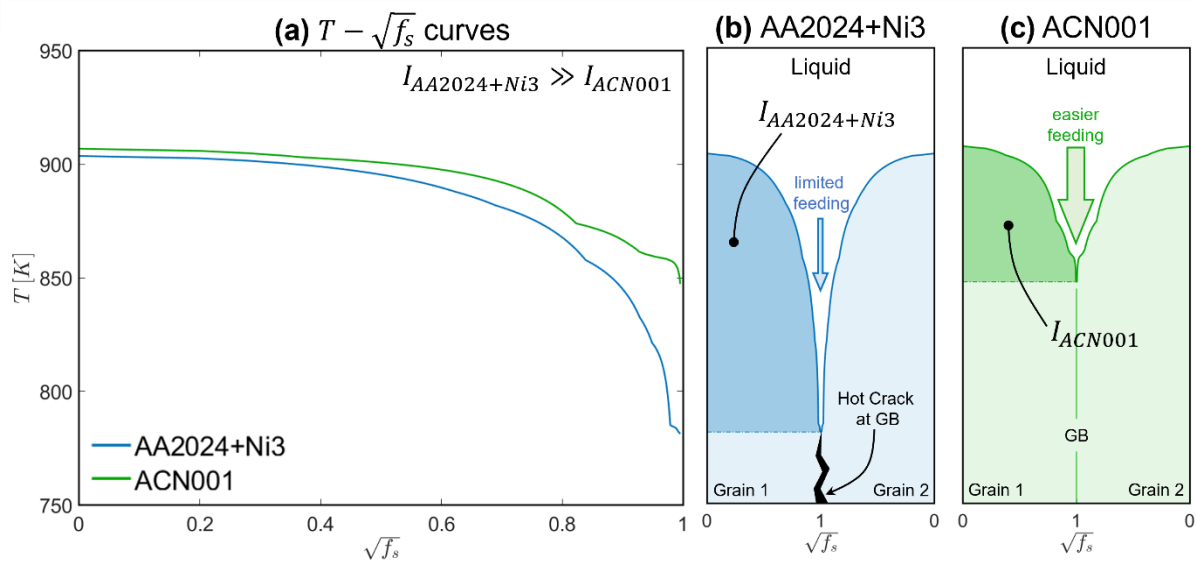
Figure 6.15: (a) $T - \sqrt{f_s}$ curves of the AA2024+Ni3 alloy (in blue) and the ACN001 composition (in green) designed in the present work. (b) and (c) depict the solid/liquid interface of AA2024+Ni3 and ACN001, respectively. These were computed in Matlab by the coupling of two specular solidification paths forming Grain 1 and Grain 2, respectively. In these sub-figures the growing solid grains are highlighted in lighter colours, while the feeding integrals by darker regions. A marked difference between the values of I for AA2024+Ni3 and ACN001 is observed, with prior being characterized by a feeding integral which results to be more than double of the latter. As a result, AA2024+Ni3 is expected to be characterized by limited feeding which results, as detected in the previous chapters, in the presence of hot cracks at grain boundaries.

To conclude, the I_{RDG} index based on the RDG criterion and proposed in this work is able to improve the prediction of the intrinsic hot crack propensity of an alloy due to the additional inclusion of liquid feeding. This metric can be used to compare not only aluminium alloys of the same series, but also materials with significant differences in composition, such as, 6xxx alloys and near-eutectic alloys.

6.3 Summary

This Chapter focused on the design and characterisation of a new aluminium composition able to avoid hot crack formation at high scan speeds. Specifically, a coupled computational and experimental approach involving the use of the CALPHAD method and targeted experiments was conducted to validate the calculations and screen optimal compositions. This led to the characterisation of the AlCu6NiY pseudo-binary system. It was observed that:

- as predicted, compositions with a Ni content equal or greater than 3 wt% limited hot crack formation and resulted in crack-free microstructures.
- The characterisation of the buttons containing a Ni content of 3, 6 and 9 wt% highlighted significant differences in secondary phases morphology. The -Ni3 button was characterised by globular and lamellar secondary phases while the others were formed by both coupled growth (formed by two phase dendrites) and a shell-and-core morphology.
- The buttons were surface melted to produce microstructures similar to those arising during PBF-LB/M fabrication. These higher cooling rate regimes did not lead to hot crack formation, but the morphology of the secondary compounds was affected.
- XRD analysis was conducted on the surface melted regions of the buttons investigated. Apart from Al-FCC, the -Ni3 sample showed the presence of Al_3Ni_2 and Al_7Cu_4Ni. On the other hand, in the -Ni6 and -Ni9 samples the additional presence of Al_3Ni was detected.
- Hardness measurements were conducted on the samples produced with a Ni content in between 3 and 9 wt%. A significant increase of hardness was observed

in samples characterised by a progressively higher Ni content. Specifically, from a Ni wt% equal or greater than 4, the hardness was found to be higher than that of wrought AA2024-T6. In order to avoid excessive brittleness, the AlCu6Ni6 was selected as base ternary for further investigations.

- The role of impurities (Fe and Si) and allowable solutes (Cu and Ni) was investigated using the same design map adopted to predict the hot cracking and mechanical behaviour of the pseudo AlCU6NiY system. The results showed that a maximum Fe and Si content of 0.10 wt% is not expected to drastically change the hot cracking behaviour of AlCu6Ni6. Moreover, the study of the allowable solutes confirmed that Cu and Ni in the range 5.5-6.5 wt% are characterised by a stable mechanical and hot cracking behaviour. Therefore, the ACN001 composition (Cu,Ni 5.5-6.5 wt%, Fe,Si<0.10 wt%) was gas atomised.

- The PBF-LB/M consolidation of ACN001 was investigated in a processing window characterised by relatively high scan speed (1.2 m/s) and a layer thickness of 30 μm. The effects of hatch distance and laser power were investigated by printing several cubes. The results showed that the sample produced with a power of 300W and a hatch distance of 80 μm was characterised by optimal relative density (99.91%) and the absence of macro-pores and cracks.

- XRD measurements revealed the presence of the major phases (FCC-Al, Al_3Ni, AL_3Ni_2, and Al_7Cu_4Ni) predicted via Scheil-Gulliver simulations. Nevertheless, the Fe-rich phases predicted using the CALPHAD approach were not experimentally observed. The microstructure of the as-built condition was formed by fine dendritic features in good agreement with the observations conducted on the buttons' laser melted area.

- ACN001 showed, as predicted, higher strength with respect to wrought AA2024-T6. Specifically, a yield strength of 368.27 ± 21.48 MPa, an ultimate tensile strength of 602.04 ± 7.36 MPa and an elongation at failure of 2.77 ± 0.11 % were measured.

Chapter 7

7 Conclusions

7.1 Consolidation and cracking behaviour of high-strength Al-alloys in PBF-LB/M

Chapter 4 of the present research project investigated the consolidation and cracking behaviour of AA2024 in PBF-LB/M. Absorptivity values were measured as a function of various processing regimes to inform an algorithm based on well-known mechanistic models aiming at the prediction of the presence of macro-porosities, such as, lack-of-fusion and keyhole defects. The microstructure of two samples characterised by similar relative density but produced using different PBF-LB/M regimes was analysed in detail with the specific aim to provide a comprehensive discussion of the mechanisms leading to the observed different cracking intensities. This required an investigation of the microstructural features near the hot crack tip and discussion of the solidification behaviour under different processing conditions with the use of micro-segregation models. The composition of AA2024 was then modified to highlight merits and

239

limitations of the current adopted hot cracking indices. The main conclusions are summarised in the following:

- This study shows that higher scan speeds are paired with lower powder absorptivity. However, the melting mode of AA2024 is mainly influenced by the laser power. Specifically, powers below 200W are paired with track discontinuities and conduction melting mode, while powers beyond 300W melt the alloy in pure keyhole regime. The conduction-to-keyhole melting mode is therefore found in PBF-LB/M regimes characterised by powers in between 200W and 300W which result to be paired with optimal consolidation.

- Although cracking is ubiquitously observed in the printed samples despite these being produced under an extensive range of processing conditions, a greater cracking intensity was detected in samples produced using higher laser power P and scan speed v. On the other hand, cracking is minimised in samples manufactured with low values of P and v.

- The study shows the simultaneous presence of hot cracks and solid-state (cold) cracks. Hot cracks are thought to initiate during a single melting event. These might then propagate as cold cracks along vertical grain boundaries in the subsequently deposited layers. Specimens with extensive cold cracks result in relative higher cracking density (CCL).

- Hot cracks exhibit a distinct morphology and were found predominantly between grains at high-angle grain boundaries. Site-specific TEM analysis conducted at the hot crack's tip revealed the presence of an intricate network of secondary phases (Cu- and Fe-Mn-rich) and micropores, suggesting that the latest stages of

solidification and micro-defects forming in the melt pool might play a pivotal role in hot crack formation.

- The solidification of the alloy was then evaluated using Scheil-Gulliver assumptions with and without solute trapping in order to describe how changes to the solute partitioning coefficient due to variation of laser scan speed might affect phase formation and crack susceptibility. An increase in laser scan speed cause enrichment of the Al-FCC matrix with the alloying elements. As a result, higher HCS values are measured (the maximum solidification gradients also occur at relative higher solid fractions). Increments in laser scan speed result additionally in higher strain rates. Results indicate that there is a trade-off between rates in PBF-LB/M and hot crack propensity.

- Hot cracks propagate in the subsequent solid layers due to the combination of high residual stresses and oriented high angle grain boundaries. These conditions are favoured by a higher v/P ratio, columnar grain growth and strong crystallographic texture. Crack propagation can therefore be significantly reduced by changing processing conditions appropriately.

- A modification of AA2024 with the addition of 3 wt% of Ni is able to limit the hot crack formation and subsequent propagation in the solid state. However, although the solidification range ΔT and the hot-crack-susceptibility index HCS are able to predict the hot cracking behaviour of alloys characterised by significantly different solidification paths, they do not capture significant phenomena affecting hot crack formation, such as, liquid feeding and solid thermal expansion. Therefore, new metrics need to be identified to increase the confidence in the design of bespoke compositions characterised by minimal intrinsic hot crack propensity.

The study conducted in Chapter 4 of the present research work provides new insights on the effects of PBF-LB/M processing regimes on the consolidation, hot crack's formation, and propagation in high-strength Al-alloys. It is proposed that the complex mechanisms leading to the extensive cracking in such materials cannot be captured by the parameters adopted in literature, such as, ΔT and HCS. All the aspects discussed in Chapter 4 need to be considered in the development of new practical methodologies to design and develop crack-free high-strength Al-alloys specifically tailored for the PBF-LB/M process without the use of grain refiners.

7.2 Modelling towards crack-free metal 3D printing

Chapter 5 of the present research work used a coupled modelling and experimental approach to investigate the hot cracking behaviour of high-strength Al-alloys as a function of different processing conditions. A Point Distance Variation (PDV) track characterised by four different laser scan speed regimes was experimentally carried out on a bare AA2024-T351 substrate and the analysis showed the presence of hot cracks in the regimes characterised by a higher v. A multi-physics simulation was performed to produce a digital twin of the PDV experiment and compute the dynamic thermal conditions promoting the formation of hot cracks. This led to the computation of the pressure drop at the root of the intergranular channel during solidification which informed the identification of a hot crack propensity index able to not only consider the intrinsic susceptibility of an alloy, but also the effects of the processing conditions on hot crack formation. Based on this knowledge, the build rate of AA2024 was subsequently investigated combining mechanistic models and targeted experiments. The main findings of this investigation conclude the following:

- Hot crack formation is highly influenced by the scan speed, with laser regimes adopting a point distance of 15 μm characterised by the suppression of the initiation of such detrimental defects. The use of point distances equal or higher than 45 μm results in the formation of hot cracks in AA2024 both in the laser surface melted PDV track and cubic samples produced by PBF-LB/M. Although cracking was not observed in the PD30 segment of the PDV track, its PBF-LB/M counterpart revealed the presence of hot tears highlighting the stochastic nature of such defects' formation given by the development of high pressure drop along high angle grain boundaries.

- Hot crack formation is paired with a higher propensity in the inter-pulse temporal domain owing to the development of higher pressure drops as a result of the change of pulse position. Consequently, considering the spatial distribution of the local Δp_{max}, peaks of hot crack driving force are developed along the vertical axis corresponding to the laser x-coordinate of each pulse.

- The hot crack driving force is largely influenced by the ratio between the cooling rate and square thermal gradient. Lower scan speed regimes are paired with lower $\dot{T}$ and higher G resulting in values of pressure drop below the threshold for hot crack formation in molten aluminium. On the other hand, the PD45 and PD60 regimes are characterised by higher cooling rates but lower thermal gradients, resulting in Δp_{max} values paired with cavitation and subsequent hot crack formation.

- The index Δp_{glob} proposed in this work proved to correctly predict the global propensity of each processing regime. This parameter not only addresses the local development of Δp_{max}, but also the distribution of these values in the solidifying material thus considering the global opportunity of each laser regime to develop such detrimental pressure drops along high angle grain boundaries. This approach proved to correctly highlight the transitory PD30 regime where the driving force may be sufficient but only critical if developed along weaker areas of the microstructure, namely HAGBs.

- The build rate of crack-free AA2024 can be improved by 150% increasing the layer thickness and hatch distance of the AM-PD15 regime to 50 μm and 180 μm, respectively. The measured cell size and hardness were found to be consistent across the investigated specimens and therefore the macroscopic mechanical

performances of AA2024 are expected to show minor changes with respect to the AM-PD15 case.

The great parallelism found between the PDV experiment and 3D printed samples proves the merits of single-track experiments in elucidating complex aspects related to the consolidation dynamics and cracking in PBF-LB/M. The approach proposed in Chapter 5 and the deriving global hot crack propensity index can be used to eradicate hot cracking in any alloy, enlarging the processability of difficult-to-print materials, such as, other high-strength Al-, Ni- and high-entropy alloys. The subsequent pathway to improve the build rate of low scan speed regimes can be uptaken in standard machines and it does not rely on any high-cost adaptations. The combination of these two computationally driven and experimentally validated approaches represents a foundation for the development and validation of machine learning and statistical models aiming at the identification of process-structure laws for the fabrication of crack-free parts characterised by industrially relevant build rates.

7.3 Merits of tailored alloy design for the PBF-LB/M of new high-strength Al compositions

Chapter 6 of this research work focused on the development of a custom high-strength Al-alloy characterised by exceptional hot crack resistance in regimes paired with high build rate. The hot cracking and mechanical behaviour of bespoke compositions were assessed adopting various performance indices computed from the solutes' amounts adopting the CALPHAD approach and targeted experiments to simulate the PBF-LB/M conditions without the use of powders. This guided the identification of a base ternary (AlCu6Ni6) which was subsequently developed considering the effects of impurities and allowable ranges of solutes resulting in the identification of a custom ACN001 composition which was successfully processed resulting in parts characterised by optimal relative density and exceptional strength. The main conclusions are summarised in the following:

- The CALPHAD approach coupled with the production of targeted compositions subsequently surface melted to simulate the PBF-LB/M cooling rate and solidification dynamics represents a practical powder-free approach to predict the hot cracking behaviour of bespoke compositions and experimentally evaluate their mechanical performances.

- Although the hot cracking indices adopted in the literature represent a great foundation to identify crack-resistant compositions, they are not able to capture the feeding dynamics occurring at the intergranular channel. Based on the RDG model with the assumptions of fixed thermal conditions during solidification, the I_{RDG} parameter used in this work captures not only this relevant phenomenon, but

also considers the effects of the solidification range and the hot-crack-susceptibility index. Therefore, represents an improved metrics to assess the intrinsic propensity of an alloy to form hot cracks.

-   The AlCu6NiY pseudo binary system is characterised by exceptional hot crack resistance and mechanical properties when the Ni content is higher than 3 wt%. This is achieved due to the distinct solidification characteristics of such compositions including short solidification range, optimised feeding, and extremely fine substructures.

-   The CALPHAD approach and the liquidus projection are powerful tools to not only predict the hot cracking behaviour of bespoke Al alloys, but also the precipitation sequence occurring during solidification.

-   Although high scan speed regimes are paired with high cooling rates and low thermal gradients promoting hot crack formation (as shown in Chapter 5 of the present research work), the designed ACN001 composition is characterised by exceptional printability in these regimes, resulting in improved build rates with respect to standard high-strength Al alloys. This results from its low intrinsic hot crack propensity (captured by the I_{RDG} parameter) which limits the development of detrimental pressure drops by improving the intergranular feeding. In addition to this exceptional hot crack resistance, ACN001 is characterised by great strength in the as-built condition achieved due to the extremely refined substructures nucleated during solidification.

The methodology proposed in Chapter 6 of the present research project not only represents a successful approach to design bespoke high-strength Al compositions, but also a practical powder-free solution to limit feedstock costs and development times.

247

Moreover, the use of CALPHAD approaches validated through targeted experiments and analysis results in a powerful tool to not only guide the calculation, but also explain microstructural features such as precipitation sequence and liquid feeding.

Chapter 8

8 Future work

The present research project has focused on the investigation and eradication of hot cracks in high-strength Al-alloys using multiple approaches. However, owing to the extremely complex nature of hot cracking – affected by several material- and process-related phenomena – there is still more to be done that cannot fit within the duration of the PhD. This Chapter reports a few relevant scientific areas that could be investigated to gain a better understanding and control of solidification cracking in the context of PBF-LB/M.

This research has suggested that the extensive cracking behaviour observed in AA2024 is the result of hot crack formation and subsequent propagation in the solid-state. Therefore, the suppression of hot tears during the liquid-to-solid transition – as also proven in this work – is expected to eradicate the extensive presence of cracks in high-strength Al-alloys. However, the occurrence of this dual-mechanisms phenomenon (formed by formation of solidification cracks and subsequent propagation in the solid

state) during PBF-LB/M needs to be further investigated, specifically in standard wrought alloys from the 6xxx and 7xxx series.

The results of the present research project have highlighted that selected alloying elements may extensively affect the intrinsic hot crack propensity of a given alloy. Specifically, it is of interest to investigate the effects of the impurities of iron and silicon on hot crack formation in standard wrought alloys. If present in considerable amounts, these elements may introduce low temperature eutectics promoting limited intergranular feeding and consequent hot crack formation. Moreover, this research proved that this phenomenon is also affected by selected main solutes and therefore the investigation of several wrought alloys' compositions within the standard ranges proposed by ASTM or similar may highlight chemical windows limiting hot crack formation. Most importantly, in addition to a reduced hot crack propensity, these compositions are expected to be characterised by mechanical and thermal properties within the known ranges thus promoting the uptake of additive manufacturing in established industrial applications.

One of the main aims of the present research project was the design of a custom high-strength Al alloy (ACN001) tailored for the PBF-LB/M process. Although this study has succeeded in this, the correct characterisation and optimisation of a bespoke composition is certainly a study not able to be comprehensively conducted in the course of a PhD. Therefore, a few research questions remain open. It has been shown in the present work that the ACN001 alloy is characterised by an extremely fine arrangements of dendritic substructures. Moreover, preliminary investigations have shown that the alloying system of interest (Al-Cu-Ni ternary) is characterised by the presence of couple growth in compositions closer to that of ACN001. In this context, it is of relevant scientific

importance the understanding of the thermodynamic conditions and compositional requirements leading to the presence of such peculiar substructure arrangement in the context of metal additive manufacturing. A complete understanding of this phenomenon may lead to a new class of materials with unique properties and solidification cracking resistance, tailored for the fast cooling of PBF-LB/M and similar AM manufacturing techniques.

The present research project extensively adopted a combination of modelling and experiments to investigate the formation of pores and most importantly hot cracks during PBF-LB/M. Specifically, the investigation of the hot cracking driving force and global hot crack propensity index proved to be successful tools to highlight AA2024's crack-free regimes. However, in order to exploit the merits of this approach, a few complementary research questions have been highlighted for further investigations. Research has suggested that scan speed regimes characterised by a speed equal or lower than 0.107 m/s result in the suppression of hot crack formation. However, this threshold is valid only for AA2024 and therefore there is a need to apply the methodology proposed in the present research project to other relevant engineering high-strength Al-alloys (e.g., AA7075, AA6061 and more). Moreover, this approach needs to be investigated considering different energy sources, such as, continuous-wave (CW) and modulated lasers. The conduction of multiple modelling and experimental investigation with the proposed methodology is expected to form a database large enough to develop and train a machine learning algorithm aiming at the identification of the composition-process-structure relationships affecting hot crack formation. Based on the results of this investigation, it will be possible to predict the global hot crack propensity index of any

high-strength Al alloy processed adopting any PBF-LB/M regime without the need to either run multi-physics simulations and/or additional experiments.

This research work proposed a pathway to increase the build rate of alloys characterised by low scan speed crack-free regimes. Although this approach represents an easy-to-use solution to improve the productivity of difficult-to-print materials, it is paired with limited manufacturing resolution resulting from the forced increase of layer thickness. Recently, several PBF-LB/M systems have introduced the possibility to scan a single layer using multiple lasers adopting the so-called master-slave approach in which an energy source melts the material (master) and the following one performs an in-situ heat treatment (slave). Although these systems enlarge the number of processing parameters to investigate adding processing freedom and customisation, the systematic adoption of dual-beam machines is hampered by the lack of understanding of the laser-material interaction in the event multiple sources are run simultaneously on the same portion of material. In this context, it is not well understood how the slave beam can be tailored to customise the grain structure or the thermal history experienced by the material during solidification. The change of these process/material variables may lead to the formation of a crack-free microstructure at relevant build rates, enabling the adoption of currently difficult-to-print Al-alloys, such as, AA6061 or AA7075. In order to address these scientific questions, the multi-physics model adopted in the present research may be improved with the addition of a secondary energy source aiming at the reduction of cooling rate and increase of thermal gradient in the back of the melt pool where vulnerable regions may be paired with high pressure drops. This might lead to the suppression of hot cracks in laser regimes characterised by higher scan speeds which therefore are paired with improved build rates.

Although this work successfully addressed all the research questions highlighted at the beginning of the project, the comprehensive understanding of hot cracking in PBF-LB/M leads (as discussed in the present Chapter) to multiple complementary pathways which are not only characterised by significant scientific value, but also relevant implications for the industry.

Appendix

A. Image segmentation analysis

```matlab
%% image_segmentation_defects.m - G. Del Guercio
clear all, close all, clc
pixelstommratio=429.3334; % at the magnification selected, this results to
be the conversion factor between pixels and mm

I=imread('B3S25_xz_x5_d.tif'); % load the image
I=rgb2gray(I); % move to gray scale
level=graythresh(I); % find threshold
Ithresh=imbinarize(I,level); % binarise the image
Ifilled=imfill(imcomplement(Ithresh),'holes'); % fill the holes
Icc=bwconncomp(Idil); % find connected components
voids=regionprops(Icc,'Area','Circularity','MajorAxisLength','MinorAxisLeng
th','Eccentricity','Orientation','EquivDiameter','Extent','MaxFeretProperti
es','MinFeretProperties'); % identify voids and evaluate their properties

% Thresholds
Circularity_th=0.9; % Circularity, cracks vs pores
AR_th=2; % aspect ratio
AA_th=0.05; % mm, gas pores vs LOF/Keyholes
C_th=0.7; % Circularity, LOF vs Keyholes
OR_th=45; % Orientation

% Defects analysis
condition_cracks=[voids.Circularity]<=Circularity_th &
[voids.MaxFeretDiameter]./[voids.MinFeretDiameter]>=AR_th &
abs([voids.Orientation])>=OR_th;
condition_pores=1-condition_cracks;
NTOT=size(voids,1);
ipores=1; icracks=1;
for i=1:NTOT
     voids(i).AA=mean([voids(i).MajorAxisLength
voids(i).MinorAxisLength])/pixelstommratio;
    if  condition_cracks(i)
       cracks(icracks)=voids(i);
       icracks=icracks+1;
    else
       pores(ipores)=voids(i);
       ipores=ipores+1;
    end
end
condition_kholes=[[voids.Area]./(pi/4*[voids.MajorAxisLength].^2)]>=C_th;
NPORES=ipores-1;
igaspores=1; ilofs=1; ikholes=1;
for i=1:NPORES
    if pores(i).AA<AA_th
       gaspores(igaspores)=pores(i);
       igaspores=igaspores+1;
    else
       if pores(i).Circularity>C_th
           lofs(ilofs)=pores(i);
           ilofs=ilofs+1;
```

254

```matlab
        else
            kholes(ikholes)=pores(i);
            ikholes=ikholes+1;
        end
    end
end

% Quantification
AreaTOT=prod(size(I,[1 2]));
RELATIVE_DENSITY=100*(1-sum([voids.Area])/AreaTOT);
POROSITY=sum([pores.Area])/AreaTOT*100;
GAS_PORES=sum([gaspores.Area])/AreaTOT*100;
LOFS=sum([lofs.Area])/AreaTOT*100;
KEYHOLES=sum([kholes.Area])/AreaTOT*100;
CCL=sum([cracks.MajorAxisLength])/AreaTOT*pixelstommratio;
```

B. Evaluation of powder absorptivity

```matlab
%% LMC.m - absorptivity evaluation
function output = LMC(file,material,mass,scanspeed,power)
%parameters
l = 0.006;
%material 1 is al 2 is for ss
if material == 1
    Cp0 = 0.875;
    alpha = 51.6e-5;
    else if material == 2
        Cp0 = 0.5;
        alpha = 37.7e-5;
        else if material == 3
                Cp0 = 0.914;
                alpha = 51.6e-5;
            end
    end
end

%import data
raw_data = file(:,1);
%how many data points
data_points = numel(raw_data);
if data_points >= 10000
    time_sampling = 1;
    start_point_diff = 100;
else if data_points <= 10000
        time_sampling = 100;
        start_point_diff = 1;
    end
end
%determine starting room temperature
start_room_temp = (mean(raw_data(1:(50*start_point_diff),1)))+0.4;
%get 1 second from laser on
pre_laser_1sec = (find(raw_data > start_room_temp,1))-(2000/time_sampling);
raw_data_standardised = raw_data(pre_laser_1sec:end);
%make the time series
size_of_data = numel(raw_data_standardised);
time_series = linspace(1,size_of_data,size_of_data);
time_series = time_series.';
%fit the curve
options = fitoptions('a*exp(-x/b)+c');
options.Lower = [0 0 20];
options.Upper = [Inf Inf 40];
options.StartPoint = [0.5444 62305 20];
line_fit =
fit(time_series((3000/time_sampling):end),raw_data_standardised((3000/time_
sampling):end),'a*exp(-x/b)+c',options);
%Coefficients
coefficients = coeffvalues(line_fit);
a = coefficients(1);
b = coefficients(2);
c = coefficients(3);
%creating plot fitting line
line_fit_equation = a*exp(-time_series/b)+c;
%find T0 and T1
difference_raw_fit = time_series(1:(12000/time_sampling))-
line_fit_equation(1:(12000/time_sampling));
```

```matlab
[difference_raw_fit,i] = min(abs(difference_raw_fit));
T0 = round(start_room_temp,4);
T1 = round(time_series(i),4);
%create Cp vs T graph
Cp_t = linspace(0,200,200001);
Cp_t = Cp_t.';
Cp_p(:,1) = Cp0*(1+(alpha*Cp_t(:,1)));
Cp_e = Cp_p(:,1);
%create temperature tags
TT0 = find(Cp_t == T0);
TT1 = find(Cp_t == T1);
%integrate
integration = cumtrapz(Cp_t(TT0:TT1,1),Cp_e(TT0:TT1,1));
integration_total = max(integration);
%formula
Absorp1 = (mass*integration_total) / (l/scanspeed*power);
%outputs
format short
format compact
output.Cp0 = Cp0;
output.alpha = alpha;
output.time_sampling = time_sampling;
output.start_room_temp = start_room_temp;
output.pre_laser_1sec = pre_laser_1sec;
output.T0 = T0;
output.T1 = T1;
output.integration_total = integration_total;
output.mass = mass;
output.l = l;
output.scanspeed = scanspeed;
output.power = power;
output.Absorp1 = Absorp1;
output.a = a;
output.b = b;
output.c = c;
end
```

C. User Defined Function – Multi-physics simulation

```
#include "udf.h"
#include "surf.h"
#include "cxndsearch.h"
#include "sg.h"
#include "sg_mphase.h"
#include "math.h"
#include "unsteady.h"
#include "mem.h"
#include "sg_mem.h"
#include "dpm.h"
#include "dpm_laws.h"
#include "dpm_types.h"
#include "prf.h"
#include "complex.h"


/* DPM particle variables */
#define TP_BEAM_WATTS(tp)TP_USER_REAL(tp, 0)
#define TP_IN_PARTICLE(tp)TP_USER_REAL(tp, 1)
#define TP_BOUNCES(tp)TP_USER_REAL(tp, 2)

/* volume fraction gradients in each x, y and z component */
#define C_VOF_SURF_AREA_X(c, t)C_UDMI(c, t, 0)
#define C_VOF_SURF_AREA_Y(c, t)C_UDMI(c, t, 1)
#define C_VOF_SURF_AREA_Z(c, t)C_UDMI(c, t, 2)

/* volume fraction of primary phase */
#define C_VOLUME_FRACTION(c, t)C_UDMI(c, t, 3)

/* volume fraction gradient of all directions */
#define C_VMAG(c, t)C_UDMI(c, t, 4)

/* normalised volume fraction gradients */
#define C_VOF_NX(c, t)C_UDMI(c, t, 5)
#define C_VOF_NY(c, t)C_UDMI(c, t, 6)
#define C_VOF_NZ(c, t)C_UDMI(c, t, 7)

 /* temperature gradients */
#define C_TEMP_G_X(c, t)C_UDMI(c, t, 8)
#define C_TEMP_G_Y(c, t)C_UDMI(c, t, 9)
#define C_TEMP_G_Z(c, t)C_UDMI(c, t, 10)
#define C_TEMP_G(c, t)C_UDMI(c, t, 11)

/* amount of volume fraction of primary phase that is liquid in liquid and
solidification model */
#define C_LIQUID_FRAC(c, t)C_UDMI(c, t, 12)

/* normal to surface in each direction */
#define C_SURFACE_NORM_X(c, t)C_UDMI(c, t, 13)
#define C_SURFACE_NORM_Y(c, t)C_UDMI(c, t, 14)
#define C_SURFACE_NORM_Z(c, t)C_UDMI(c, t, 15)

/* normalised surface normal in each direction */
#define C_NSURFACE_NORM_X(c, t)C_UDMI(c, t, 16)
#define C_NSURFACE_NORM_Y(c, t)C_UDMI(c, t, 17)
#define C_NSURFACE_NORM_Z(c, t)C_UDMI(c, t, 18)

/* G&R parameters */
```

```c
#define C_G_TGRAD(c, t)C_UDMI(c, t, 19)
#define C_R_SOLID(c, t)C_UDMI(c, t, 20)
#define C_GR(c, t)C_UDMI(c, t, 21)
#define C_GDIVR(c, t)C_UDMI(c, t, 22)

/* max temperature of the metal phase */
#define C_MAX_METAL_TEMP(c, t)C_UDMI(c, t, 23)

/* Power modulation*/
#define C_LASER_POWER_MOD(c, t)C_UDMI(c, t, 24)

/* initial irradiance in w/m2 */
#define C_LASERM2_START(c, t)C_UDMI(c, t, 25)

/* free surface tag */
#define C_FREE_SURFACE(c, t)C_UDMI(c, t, 26)

/* amount of power the cell has been given in W */
#define C_CELL_WATTSM2(c, t)C_UDMI(c, t, 27)

/* viewing power modulation */
#define C_LASER_POWER_MOD2(c, t)C_UDMI(c, t, 28)

/* heat source term for energy equation */
#define C_LASERM3_HST(c, t)C_UDMI(c, t, 29)

/* heat losses through radiation and evaporation */
#define C_HEATLOSS_HST(c, t)C_UDMI(c, t, 30)

/* DCP smoothing factor */
#define C_DCP(c, t)C_UDMI(c, t, 31)

/* momentum sources */
#define C_X_MOM_SOURCE(c, t)C_UDMI(c, t, 32)
#define C_RECOIL_PRESSURE_X(c, t)C_UDMI(c, t, 33)
#define C_MARANGONI_FLOW_X(c, t)C_UDMI(c, t, 34)
#define C_Y_MOM_SOURCE(c, t)C_UDMI(c, t, 35)
#define C_RECOIL_PRESSURE_Y(c, t)C_UDMI(c, t, 36)
#define C_MARANGONI_FLOW_Y(c, t)C_UDMI(c, t, 37)
#define C_Z_MOM_SOURCE(c, t)C_UDMI(c, t, 38)
#define C_RECOIL_PRESSURE_Z(c, t)C_UDMI(c, t, 39)
#define C_MARANGONI_FLOW_Z(c, t)C_UDMI(c, t, 40)

#define C_CELL_WATTS2(c, t)C_UDMI(c, t, 41)
#define C_ENERGY_IN(c, t)C_UDMI(c, t, 42)
#define C_ENERGY_AB(c, t)C_UDMI(c, t, 43)

#define C_PERCENT_DONE(c, t)C_UDMI(c, t, 44)

#define C_TEMP_TAG(c, t)C_UDMI(c, t, 45)

#define C_AREA(c, t)C_UDMI(c, t, 46)

#define C_STRAINRATE(c, t)C_UDMI(c, t, 47)
#define C_VOL_MUSH(c, t)C_UDMI(c, t, 48)

/* global properties */
#define gauss_iv 0 /* 0 is gauss, 1 is inverse solution */
#define laser_on 10 /* timesteps after laser comes on */
```

```
/* Gaussian laser parameters */
#define pulsed_laser 1
#define laser_power 200.0
#define laser_base 0.0
#define laser_vel 0.5
#define point_distance 60e-6
#define exposure_time (point_distance / laser_vel)
#define jump_delay 20e-6
#define e_d_time (exposure_time + jump_delay)
#define laser_spot_rad 35e-6
#define init_x 100e-6
#define rtxnf_ab 0.5

/* Point Distance Variation */
#define PD1 15.0e-06
#define PD2 30.0e-06
#define PD3 45.0e-06
#define PD4 60.0e-06

#define nb_pulse 5 /* Number of pulses for each Point Distance */

#define dx1 nb_pulse * PD1
#define dx2 nb_pulse * PD2 + dx1
#define dx3 nb_pulse * PD3 + dx2

/* domain parameters */
#define track_length 600e-6
#define cell_size 3e-6
#define substrate_height 150e-6
#define laser_off 20 * e_d_time /*(track_length / laser_vel)*/
#define reduce_p_radius 1e-6
#define increase_pbf_height (substrate_height)
#define source_limit 9e17

/* material parameters */
#define index_metal (2.8 + (7.8 * I))
#define latent_vap 9.46e6
#define ev_atom 3.225
#define molar_mass 0.02698
#define boiling_temp 2743.0
#define surface_tension 0.84
#define temp_surface_tension 0.35e-3
#define viscosity 0.0013
#define CTE 2.1e-5

/* parameters for inverse solution spot temperatures */

//static real magic_power;
//static real magic_powerm3;

//static int last_ts = -1;
static ND_Search* domain_table = NULL;

DEFINE_ADJUST(var_allocation, domain)
{
#if !RP_HOST
        Thread* t;
        Thread** pt;
        cell_t c;
        int phase_domain_index = 0;
```

```
        Domain* pDomain = DOMAIN_SUB_DOMAIN(domain, phase_domain_index);
        real x[ND_ND];
        real max_metal_temp1 = 0.0;
        real max_metal_temp1_max;
        real surface_normal_out[3];
        CX_Cell_Id* cx_cell;
        real vol_mush;
        real vol_mush_global;

        /* allocation of memory for gradients */
        {
                Alloc_Storage_Vars(pDomain, SV_VOF_RG, SV_VOF_G, SV_NULL);
                Scalar_Reconstruction(pDomain, SV_VOF, -1, SV_VOF_RG, NULL);
                Scalar_Derivatives(pDomain, SV_VOF, -1, SV_VOF_G, SV_VOF_RG,
Vof_Deriv_Accumulate);
        }
        {
                Alloc_Storage_Vars(domain, SV_T_RG, SV_T_G, SV_NULL);
                T_derivatives(domain);
                Free_Storage_Vars(domain, SV_T_RG, SV_NULL);
        }

        mp_thread_loop_c(t, domain, pt)
                if (FLUID_THREAD_P(t))
                {
                        Thread* ppt = pt[phase_domain_index];
                        begin_c_loop(c, t)
                        {
                                C_VOF_SURF_AREA_X(c, t) = C_VOF_G(c, ppt)[0];
                                C_VOF_SURF_AREA_Y(c, t) = C_VOF_G(c, ppt)[1];
                                C_VOF_SURF_AREA_Z(c, t) = C_VOF_G(c, ppt)[2];
                                C_VOLUME_FRACTION(c, t) = C_VOF(c, ppt);
                                C_VMAG(c, t) = ND_MAG(C_VOF_SURF_AREA_X(c, t),
C_VOF_SURF_AREA_Y(c, t), C_VOF_SURF_AREA_Z(c, t));
                                C_AREA(c, t) = C_VOLUME(c, t) * NV_MAG(C_VOF_G(c,
ppt));

                                C_VOF_NX(c, t) = C_VOF_G(c, ppt)[0] /
NV_MAG(C_VOF_G(c, ppt)); /* nx */
                                C_VOF_NY(c, t) = C_VOF_G(c, ppt)[1] /
NV_MAG(C_VOF_G(c, ppt)); /* ny */
                                C_VOF_NZ(c, t) = C_VOF_G(c, ppt)[2] /
NV_MAG(C_VOF_G(c, ppt)); /* nz */

                                C_TEMP_G_X(c, t) = C_T_G(c, t)[0];          /*
temp_g_x */
                                C_TEMP_G_Y(c, t) = C_T_G(c, t)[1];          /*
temp_g_y */
                                C_TEMP_G_Z(c, t) = C_T_G(c, t)[2];          /*
temp_g_z */

                                C_LIQUID_FRAC(c, t) = C_LIQF(c, ppt);

                                NV_VS(surface_normal_out, =, C_VOF_G(c, ppt), *, -
1.0);

                                C_SURFACE_NORM_X(c, t) = surface_normal_out[0];
                                C_SURFACE_NORM_Y(c, t) = surface_normal_out[1];
                                C_SURFACE_NORM_Z(c, t) = surface_normal_out[2];
```

261

```c
                                C_NSURFACE_NORM_X(c, t) = surface_normal_out[0] /
NV_MAG(surface_normal_out);
                                C_NSURFACE_NORM_Y(c, t) = surface_normal_out[1] /
NV_MAG(surface_normal_out);
                                C_NSURFACE_NORM_Z(c, t) = surface_normal_out[2] /
NV_MAG(surface_normal_out);

                                C_PERCENT_DONE(c, t) = ((laser_vel * CURRENT_TIME)
/ track_length) * 100.0;

                                /* G&R module where temperature gradients and
solidification rates are assignined */
                                if (C_LIQUID_FRAC(c, t) > 0.0 &&
C_VOLUME_FRACTION(c, t) > 0.1)
                                {
                                        C_G_TGRAD(c, t) = fabs(ND_MAG(C_TEMP_G_X(c,
t), C_TEMP_G_Y(c, t), C_TEMP_G_Z(c, t)));
                                        C_R_SOLID(c, t) = fabs(laser_vel *
(C_TEMP_G_X(c, t) / C_G_TGRAD(c, t)));
                                        C_GR(c, t) = C_G_TGRAD(c, t) * C_R_SOLID(c,
t);
                                        C_GDIVR(c, t) = C_G_TGRAD(c, t) /
C_R_SOLID(c, t);

                                        C_STRAINRATE(c, t) = CTE * C_G_TGRAD(c, t) *
C_R_SOLID(c, t);
                                }

                                /* max metal temperature */
                                if (C_VOLUME_FRACTION(c, t) > 0.5)
                                {
                                        if (C_T(c, t) > max_metal_temp1 ||
max_metal_temp1 == 0.0)
                                        {
                                                max_metal_temp1 = C_T(c, t);
                                        }
                                }

                                if (C_VOLUME_FRACTION(c, t) > 0.2 &&
C_LIQUID_FRAC(c, t) > 0.0)
                                {
                                        C_TEMP_TAG(c, t) = 1.0;
                                }

                                if (C_VOLUME_FRACTION(c, t) > 0.1)
                                {
                                        if ((C_LIQUID_FRAC(c, t) > 0.0) &&
(C_LIQUID_FRAC(c, t) < 1.0))
                                        {
                                                vol_mush += C_VOLUME(c, t) *
C_VOLUME_FRACTION(c, t);
                                        }
                                }
                        }
                end_c_loop(c, t)
            }
    Free_Storage_Vars(pDomain, SV_T_RG, SV_VOF_RG, SV_VOF_G, SV_NULL);
    Free_Storage_Vars(domain, SV_T_G, SV_NULL);

    if (gauss_iv == 0)
```

```c
        {
                max_metal_temp1_max = PRF_GRHIGH1(max_metal_temp1);
        }

        vol_mush_global = PRF_GRSUM1(vol_mush);

        /* loop to assign the max metal temperature so that it can be
measured in the console */
        mp_thread_loop_c(t, domain, pt)
                if (FLUID_THREAD_P(t))
                {
                        Thread* ppt = pt[phase_domain_index];
                        begin_c_loop(c, t)
                        {
                                if (gauss_iv == 0)
                                {
                                        C_MAX_METAL_TEMP(c, t) = max_metal_temp1_max;
                                }

                                C_VOL_MUSH(c, t) = vol_mush_global;

                        }
                        end_c_loop(c, t)
                }
        Free_Storage_Vars(pDomain, SV_T_RG, SV_VOF_RG, SV_VOF_G, SV_NULL);
        Free_Storage_Vars(domain, SV_T_G, SV_NULL);
#endif
}

DEFINE_DPM_BODY_FORCE(dpm_body_force, p, dir)
{
        cell_t c;
        Thread* ct;
        return(0.0);
}

DEFINE_DPM_DRAG(zero_drag, re, p)
{
        return 0.0;
}

DEFINE_DPM_SCALAR_UPDATE(RayTracing, c, t, initialize, tp)
{
        c = P_CELL(tp);
        t = P_CELL_THREAD(tp);
        real x[ND_ND];

        /* variables for polimi */
        real multiplyer = 1.0;
        real time2 = fmod(CURRENT_TIME, e_d_time);

        /* variables for gaussian laser */
        real laser_position = laser_vel * CURRENT_TIME;
        real laser_power_mod;
        real laserm2;
        real xp, yp, fp;

        /* variables for fresnel equation */
        double complex index = index_metal;
        double complex cnums;
```

263

```c
        double complex cdems;
        double complex cnump;
        double complex cdemp;
        double complex Spol;
        double complex Ppol;
        double complex rf;
        real Ab;
        real cos_angle;
        real sin_angle;

        real norm[ND_ND];
        real nonorm[ND_ND];
        real inc[ND_ND];
        real normal_velocity;



        /* pulsed laser modulation, decides the laser position during the
laser pass */
        if (pulsed_laser == 1)
        {
                /* Point Distance Variation in function of the time step */

                if ( (floor((CURRENT_TIME) / (nb_pulse * e_d_time)) + 1.0) == 1
)
                {
                        laser_position = (floor((CURRENT_TIME) / e_d_time) + 1.0)
* PD1;
                }
                else if ( (floor((CURRENT_TIME) / (nb_pulse * e_d_time)) + 1.0)
== 2 )
                {
                        laser_position = dx1 + (floor((CURRENT_TIME) / e_d_time)
+ 1.0 - nb_pulse) * PD2;
                }
                else if ((floor((CURRENT_TIME) / (nb_pulse * e_d_time)) + 1.0)
== 3)
                {
                        laser_position = dx2 + (floor((CURRENT_TIME) / e_d_time)
+ 1.0 - (2 * nb_pulse)) * PD3;
                }
                else if ((floor((CURRENT_TIME) / (nb_pulse * e_d_time)) + 1.0)
== 4)
                {
                        laser_position = dx3 + (floor((CURRENT_TIME) / e_d_time)
+ 1.0 - (3 * nb_pulse)) * PD4;
                        /*laser_pos = init_x + dx3 +
(floor(current_time/e_d_time)-11)*PD4*/
                }

                /* Turns the laser on or off depending on the pulse */
                if (time2 < (e_d_time - jump_delay))
                {
                        multiplyer = 1.0;
                }
                else if (time2 >= (e_d_time - jump_delay))
                {
                        multiplyer = 0;
                }
        }
```

```
      /* laser irradiance in W/m2 is calculated */
      C_CENTROID(x, c, t);
      laser_power_mod = (laser_power * multiplyer) + laser_base;
      fp = (2.0 * laser_power_mod) / (M_PI * SQR(laser_spot_rad));
      xp = SQR(x[0] - laser_position - init_x);
      yp = SQR(x[1] - 0.0);
      laserm2 = fp * exp((-2.0 * (xp + yp)) / SQR(laser_spot_rad));

      C_LASER_POWER_MOD(c, t) = laser_power_mod;

      /* inital particle power in watts is given */
      if (initialize)
      {
            TP_BEAM_WATTS(tp) = laserm2;
            TP_IN_PARTICLE(tp) = 0.0;
            TP_BOUNCES(tp) = 0.0;
            C_LASERM2_START(c, t) = laserm2;
            C_ENERGY_IN(c, t) = (laserm2 * SQR(cell_size)) / C_VOLUME(c,
t);
      }

      /* this part deletes the particle if it travels inside a particle */
      if (C_VOLUME_FRACTION(c, t) == 1.0 && C_VMAG(c, t) == 0.0)
      {
            TP_IN_PARTICLE(tp) += 1.0;
      }

      if (TP_IN_PARTICLE(tp) > 4.0)
      {
            MARK_PARTICLE(tp, P_FL_REMOVED);
            P_DIAM(tp) = 0.0;
            return;
      }

      /* free surface finder */
      C_FREE_SURFACE(c, t) = 0.0;

      if (laserm2 > 1.0)
      {
            if ((C_VMAG(c, t) > 90000.0) && (C_VOLUME_FRACTION(c, t) >
0.1))
            {
                  C_FREE_SURFACE(c, t) = 1.0;

                  NV_D(norm, =, C_NSURFACE_NORM_X(c, t),
C_NSURFACE_NORM_Y(c, t), C_NSURFACE_NORM_Z(c, t));
                  NV_D(nonorm, =, C_SURFACE_NORM_X(c, t),
C_SURFACE_NORM_Y(c, t), C_SURFACE_NORM_Z(c, t));
                  NV_V(inc, =, TP_VEL(tp));
                  normal_velocity = NV_DOT(inc, norm);
                  if (normal_velocity >= 0.0)
                  {
                        return;                  /* particle is coming from
the phase side */
                  }
                  normal_velocity *= 2.0;
                  NV_VS(inc, -=, norm, *, normal_velocity);
```

```
                cos_angle = ((NV_DOT(inc, nonorm)) / (NV_MAG(inc) *
NV_MAG(nonorm)));
                sin_angle = (sqrt(1.0 - SQR(cos_angle)));
                cnums = cos_angle - csqrt((cpow(index, 2)) -
(cpow(sin_angle, 2)));
                cdems = cos_angle + csqrt((cpow(index, 2)) -
(cpow(sin_angle, 2)));
                cnump = (cpow(index, 2) * cos_angle) - csqrt(cpow(index,
2) - (cpow(sin_angle, 2)));
                cdemp = (cpow(index, 2) * cos_angle) + csqrt(cpow(index,
2) - (cpow(sin_angle, 2)));
                Spol = (cpow(cabs(cnums / cdems), 2));
                Ppol = (cpow(cabs(cnump / cdemp), 2));
                rf = (0.5 * Spol) + (0.5 * Ppol);
                Ab = 1.0 - rf;

                C_CELL_WATTSM2(c, t) += TP_BEAM_WATTS(tp) * Ab;
                TP_BEAM_WATTS(tp) -= TP_BEAM_WATTS(tp) * Ab;

                TP_BOUNCES(tp) += 1.0;
                NV_V(TP_VEL(tp), =, inc);
            }
        }
        else
        {
            C_CENTROID(x, c, t);
            if (x[2] > (substrate_height + 20e-6))
            {
                MARK_PARTICLE(tp, P_FL_REMOVED);
                P_DIAM(tp) = 0.0;
            }
        }
    }
}


DEFINE_EXECUTE_AT_END(reset)
{
    Domain* d;
    Thread* t;
    cell_t c;
    d = Get_Domain(1);

    thread_loop_c(t, d)
    {
        if (FLUID_THREAD_P(t))
        {
            begin_c_loop(c, t)
            {
                /* this section resets values in the ray tracing to
zero after each timestep and makes values available for console */
                C_LASER_POWER_MOD2(c, t) = C_LASER_POWER_MOD(c, t);
                C_CELL_WATTS2(c, t) = C_CELL_WATTSM2(c, t);

                C_LASER_POWER_MOD(c, t) = 0.0;
                C_LASERM2_START(c, t) = 0.0;
                C_CELL_WATTSM2(c, t) = 0.0;

            }
            end_c_loop(c, t)
        }
```

```c
        }
}

DEFINE_SOURCE(LaserEnergy, c, t, dS, eqn)
{
    real source = 0.0;

    if (gauss_iv == 0)
    {
        C_ENERGY_AB(c, t) = 0.0;

        if (N_TIME > laser_on)
        {
            if ((CURRENT_TIME < laser_off) && (C_VOLUME_FRACTION(c,
t) > 0.1))
            {
                source = (C_CELL_WATTSM2(c, t) * C_AREA(c, t)) /
(C_VOLUME(c, t));

                C_ENERGY_AB(c, t) = (C_CELL_WATTSM2(c, t) *
C_AREA(c, t)) / (C_VOLUME(c, t));

                if (source > source_limit)
                {
                    source = source_limit;
                }
            }
        }
    }

    dS[eqn] = 0.0;
    C_LASERM3_HST(c, t) = source;

    return source;
}

DEFINE_SOURCE(HeatLosses, c, t, dS, eqn)
{
    Thread* g, * w;
    g = THREAD_SUB_THREAD(t, 0);
    w = THREAD_SUB_THREAD(t, 1);
    real T = C_T(c, t);
    real source = 0.0;
    real DCP;
    real evap_heat_loss = 0.0;
    real rad_loss, fp1, sp1;

    // C_CP : specific heat
    // C_R  : density

    // Equation 18 : "smoothing term"
    DCP = (2.0 * C_R(c, t) * C_CP(c, t)) / ((C_R(c, g) * C_CP(c, g)) +
(C_R(c, w) * C_CP(c, w)));

    if (T > boiling_temp)
    {
        fp1 = -0.82 * ((latent_vap * molar_mass) / (sqrt(2.0 * M_PI *
molar_mass * 8.314 * T))) * 101000.0;
        sp1 = exp((latent_vap * molar_mass * (T - boiling_temp)) /
(8.314 * T * boiling_temp));
```

267

```
            evap_heat_loss = fp1 * sp1;
        }

        rad_loss = -5.67e-8 * 0.26 * ((pow(T, 4.0)) - (pow(300.0, 4.0)));

        source = (rad_loss + evap_heat_loss) * C_VMAG(c, t) * DCP;

        if (source > 0.0)
        {
            source = 0.0;
        }

        if (source < (-source_limit))
        {
            source = -source_limit;
        }

        dS[eqn] = 0.0;
        C_HEATLOSS_HST(c, t) = source;
        C_DCP(c, t) = DCP;
        return source;
}

DEFINE_SOURCE(x_mom, c, t, dS, eqn)
{
        Thread* g, * w;
        g = THREAD_SUB_THREAD(t, 0);
        w = THREAD_SUB_THREAD(t, 1);
        real source = 0.0;
        real recoil_pressure = 0.0;
        real marangoni_flow = 0.0;
        real D;
        real T = C_T(c, t);
        D = (2.0 * C_R(c, t)) / ((C_R(c, g) + C_R(c, w)));

        if (C_VMAG(c, t) != 0)
        {
            if (T > boiling_temp)
            {
                recoil_pressure = (0.54 * 101000.0 * exp((latent_vap *
molar_mass * (T - boiling_temp)) / (8.314 * T * boiling_temp))) *
C_VOF_NX(c, t);
            }
            if (C_LIQUID_FRAC(c, t) > 0)
            {
                marangoni_flow = temp_surface_tension * (C_TEMP_G_X(c, t)
- (C_VOF_NX(c, t) * (ND_DOT(C_VOF_NX(c, t), C_VOF_NY(c, t), C_VOF_NZ(c, t),
C_TEMP_G_X(c, t), C_TEMP_G_Y(c, t), C_TEMP_G_Z(c, t)))));
            }
        }

        source = (recoil_pressure + marangoni_flow) * C_VMAG(c, t) * D;
        dS[eqn] = 0.0;

        C_X_MOM_SOURCE(c, t) = fabs(source);
        C_RECOIL_PRESSURE_X(c, t) = recoil_pressure;
        C_MARANGONI_FLOW_X(c, t) = marangoni_flow;

        return source;
}
```

```
DEFINE_SOURCE(y_mom, c, t, dS, eqn)
{
      Thread* g, * w;
      g = THREAD_SUB_THREAD(t, 0);
      w = THREAD_SUB_THREAD(t, 1);
      real source = 0.0;
      real recoil_pressure = 0.0;
      real marangoni_flow = 0.0;
      real D;
      real T = C_T(c, t);

      D = (2.0 * C_R(c, t)) / ((C_R(c, g) + C_R(c, w)));

      if (C_VMAG(c, t) != 0)
      {
            if (T > boiling_temp)
            {
                  recoil_pressure = (0.54 * 101000.0 * exp((latent_vap *
molar_mass * (T - boiling_temp)) / (8.314 * T * boiling_temp))) *
C_VOF_NY(c, t);
            }
            if (C_LIQUID_FRAC(c, t) > 0)
            {
                  marangoni_flow = temp_surface_tension * (C_TEMP_G_Y(c, t)
- (C_VOF_NY(c, t) * (ND_DOT(C_VOF_NX(c, t), C_VOF_NY(c, t), C_VOF_NZ(c, t),
C_TEMP_G_X(c, t), C_TEMP_G_Y(c, t), C_TEMP_G_Z(c, t)))));
            }
      }

      source = (recoil_pressure + marangoni_flow) * C_VMAG(c, t) * D;
      dS[eqn] = 0.0;

      C_Y_MOM_SOURCE(c, t) = fabs(source);
      C_RECOIL_PRESSURE_Y(c, t) = recoil_pressure;
      C_MARANGONI_FLOW_Y(c, t) = marangoni_flow;

      return source;
}

DEFINE_SOURCE(z_mom, c, t, dS, eqn)
{
      Thread* g, * w;
      g = THREAD_SUB_THREAD(t, 0);
      w = THREAD_SUB_THREAD(t, 1);
      real source = 0.0;
      real recoil_pressure = 0.0;
      real marangoni_flow = 0.0;
      real D;
      real T = C_T(c, t);

      D = (2.0 * C_R(c, t)) / ((C_R(c, g) + C_R(c, w)));

      if (C_VMAG(c, t) != 0)
      {
            if (T > boiling_temp)
            {
                  recoil_pressure = (0.54 * 101000.0 * exp((latent_vap *
molar_mass * (T - boiling_temp)) / (8.314 * T * boiling_temp))) *
C_VOF_NZ(c, t);
```

```
                }
                if (C_LIQUID_FRAC(c, t) > 0)
                {
                        marangoni_flow = temp_surface_tension * (C_TEMP_G_Z(c, t)
- (C_VOF_NZ(c, t) * (ND_DOT(C_VOF_NX(c, t), C_VOF_NY(c, t), C_VOF_NZ(c, t),
C_TEMP_G_X(c, t), C_TEMP_G_Y(c, t), C_TEMP_G_Z(c, t)))));
                }
        }

        source = (recoil_pressure + marangoni_flow) * C_VMAG(c, t) * D;
        dS[eqn] = 0.0;

        C_Z_MOM_SOURCE(c, t) = fabs(source);
        C_RECOIL_PRESSURE_Z(c, t) = recoil_pressure;
        C_MARANGONI_FLOW_Z(c, t) = marangoni_flow;

        return source;
}

DEFINE_PROPERTY(surface_tensionn, c, t)
{
        real surface_tension1 = 0.0;
        if (C_LIQUID_FRAC(c, t) > 0)
        {
                surface_tension1 = surface_tension;
        }

        return surface_tension1;
}

DEFINE_PROPERTY(viscosityy, c, t)
{
        real viscosity1 = 10.0;

        if (C_LIQUID_FRAC(c, t) > 0)
        {
                viscosity1 = viscosity;
        }

        return viscosity1;
}

DEFINE_INIT(patching, domain)
{
#if !RP_HOST
        Thread* t, ** pt;
        cell_t c;
        real x[ND_ND];
        int num = 1064;
        int i = 1;
        int n = 0;
        int aa, bb, cc;
        real sphere_radius, disx, disy, disz;
        real location[3];
        real sphere_centre[3];
        real Zc = 77.57e-06;
        real domain_radius = 60e-06;

        mp_thread_loop_c(t, domain, pt)
        {
```

```
                    if (FLUID_THREAD_P(t))
                    {
                            begin_c_loop(c, t)
                            {
                                    C_VOF(c, pt[0]) = 0.0;

                                    C_LASER_POWER_MOD(c, t) = 0.0;
                                    C_LASERM2_START(c, t) = 0.0;
                                    C_CELL_WATTSM2(c, t) = 0.0;
                                    C_TEMP_TAG(c, t) = 0.0;

                                    //magic_power = 0.1;
                                    //magic_powerm3 = 0.1;

                                    C_CENTROID(x, c, t); /* Before, everything was
fluid ; Now we change what could be solid (if below substrate height  */
                                    if (x[2] < substrate_height) /* x2: z coordinates*/
                                    {
                                            C_VOF(c, pt[0]) = 1.0; /* si sous substrate
=> metal */
                                    }

                            }
                            C_VOF(c, pt[1]) = 1.0 - C_VOF(c, pt[0]);
                            end_c_loop(c, t)
                    }
            }
    Message0("\n Initialised LPBF");
    Message0("\n Type: %d ", gauss_iv);
    Message0("\n Pulsed: %d ", pulsed_laser);
    Message0("\n LaserPower: %g", laser_power);
    Message0("\n LaserBase: %g", laser_base);
    Message0("\n LaserVel: %g", laser_vel);
    Message0("\n PD: %g", point_distance);
    Message0("\n ET: %g", exposure_time);
    Message0("\n LaserSpot: %g", laser_spot_rad);
    Message0("\n InitX: %g", init_x);
    Message0("\n TrackLength: %g", track_length);
    Message0("\n CellSize: %g", cell_size);
    Message0("\n SubstrateHeight: %g", substrate_height);
    Message0("\n LaserPower: %g", laser_power);
    Message0("\n LVAP: %g", latent_vap);
    Message0("\n MM: %g", molar_mass);
    Message0("\n Boiling: %g", boiling_temp);
    Message0("\n ST: %g", surface_tension);
    Message0("\n TST: %g", temp_surface_tension);
    Message0("\n Viscosity: %g", viscosity);

#endif
}
```

D. Matlab routines for the prediction of the presence of lack-of-fusion and keyholes

D.1 pp_selector.m

```matlab
%% Definition of the investigated processing conditions
clear all, clc
powers=[100:20:400]'; % W, initialize the investigated powers
speeds=[0.5:0.25:1.5]'; % m/s, initialize the investigated scan speeds
NPOWERS=length(powers); % compute the number of investigated powers
NSPEEDS=length(speeds); % compute the number of investigated scan speeds
NTOT=NPOWERS*NSPEEDS; % compute the number of total P-v combinations
investigated
absorpt=load('computed_absorptivity.txt'); % load the trend of absorptivity
NEnthalpy_th=6; % Norm. Enthalpy Threshold
T0=300; % ambient temperature
k=193; % W/mK thermal conductivity of the material
rho=2780; % kg/m3 density
cp=875; % J/kgK specific heat
alfa=k/(rho*cp); % thermal diffusivity
T_start=638+273; % K temperature at the start of the solidification aka T
liquidus
T_last=502+273; % K temperature at the end of the solidification aka T
solidus
dspot=75*10^(-6); % m spot diameter
% Define and initialize the parameters' structure variable
i=0;
for ipowers=1:NPOWERS
    for ispeeds=1:NSPEEDS
        i=i+1;
        parameters(i).power=powers(ipowers);
        parameters(i).speed=speeds(ispeeds);
    end
end
% Add absorptivity and other process parameters to the structure variable
for i=1:NTOT
    parameters(i).absorptivity=absorpt(i);
    parameters(i).hatchd=120*10^(-6); % hatch distance in meters
    parameters(i).layert=30*10^(-6); % layer thickness in meters
    parameters(i).cflag=0;
    parameters(i).flag=0;
end
% Run Evaluations
for i=1:NTOT
    P=parameters(i).power;
    V=parameters(i).speed;
    lambda=parameters(i).absorptivity;
    L=parameters(i).layert;
    H=parameters(i).hatchd;
    run Rosenthal.m;
    parameters(i).mp_depth=d; % melt pool depth
    parameters(i).mp_length=l; % melt pool length
    parameters(i).mp_width=w; % melt pool widht

parameters(i).TANG_PARAMETER=sqrt((parameters(i).hatchd/parameters(i).mp_wi
```

```
dth)^2+(parameters(i).layert/parameters(i).mp_depth)^2); % evaluate the
Tang parameter

parameters(i).NEnthalpy=lambda*P/(rho*cp*T_start*sqrt(pi*k/(rho*cp)*V*dspot
^3));
end
% Flags are given depending on the Tang Parameter and Normalized Enthalpy
thresholds
for i=1:NTOT
    if parameters(i).TANG_PARAMETER<=1 % LOF condition
        parameters(i).cflag=1; % P-v is expected to have LOF
        if parameters(i).NEnthalpy<=NEnthalpy_th % Keyhole condition
            parameters(i).cflag=2; % P-v is expected to have keyholes
        end
    end
end
```

D.2 Rosenthal.m

```
% Initialize a domain
N=2000;
x=linspace(-0.002,0.002,N+1);
y=linspace(-0.002,0.002,N+1);
z=linspace(-0.004,0,N+1);
[X,Y]=meshgrid(x,y);
% Compute temperature trend on the x-y plane
T_planeXY=T0+lambda*P./(2*pi*k*sqrt(X.^2+Y.^2)).*exp(-
V*(sqrt(X.^2+Y.^2)+X)/(2*alfa));
[X,Z]=meshgrid(x,z);
% Compute temperature trend on the x-z plane
T_planeXZ=T0+lambda*P./(2*pi*k*sqrt(X.^2+Z.^2)).*exp(-
V*(sqrt(X.^2+Z.^2)+X)/(2*alfa));
tx=T_planeXY(N/2+1,:);
ty=T_planeXY(:,N/2+1);
tz=T_planeXZ(:,N/2+1);
% Compute width
w=0;
for iyy=1:N+1
    ty=T_planeXY(:,iyy);
    range_y=ty(ty>T_last);
    if length(range_y)*(y(end)-y(end-1))>=w
        w=length(range_y)*(y(end)-y(end-1));
    end
    clear ty
end
% Compute depth
d=0;
for izz=1:N+1
    tz=T_planeXZ(:,izz);
    range_z=tz(tz>T_last);
    if length(range_z)*(z(end)-z(end-1))>=d
        d=length(range_z)*(z(end)-z(end-1));
    end
    clear tz
end
% Compute length
range_x=tx(tx>T_last);
l=length(range_x)*(x(end)-x(end-1));
```

Bibliography

[1]   D. Blanco, E.M. Rubio, R.M. Lorente-Pedreille, M.A. Sáenz-Nuño, Sustainable Processes in Aluminium, Magnesium, and Titanium Alloys Applied to the Transport Sector: A Review, Metals (Basel). 12 (2022). https://doi.org/10.3390/met12010009.

[2]   A.C. Serrenho, J.B. Norman, J.M. Allwood, The impact of reducing car weight on global emissions: the future fleet in Great Britain, Philos. Trans. R. Soc. A Math. Phys. Eng. Sci. 375 (2017) 20160364. https://doi.org/10.1098/rsta.2016.0364.

[3]   W.E. Frazier, Metal Additive Manufacturing: A Review, J. Mater. Eng. Perform. 23 (2014) 1917–1928. https://doi.org/10.1007/s11665-014-0958-z.

[4]   T. DebRoy, H.L. Wei, J.S. Zuback, T. Mukherjee, J.W. Elmer, J.O. Milewski, A.M. Beese, A. Wilson-Heid, A. De, W. Zhang, Additive manufacturing of metallic components – Process, structure and properties, Prog. Mater. Sci. 92 (2018) 112–224. https://doi.org/https://doi.org/10.1016/j.pmatsci.2017.10.001.

[5]   D. Zhang, S. Sun, D. Qiu, M.A. Gibson, M.S. Dargusch, M. Brandt, M. Qian, M. Easton, Metal Alloys for Fusion-Based Additive Manufacturing, Adv. Eng. Mater. 20 (2018). https://doi.org/10.1002/adem.201700952.

[6]   N.T. Aboulkhair, M. Simonelli, L. Parry, I. Ashcroft, C. Tuck, R. Hague, 3D printing of Aluminium alloys: Additive Manufacturing of Aluminium alloys using selective laser melting, Prog. Mater. Sci. 106 (2019) 100578. https://doi.org/10.1016/j.pmatsci.2019.100578.

[7]   C. Kamath, B. El-Dasher, G.F. Gallegos, W.E. King, A. Sisto, Density of additively-manufactured, 316L SS parts using laser powder-bed fusion at powers up to 400 W, Int. J. Adv. Manuf. Technol. 74 (2014) 65–78.

[8]   N.T. Aboulkhair, Additive manufacture of an aluminium alloy: processing, microstructure, and mechanical properties, (2016).

[9]   L. Thijs, K. Kempen, J.-P. Kruth, J. Van Humbeeck, Fine-structured aluminium products with controllable texture by selective laser melting of pre-alloyed

AlSi10Mg powder, Acta Mater. 61 (2013) 1809–1819. https://doi.org/https://doi.org/10.1016/j.actamat.2012.11.052.

[10] N.T. Aboulkhair, I. Maskery, C. Tuck, I. Ashcroft, N.M. Everitt, On the formation of AlSi10Mg single tracks and layers in selective laser melting: Microstructure and nano-mechanical properties, J. Mater. Process. Technol. 230 (2016) 88–98.

[11] V. Matilainen, H. Piili, A. Salminen, T. Syvänen, O. Nyrhilä, Characterization of process efficiency improvement in laser additive manufacturing, Phys. Procedia. 56 (2014) 317–326.

[12] M. Garibaldi, I. Ashcroft, M. Simonelli, R. Hague, Metallurgy of high-silicon steel parts produced using Selective Laser Melting, Acta Mater. 110 (2016) 207–216. https://doi.org/10.1016/j.actamat.2016.03.037.

[13] N. Gardan, Knowledge management for topological optimization integration in additive manufacturing, Int. J. Manuf. Eng. 2014 (2014).

[14] J. Brennan-Craddock, D. Brackett, R. Wildman, R. Hague, The design of impact absorbing structures for additive manufacture, in: J. Phys. Conf. Ser., IOP Publishing, 2012: p. 12042.

[15] D.J. Brackett, I.A. Ashcroft, R.D. Wildman, R.J.M. Hague, An error diffusion based method to generate functionally graded cellular structures, Comput. Struct. 138 (2014) 102–111.

[16] C. Yan, L. Hao, A. Hussein, D. Raymont, Evaluations of cellular lattice structures manufactured using selective laser melting, Int. J. Mach. Tools Manuf. 62 (2012) 32–38.

[17] C. Qiu, S. Yue, N.J.E. Adkins, M. Ward, H. Hassanin, P.D. Lee, P.J. Withers, M.M. Attallah, Influence of processing conditions on strut structure and compressive properties of cellular lattice structures fabricated by selective laser melting, Mater. Sci. Eng. A. 628 (2015) 188–197.

[18] W.T. Carter, M.G. Jones, Direct laser sintering of metals, in: 1993 Int. Solid Free. Fabr. Symp., 1993.

[19] A. Zadi-Maad, R. Rohib, A. Irawan, Additive manufacturing for steels: A review, in:

IOP Conf. Ser. Mater. Sci. Eng., IOP Publishing, 2018: p. 12028.

[20] C.Y. Yap, C.K. Chua, Z.L. Dong, Z.H. Liu, D.Q. Zhang, L.E. Loh, S.L. Sing, Review of selective laser melting: Materials and applications, Appl. Phys. Rev. 2 (2015) 41101.

[21] D. Lynch, Improved Selective Laser Melting Processing of Aluminium-Silicon-Magnesium Alloys, The University of Liverpool (United Kingdom), 2019.

[22] M.M. Attallah, R. Jennings, X. Wang, L.N. Carter, Additive manufacturing of Ni-based superalloys: The outstanding issues, MRS Bull. 41 (2016) 758–764.

[23] S.C. Altıparmak, V.A. Yardley, Z. Shi, J. Lin, Challenges in additive manufacturing of high-strength aluminium alloys and current developments in hybrid additive manufacturing, Int. J. Light. Mater. Manuf. 4 (2021) 246–261. https://doi.org/https://doi.org/10.1016/j.ijlmm.2020.12.004.

[24] S. Bahl, K. Sisco, Y. Yang, F. Theska, S. Primig, L.F. Allard, R.A. Michi, C. Fancher, B. Stump, R. Dehoff, Al-Cu-Ce (-Zr) alloys with an exceptional combination of additive processability and mechanical properties, Addit. Manuf. 48 (2021) 102404.

[25] H.R. Kotadia, G. Gibbons, A. Das, P.D. Howes, A review of Laser Powder Bed Fusion Additive Manufacturing of aluminium alloys: Microstructure and properties, Addit. Manuf. 46 (2021) 102155. https://doi.org/https://doi.org/10.1016/j.addma.2021.102155.

[26] A.S.M.I.H. Committee, Properties and selection: nonferrous alloys and special-purpose materials, ASM Int. 2 (1992) 1143–1144.

[27] W. Xu, Y. Luo, W. Zhang, M. Fu, Comparative study on local and global mechanical properties of bobbin tool and conventional friction stir welded 7085-T7452 aluminum thick plate, J. Mater. Sci. Technol. 34 (2018) 173–184. https://doi.org/https://doi.org/10.1016/j.jmst.2017.05.015.

[28] J.C. Williams, E.A. Starke, Progress in structural materials for aerospace systems11The Golden Jubilee Issue—Selected topics in Materials Science and Engineering: Past, Present and Future, edited by S. Suresh., Acta Mater. 51 (2003) 5775–5799. https://doi.org/https://doi.org/10.1016/j.actamat.2003.08.023.

[29] J.R. Davis, Asm Specialty Handbook: Aluminum & Aluminum Alloys, ASM international, 1993.

[30] D. Raabe, C.C. Tasan, E.A. Olivetti, Strategies for improving the sustainability of structural metals, Nature. 575 (2019) 64–74.

[31] A. Aversa, G. Marchese, A. Saboori, E. Bassini, D. Manfredi, S. Biamino, D. Ugues, P. Fino, M. Lombardi, New aluminum alloys specifically designed for laser powder bed fusion: A review, Materials (Basel). 12 (2019). https://doi.org/10.3390/ma12071007.

[32] S. Kou, Welding metallurgy, New Jersey, USA. (2003) 431–446.

[33] S. Begoc, F. Montredon, G. Pommatau, G. Leger, M. Gas, S. Eyrignoux, Additive manufacturing of Scalmalloy® satellite parts, Proc. 8th Eur. Conf. Aeronaut. Sp. Sci. (2019) 1–15. https://doi.org/10.13009/EUCASS2019-677.

[34] S. Lathabai, P.G. Lloyd, The effect of scandium on the microstructure, mechanical properties and weldability of a cast Al-Mg alloy, Acta Mater. 50 (2002) 4275–4292. https://doi.org/10.1016/S1359-6454(02)00259-8.

[35] H. Zhang, D. Gu, J. Yang, D. Dai, T. Zhao, C. Hong, A. Gasser, R. Poprawe, Selective laser melting of rare earth element Sc modified aluminum alloy: Thermodynamics of precipitation behavior and its influence on mechanical properties, Addit. Manuf. 23 (2018) 1–12. https://doi.org/10.1016/j.addma.2018.07.002.

[36] D. Buchbinder, H. Schleifenbaum, S. Heidrich, W. Meiners, J. Bültmann, High power selective laser melting (HP SLM) of aluminum parts, Phys. Procedia. 12 (2011) 271–278.

[37] T.H.C. Childs, C. Hauser, Raster scan selective laser melting of the surface layer of a tool steel powder bed, Proc. Inst. Mech. Eng. Part B J. Eng. Manuf. 219 (2005) 379–384.

[38] A. V Gusarov, J.-P. Kruth, Modelling of radiation transfer in metallic powders at laser treatment, Int. J. Heat Mass Transf. 48 (2005) 3423–3434.

[39] A.T. Clare, W.J. Reynolds, J.W. Murray, N.T. Aboulkhair, M. Simonelli, M. Hardy, D.M. Grant, C. Tuck, Laser calorimetry for assessment of melting behaviour in multi-

walled carbon nanotube decorated aluminium by laser powder bed fusion, CIRP Ann. 69 (2020) 197–200.

[40] K. V Yang, P. Rometsch, T. Jarvis, J. Rao, S. Cao, C. Davies, X. Wu, Porosity formation mechanisms and fatigue response in Al-Si-Mg alloys made by selective laser melting, Mater. Sci. Eng. A. 712 (2018) 166–174.

[41] G.M. Oreper, J. Szekely, Heat- and fluid-flow phenomena in weld pools, J. Fluid Mech. 147 (1984) 53–79. https://doi.org/DOI: 10.1017/S0022112084001981.

[42] R.W. Messler Jr, Principles of welding: processes, physics, chemistry, and metallurgy, John Wiley & Sons, 2008.

[43] H. Wu, J. Li, Z. Wei, P. Wei, Effect of processing parameters on forming defects during selective laser melting of AlSi10Mg powder, Rapid Prototyp. J. 26 (2020) 871–879. https://doi.org/10.1108/RPJ-07-2018-0184.

[44] W.J. Sames, F. Medina, W.H. Peter, S.S. Babu, R.R. Dehoff, Effect of process control and powder quality on Inconel 718 produced using electron beam melting, in: 8th Int. Symp. Superalloy 718 Deriv, 2014: pp. 409–423.

[45] A. Association, Aluminum: properties and physical metallurgy, ASM international, 1984.

[46] E. Louvis, P. Fox, C.J. Sutcliffe, Selective laser melting of aluminium components, J. Mater. Process. Technol. 211 (2011) 275–284. https://doi.org/https://doi.org/10.1016/j.jmatprotec.2010.09.019.

[47] H.D. Carlton, A. Haboub, G.F. Gallegos, D.Y. Parkinson, A.A. MacDowell, Damage evolution and failure mechanisms in additively manufactured stainless steel, Mater. Sci. Eng. A. 651 (2016) 406–414.

[48] T. Mukherjee, T. DebRoy, Mitigation of lack of fusion defects in powder bed fusion additive manufacturing, J. Manuf. Process. 36 (2018) 442–449. https://doi.org/https://doi.org/10.1016/j.jmapro.2018.10.028.

[49] M. Tang, P.C. Pistorius, J.L. Beuth, Prediction of lack-of-fusion porosity for powder bed fusion, Addit. Manuf. 14 (2017) 39–48.

[50] M. Tang, P.C. Pistorius, J. Beuth, Geometric model to predict porosity of part produced in powder bed system, Mater. Sci. Technol. Proc. (2015) 129–136.

[51] D. Rosenthal, Mathematical theory of heat distribution during welding and cutting, Weld. J. 20 (1941) 220–234.

[52] R. Rai, J.W. Elmer, T.A. Palmer, T. DebRoy, Heat transfer and fluid flow during keyhole mode laser welding of tantalum, Ti–6Al–4V, 304L stainless steel and vanadium, J. Phys. D. Appl. Phys. 40 (2007) 5753.

[53] R. Xiao, X. Zhang, Problems and issues in laser beam welding of aluminum–lithium alloys, J. Manuf. Process. 16 (2014) 166–175.

[54] A. Matsunawa, N. Seto, K. Jong-Do, M. Mizutani, S. Katayama, Observation of keyhole and molten pool behaviour in high power laser welding: Mechanism of porosity formation and its suppression method, Trans. JWRI. 30 (2001) 13–27.

[55] T. Fuhrich, P. Berger, H. Hügel, Marangoni effect in laser deep penetration welding of steel, J. Laser Appl. 13 (2001) 178–186. https://doi.org/10.2351/1.1404412.

[56] R. Lin, H. Wang, F. Lu, J. Solomon, B.E. Carlson, Numerical study of keyhole dynamics and keyhole-induced porosity formation in remote laser welding of Al alloys, Int. J. Heat Mass Transf. 108 (2017) 244–256. https://doi.org/https://doi.org/10.1016/j.ijheatmasstransfer.2016.12.019.

[57] M. Qu, Q. Guo, L.I. Escano, A. Nabaa, S.M.H. Hojjatzadeh, Z.A. Young, L. Chen, Controlling process instability for defect lean metal additive manufacturing, Nat. Commun. 13 (2022) 1–8. https://doi.org/10.1038/s41467-022-28649-2.

[58] A.A. Martin, N.P. Calta, S.A. Khairallah, J. Wang, P.J. Depond, A.Y. Fong, V. Thampy, G.M. Guss, A.M. Kiss, K.H. Stone, C.J. Tassone, J. Nelson Weker, M.F. Toney, T. van Buuren, M.J. Matthews, Dynamics of pore formation during laser powder bed fusion additive manufacturing, Nat. Commun. 10 (2019) 1–10. https://doi.org/10.1038/s41467-019-10009-2.

[59] S.M.H. Hojjatzadeh, N.D. Parab, W. Yan, Q. Guo, L. Xiong, C. Zhao, M. Qu, L.I. Escano, X. Xiao, K. Fezzaa, W. Everhart, T. Sun, L. Chen, Pore elimination mechanisms during 3D printing of metals, Nat. Commun. 10 (2019) 1–8.

https://doi.org/10.1038/s41467-019-10973-9.

[60] Z. Gan, O.L. Kafka, N. Parab, C. Zhao, L. Fang, O. Heinonen, T. Sun, W.K. Liu, Universal scaling laws of keyhole stability and porosity in 3D printing of metals, Nat. Commun. 12 (2021). https://doi.org/10.1038/s41467-021-22704-0.

[61] W.E. King, H.D. Barth, V.M. Castillo, G.F. Gallegos, J.W. Gibbs, D.E. Hahn, C. Kamath, A.M. Rubenchik, Observation of keyhole-mode laser melting in laser powder-bed fusion additive manufacturing, J. Mater. Process. Technol. 214 (2014) 2915–2925.

[62] L. Katgerman, D.G. Eskin, In search of the prediction of hot cracking in aluminium alloys, in: Hot Crack. Phenom. Welds II, Springer, 2008: pp. 11–26.

[63] M.S. Kenevisi, Y. Yu, F. Lin, A review on additive manufacturing of Al–Cu (2xxx) aluminium alloys, processes and defects, Mater. Sci. Technol. 37 (2021) 805–829.

[64] L.P. Connor, Welding Metallurgy, Weld. Handb. (1987) 89–124. https://doi.org/10.1007/978-1-349-10624-0_4.

[65] C.E. Cross, On the origin of weld solidification cracking, in: Hot Crack. Phenom. Welds, Springer, 2005: pp. 3–18.

[66] N. Kouraytem, P.-J. Chiang, R. Jiang, C. Kantzos, J. Pauza, R. Cunningham, Z. Wu, G. Tang, N. Parab, C. Zhao, K. Fezzaa, T. Sun, A.D. Rollett, Solidification crack propagation and morphology dependence on processing parameters in AA6061 from ultra-high-speed x-ray visualization, Addit. Manuf. 42 (2021) 101959. https://doi.org/https://doi.org/10.1016/j.addma.2021.101959.

[67] Y. Chen, S.J. Clark, D.M. Collins, S. Marussi, S.A. Hunt, D.M. Fenech, T. Connolley, R.C. Atwood, O. V Magdysyuk, G.J. Baxter, M.A. Jones, C.L.A. Leung, P.D. Lee, Correlative Synchrotron X-ray Imaging and Diffraction of Directed Energy Deposition Additive Manufacturing, Acta Mater. 209 (2021) 116777. https://doi.org/https://doi.org/10.1016/j.actamat.2021.116777.

[68] T. Sun, W. Tan, L. Chen, A. Rollett, In situ/operando synchrotron x-ray studies of metal additive manufacturing, MRS Bull. 45 (2020) 927–933. https://doi.org/DOI: 10.1557/mrs.2020.275.

[69] D. Wang, Z. Wang, K. Li, J. Ma, W. Liu, Z. Shen, Cracking in laser additively

manufactured W: Initiation mechanism and a suppression approach by alloying, Mater. Des. 162 (2019) 384–393.

[70] L.N. Carter, M.M. Attallah, R.C. Reed, Laser powder bed fabrication of nickel-base superalloys: influence of parameters; characterisation, quantification and mitigation of cracking, Superalloys. 2012 (2012) 2826–2834.

[71] A. Hariharan, L. Lu, J. Risse, A. Kostka, B. Gault, E.A. Jägle, D. Raabe, Misorientation-dependent solute enrichment at interfaces and its contribution to defect formation mechanisms during laser additive manufacturing of superalloys, Phys. Rev. Mater. 3 (2019) 123602.

[72] N. Coniglio, C.E. Cross, Initiation and growth mechanisms for weld solidification cracking, Int. Mater. Rev. 58 (2013) 375–397.

[73] R. Giorjao, B. Sutton, A. Ramirez, New composition based technique for solidification cracking resistance evaluation, Metall. Mater. Trans. A. 52 (2021) 2512–2521.

[74] T.W. Clyne, C. TW, The influence of composition on solidification cracking susceptibility in binary alloy systems, (1981).

[75] T.W. Clyne, M. Wolf, W. Kurz, The effect of melt composition on solidification cracking of steel, with particular reference to continuous casting, Metall. Trans. B. 13 (1982) 259–266.

[76] M. Rappaz, J.-M. Drezet, M. Gremaud, A new hot-tearing criterion, Metall. Mater. Trans. A. 30 (1999) 449–455.

[77] W.H. Suyitno, W.H. Kool, L. Katgerman, Integrated approach for prediction of hot tearing, Metall. Mater. Trans. A Phys. Metall. Mater. Sci. 40 (2009) 2388–2400. https://doi.org/10.1007/s11661-009-9941-y.

[78] S. Kou, A criterion for cracking during solidification, Acta Mater. 88 (2015) 366–374.

[79] S. Kou, A simple index for predicting the susceptibility to solidification cracking, Weld. J. 94 (2015) 374s–388s.

[80] J. Campbell, Complete casting handbook: metal casting processes, metallurgy, techniques and design, Butterworth-Heinemann, 2015.

[81] J.-M. Drezet, D. Allehaux, Application of the rappaz-drezet-gremaud hot tearing criterion to welding of aluminium alloys, in: Hot Crack. Phenom. Welds II, Springer, 2008: pp. 27–45.

[82] C.E. Cross, N. Coniglio, P. Schempp, M. Mousavi, Critical conditions for weld solidification crack growth, in: Hot Crack. Phenom. Welds III, Springer, 2011: pp. 25–41.

[83] Z. Sun, X.P. Tan, M. Descoins, D. Mangelinck, S.B. Tor, C.S. Lim, Revealing hot tearing mechanism for an additively manufactured high-entropy alloy via selective laser melting, Scr. Mater. 168 (2019) 129–133. https://doi.org/10.1016/j.scriptamat.2019.04.036.

[84] E. Scheil, Bemerkungen zur schichtkristallbildung, Int. J. Mater. Res. 34 (1942) 70–72.

[85] T. Soysal, S. Kou, A simple test for assessing solidification cracking susceptibility and checking validity of susceptibility prediction, Acta Mater. 143 (2018) 181–197.

[86] M. Raissi, A. Yazdani, G.E. Karniadakis, Hidden fluid mechanics: Learning velocity and pressure fields from flow visualizations, Science (80-.). 367 (2020) 1026–1030. https://doi.org/10.1126/science.aaw4741.

[87] S. Karimpouli, P. Tahmasebi, Physics informed machine learning: Seismic wave equation, Geosci. Front. 11 (2020) 1993–2001. https://doi.org/https://doi.org/10.1016/j.gsf.2020.07.007.

[88] B. Mondal, T. Mukherjee, T. DebRoy, Crack free metal printing using physics informed machine learning, Acta Mater. 226 (2022) 117612. https://doi.org/https://doi.org/10.1016/j.actamat.2021.117612.

[89] B.A. Fulcher, D.K. Leigh, T.J. Watt, Comparison of AlSi10Mg and Al 6061 processed through DMLS, in: 2014 Int. Solid Free. Fabr. Symp., University of Texas at Austin, 2014.

[90] C.E. Roberts, D. Bourell, T. Watt, J. Cohen, A Novel Processing Approach for Additive

Manufacturing of Commercial Aluminum Alloys, Phys. Procedia. 83 (2016) 909–917. https://doi.org/https://doi.org/10.1016/j.phpro.2016.08.095.

[91] S. Dadbakhsh, R. Mertens, K. Vanmeensel, J. Vleugels, J. Van Humbeeck, J.-P. Kruth, In situ alloying and reinforcing of Al6061 during selective laser melting, Procedia CIRP. 74 (2018) 39–43.

[92] A. Mehta, L. Zhou, T. Huynh, S. Park, H. Hyer, S. Song, Y. Bai, D.D. Imholte, N.E. Woolstenhulme, D.M. Wachs, Y. Sohn, Additive manufacturing and mechanical properties of the dense and crack free Zr-modified aluminum alloy 6061 fabricated by the laser-powder bed fusion, Addit. Manuf. 41 (2021) 101966. https://doi.org/https://doi.org/10.1016/j.addma.2021.101966.

[93] S.Z. Uddin, L.E. Murr, C.A. Terrazas, P. Morton, D.A. Roberson, R.B. Wicker, Processing and characterization of crack-free aluminum 6061 using high-temperature heating in laser powder bed fusion additive manufacturing, Addit. Manuf. 22 (2018) 405–415.

[94] N. Qbau, N.D. Nam, N.X. Ca, N.T. Hien, The crack healing effect of scandium in aluminum alloys during laser additive manufacturing, J. Manuf. Process. 50 (2020) 241–246.

[95] A.H. Maamoun, Y.F. Xue, M.A. Elbestawi, S.C. Veldhuis, The effect of selective laser melting process parameters on the microstructure and mechanical properties of Al6061 and AlSi10Mg alloys, Materials (Basel). 12 (2018) 12.

[96] A. Sonawane, G. Roux, J.-J. Blandin, A. Despres, G. Martin, Cracking mechanism and its sensitivity to processing conditions during laser powder bed fusion of a structural aluminum alloy, Materialia. 15 (2021) 100976.

[97] M. Opprecht, J.-P. Garandet, G. Roux, C. Flament, M. Soulier, A solution to the hot cracking problem for aluminium alloys manufactured by laser beam melting, Acta Mater. 197 (2020) 40–53.

[98] L.-E. Loh, C.-K. Chua, W.-Y. Yeong, J. Song, M. Mapar, S.-L. Sing, Z.-H. Liu, D.-Q. Zhang, Numerical investigation and an effective modelling on the Selective Laser Melting (SLM) process with aluminium alloy 6061, Int. J. Heat Mass Transf. 80 (2015) 288–300. https://doi.org/https://doi.org/10.1016/j.ijheatmasstransfer.2014.09.014.

[99] C.M. Gourlay, A.K. Dahle, Dilatant shear bands in solidifying metals, Nature. 445 (2007) 70–73. https://doi.org/10.1038/nature05426.

[100] W. Liu, S. Huang, S. Du, T. Gao, Z. Zhang, X. Chen, L. Huang, The Effects of Heat Treatment on Microstructure and Mechanical Properties of Selective Laser Melting 6061 Aluminum Alloy, Micromachines. 13 (2022) 1059.

[101] Y.D. Jia, P. Ma, K.G. Prashanth, G. Wang, J. Yi, S. Scudino, F.Y. Cao, J.F. Sun, J. Eckert, Microstructure and thermal expansion behavior of Al-50Si synthesized by selective laser melting, J. Alloys Compd. 699 (2017) 548–553.

[102] P. Wang, H.C. Li, K.G. Prashanth, J. Eckert, S. Scudino, Selective laser melting of Al-Zn-Mg-Cu: Heat treatment, microstructure and mechanical properties, J. Alloys Compd. 707 (2017) 287–290.

[103] G. Li, X. Li, C. Guo, Y. Zhou, Q. Tan, W. Qu, X. Li, X. Hu, M.-X. Zhang, Q. Zhu, Investigation into the effect of energy density on densification, surface roughness and loss of alloying elements of 7075 aluminium alloy processed by laser powder bed fusion, Opt. Laser Technol. 147 (2022) 107621.

[104] Y. Guo, W. Wei, W. Shi, X. Zhou, H. Huang, S. Wen, X. Wu, K. Gao, L. Rong, P. Qi, Effect of aging treatment on phase evolution and mechanical properties of selective laser melted Al-Mg-Er-Zr alloy, Mater. Lett. 327 (2022) 133001.

[105] N. Kaufmann, M. Imran, T.M. Wischeropp, C. Emmelmann, S. Siddique, F. Walther, Influence of process parameters on the quality of aluminium alloy en AW 7075 using Selective Laser Melting (SLM), Phys. Procedia. 83 (2016) 918–926. https://doi.org/10.1016/j.phpro.2016.08.096.

[106] T. Wang, Y. Wang, X. Yang, B. Chen, H. Zhu, Cracks and process control in laser powder bed fusion of Al-Zn-Mg alloy, J. Manuf. Process. 81 (2022) 571–579. https://doi.org/10.1016/j.jmapro.2022.06.066.

[107] A.P. Babu, S. Choudhary, J.C. Griffith, A. Huang, N. Birbilis, On the corrosion of a high solute Al-Zn-Mg alloy produced by laser powder bed fusion, Corros. Sci. 189 (2021) 109626.

[108] W. Reschetnik, J.-P. Brüggemann, M.E. Aydinöz, O. Grydin, K.-P. Hoyer, G. Kullmer,

H.A. Richard, Fatigue crack growth behavior and mechanical properties of additively processed EN AW-7075 aluminium alloy, Procedia Struct. Integr. 2 (2016) 3040–3048.

[109] W. Stopyra, K. Gruber, I. Smolina, T. Kurzynowski, B. Kuźnicka, Laser powder bed fusion of AA7075 alloy: Influence of process parameters on porosity and hot cracking, Addit. Manuf. 35 (2020) 101270.

[110] J.H. Martin, B.D. Yahata, J.M. Hundley, J.A. Mayer, T.A. Schaedler, T.M. Pollock, 3D printing of high-strength aluminium alloys, Nature. 549 (2017) 365–369. https://doi.org/10.1038/nature23894.

[111] T. Qi, H. Zhu, H. Zhang, J. Yin, L. Ke, X. Zeng, Selective laser melting of Al7050 powder: Melting mode transition and comparison of the characteristics between the keyhole and conduction mode, Mater. Des. 135 (2017) 257–266.

[112] Q. Tan, Z. Fan, X. Tang, Y. Yin, G. Li, D. Huang, J. Zhang, Y. Liu, F. Wang, T. Wu, X. Yang, H. Huang, Q. Zhu, M.-X. Zhang, A novel strategy to additively manufacture 7075 aluminium alloy with selective laser melting, Mater. Sci. Eng. A. 821 (2021) 141638. https://doi.org/https://doi.org/10.1016/j.msea.2021.141638.

[113] S. Heiland, B. Milkereit, K.-P. Hoyer, E. Zhuravlev, O. Kessler, M. Schaper, Requirements for Processing High-Strength AlZnMgCu Alloys with PBF-LB/M to Achieve Crack-Free and Dense Parts, Materials (Basel). 14 (2021) 7190.

[114] J. Yi, C. Chang, X. Yan, Y. Xie, Y. Liu, M. Liu, K. Zhou, A novel hierarchical manufacturing method of the selective laser melted Al 7075 alloy, Mater. Charact. 191 (2022) 112124.

[115] T. Wang, Y. Wang, X. Yang, B. Chen, H. Zhu, Cracks and process control in laser powder bed fusion of Al-Zn-Mg alloy, J. Manuf. Process. 81 (2022) 571–579.

[116] A.P. Babu, A. Huang, N. Birbilis, On the heat treatment and mechanical properties of a high solute Al–Zn–Mg alloy processed through laser powder bed fusion process, Mater. Sci. Eng. A. 807 (2021) 140857.

[117] M. Karg, B. Ahuja, S. Kuryntsev, A. Gorunov, M. Schmidt, Processability of high strength Aluminum-Copper alloys AW-2022 and 2024 by Laser Beam Melting in

Powder Bed, in: 2014 Int. Solid Free. Fabr. Symp., University of Texas at Austin, 2014.

[118] Y. Qi, H. Zhang, X. Nie, Z. Hu, H. Zhu, X. Zeng, A high strength Al–Li alloy produced by laser powder bed fusion: Densification, microstructure, and mechanical properties, Addit. Manuf. 35 (2020) 101346.

[119] Q. Tan, Y. Liu, Z. Fan, J. Zhang, Y. Yin, M.-X. Zhang, Effect of processing parameters on the densification of an additively manufactured 2024 Al alloy, J. Mater. Sci. Technol. 58 (2020) 34–45.

[120] X. Nie, Z. Chen, Y. Qi, H. Zhang, C. Zhang, Z. Xiao, H. Zhu, Effect of defocusing distance on laser powder bed fusion of high strength Al–Cu–Mg–Mn alloy, Virtual Phys. Prototyp. 15 (2020) 325–339. https://doi.org/10.1080/17452759.2020.1760895.

[121] M.C.H. Karg, B. Ahuja, S. Wiesenmayer, S.V. Kuryntsev, M. Schmidt, Effects of process conditions on the mechanical behavior of aluminium wrought alloy EN AW-2219 (AlCu6Mn) additively manufactured by laser beam melting in powder bed, Micromachines. 8 (2017) 23.

[122] B. Ahuja, M. Karg, K.Y. Nagulin, M. Schmidt, Fabrication and Characterization of High Strength Al-Cu Alloys Processed Using Laser Beam Melting in Metal Powder Bed, Phys. Procedia. 56 (2014) 135–146. https://doi.org/https://doi.org/10.1016/j.phpro.2014.08.156.

[123] X. Nie, H. Zhang, H. Zhu, Z. Hu, L. Ke, X. Zeng, Analysis of processing parameters and characteristics of selective laser melted high strength Al-Cu-Mg alloys: From single tracks to cubic samples, J. Mater. Process. Technol. 256 (2018) 69–77. https://doi.org/https://doi.org/10.1016/j.jmatprotec.2018.01.030.

[124] M. Rasch, J. Heberle, M.A. Dechet, D. Bartels, M.R. Gotterbarm, L. Klein, A. Gorunov, J. Schmidt, C. Körner, W. Peukert, M. Schmidt, Grain structure evolution of Al-Cu alloys in powder bed fusion with laser beam for excellent mechanical properties, Materials (Basel). 13 (2020). https://doi.org/10.3390/ma13010082.

[125] P. Wang, C. Gammer, F. Brenne, K.G. Prashanth, R.G. Mendes, M.H. Rümmeli, T. Gemming, J. Eckert, S. Scudino, Microstructure and mechanical properties of a heat-treatable Al-3.5Cu-1.5Mg-1Si alloy produced by selective laser melting, Mater. Sci.

Eng. A. 711 (2018) 562–570. https://doi.org/10.1016/j.msea.2017.11.063.

[126] Y. Wang, X. Lin, Y. Zhao, T. Zhang, J. Fu, N. Zheng, Z. Wang, W. Huang, Cracking mechanism and its susceptibility to scanning speed during laser power bed fusion processed high-strength 2024Al alloy, Mater. Charact. 194 (2022) 112344. https://doi.org/https://doi.org/10.1016/j.matchar.2022.112344.

[127] H. Zhang, H. Zhu, T. Qi, Z. Hu, X. Zeng, Selective laser melting of high strength Al-Cu-Mg alloys: Processing, microstructure and mechanical properties, Mater. Sci. Eng. A. 656 (2016) 47–54. https://doi.org/10.1016/j.msea.2015.12.101.

[128] O. Gharbi, D. Jiang, D.R. Feenstra, S.K. Kairy, Y. Wu, C.R. Hutchinson, N. Birbilis, On the corrosion of additively manufactured aluminium alloy AA2024 prepared by selective laser melting, Corros. Sci. 143 (2018) 93–106. https://doi.org/10.1016/j.corsci.2018.08.019.

[129] Y. Qi, H. Zhang, J. Zhu, X. Nie, Z. Hu, H. Zhu, X. Zeng, Mechanical behavior and microstructure evolution of Al-Cu-Mg alloy produced by laser powder bed fusion: Effect of heat treatment, Mater. Charact. 165 (2020) 110364. https://doi.org/https://doi.org/10.1016/j.matchar.2020.110364.

[130] D.G. McCartney, Grain refining of aluminium and its alloys using inoculants, Int. Mater. Rev. 34 (1989) 247–260.

[131] H. Fredriksson, A. Olsson, Mechanism of transition from columnar to equiaxed zone in ingots, Mater. Sci. Technol. 2 (1986) 508–516.

[132] S.C. Flood, J.D. Hunt, Columnar and equiaxed growth: II. Equiaxed growth ahead of a columnar front, J. Cryst. Growth. 82 (1987) 552–560.

[133] J.D. Hunt, Steady state columnar and equiaxed growth of dendrites and eutectic, Mater. Sci. Eng. 65 (1984) 75–83.

[134] W. Kurz, C. Bezençon, M. Gäumann, Columnar to equiaxed transition in solidification processing, Sci. Technol. Adv. Mater. 2 (2001) 185.

[135] M. Easton, D. StJohn, Grain refinement of aluminum alloys: Part I. the nucleant and solute paradigms—a review of the literature, Metall. Mater. Trans. A. 30 (1999) 1613–1623.

[136] W. Kurz, D.J. Fisher, Fundamentals of solidification, 1984.

[137] P. Schempp, M. Rethmeier, Understanding grain refinement in aluminium welding, Weld. World. 59 (2015) 767–784. https://doi.org/10.1007/s40194-015-0251-2.

[138] A.L. Greer, A.M. Bunn, A. Tronche, P. V Evans, D.J. Bristow, Modelling of inoculation of metallic melts: application to grain refinement of aluminium by Al–Ti–B, Acta Mater. 48 (2000) 2823–2835.

[139] P.H. Desnain, Y. Fautrelle, J.-L. Meyer, J.-P. Riquet, F. Durand, Prediction of equiaxed grain density in multicomponent alloys, stirred electromagnetically, Acta Metall. Mater. 38 (1990) 1513–1523.

[140] M.A. Easton, D.H. StJohn, Partitioning of titanium during solidification of aluminium alloys, Mater. Sci. Technol. 16 (2000) 993–1000.

[141] R.S. Mishra, S. Thapliyal, Design approaches for printability-performance synergy in Al alloys for laser-powder bed additive manufacturing, Mater. Des. 204 (2021) 109640. https://doi.org/10.1016/j.matdes.2021.109640.

[142] M.A. Easton, D.H. StJohn, A model of grain refinement incorporating alloy constitution and potency of heterogeneous nucleant particles, Acta Mater. 49 (2001) 1867–1878. https://doi.org/https://doi.org/10.1016/S1359-6454(00)00368-2.

[143] M.-X. Zhang, P.M. Kelly, M.A. Easton, J.A. Taylor, Crystallographic study of grain refinement in aluminum alloys using the edge-to-edge matching model, Acta Mater. 53 (2005) 1427–1438. https://doi.org/https://doi.org/10.1016/j.actamat.2004.11.037.

[144] P.M. Kelly, M.-X. Zhang, Edge-to-edge matching—The fundamentals, Metall. Mater. Trans. A. 37 (2006) 833–839.

[145] G.J. Shiflet, J.H. van der Merwe, The role of structural ledges as misfit-compensating defects: fcc-bcc interphase boundaries, Metall. Mater. Trans. A. 25 (1994) 1895–1903.

[146] K.E. Knipling, D.C. Dunand, D.N. Seidman, Criteria for developing castable, creep-resistant aluminum-based alloys–A review, Int. J. Mater. Res. 97 (2006) 246–265.

[147] A.M. Samuel, S.A. Alkahtani, H.W. Doty, F.H. Samuel, Role of Zr and Sc addition in controlling the microstructure and tensile properties of aluminum–copper based alloys, Mater. Des. 88 (2015) 1134–1144.

[148] J. Liu, P. Yao, N. Zhao, C. Shi, H. Li, X. Li, D. Xi, S. Yang, Effect of minor Sc and Zr on recrystallization behavior and mechanical properties of novel Al–Zn–Mg–Cu alloys, J. Alloys Compd. 657 (2016) 717–725.

[149] A.B. Spierings, K. Dawson, T. Heeling, P.J. Uggowitzer, R. Schäublin, F. Palm, K. Wegener, Microstructural features of Sc-and Zr-modified Al-Mg alloys processed by selective laser melting, Mater. Des. 115 (2017) 52–63.

[150] A.B. Spierings, K. Dawson, K. Kern, F. Palm, K. Wegener, SLM-processed Sc-and Zr-modified Al-Mg alloy: Mechanical properties and microstructural effects of heat treatment, Mater. Sci. Eng. A. 701 (2017) 264–273.

[151] Y. Shi, P. Rometsch, K. Yang, F. Palm, X. Wu, Characterisation of a novel Sc and Zr modified Al–Mg alloy fabricated by selective laser melting, Mater. Lett. 196 (2017) 347–350.

[152] K. V. Yang, Y. Shi, F. Palm, X. Wu, P. Rometsch, Columnar to equiaxed transition in Al-Mg(-Sc)-Zr alloys produced by selective laser melting, Scr. Mater. 145 (2018) 113–117. https://doi.org/10.1016/j.scriptamat.2017.10.021.

[153] J. Bi, Z. Lei, Y. Chen, X. Chen, Z. Tian, J. Liang, X. Zhang, X. Qin, Microstructure and mechanical properties of a novel Sc and Zr modified 7075 aluminum alloy prepared by selective laser melting, Mater. Sci. Eng. A. 768 (2019) 138478.

[154] H. Tang, Y. Geng, S. Bian, J. Xu, Z. Zhang, An ultra-high strength over 700 MPa in Al-Mn-Mg-Sc-Zr alloy fabricated by selective laser melting, Acta Metall. Sin. (English Lett. 35 (2022) 466–474.

[155] J. Røyset, N. Ryum, Scandium in aluminium alloys, Int. Mater. Rev. 50 (2005) 19–44. https://doi.org/10.1179/174328005X14311.

[156] K. Schmidtke, F. Palm, A. Hawkins, C. Emmelmann, Process and mechanical properties: Applicability of a scandium modified Al-alloy for laser additive manufacturing, Phys. Procedia. 12 (2011) 369–374.

https://doi.org/10.1016/j.phpro.2011.03.047.

[157] N. Qbau, N.D. Nam, N.T. Hien, N.X. Ca, Development of light weight high strength aluminum alloy for selective laser melting, J. Mater. Res. Technol. 9 (2020) 14075–14081.

[158] Q. Jia, P. Rometsch, S. Cao, K. Zhang, X. Wu, Towards a high strength aluminium alloy development methodology for selective laser melting, Mater. Des. 174 (2019) 107775. https://doi.org/https://doi.org/10.1016/j.matdes.2019.107775.

[159] Q. Jia, P. Rometsch, P. Kürnsteiner, Q. Chao, A. Huang, M. Weyland, L. Bourgeois, X. Wu, Selective laser melting of a high strength AlMnSc alloy: Alloy design and strengthening mechanisms, Acta Mater. 171 (2019) 108–118.

[160] A. Muhammad, C. Xu, W. Xuejiao, S. Hanada, H. Yamagata, L. Hao, M. Chaoli, High strength aluminum cast alloy: A Sc modification of a standard Al–Si–Mg cast alloy, Mater. Sci. Eng. A. 604 (2014) 122–126.

[161] F. Wang, Z. Liu, D. Qiu, J.A. Taylor, M.A. Easton, M.-X. Zhang, Revisiting the role of peritectics in grain refinement of Al alloys, Acta Mater. 61 (2013) 360–370. https://doi.org/https://doi.org/10.1016/j.actamat.2012.09.075.

[162] H. Hu, M. Zhao, X. Wu, Z. Jia, R. Wang, W. Li, Q. Liu, The structural stability, mechanical properties and stacking fault energy of Al3Zr precipitates in Al-Cu-Zr alloys: HRTEM observations and first-principles calculations, J. Alloys Compd. 681 (2016) 96–108.

[163] R. Xu, R. Li, T. Yuan, P. Niu, M. Wang, Z. Lin, Microstructure, metallurgical defects and hardness of Al–Cu–Mg–Li–Zr alloy additively manufactured by selective laser melting, J. Alloys Compd. 835 (2020) 155372.

[164] H. Zhang, H. Zhu, X. Nie, J. Yin, Z. Hu, X. Zeng, Effect of Zirconium addition on crack, microstructure and mechanical behavior of selective laser melted Al-Cu-Mg alloy, Scr. Mater. 134 (2017) 6–10. https://doi.org/https://doi.org/10.1016/j.scriptamat.2017.02.036.

[165] X. Nie, H. Zhang, H. Zhu, Z. Hu, X. Zeng, The effect of processing parameter on zirconium modified Al-Cu-Mg alloys fabricated by selective laser melting, in: 2018

Int. Solid Free. Fabr. Symp., University of Texas at Austin, 2018.

[166] X. Nie, H. Zhang, H. Zhu, Z. Hu, L. Ke, X. Zeng, Effect of Zr content on formability, microstructure and mechanical properties of selective laser melted Zr modified Al-4.24 Cu-1.97 Mg-0.56 Mn alloys, J. Alloys Compd. 764 (2018) 977–986.

[167] X. Nie, H. Zhang, H. Zhu, Z. Hu, Y. Qi, X. Zeng, On the role of Zr content into Portevin-Le Chatelier (PLC) effect of selective laser melted high strength Al-Cu-Mg-Mn alloy, Mater. Lett. 248 (2019) 5–7.

[168] L. Li, R. Li, T. Yuan, C. Chen, Z. Zhang, X. Li, Microstructures and tensile properties of a selective laser melted Al–Zn–Mg–Cu (Al7075) alloy by Si and Zr microalloying, Mater. Sci. Eng. A. 787 (2020) 139492. https://doi.org/10.1016/j.msea.2020.139492.

[169] J.R. Croteau, S. Griffiths, M.D. Rossell, C. Leinenbach, C. Kenel, V. Jansen, D.N. Seidman, D.C. Dunand, N.Q. Vo, Microstructure and mechanical properties of Al-Mg-Zr alloys processed by selective laser melting, Acta Mater. 153 (2018) 35–44. https://doi.org/10.1016/j.actamat.2018.04.053.

[170] S. Griffiths, M.D. Rossell, J. Croteau, N.Q. Vo, D.C. Dunand, C. Leinenbach, Effect of laser rescanning on the grain microstructure of a selective laser melted Al-Mg-Zr alloy, Mater. Charact. 143 (2018) 34–42.

[171] J. Zhang, J. Gao, B. Song, L. Zhang, C. Han, C. Cai, K. Zhou, Y. Shi, A novel crack-free Ti-modified Al-Cu-Mg alloy designed for selective laser melting, Addit. Manuf. 38 (2021) 101829.

[172] Q. Tan, J. Zhang, Q. Sun, Z. Fan, G. Li, Y. Yin, Y. Liu, M.-X. Zhang, Inoculation Treatment of an Additively Manufactured 2024 Aluminium Alloy with Titanium Nanoparticles, SSRN Electron. J. (2020). https://doi.org/10.2139/ssrn.3592041.

[173] Z. Fan, X. Yan, Z. Fu, B. Niu, J. Chen, Y. Hu, C. Chang, J. Yi, In situ formation of D022-Al3Ti during selective laser melting of nano-TiC/AlSi10Mg alloy prepared by electrostatic self-assembly, Vacuum. 188 (2021) 110179.

[174] X. Zhang, Z. Xiao, W. Yu, C.K. Chua, L. Zhu, Z. Wang, P. Xue, S. Tan, Y. Wu, H. Zheng, Influence of erbium addition on the defects of selective laser-melted 7075

aluminium alloy, Virtual Phys. Prototyp. 17 (2022) 406–418.

[175] Q. Li, G. Li, X. Lin, D. Zhu, J. Jiang, S. Shi, F. Liu, W. Huang, K. Vanmeensel, Development of a high strength Zr/Sc/Hf-modified Al-Mn-Mg alloy using Laser Powder Bed Fusion: Design of a heterogeneous microstructure incorporating synergistic multiple strengthening mechanisms, Addit. Manuf. 57 (2022) 102967.

[176] B.S. Murty, S.A. Kori, M. Chakraborty, Grain refinement of aluminium and its alloys by heterogeneous nucleation and alloying, Int. Mater. Rev. 47 (2002) 3–29. https://doi.org/10.1179/095066001225001049.

[177] Z. Fan, Y. Wang, Y. Zhang, T. Qin, X.R. Zhou, G.E. Thompson, T. Pennycook, T. Hashimoto, Grain refining mechanism in the Al/Al–Ti–B system, Acta Mater. 84 (2015) 292–304.

[178] B. Huang, Y. Liu, Z. Zhou, W. Cheng, X. Liu, Selective laser melting of 7075 aluminum alloy inoculated by Al–Ti–B: Grain refinement and superior mechanical properties, Vacuum. 200 (2022) 111030.

[179] M.N. Patel, D. Qiu, G. Wang, M.A. Gibson, A. Prasad, D.H. StJohn, M.A. Easton, Understanding the refinement of grains in laser surface remelted Al–Cu alloys, Scr. Mater. 178 (2020) 447–451.

[180] P. Wang, C. Gammer, F. Brenne, T. Niendorf, J. Eckert, S. Scudino, A heat treatable TiB2/Al-3.5 Cu-1.5 Mg-1Si composite fabricated by selective laser melting: Microstructure, heat treatment and mechanical properties, Compos. Part B Eng. 147 (2018) 162–168.

[181] L.I. Pengting, T. Wenjie, W. Dong, L.I.U. Xiangfa, Grain refining potency of LaB6 on aluminum alloy, J. Rare Earths. 30 (2012) 1172–1176.

[182] J. Ding, C. Cui, Y. Sun, J. Ding, L. Zhao, S. Cui, Preparation of in-situ NdB6 nanoparticles and their reinforcement effect on Al–Cu–Mn alloy, J. Alloys Compd. 806 (2019) 393–400.

[183] S. Liu, C. Cui, X. Wang, C. Han, H. Chen, J. Shi, Interfacial microstructure and nucleating mechanism of melt-spun CeB6/Al composite inoculant, Appl. Surf. Sci. 431 (2018) 202–206.

[184] J. Ding, C. Cui, Y. Sun, J. Ding, L. Zhao, S. Cui, Microstructures and mechanical properties of in-situ CaB6 ceramic particles reinforced Al-Cu-Mn composite, Ceram. Int. 45 (2019) 21668–21675.

[185] P. Mair, V.S. Goettgens, T. Rainer, N. Weinberger, I. Letofsky-Papst, S. Mitsche, G. Leichtfried, Laser powder bed fusion of nano-CaB6 decorated 2024 aluminum alloy, J. Alloys Compd. 863 (2021) 158714. https://doi.org/10.1016/j.jallcom.2021.158714.

[186] J.E. Hatch, Aluminium Propertiesand Physical Metallurgy, Ohio, Am. Soc. (1984).

[187] W.-Y. Li, C. Zhang, X.P. Guo, G. Zhang, H.L. Liao, C. Coddet, Deposition characteristics of Al–12Si alloy coating fabricated by cold spraying with relatively large powder particles, Appl. Surf. Sci. 253 (2007) 7124–7130. https://doi.org/https://doi.org/10.1016/j.apsusc.2007.02.142.

[188] T. Kimura, T. Nakamoto, M. Mizuno, H. Araki, Effect of silicon content on densification, mechanical and thermal properties of Al-xSi binary alloys fabricated using selective laser melting, Mater. Sci. Eng. A. 682 (2017) 593–602.

[189] M.L. Montero-Sistiaga, R. Mertens, B. Vrancken, X. Wang, B. Van Hooreweder, J.-P. Kruth, J. Van Humbeeck, Changing the alloy composition of Al7075 for better processability by selective laser melting, J. Mater. Process. Technol. 238 (2016) 437–445. https://doi.org/https://doi.org/10.1016/j.jmatprotec.2016.08.003.

[190] Y. Otani, S. Sasaki, Effects of the addition of silicon to 7075 aluminum alloy on microstructure, mechanical properties, and selective laser melting processability, Mater. Sci. Eng. A. 777 (2020) 139079.

[191] A. Aversa, G. Marchese, D. Manfredi, M. Lorusso, F. Calignano, S. Biamino, M. Lombardi, P. Fino, M. Pavese, Laser powder bed fusion of a high strength Al-Si-Zn-Mg-Cu alloy, Metals (Basel). 8 (2018) 300.

[192] M.A. Easton, H. Wang, J. Grandfield, C.J. Davidson, D.H. StJohn, L.D. Sweet, M.J. Couper, Observation and prediction of the hot tear susceptibility of ternary Al-Si-Mg alloys, Metall. Mater. Trans. A. 43 (2012) 3227–3238.

[193] Y. Geng, Q. Wang, Y. Wang, Q. Zang, S. Mi, J. Xu, Y. Xiao, Y. Wu, J. Luan, Microstructural

evolution and strengthening mechanism of high-strength AlSi8. 1 Mg1. 4 alloy produced by selective laser melting, Mater. Des. 218 (2022) 110674.

[194] Industrial Metallurgists, The Aluminium-Copper phase diagram, (n.d.). https://www.imetllc.com/phase-diagram/.

[195] P. Wang, L. Deng, K.G. Prashanth, S. Pauly, J. Eckert, S. Scudino, Microstructure and mechanical properties of Al-Cu alloys fabricated by selective laser melting of powder mixtures, J. Alloys Compd. 735 (2018) 2263–2266.

[196] Z. Hu, H. Zhu, X. Nie, C. Zhang, H. Zhang, X. Zeng, On the role of atmospheric oxygen into mechanical properties and fracture behavior of selective laser melted AlCu5MnCdVA, Mater. Des. 150 (2018) 18–27.

[197] Z. Hu, H. Zhang, H. Zhu, Z. Xiao, X. Nie, X. Zeng, Microstructure, mechanical properties and strengthening mechanisms of AlCu5MnCdVA aluminum alloy fabricated by selective laser melting, Mater. Sci. Eng. A. 759 (2019) 154–166. https://doi.org/10.1016/j.msea.2019.04.114.

[198] Z. Hu, Y. Qi, S. Gao, X. Nie, H. Zhang, H. Zhu, X. Zeng, Aging responses of an Al-Cu alloy fabricated by selective laser melting, Addit. Manuf. 37 (2021) 101635.

[199] Z. Hu, X. Nie, Y. Qi, H. Zhang, H. Zhu, Cracking criterion for high strength Al–Cu alloys fabricated by selective laser melting, Addit. Manuf. 37 (2021) 101709.

[200] M.C.H. Karg, M. Rasch, K. Schmidt, S.A.E. Spitzer, T.F. Karsten, D. Schlaug, C.-R. Biaciu, A.I. Gorunov, M. Schmidt, Laser alloying advantages by dry coating metallic powder mixtures with SiOx nanoparticles, Nanomaterials. 8 (2018) 862.

[201] A. Plotkowski, O. Rios, N. Sridharan, Z. Sims, K. Unocic, R.T. Ott, R.R. Dehoff, S.S. Babu, Evaluation of an Al-Ce alloy for laser additive manufacturing, Acta Mater. 126 (2017) 507–519.

[202] L.F. Mondolfo, Aluminum alloys: structure and properties, Elsevier, 2013.

[203] H.E. Bishop, Some electron backscattering measurements for solid targets, Opt. Des Rayons X Microanal. 153 (1966).

[204] S.S. van-Bavel, E. Sourty, J. Loos, Three-dimensional nanoscale organization of bulk

heterojunction polymer solar cells., Nano Lett. 9 (2009) 507–513.

[205] B.D. Cullity, Elements of X-ray Diffraction, Addison-Wesley Publishing, 1956.

[206] ResoDyn, ResonantAcoustic ® Mixing, (n.d.) 1–8.

[207] P.J. Spencer, A brief history of CALPHAD, Calphad. 32 (2008) 1–8. https://doi.org/https://doi.org/10.1016/j.calphad.2007.10.001.

[208] J.O. Andersson, T. Helander, L. Höglund, P. Shi, B. Sundman, Thermo-Calc & DICTRA, computational tools for materials science, Calphad Comput. Coupling Phase Diagrams Thermochem. 26 (2002) 273–312. https://doi.org/10.1016/S0364-5916(02)00037-8.

[209] Thermo-Calc, TCAL6: TCS Al-based Allot Database, (2019). https://thermocalc.com/products/databases/aluminum-based-alloys/.

[210] Ansys Fluent Theory Guide, Ansys Fluent Theory Guide, ANSYS Inc., USA. 15317 (2021) 724–746. http://scholar.google.com/scholar?hl=en&btnG=Search&q=intitle:ANSYS+FLUENT+Theory+Guide#0.

[211] T.S. Piwonka, M.C. Flemings, Pore formation in solidification, Aime Met Soc Trans. 236 (1966) 1157–1165.

[212] K. Kubo, R.D. Pehlke, Mathematical modeling of porosity formation in solidification, Metall. Trans. B. 16 (1985) 359–366.

[213] F. Rösler, D. Brüggemann, Shell-and-tube type latent heat thermal energy storage: numerical analysis and comparison with experiments, Heat Mass Transf. 47 (2011) 1027. https://doi.org/10.1007/s00231-011-0866-9.

[214] O. Andreau, I. Koutiri, P. Peyre, J.-D. Penot, N. Saintier, E. Pessard, T. De Terris, C. Dupuy, T. Baudin, Texture control of 316L parts by modulation of the melt pool morphology in selective laser melting, J. Mater. Process. Technol. 264 (2019) 21–31. https://doi.org/https://doi.org/10.1016/j.jmatprotec.2018.08.049.

[215] C. Tang, K.Q. Le, C.H. Wong, Physics of humping formation in laser powder bed fusion, Int. J. Heat Mass Transf. 149 (2020) 119172.

[216] C.D. Boley, S.A. Khairallah, A.M. Rubenchik, Calculation of laser absorption by metal powders in additive manufacturing, Appl. Opt. 54 (2015) 2477–2482.

[217] B. Liu, G. Fang, L. Lei, W. Liu, A new ray tracing heat source model for mesoscale CFD simulation of selective laser melting (SLM), Appl. Math. Model. 79 (2020) 506–520.

[218] A.D. Rakić, Algorithm for the determination of intrinsic optical constants of metal films: application to aluminum, Appl. Opt. 34 (1995) 4755–4767.

[219] S. Krishnan, P.C. Nordine, Optical properties of liquid aluminum in the energy range 1.2–3.5 eV, Phys. Rev. B. 47 (1993) 11780.

[220] J. Trapp, A.M. Rubenchik, G. Guss, M.J. Matthews, In situ absorptivity measurements of metallic powders during laser powder-bed fusion additive manufacturing, Appl. Mater. Today. 9 (2017) 341–349.

[221] J. Newman, Physics of the life sciences, Springer Science & Business Media, 2010.

[222] K.C. Mills, Recommended values of thermophysical properties for selected commercial alloys, Woodhead Publishing, 2002.

[223] A.E. Gheribi, P. Chartrand, Temperature and oxygen adsorption coupling effects upon the surface tension of liquid metals, Sci. Rep. 9 (2019) 1–9.

[224] C. Tang, J.L. Tan, C.H. Wong, A numerical investigation on the physical mechanisms of single track defects in selective laser melting, Int. J. Heat Mass Transf. 126 (2018) 957–968.

[225] G.V. Kumar, M. Kampili, S. Kelm, K.A. Prakash, H.-J. Allelein, CFD modelling of buoyancy driven flows in enclosures with relevance to nuclear reactor safety, Nucl. Eng. Des. 365 (2020) 110682.

[226] M. Leitner, T. Leitner, A. Schmon, K. Aziz, G. Pottlacher, Thermophysical properties of liquid aluminum, Metall. Mater. Trans. A. 48 (2017) 3036–3045.

[227] J.M. Drezet, M.S.F. Lima, J.D. Wagnière, M. Rappaz, W. Kurz, Crack-free aluminium alloy welds using a twin laser process, Weld. World. 52 (2008) 87–94.

[228] A. Standard, E8/E8M, Stand. Test Methods Tens. Test. Met. Mater. 3 (2011) 66.

[229] A. Standard, E384, Microindentation Hardness Mater. 14 (2002) 1–24.

[230] M. Tang, P.C. Pistorius, S. Narra, J.L. Beuth, Rapid Solidification: Selective Laser Melting of AlSi10Mg, Jom. 68 (2016) 960–966. https://doi.org/10.1007/s11837-015-1763-3.

[231] W.E. King, H.D. Barth, V.M. Castillo, G.F. Gallegos, J.W. Gibbs, D.E. Hahn, C. Kamath, A.M. Rubenchik, Observation of keyhole-mode laser melting in laser powder-bed fusion additive manufacturing, J. Mater. Process. Technol. 214 (2014) 2915–2925. https://doi.org/10.1016/j.jmatprotec.2014.06.005.

[232] R. Pokharel, L. Balogh, D.W. Brown, B. Clausen, G.T. Gray, V. Livescu, S.C. Vogel, S. Takajo, Signatures of the unique microstructure of additively manufactured steel observed via diffraction, Scr. Mater. 155 (2018) 16–20. https://doi.org/10.1016/j.scriptamat.2018.06.008.

[233] G. Li, S.D. Jadhav, A. Martín, M.L. Montero-Sistiaga, J. Soete, M.S. Sebastian, C.M. Cepeda-Jiménez, K. Vanmeensel, Investigation of Solidification and Precipitation Behavior of Si-Modified 7075 Aluminum Alloy Fabricated by Laser-Based Powder Bed Fusion, Metall. Mater. Trans. A Phys. Metall. Mater. Sci. 52 (2021) 194–210. https://doi.org/10.1007/s11661-020-06073-9.

[234] Y. Li, D. Gu, Parametric analysis of thermal behavior during selective laser melting additive manufacturing of aluminum alloy powder, Mater. Des. 63 (2014) 856–867. https://doi.org/https://doi.org/10.1016/j.matdes.2014.07.006.

[235] N.T. Aboulkhair, N.M. Everitt, I. Ashcroft, C. Tuck, Reducing porosity in AlSi10Mg parts processed by selective laser melting, Addit. Manuf. 1–4 (2014) 77–86. https://doi.org/https://doi.org/10.1016/j.addma.2014.08.001.

[236] A.A. Griffith, G.I. Taylor, VI. The phenomena of rupture and flow in solids, Philos. Trans. R. Soc. London. Ser. A, Contain. Pap. a Math. or Phys. Character. 221 (1921) 163–198. https://doi.org/10.1098/rsta.1921.0006.

[237] X. Liu, Q. Zhu, Y. Kang, Y. Zuo, R. Wang, Z. Li, An investigation of direct-chill cast 2024 aluminum alloy under the influence of high shearing with regards to different shear positions, J. Mater. Process. Technol. 279 (2020) 116547.

[238] C. Zhiqiang, J. Fei, Z. Xingguo, H. Hai, J. Junze, Microstructures and mechanical characteristics of electromagnetic casting and direct-chill casting 2024 aluminum alloys, Mater. Sci. Eng. A. 327 (2002) 133–137.

[239] N.A. Ahmad, A.A. Wheeler, W.J. Boettinger, G.B. McFadden, Solute trapping and solute drag in a phase-field model of rapid solidification, Phys. Rev. E. 58 (1998) 3436–3450. https://doi.org/10.1103/PhysRevE.58.3436.

[240] M.J. Aziz, Model for solute redistribution during rapid solidification, J. Appl. Phys. 53 (1982) 1158–1168. https://doi.org/10.1063/1.329867.

[241] M.J. Aziz, An atomistic model of solute trapping, Rapid Solidif. Process. Princ. Technol. III. (1982) 113–117.

[242] M.J. Aziz, T. Kaplan, Continuous growth model for interface motion during alloy solidification, Acta Metall. 36 (1988) 2335–2347. https://doi.org/https://doi.org/10.1016/0001-6160(88)90333-1.

[243] U. Scipioni Bertoli, B.E. MacDonald, J.M. Schoenung, Stability of cellular microstructure in laser powder bed fusion of 316L stainless steel, Mater. Sci. Eng. A. 739 (2019) 109–117. https://doi.org/10.1016/j.msea.2018.10.051.

[244] F.H. Froes, Y.-W. Kim, S. Krishnamurthy, Rapid solidification of lightweight metal alloys, Mater. Sci. Eng. A. 117 (1989) 19–32.

[245] D.G. Eskin, Suyitno, L. Katgerman, Mechanical properties in the semi-solid state and hot tearing of aluminium alloys, Prog. Mater. Sci. 49 (2004) 629–711. https://doi.org/https://doi.org/10.1016/S0079-6425(03)00037-9.

[246] M.L. Montero Sistiaga, R. Mertens, B. Vrancken, X. Wang, B. Van Hooreweder, J.P. Kruth, J. Van Humbeeck, Changing the alloy composition of Al7075 for better processability by selective laser melting, J. Mater. Process. Technol. 238 (2016) 437–445. https://doi.org/10.1016/j.jmatprotec.2016.08.003.

[247] S. Chandra, X. Tan, R.L. Narayan, C. Wang, S.B. Tor, G. Seet, A generalised hot cracking criterion for nickel-based superalloys additively manufactured by electron beam melting, Addit. Manuf. 37 (2021) 101633. https://doi.org/10.1016/j.addma.2020.101633.

[248] C. Hagenlocher, D. Weller, R. Weber, T. Graf, Analytical Description of the Influence of the Welding Parameters on the Hot Cracking Susceptibility of Laser Beam Welds in Aluminum Alloys, Metall. Mater. Trans. A Phys. Metall. Mater. Sci. 50 (2019) 5174–5180. https://doi.org/10.1007/s11661-019-05430-7.

[249] H. Matyja, The effect of cooling rate on the dendrite spacing in splat-cooled aluminium alloys, J. Inst. Met. 96 (1968) 30–32.

[250] M.C.H. Karg, B. Ahuja, S. Wiesenmayer, S.V. Kuryntsev, M. Schmidt, Effects of process conditions on the mechanical behavior of aluminium wrought alloy EN AW-2219 (AlCu6Mn) additively manufactured by laser beam melting in powder bed, Micromachines. 8 (2017) 1–11. https://doi.org/10.3390/mi8010023.

[251] M. M'hamdi, A. Mo, H.G. Fjær, TearSim: A two-phase model addressing hot tearing formation during aluminum direct chill casting, Metall. Mater. Trans. A Phys. Metall. Mater. Sci. 37 (2006) 3069–3083. https://doi.org/10.1007/s11661-006-0188-6.

[252] E. Orowan, Fracture and strength of solids, Reports Prog. Phys. 12 (1949) 185.

[253] J. Pelleg, Mechanical properties of materials, Springer Science & Business Media, 2012.

[254] M.F. Ashby, D. Cebon, Materials selection in mechanical design, Le J. Phys. IV. 3 (1993) C7-1.

[255] P. Mercelis, J.P. Kruth, Residual stresses in selective laser sintering and selective laser melting, Rapid Prototyp. J. 12 (2006) 254–265. https://doi.org/10.1108/13552540610707013.

[256] L.A. Parry, Investigation of Residual Stress, (n.d.).

[257] T. Mukherjee, W. Zhang, T. DebRoy, An improved prediction of residual stresses and distortion in additive manufacturing, Comput. Mater. Sci. 126 (2017) 360–372. https://doi.org/10.1016/j.commatsci.2016.10.003.

[258] D. Buchbinder, W. Meiners, N. Pirch, K. Wissenbach, J. Schrage, Investigation on reducing distortion by preheating during manufacture of aluminum components using selective laser melting, J. Laser Appl. 26 (2014) 12004.

[259] Z. Sun, X. Tan, C. Wang, M. Descoins, D. Mangelinck, S.B. Tor, E.A. Jägle, S. Zaefferer, D. Raabe, Reducing hot tearing by grain boundary segregation engineering in additive manufacturing: example of an AlxCoCrFeNi high-entropy alloy, Acta Mater. 204 (2021) 116505. https://doi.org/https://doi.org/10.1016/j.actamat.2020.116505.

[260] E. Chauvet, P. Kontis, E.A. Jägle, B. Gault, D. Raabe, C. Tassin, J.-J. Blandin, R. Dendievel, B. Vayre, S. Abed, G. Martin, Hot cracking mechanism affecting a non-weldable Ni-based superalloy produced by selective electron Beam Melting, Acta Mater. 142 (2018) 82–94. https://doi.org/https://doi.org/10.1016/j.actamat.2017.09.047.

[261] J.N. Ghoussoub, Y.T. Tang, C. Panwisawas, A. Németh, R.C. Reed, On the Influence of Alloy Chemistry and Processing Conditions on Additive Manufacturability of Ni-Based Superalloys, Miner. Met. Mater. Ser. (2020) 153–162. https://doi.org/10.1007/978-3-030-51834-9_15.

[262] M.J. Benoit, S.M. Zhu, T.B. Abbott, M.A. Easton, Evaluation of the Effect of Rare Earth Alloying Additions on the Hot Tearing Susceptibility of Aluminum Alloy 7150 During Rapid Solidification, Metall. Mater. Trans. A Phys. Metall. Mater. Sci. 51 (2020) 5213–5227. https://doi.org/10.1007/s11661-020-05930-x.

[263] N. Afzal, T. Shah, R. Ahmad, Microstructural features and mechanical properties of artificially aged AA2024, Strength Mater. 45 (2013) 684–692. https://doi.org/10.1007/s11223-013-9504-8.

[264] Q. Tan, Y. Liu, Z. Fan, J. Zhang, Y. Yin, M.X. Zhang, Effect of processing parameters on the densification of an additively manufactured 2024 Al alloy, J. Mater. Sci. Technol. 58 (2020) 34–45. https://doi.org/10.1016/j.jmst.2020.03.070.

[265] S. Li, H. Xiao, K. Liu, W. Xiao, Y. Li, X. Han, J. Mazumder, L. Song, Melt-pool motion, temperature variation and dendritic morphology of Inconel 718 during pulsed- and continuous-wave laser additive manufacturing: A comparative study, Mater. Des. 119 (2017) 351–360. https://doi.org/10.1016/j.matdes.2017.01.065.

[266] J. Campbell, Castings practice: the ten rules of castings, Elsevier, 2004.

[267] H. Zhang, H. Zhu, T. Qi, Z. Hu, X. Zeng, Selective laser melting of high strength Al–

Cu–Mg alloys: Processing, microstructure and mechanical properties, Mater. Sci. Eng. A. 656 (2016) 47–54. https://doi.org/https://doi.org/10.1016/j.msea.2015.12.101.

[268] Z.W. Chen, M.A.L. Phan, K. Darvish, Grain growth during selective laser melting of a Co–Cr–Mo alloy, J. Mater. Sci. 52 (2017) 7415–7427.

[269] M. Rappaz, A. Jacot, W.J. Boettinger, Last-stage solidification of alloys: Theoretical model of dendrite-arm and grain coalescence, Metall. Mater. Trans. A Phys. Metall. Mater. Sci. 34 A (2003) 467–479. https://doi.org/10.1007/s11661-003-0083-3.

[270] P. Das, R. Chandran, R. Samant, S. Anand, Optimum Part Build Orientation in Additive Manufacturing for Minimizing Part Errors and Support Structures, Procedia Manuf. 1 (2015) 343–354. https://doi.org/https://doi.org/10.1016/j.promfg.2015.09.041.

[271] T.H. Courtney, Mechanical behavior of materials, Waveland Press, 2005.

[272] H.W.L. Phillips, Annotated equilibrium diagrams of some aluminium alloy systems, Institute of metals, 1959.

[273] M. Rajabi, M. Vahidi, A. Simchi, P. Davami, Effect of rapid solidification on the microstructure and mechanical properties of hot-pressed Al–20Si–5Fe alloys, Mater. Charact. 60 (2009) 1370–1381. https://doi.org/https://doi.org/10.1016/j.matchar.2009.06.014.

[274] Effect of iron and silicon in aluminium and its alloys, Trans Tech Publ, Switzerland, 1990. http://inis.iaea.org/search/search.aspx?orig_q=RN:23000622.

[275] D.G. McCartney, J.D. Hunt, R.M. Jordan, The Structures Expected in a Simple Ternary Eutectic System: Part I . Theory, Metall. Trans. A. 11 (1980) 1243–1249.

[276] S. Kou, Transport phenomena and materials processing, 1996.